Hassall, Neil (2010) *Spin observables in kaon photoproduction from the neutron in a Deuterium target with CLAS.* PhD thesis.

http://theses.gla.ac.uk/1922/

Copyright and moral rights for this thesis are retained by the author

A copy can be downloaded for personal non-commercial research or study, without prior permission or charge

This thesis cannot be reproduced or quoted extensively from without first obtaining permission in writing from the Author

The content must not be changed in any way or sold commercially in any format or medium without the formal permission of the Author

When referring to this work, full bibliographic details including the author, title, awarding institution and date of the thesis must be given

Glasgow Theses Service
http://theses.gla.ac.uk/
theses@gla.ac.uk

Spin Observables in Kaon Photoproduction from the bound Neutron in a Deuterium target with CLAS

Neil Hassall

Presented as a Thesis for the Degree of Doctor of Philosophy

Nuclear Physics Group
Department of Physics and Astronomy
University of Glasgow

© N.Hassall 2010

Abstract

This work presents the first ever measurements of several polarization observables for the reactions $\overrightarrow{\gamma}d \rightarrow K^0\Lambda$ (p_s) and $\overrightarrow{\gamma}d \rightarrow K^0\Sigma^0$ (p_s). The data were collected in the spring of 2007 at the Thomas Jefferson National Accelerator Facility, using a linearly polarized photon beam in the energy range 1.3 to 2.3 GeV. In addition to measuring the single polarization observables, the photon beam asymmetry, target asymmetry and hyperon recoil polarization, measurements are made for the double polarization observables O_x and O_z.

The aim of the experiment was to search for "missing" baryon resonances produced by the process of strangeness photoproduction on the deuteron. These excited baryon states are predicted by $SU(6) \otimes O(3)$ symmetric quark models but are so far undetected in experiment.

The photon asymmetry for the $K^0\Lambda$ channel is found to be positive for the mid to forward angles over all energies. The backward angles show a negative photon asymmetry at energies above 1.5 GeV. The photon asymmetry remains flat for energies up to 1.5 GeV, where it then begins to show a peak at approximately $\cos(\theta_{cm}^{K^0}) \backsimeq 0$ for photon energies between 1.5 GeV to 1.9 GeV. At photon energies greater than 1.9 GeV, the asymmetry rises at forward angles, exhibiting a very strong signal at forward angles at energies between 2.1 GeV and 2.3 GeV. The photon asymmetry for the $K^0\Sigma^0$ channel is largely negative over all energies except at very forward angles. At 1.3 GeV, the asymmetry is relatively flat till 1.5 GeV where it gradually rises to a positive value at forward angles. From 1.7 GeV to 1.9 GeV, the asymmetry has a stronger signal at backward angles with it tending to small values close to zero at mid to forward angles. The 2.1 GeV setting again shows a strong asymmetry at backward angles with it rising to a positive value at a forward angle. There is a mid to forward angle peak forming at the 2.3 GeV setting with it then rising to a positive value at the forward angles.

The recoil polarization for the $K^0\Lambda$ channel is positive over the full angular range for energies between 1.225 GeV and 1.525 GeV. For energies between 1.675 GeV and 2.275 GeV the recoil polarization becomes negative at backward angles and positive at mid to forward angles. The $K^0\Sigma^0$ channel recoil polarizations are predominantly positive except at back to mid angles at 1.525 GeV and the backward angles in the 1.825 and 2.125 GeV data.

The results for O_x for $K^0\Lambda$ show a strong polarization signal at the lowest energy, 1.2 GeV over all $\cos(\theta_{cm}^{K^0})$ angles. For energies beyond 1.6 GeV, the

polarization becomes weaker and negative in most angular bins. For O_z the polarization transfer is small over all kinematics. In the $K^0\Sigma^0$ case the polarization transfer is strongest at the backward angles for O_x. For O_z the polarization is in general small. However there is a large polarization transfer at the backward angles for the 2.3 GeV data. The target asymmetry results for $K^0\Lambda$ at 1.2 GeV show a strong positive signal. The data between 1.6 GeV and 1.8 GeV show a change in sign of the asymmetry and are in general flat. For the $K^0\Sigma^0$ channel the data are almost all consistent with zero over all kinematics.

A comparison of the photon asymmetry for the free proton and bound neutron found that for the $K\Lambda$ channel the 1.3 GeV and 1.5 GeV data exhibit some good overlap between the proton and neutron data. The 1.7 GeV and 1.9 GeV data show some difference at the backward angles. The proton data is positive over all angles where as the neutron data is negative at backward angles. The 2.1 GeV data for the proton starts to fall to zero showing a similar trend to the neutron data. There is a difference in sign between the proton and neutron data at backward angles. The comparison of the $K\Sigma^0$ results shows a sign difference in the photon asymmetry over all but the extreme forward angles over all energies. The free proton results are positive over all kinematics. The neutron results are negative except at the extreme forward angles where the asymmetry is positive.

The hyperon recoil polarization comparison between the free proton and bound neutron for the $K^0\Lambda$ channel shows some agreement at mid to forward angles as one moves to higher photon energies. In the $K\Sigma^0$ case, the results from the neutron are predominantly positive over all energies. The results from the proton show a good proportion of the data to be negative.

The data have some preliminary interpretation with respect to the current Kaon-MAID and Regge-plus-resonance models. However, until the theoretical models improve no strong claim of finding a missing resonance can be made.

Declaration

The data presented in this thesis were obtained as part of the g13b collaboration at the Thomas Jefferson National Accelerator Facility, Virginia, USA, and the Nuclear Physics Experiment Group, The University of Glasgow. I participated fully in the preparation and execution of the experiment. The analysis of the experimental data is my own work. This thesis was composed by myself.

Neil Hassall

April 2010

Acknowledgements

First of all, I would like to say that without the help, love and support of a number of people then this thesis would not have been possible. Those in the Glasgow NPE group who should be singled out are Prof. Guenter Rosner who as the head of the NPE group offered me the chance to do a PhD and begin my research career. My supervisor Dr Ken Livingston deserves a very special thank you for all the help, advice and constructive criticism given during the course of my PhD.

My days at Jefferson Lab were made all the better by New York's finest medical physicist Joe Santoro. I really enjoyed our time at the lab and will never forget your help and kindness during my stays in Newport News. I hope to see you again someday soon!

When not enjoying the delights of Virginia, my working days in Glasgow were made all the better by my past and present office buddies. Namely, Craig Paterson, Russell Johnstone, Parada Hutauruk, Stuart Fegan and Joe Mancell.

Contents

1 Introduction **1**
1.1 QCD - Quantum Chromo-Dynamics 3
1.2 Baryon Spectroscopy 5
1.2.1 Constituent Quark Model 6
1.2.2 Missing Resonances 7
1.3 Kaons and Hyperons 10
1.4 Coherent Bremsstrahlung 12
1.5 Spin Observables in Pseudo-scalar meson Photoproduction 12
1.5.1 Formalism 12
1.5.2 Experimental Extraction of Spin Observables 15
1.6 Summary 16

2 Previous Experiments and Theoretical Background **18**
2.1 Previous Experiments 18
2.1.1 Deuteron Experiments at Jefferson Lab 19
2.1.2 Deuteron Experiments at other facilities 20
2.1.3 K^0 Differential Cross-Section Results - Laboratory of Nuclear Science (LNS) 24
2.2 Polarization Observables 24
2.3 Coupled-channels model 27
2.4 Isobar Models 29
2.5 Multi-pole and Partial Wave Analyses 33
2.6 Regge Models 37
2.7 Summary 39

3 Experimental Set-up **43**
3.1 Introduction 43
3.2 The Accelerator Facility 43
3.3 Coherent Bremsstrahlung Facility 44

3.4 Target 53
3.5 The CEBAF Large Acceptance Spectrometer (CLAS) 53
3.6 Beamline Devices 60
3.7 Trigger System 61
3.8 Summary 63

4 Data Processing and Calibrations 64
4.1 Data Processing and Run Conditions 64
4.2 Subsystem Calibrations 66
4.2.1 Start Counter Calibration 66
4.2.2 Photon Tagger Calibration / Beam RF 67
4.2.3 Time of Flight Calibration 71
4.2.4 Drift Chamber Calibration 75
4.2.5 Electromagnetic Calorimeters Calibration 76
4.3 Photon Polarization 77
4.4 Summary 81

5 Data Analysis 82
5.1 Data Skim and Event Selection 82
5.2 Extraction of Σ 102
5.3 Extraction of Recoil Polarization 107
5.3.1 Detector Simulation 114
5.3.2 Phase Space Event Generator 114
5.3.3 GSIM and GPP 116
5.3.4 Measuring Detector Acceptance 116
5.3.5 Hyperon Recoil Polarization 120
5.4 Target Asymmetry 123
5.5 Double Polarization Observables O_x and O_z 124
5.5.1 2-Dimensional Fit 125
5.6 Systematic Uncertainties 125
5.7 Summary 129

6 Results and Discussion 131
6.1 Preview of Model Comparisons 132
6.2 Photon Asymmetry 138
6.2.1 Photon asymmetry results $K^0\Lambda$ 138
6.2.2 Photon asymmetry for $K^0\Sigma^0$ 141
6.3 Recoil Polarization 144

6.3.1 Discussion of recoil polarization results for $K^0\Lambda$ 144
6.3.2 Discussion of recoil polarization results for $K^0\Sigma^0$ 150
6.4 Target Asymmetry 150
6.4.1 Discussion of target polarization results for $K^0\Lambda$ 154
6.4.2 Discussion of target polarization results for $K^0\Sigma^0$ 154
6.5 Double Polarization Observables, O_x and O_z 161
6.5.1 Discussion of O_x/O_z results for $K^0\Lambda$ 161
6.5.2 Discussion of O_x/O_z results for $K^0\Sigma^0$ 161
6.6 Comparison of Photon Asymmetry and Hyperon Recoil Polarization with the free proton 168
6.7 Conclusions 175

Bibliography **183**

List of Figures

1.1 Photoproduction cross-section on the proton in the energy range E_γ= 0.2 - 2.0 GeV. 2
1.2 Diagram showing the production and decay of the $K^0\Lambda$ and $K^0\Sigma^0$ reactions. 3
1.3 Octet of light spin 1/2 baryons. Arranged in terms of their charge and strangeness. 4
1.4 Mass predictions (in MeV) for Nγ, Nπ and KΛ final states from the relativised quark model of Capstick and Roberts [1]. 9
1.5 Mass predictions (in MeV) for Nγ, Nπ and KΣ final states from the relativised quark model of Capstick and Roberts [1]. 10

2.1 Total cross-section for Λ and Σ photoproduction on the proton [21]. 19
2.2 C_x (top) and C_z (bottom) double spin observables for the $\gamma p \rightarrow K^+\Lambda$ channel as measured at CLAS [22]. The model calculations used for comparison are: Kaon-MAID [41] (dashed green), partial wave analysis [42] (blue), Regge-plus-resonance [43] (solid red), Gent model [44] (magenta). 21
2.3 Differential cross-sections for $\gamma n \rightarrow K^+\Sigma^-$ (circle) and $\gamma p \rightarrow K^+\Sigma^0$ (squares). 22
2.4 Photon beam asymmetries for $\gamma n \rightarrow K^+\Sigma^-$ (circle) and $\gamma p \rightarrow K^+\Sigma^0$ (squares). 23
2.5 Momentum Spectra for K^0 with calculated cross-sections using the elementary amplitudes of Kaon-MAID (a to d) and SLA (e to h) models. 24
2.6 Definition of the unprimed and primed coordinate systems as used in the literature. 26
2.7 Differential cross-sections for $\gamma p \rightarrow K^+\Lambda$ at high W, given as a function of the kaon angle in the centre of mass system. 28

2.8 CSI model predictions for the seven spin observables in the $\gamma n \rightarrow K^0\Lambda$ channel as a function of kaon angle in the centre of mass reference frame. 30
2.9 Feynman diagrams for the electromagnetic production of kaons on the nucleon. 31
2.10 Energy dependent normalization factor from reference [42]. 34
2.11 Beam asymmetries as a function of W for $\gamma p \rightarrow K^+\Lambda$ from LEPS [48] and Recoil polarization results from CLAS [21]. 35
2.12 Multi-pole fits [27] to the photon asymmetry data from LEPS [48]. 36
2.13 Multi-pole fits [27] to the target asymmetry data from reference [71]. 36
2.14 Regge model calculations from [43, 73] compared to cross-section and photon asymmetry results from CLAS and SAPHIR. 38
2.15 Energy scales used in the Regge-plus-resonance approach. Figure from reference [75]. 39
2.16 Regge-plus-resonance calculations [68] for the photon asymmetry for the KΛ channel compared to the LEPS data [48]. 40
2.17 Regge-plus-resonance calculations [68] for the Λ recoil polarization compared to the CLAS data [30]. 41

3.1 Representation of the layout of Hall B showing the locations of the CLAS detector and the photon tagging spectrometer in the bottom right of the picture. 44
3.2 Racetrack configuration of the CEBAF at Jefferson Lab. 45
3.3 Schematic layout of the coherent Bremsstrahlung facility in Hall B. 46
3.4 Energy/Enhancement spectra from amorphous and diamond radiators. 47
3.5 The George Washington Universities Goniometer in test condition. The target ladder can be seen in the centre of the device. 48
3.6 Goniometer target ladder. The different radiators and their thickness are shown. 49
3.7 The active collimator shown under test conditions. 50
3.8 Schematic diagram of the photon tagger. 51
3.9 Schematic representation of the photon tagger, showing the relative positions of the T and E-counters. 51
3.10 The 40cm long g13b target cell. 53
3.11 Schematic diagram of the CEBAF Large Acceptance Spectrometer with the subsystem components peeled away. 54

3.12 Photograph of the CLAS detector in Hall B with the Time of Flight system removed. 55
3.13 Photograph of the six magnetic coils of CLAS 56
3.14 Schematic layout of the Start Counter at CLAS. 57
3.15 Cross section of the Drift Chambers (left) and regions 2 and 3 of the drift chamber shown in their installed positions on the torus cryostat (right). 58
3.16 A Schematic view of a single sector of the time of flight system. . 59
3.17 Diagram showing the three different views of the electromagnetic calorimeter. 60
3.18 The relative positioning of the pair spectrometer and total absorption shower counter downstream of CLAS. 61

4.1 Start counter calibration plots showing before calibration (top) and after (bottom). 68
4.2 Tagger calibration plots for a well calibrated run. 70
4.3 Example of the attenuation length calibration with the fit shown in red. 73
4.4 Example of the geometric mean distribution with the Gaussian plus 2nd order polynomial fit shown in red. 74
4.5 Example effective velocity distribution with the fit shown in red. . 75
4.6 Paddle-to-paddle calibration showing all paddles in all sectors aligned to zero. 76
4.7 Enhancement plot zoomed in on coherent peak region. Solid black line is the polynomial fit to the coherent edge. Red vertical line denotes coherent edge position. 77
4.8 Enhancement of tagger scaler spectra and resultant polarization. . 78
4.9 Enhancement of tagger scaler spectra and resultant polarization over a wide range of coherent peak positions. 79
4.10 Coherent peak stability over one run. Fluctuations in coherent peak position around the nominal value of 1300 MeV are clearly shown. 80

5.1 TOF mass^2 of protons and pions as detected in CLAS. 84
5.2 Tagger vertex time subtracted from the TOF vertex time for all photons. 86
5.3 Missing mass of the reaction d(γ,p $\pi^+\pi^-\pi^-$)X. Red line at the lower end is the 3σ cut and at the upper end is 5σ. 86

5.4 Spectator momentum distribution from a deuteron using the Paris potential. 87
5.5 Missing momentum of the exclusive reaction d(γ,p $\pi^+\pi^-\pi^-$)X. . . 88
5.6 Missing spectator momentum versus the cos(θ_p) spectator angular distribution in the lab frame. 88
5.7 Vertex timing difference between the photon and the four detected charged particles. 89
5.8 $K^0$and Λ invariant masses with fits. 91
5.9 Invariant K^0 mass with (yellow) and without (green) 3σ cuts on the Λ particle. 92
5.10 Invariant Λ mass with (yellow) and without (green) 3σ cuts on the K^0 mass. 92
5.11 Primary z-vertex distribution. This shows most particles primary z-vertex was within the target volume. 92
5.12 K^0 path length and lifetime. 94
5.13 Λ path length and lifetime. 95
5.14 Energy loss of proton (top), π^+(middle) and π^-(bottom). 96
5.15 Proton, π^+, π_1^-, π_2^- θ versus ϕ distributions in the lab frame from top left to bottom right respectively. Red lines show where fiducial cuts are applied. 97
5.16 Hyperon separation where the x-axis is the MM($K^0\Lambda$) from the deuteron while the y-axis has MM(K^0) from a free neutron target. 99
5.17 MM(K^0) in the range $0.87 <$ MM($K^0\Lambda$) < 0.965 for Λ events (top). MM(K^0) in the range $0.965 <$ MM($K^0\Lambda$) < 1.1 for Σ^0 events (bottom). 100
5.18 Missing momentum of spectator proton for Λ events (blue) cut at 200 MeV/c and for Σ^0 events (red) cut at 277 MeV/c. 101
5.19 Voigtian fitting routine for one angular bin to extract Λ and Σ^0 yields for Λ beam asymmetry correction. 103
5.20 Photon energy distributions and non-uniform angular binning. . . 104
5.21 Non-uniform angular bins superimposed on the cos($\theta_{cm}^{K^0}$) spectrum. 105
5.22 ϕ-yield of kaons for the parallel and perpendicular polarization settings. Resultant asymmetry of the two polarization settings. . . 108
5.23 Cos2Φ fits of the $K^0\Lambda$ beam asymmetry for E_γ= 1.9 GeV. 109
5.24 Cos2Φ fits of the $K^0\Sigma^0$ beam asymmetry for E_γ= 1.9 GeV. 110
5.25 Photon asymmetry as a function of cos($\theta_{cm}^{K^0}$) at E_γ=1.9 GeV for the $K^0\Lambda$ channel. 111

5.26 Photon asymmetry for the $K^0\Lambda$ channel as a function of $\cos\theta_{cm}^{K^0}$ for E_γ= 1.9 GeV. 112
5.27 Photon asymmetry for the $K^0\Sigma^0$ channel as a function of $\cos\theta_{cm}^{K^0}$ for E_γ= 1.9 GeV. 112
5.28 χ^2 values per degree of freedom for the $K^0\Lambda$ (top) and $K^0\Sigma^0$ (bottom) channels. 113
5.29 Flow chart displaying the steps used for the analysis and simulation that are needed to extract the hyperon recoil polarization. 115
5.30 ϕ distributions from real data (blue) and simulation (red) for the proton (top left), π^+ (top right), π_1^- (bottom left) and π_2^- (bottom right). 117
5.31 θ distributions from real data (blue) and simulation (red) for the proton (top left), π^+ (top right), π_1^- (bottom left) and π_2^- (bottom right) 118
5.32 t-distributions and θ distributions for the original and modified generated events. 119
5.33 Plot showing the effect of correcting the acceptance as a function of both $\cos\theta_y$ and $\cos\theta_{cm}^{K^0}$ simultaneously on the final proton yield for the original flat phase space and the modified phase space. . . 120
5.34 Linear fits of the acceptance corrected proton yield $\theta_{\Lambda_{RF}}^P$ for E_γ= 1.675 GeV. The range in angle is from $\cos(\theta_{cm}^{K^0})$ = -0.8 in the upper left to $\cos(\theta_{cm}^{K^0})$ = 0.9 in the bottom right. 121
5.35 Recoil Λ polarization plotted as a function of $\cos(\theta_{cm}^{K^0})$ for the energy range $1.6 < E_\gamma < 1.75$ GeV. All error bars are statistical, systematic errors will be considered later. 122
5.36 Two dimensional distribution over Φ and θ_y (top left) with the resultant two dimensional fit superimposed (top right). 123
5.37 χ^2 values from the two dimensional fits used to extract the target asymmetry. These values are from fits over the full kinematic range. 124
5.38 The 2-dimensional asymmetry over Φ and θ_i plotted for the x-component of the recoil polarization. These plots are for a photon energy of 1.9 GeV, integrated over the angular range $\cos(\theta_{cm}^{K^0})$ = 0.4 to 1.0. 124
5.39 Example of the two dimensional fit for one E_γ and one $\cos(\theta_{CM}^{K^0})$ bin for the x-component of the hyperon polarization. Plots for the z-component are similar. 125

5.40 χ^2 per degree of freedom values from the two dimensional fits used to extract the O_x (top) and O_z (bottom) double polarization observables for the $K^0\Lambda$ channel. 126
5.41 O_x observable for the $K^0\Lambda$ channel (top) and for the $K^0\Sigma^0$ channel (bottom). O_x is plotted as a function of $\cos(\theta_{cm}^{K^0})$ for E_γ= 1.9 GeV. 127
5.42 O_z observable for the $K^0\Lambda$ channel (top) and for the $K^0\Sigma^0$ channel (bottom). O_z is plotted as a function of $\cos\theta_{cm}^{K^0}$ for E_γ= 1.9 GeV. 128

6.1 Model comparisons for the photon asymmetry for the $K^0\Lambda$ channel at 1.9 GeV. 133
6.2 Model comparisons for the hyperon recoil polarization for the $K^0\Lambda$ channel at 1.9 GeV. 134
6.3 Model comparisons for the target asymmetry for the $K^0\Lambda$ channel at 1.9 GeV. 135
6.4 Model comparisons for the double polarization observable O_x for the $K^0\Lambda$ channel at 1.9 GeV. 136
6.5 Model comparisons for the double polarization observable O_z for the $K^0\Lambda$ channel at 1.9 GeV. 137
6.6 Photon asymmetries for the reaction $\gamma n \rightarrow K^0\Lambda$ as a function of $\cos(\theta_{cm}^{K^0})$ ranging from E_γ= 1.3 GeV (top left) to 2.3 GeV (bottom right). 139
6.7 Photon asymmetries for the reaction $\gamma n \rightarrow K^0\Lambda$ as a function of $\cos(\theta_{cm}^{K^0})$ ranging from E_γ= 1.3 GeV (top left) to 2.3 GeV (bottom right). 140
6.8 Photon asymmetries for the reaction $\gamma n \rightarrow K^0\Sigma^0$ as a function of $\cos(\theta_{cm}^{K^0})$ ranging from E_γ= 1.3 GeV (top left) to 2.3 GeV (bottom right). 142
6.9 Photon asymmetries for the reaction $\gamma n \rightarrow K^0\Sigma^0$ as a function of $\cos(\theta_{cm}^{K^0})$ ranging from E_γ= 1.3 GeV (top left) to 2.3 GeV (bottom right). 143
6.10 Photon asymmetries for the reaction $\gamma n \rightarrow K^0\Lambda$ as a function of E_γ ranging from $\cos(\theta_{cm}^{K^0})$= -0.6 (top left) to 0.795 (bottom right). . . 145
6.11 Photon asymmetries for the reaction $\gamma n \rightarrow K^0\Sigma^0$ as a function of E_γ ranging from $\cos(\theta_{cm}^{K^0})$= -0.6 (top left) to 0.795 (bottom right). 146
6.12 Hyperon recoil polarization for the reaction $\gamma n \rightarrow K^0\Lambda$ as a function of $\cos(\theta_{cm}^{K^0})$ ranging from E_γ= 1.225 GeV (top left) to 2.275 GeV (bottom right). 147

6.13 Hyperon recoil polarization for the reaction $\gamma n \rightarrow K^0\Lambda$ as a function of $\cos(\theta_{cm}^{K^0})$ ranging from E_γ= 1.225 GeV (top left) to 2.275 GeV (bottom right). 148
6.14 Hyperon recoil polarization for the reaction $\gamma n \rightarrow K^0\Lambda$ as a function of E_γ ranging from $\cos(\theta_{CM}^{K^0})$ = -0.6 (top left) to 0.795 (bottom right).149
6.15 Hyperon recoil polarization for the reaction $\gamma n \rightarrow K^0\Sigma^0$ as a function of $\cos(\theta_{cm}^{K^0})$ ranging from E_γ= 1.225 GeV (top left) to 2.275 GeV (bottom right). 151
6.16 Hyperon recoil polarization for the reaction $\gamma n \rightarrow K^0\Sigma^0$ as a function of $\cos(\theta_{cm}^{K^0})$ ranging from E_γ= 1.225 GeV (top left) to 2.275 GeV (bottom right). 152
6.17 Hyperon recoil polarization for the reaction $\gamma n \rightarrow K^0\Sigma^0$ as a function of E_γ ranging from $\cos(\theta_{CM}^{K^0})$ = -0.6 (top left) to 0.795 (bottom right). 153
6.18 Target asymmetry for the reaction $\gamma n \rightarrow K^0\Lambda$ as a function of $\cos(\theta_{cm}^{K^0})$ ranging from E_γ= 1.2 GeV (top left) to 2.2 GeV (bottom right). . 155
6.19 Target asymmetry for the reaction $\gamma n \rightarrow K^0\Lambda$ as a function of $\cos(\theta_{cm}^{K^0})$ ranging from E_γ= 1.2 GeV (top left) to 2.2 GeV (bottom right). . 156
6.20 Target asymmetry for the reaction $\gamma n \rightarrow K^0\Lambda$ as a function of E_γ ranging from $\cos(\theta_{CM}^{K^0})$ = -0.4 (left) to 0.72 (right). 157
6.21 Target asymmetry for the reaction $\gamma n \rightarrow K^0\Sigma^0$ as a function of $\cos(\theta_{cm}^{K^0})$ ranging from E_γ= 1.2 GeV (top left) to 2.2 GeV (bottom right). 158
6.22 Target asymmetry for the reaction $\gamma n \rightarrow K^0\Sigma^0$ as a function of $\cos(\theta_{cm}^{K^0})$ ranging from E_γ= 1.2 GeV (top left) to 2.2 GeV (bottom right). 159
6.23 Target asymmetry for the reaction $\gamma n \rightarrow K^0\Sigma^0$ as a function of E_γ ranging from $\cos(\theta_{CM}^{K^0})$ = -0.4 (top left) to 0.72 (bottom left). . . 160
6.24 O_x double polarization observable for the reaction $\gamma n \rightarrow K^0\Lambda$ as a function of $\cos(\theta_{cm}^{K^0})$ ranging fr$_{x_x}$om E_γ= 1.2 GeV (top left) to 2.2 GeV (bottom right). 162
6.25 O_z double polarization observable for the reaction $\gamma n \rightarrow K^0\Lambda$ as a function of $\cos(\theta_{cm}^{K^0})$ ranging from E_γ= 1.2 GeV (top left) to 2.2 GeV (bottom right). 163
6.26 O_x double polarization observable for the reaction $\gamma n \rightarrow K^0\Lambda$ as a function of $\cos(\theta_{cm}^{K^0})$ ranging from E_γ= 1.2 GeV (top left) to 2.2 GeV (bottom right). 164

6.27 O_z double polarization observable for the reaction $\gamma n \rightarrow K^0\Lambda$ as a function of $\cos(\theta_{cm}^{K^0})$ ranging from E_γ= 1.2 GeV (top left) to 2.2 GeV (bottom right). 165
6.28 O_x double polarization observable for the reaction $\gamma n \rightarrow K^0\Lambda$ as a function of E_γ ranging from $\cos(\theta_{CM}^{K^0})$ = -0.4 (left) to 0.72 (right). 166
6.29 O_z double polarization observable for the reaction $\gamma n \rightarrow K^0\Lambda$ as a function of E_γ ranging from $\cos(\theta_{CM}^{K^0})$ = -0.4 (left) to 0.72 (right). 167
6.30 O_x double polarization observable for the reaction $\gamma n \rightarrow K^0\Sigma^0$ as a function of $\cos(\theta_{cm}^{K^0})$ ranging from E_γ= 1.3 GeV (top left) to 2.3 GeV (bottom right). 169
6.31 O_z double polarization observable for the reaction $\gamma n \rightarrow K^0\Sigma^0$ as a function of $\cos(\theta_{cm}^{K^0})$ ranging from E_γ= 1.3 GeV (top left) to 2.3 GeV (bottom right). 170
6.32 O_x double polarization observable for the reaction $\gamma n \rightarrow K^0\Sigma^0$ as a function of $\cos(\theta_{cm}^{K^0})$ ranging from E_γ= 1.2 GeV (top left) to 2.2 GeV (bottom right). 171
6.33 O_z double polarization observable for the reaction $\gamma n \rightarrow K^0\Sigma^0$ as a function of $\cos(\theta_{cm}^{K^0})$ ranging from E_γ= 1.2 GeV (top left) to 2.2 GeV (bottom right). 172
6.34 O_x double polarization observable for the reaction $\gamma n \rightarrow K^0\Sigma^0$ as a function of E_γ ranging from $\cos(\theta_{CM}^{K^0})$ = -0.4 (left) to 0.72 (right). 173
6.35 O_z double polarization observable for the reaction $\gamma n \rightarrow K^0\Sigma^0$ as a function of E_γ ranging from $\cos(\theta_{CM}^{K^0})$ = -0.4 (left) to 0.72 (right). 174
6.36 Photon asymmetry results for the $K\Lambda$ channel from the free proton (black triangles) compared to the results from the bound neutron (green circles). 176
6.37 Photon asymmetry results for the $K\Sigma^0$ channel from the free proton (black triangles) compared to the results from the bound neutron (green circles). 177
6.38 Hyperon recoil polarization results for the $K\Lambda$ channel from the free proton (black triangles) compared to the results from the bound neutron (green circles). 178
6.39 Hyperon recoil polarization results for the $K\Sigma^0$ channel from the free proton (black triangles) compared to the results from the bound neutron (green circles). 179

List of Tables

1.1 The SU(6) $\otimes$ O(3) supermultiplet assignments from the QCD improved model of Forsyth and Cutkosky [14]. 8
1.2 Spin observables with their transversity representations and the type of observable. Table produced from reference [26]. 14

2.1 Preliminary properties of the $D_{13}(1900)$ resonance extracted from proton data. 28
2.2 Preliminary electromagnetic helicity amplitudes in $10^{-3}\text{GeV}^{-1/2}$ for the D_{13} (1900) resonance extracted from proton data. 29
2.3 Table showing the amplitudes included in the Kaon-MAID isobar model [41]. 31

4.1 Table summarising the g13b running conditions. 64
4.2 Electron beam and photon beam settings with total triggers for each polarization plane setting and mean polarizations. 65

5.1 PDG and fitted masses of the K^0 and Λ particles. 90
5.2 Table showing the PDG and measured decay constants ($\frac{1}{\tau}$, where τ is the particle lifetime) for the K^0 and the Λ. 93
5.3 Table of all major analysis cuts. 102
5.4 Systematic uncertainties for the Σ, O_x, O_z, P and T polarization observables. 129

Chapter 1

Introduction

In the 1950's, experiments revealed that hadrons are not fundamental particles and have some internal structure. This was the beginning of a new era of sub-atomic physics which describes the nature of hadrons in the context of quarks and gluons. The fundamental laws of quark and gluon interactions are explained by Quantum Chromo-Dynamics (QCD). At low energies the hadrons look like structureless particles. At medium energies the substructure of hadrons can be explored. At very high energies (few hundred GeV) the complex nature of quarks and gluons inside the hadrons can be observed. At higher energies the strong coupling constant becomes much smaller than 1 and QCD can be treated perturbatively. At medium energies of 1 - 3 GeV where many of the resonant states of the nucleon exist, the coupling constant of the strong interaction is of order 1 and perturbation theory can no longer be used. Detailed experimental information on the structure of hadrons, in particular nucleons, can be obtained by understanding their excited states (i.e nucleon resonances). The internal structure of the nucleon is reflected in its excitation spectrum. Knowledge on nucleon resonances can be gained from experiments which involve the transfer of energy to the nucleon by a hadronic or electromagnetic probe. This energy transfer leaves the nucleonic system in one of its excited states which is then followed by a decay into the final state. The properties of these final states can be analysed and will yield information on the complex structure of the nucleon. The model which explains basic ground states of the hadrons is known as the constituent quark model. The basics of the constituent quark model are outlined in section 1.2.1. There are several other models which describe the excitation spectrum of baryons. However, most models suffer from the problem of predicting far more resonances than have been detected experimentally [1].

Figure 1.1 shows the total cross-section for various reactions on the proton, as

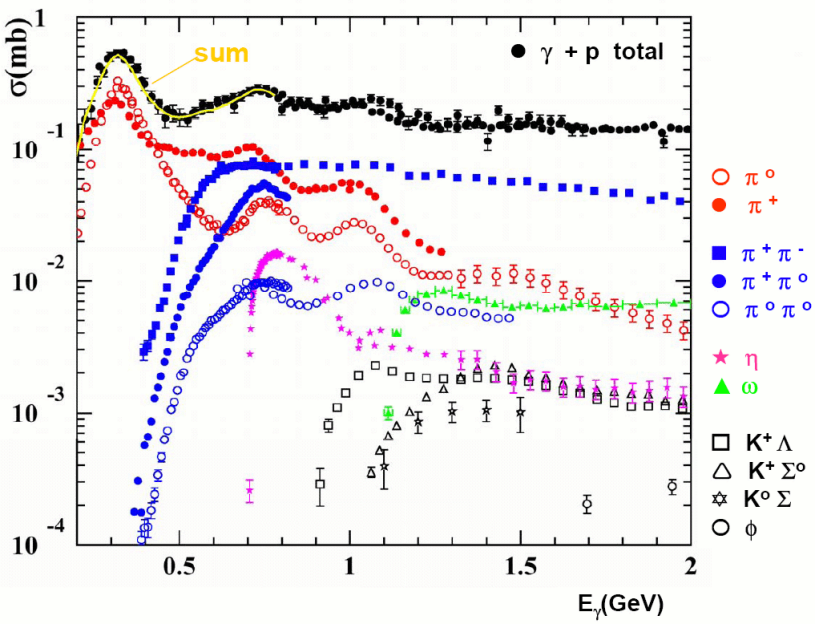

Figure 1.1: Photoproduction cross-section on the proton in the energy range E_γ= 0.2 - 2.0 GeV.

there are no total cross-section data on the neutron. As the energy increases, one moves into higher resonance regions where the threshold for more decay modes is surpassed and it becomes non-trivial to identify individual resonant states.

Resonances are also very short lived and have large overlapping decay widths which adds to the difficulty in detecting them. One solution is to use the spin orientation of the incoming beam, recoiling baryon and the target nuclei to extract spin observables from the reaction dynamics. Using a polarized beam and target, along with the ability to measure the recoil baryon polarization allows for the measurement of various polarization observables. These polarization observables have been shown to be very sensitive to the underlying physics of the reaction and will provide additional information to the cross-section [2, 3]. Several measurements have been made on the proton, however, this work will describe the first measurement of polarization observables on the neutron.

From Figure 1.1, one can see that the cross-sections for $K^+\Lambda$ and $K^+\Sigma^0$ photoproduction are approximately two orders of magnitude smaller than for single pion production. It is expected that cross-sections for $K^0\Lambda$ and $K^0\Sigma^0$ should not differ greatly from that of the charged K^+ to first order. Studying multi-particle final states is experimentally difficult as a large number of reaction events have to be produced. This requires a facility capable of detecting several decay products in order to gain a large event sample. Jefferson lab provides the ideal experimental facility to carry out this work. The Continuous Electron

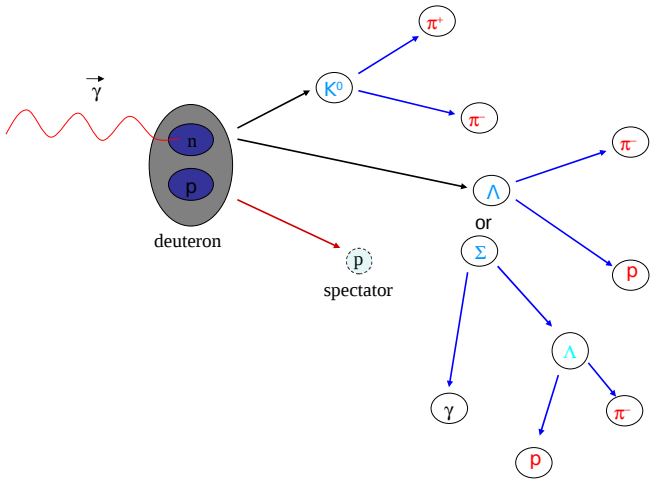

Figure 1.2: Diagram showing the production and decay of the $K^0\Lambda$ and $K^0\Sigma^0$ reactions.

Beam Accelerator Facility (CEBAF) delivers a high luminosity beam capable of producing a large number of reaction events. The CEBAF Large Acceptance Spectrometer (CLAS) detector has a near 4π acceptance for charged particles, making this facility the ideal place to study the strangeness production reactions $K^0\Lambda$ and $K^0\Sigma^0$ from the neutron. Figure 1.2 shows the production and decay of these reactions and displays the multiple particles in the final state.

This chapter will provide a brief introduction to the theory of the strong interaction and explain the difficulties in applying the theory in the resonance region. A short introduction to the quark model will be given, followed by the topic of baryon spectroscopy and the physics issues addressed in this work. The process of strangeness production and the basic formalism of polarization observables will then be discussed, with a focus on the measurements that will be described in this work.

1.1 QCD - Quantum Chromo-Dynamics

Hadrons are strongly interacting particles and so are governed by QCD, which is a non-abelian gauge theory of coloured quarks. The complicated array of subatomic particles within the standard model is well described by QCD. The particles can consist of an arrangement of quarks, currently believed to come in six flavours: up, down, strange, charm, top and bottom. QCD can account for the rich variety of hadronic states through the combination of different quantum

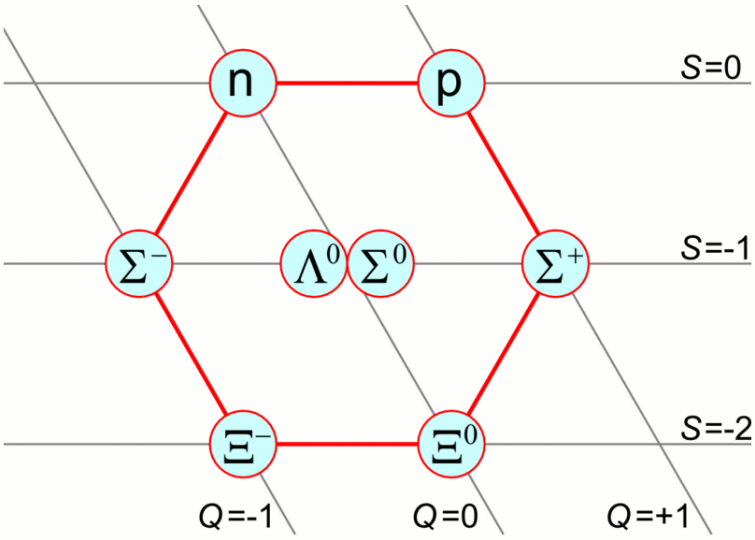

Figure 1.3: Octet of light spin 1/2 baryons. Arranged in terms of their charge and strangeness.

numbers introduced at various stages during the development of the standard model, such as isospin and flavour [4].

Heisenberg introduced isospin as a quantum number related to the strong interaction to describe various related symmetries for the proton and neutron [5]. This SU(2) symmetry was used to account for the near degeneracy of the proton and neutron masses, as well as the invariance of the strength of the nuclear force under exchange of nucleons. The true symmetry of isospin arises from the invariance of the strong interaction Hamiltonian under the action of an SU(2) Lie group. The strangeness quantum number was introduced by Gell-Mann [6] to further account for the increasing number of strongly interacting states being discovered by experiment. This allowed for hadrons that displayed similar properties to be grouped according to the so-called "eight-fold way". This arrangement is a consequence of flavour symmetry between the quarks. Since QCD is fully independent of quark flavour, any distinction between different quarks is entirely from their mass differences. Figure 1.3 shows the baryon octet of light spin 1/2 baryons, including the Λ and Σ^0.

A further problem to be solved was the existence of the Δ^{++} state. This particle remained a mystery as it was composed of three up quarks with parallel spins, hence it has an overall symmetric spin-flavour structure. Quarks are fermions which satisfy an anti-symmetric wave function. Han, Nambu and Greenberg independently introduced a new quantum number for quarks called colour, which would resolve this issue [7, 8]. This new quantum number was required to have three degrees of freedom called red, green and blue and was described

by an $SU(3)_c$ gauge group with non-abelian internal symmetry. One property of QCD is that of confinement. This means that as the distance between two colour charges increases the force between them does not decrease. Quarks therefore cannot be liberated from the hadrons and this explains why no free quarks have ever been observed experimentally.

The strong interaction has another feature in that it becomes weaker and easier to calculate at higher energies. This phenomena is called asymptotic freedom and is a result of the strong coupling constant α_s decreasing with increasing energy. Asymptotic freedom occurs when the exchange momentum is very large and the mathematics of the gauge theory become simplified. At high energies the quarks effectively become free moving, non-interacting particles within the nucleons. Well established principles for electromagnetic interactions in Quantum Electro-Dynamics can then be applied to quarks and gluons at high energies. In the limit of non-relativistic heavy quark states, QCD is also simplified. In this domain the quark can be viewed as a static source of gluon field and corrections can be systematically applied in perturbation theory.

The strong coupling constant α_s approaches unity at low energies and momenta. In this regime it is no longer possible to carry out expansions in powers of α_s and QCD becomes non-perturbative. Non-perturbative QCD describes many areas of hadronic physics, where there are no rigorous solutions. This is a problem when one wants to understand how quarks combine to build nucleons, as well as gaining a deeper understanding of the excited baryon spectrum.

Lattice QCD attempts to solve non-perturbative QCD on a discretised Euclidean space-time lattice. A recent lattice calculation [9] was able to predict masses of the two lowest state octet and decuplet baryons. However, despite the major advances in past few years, lattice QCD still cannot predict the baryon spectrum or the properties of resonances from first principles.

1.2 Baryon Spectroscopy

Meson photoproduction is an important topic within baryon spectroscopy. It allows an opportunity to accurately determine parameters of known resonances and can aid in the discovery of new baryon states. The non-perturbative nature of QCD at low momenta and energy, as well as the still developmental status of lattice QCD, has forced hadronic physics to rely on phenomenological quark models to make predictions about the baryon spectrum. Though the models vary in structure, they all employ the same technique of reducing the complicated quark-

gluon soup of QCD to a simpler system of constituent quarks interacting in an inter-quark potential. These quark models can predict the existence of multiple excited nucleon states. The states are then classified by a L_{2I2J} notation, where L is the orbital angular momentum of the resonance, I is the isospin and J is the total angular momentum. Quantum numbers such as orbital angular momentum, spin, isospin and parity are used to identify baryon resonances. These quantum numbers identify the partial waves responsible for their excitation. Baryon resonances are categorised by their appearance in a given partial wave. An example of such a sequence are the $D_{13}(1520)$, $D_{13}(1700)$ and $D_{13}(2080)$ resonances listed by the Particle Data Group (PDG) [10].

1.2.1 Constituent Quark Model

The constituent quark model allows for the classification of hadrons in terms of the constituent or valence quarks. Hadrons are identified by the quantum numbers of the quarks that make them up. They are denoted in terms of the quark flavour and Poincare symmetry, J^{PC}, where J is the angular momentum, P is the intrinsic parity and C is the charge conjugation. After the introduction of strangeness by Gell-Mann and Zweig [6] the baryon spectrum was unfolded in the $3 \otimes 3 \otimes 3$ symmetry of the SU(3) quark model. Introducing quark spins and orbital angular momentum excitations allows for the prediction of a rich spectrum of nucleon resonances based on SU(6) $\otimes$ O(3) symmetric quark models.

Faiman and Hendry [11] developed a quark shell model based on harmonic oscillator forces as an initial attempt at unfolding the baryon spectrum. Their idea was based on the familiar principles of a particle moving within a three dimensional harmonic oscillator potential. From this it was possible to predict a spectrum of baryons that was consistent with the data of that time. Forsyth and Cutkosky [12] developed an improved QCD quark-shell model to fit masses and elastic widths of the S = 0 baryons. This model was based on a decay operator with the form $S(g_1 P_q + g_2 P_{-q})$, where P_q and P_{-q} are the created quark and anti-quark momenta and S is their combined spin. The model included a number of baryon resonances, many of which were found to be in good agreement with existing data. Further work by Koniuk and Isgur [13] using an elementary meson emission model allowed for predictions of non-strange baryon decays up to the N = 2 band in both $K^+\Lambda$ and $K^+\Sigma^0$ photoproduction. In their reaction scheme a kaon, that is treated as point-like, couples directly to the quarks in the initial baryon. All of the models described here are able to predict a large spectrum of non-strange baryon states that should couple strongly to the strange

decay channels. States that are then found by experiment, along with how well their properties compare with the calculations will determine how successful the numerous models are at describing the strangeness photoproduction process.

The current understanding of hadrons is based on effective degrees of freedom. Constituent quark models based on SU(6) $\oplus$ O(3) symmetry consist of three constituent quarks and have been successful in describing the low lying states but also predict many more states yet undetected by experiment [14]. The non-observation of these states is either due to their weak coupling to the formation channels that have been used or reflects a more fundamental aspect of baryon structure, such as the strong correlation between a pair of quarks [15]. The di-quark model suggests two of the three constituent quarks are coupled and thus reducing the number of degrees of freedom, hence fewer allowed states. This issue can only be resolved if measurements unambiguously identify some of the missing states that would not be compatible with the di-quark model. Quark model calculations have shown that some of the resonances should couple strongly to photoproduction reactions with strange decay channels such as the channels studied for this thesis.

Several major developments have been made in resonance physics over the past few years. The theoretical side has seen the introduction of coupled channels analysis that include pion, eta, and kaon production, which show promise in resolving the ambiguities present when the resonance parameters are extracted from partial-wave analysis from earlier isobaric models [16, 17]. Within the coupled channels framework, data of reasonable quality in many channels is a more effective constraint than precise data in only a few channels. This means it is very important to move away from sole pion production on the proton and investigate other decay channels from the proton and neutron. The full power of coupled channels analysis can only be seen when there are several observables available for each channel. As a wealth of information has been gathered for the proton, it is important to have data on the neutron. This is easiest achieved through a deuterium target as it has a simple two nucleon structure. This does add a further complication in that the target nucleon is no longer stationary and re-scattering effects must therefore be taken into account.

1.2.2 Missing Resonances

Most of the information on the nucleon excitation spectrum has been extracted from pion-induced and pion-production reactions. The quark model [1] predicts the existence of a number of nucleon resonances that have not yet been observed

Table 1.1: The SU(6) $\otimes$ O(3) supermultiplet assignments from the QCD improved model of Forsyth and Cutkosky [14].

N^*	**Status**	$SU(6) \otimes O(3)$	**Parity**	Δ^*	**Status**	$SU(6) \otimes O(3)$
P_{11} (938)	****	$(56, 0^+)$	+	P_{33} (1232)	****	$(56, 0^+)$
S_{11} (1535)	****	$(70, 1^-)$				
S_{11} (1650)	****	$(70, 1^-)$		S_{31} (1620)	****	$(70, 1^-)$
D_{13} (1520)	****	$(70, 1^-)$	-	D_{33} (1700)	****	$(70, 1^-)$
D_{13} (1700)	***	$(70, 1^-)$				
D_{15} (1675)	****	$(70, 1^-)$				
P_{11} (1520)	****	$(56, 0^+)$		P_{31} (1875)	****	$(56, 2^+)$
P_{11} (1710)	***	$(70, 0^+)$	+	P_{31} (1835)		$(70, 0^+)$
P_{11} (1880)		$(70, 2^+)$				
P_{11} (1975)		$(20, 1^+)$				
P_{13} (1720)	****	$(56, 2^+)$		P_{33} (1600)	***	$(56, 0^+)$
P_{13} (1870)	*	$(70, 0^+)$		P_{33} (1920)	***	$(56, 2^+)$
P_{13} (1910)		$(70, 2^+)$	+	P_{33} (1985)		$(70, 2^+)$
P_{13} (1950)		$(70, 2^+)$				
P_{13} (2030)		$(20, 1^+)$				
F_{15} (1680)	****	$(56, 2^+)$		F_{35} (1905)	****	$(56, 2^+)$
F_{15} (2000)	**	$(70, 2^+)$	+	F_{35} (2000)	**	$(70, 2^+)$
F_{15} (1995)		$(70, 2^+)$				
F_{17} (1990)	**	$(70, 2^+)$	+	F_{37} (1950)	****	$(56, 2^+)$

experimentally. The missing resonance problem can be seen in Table 1.1. This shows the states predicted by the SU(6) $\otimes$ O(3) quark model from Forsyth and Cutkosky, along with their PDG ratings [18].

A significant number of the predicted states in this Table 1.1 have either zero or one star ratings, suggesting that there is no or very little experimental evidence for their existence.

There are a few explanations why some of the missing resonances have not yet been observed experimentally. One such explanation suggests that the current quark models have an intrinsic flaw and require some fundamental modification. Di-quark models [15, 19, 20] are based on the assumption that two of the quarks exist inside the nucleon in a tightly bound state. A low energy configuration is formed when the two quarks are correlated in this way, therefore reducing the number of internal degrees of freedom of the nucleon. This lowers the level density of baryon resonances and removes a large number of the missing states from the predictions.

An alternative explanation would suggest that measurements to date are simply not sensitive to these missing states, with the majority of the existing data coming from pion production experiments involving πN final states. Capstick and Roberts have shown in reference [1] that some of these missing resonances should couple strongly to strange baryon final states produced in photoproduction experiments. Their model describes baryon decays in a relativised scheme based on a $^3P_0$ creation model. Their calculation takes into account the finite spatial extent of the final meson as well as including the excited strange baryons

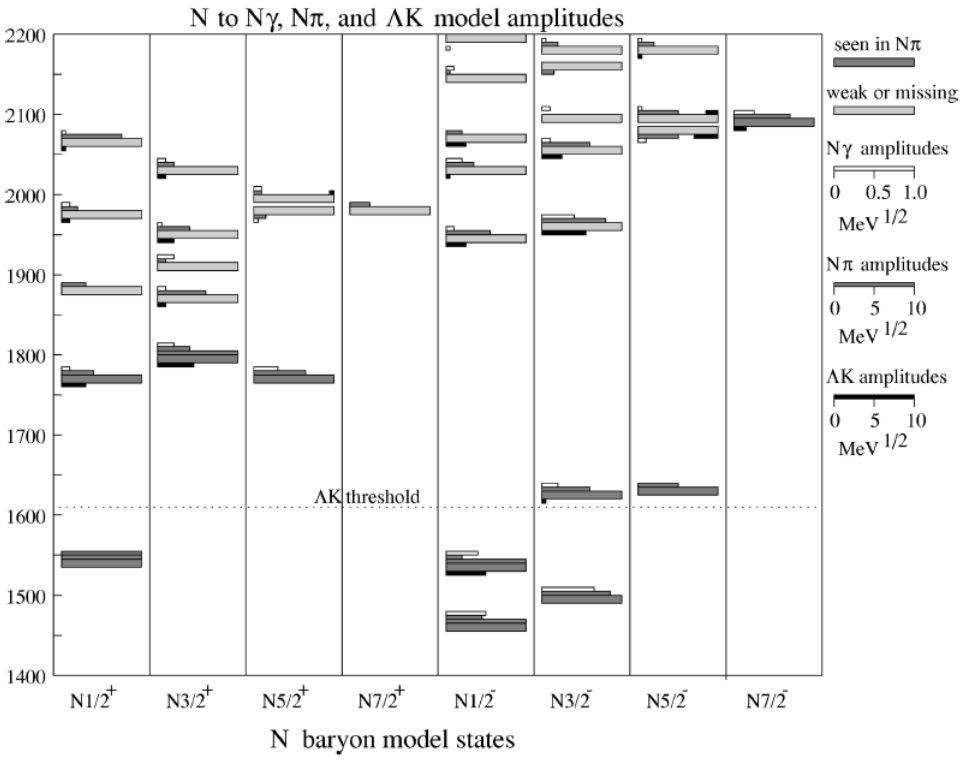

Figure 1.4: Mass predictions (in MeV) for Nγ, Nπ and KΛ final states from the relativised quark model of Capstick and Roberts [1].

$\Lambda(1405)$, $\Lambda(1520)$, and $\Sigma(1385)$ along with K^* excited mesons. The model makes predictions for a series of negative and positive parity states up to the N = 3 band. Examples of their calculations for KΛ and KΣ channels are shown in Figures 1.4 and 1.5 respectively.

The heavy uniform width bars show states that have been well established in partial wave analyses, whilst the light bars represent states that are weakly established or missing. The signs and magnitudes of the predicted amplitudes for both decay channels are in good agreement with those extracted from the well established states. For the KΛ channel, Capstick and Roberts predicted that there should be several negative parity states in the N = 3 band that should be clearly observed by experiment. The two star N(2080) D_{13}= $[\mathrm{N}\frac{3}{2}^-]_3(1960)$ state is predicted to be clearly evident in a precision measurement of $\gamma n \rightarrow K^0\Lambda$. They also predict the existence of the weakly established N(2090) S_{11}= $[\mathrm{N}\frac{1}{2}^-]_3(1945)$. In the $K^0\Sigma^0$ reaction, their calculations suggest an important contribution from the $\Delta(1910)P_{31} = [\Delta\frac{1}{2}^+]_2(1875)$ for which only an upper limit is quoted by the PDG [18].

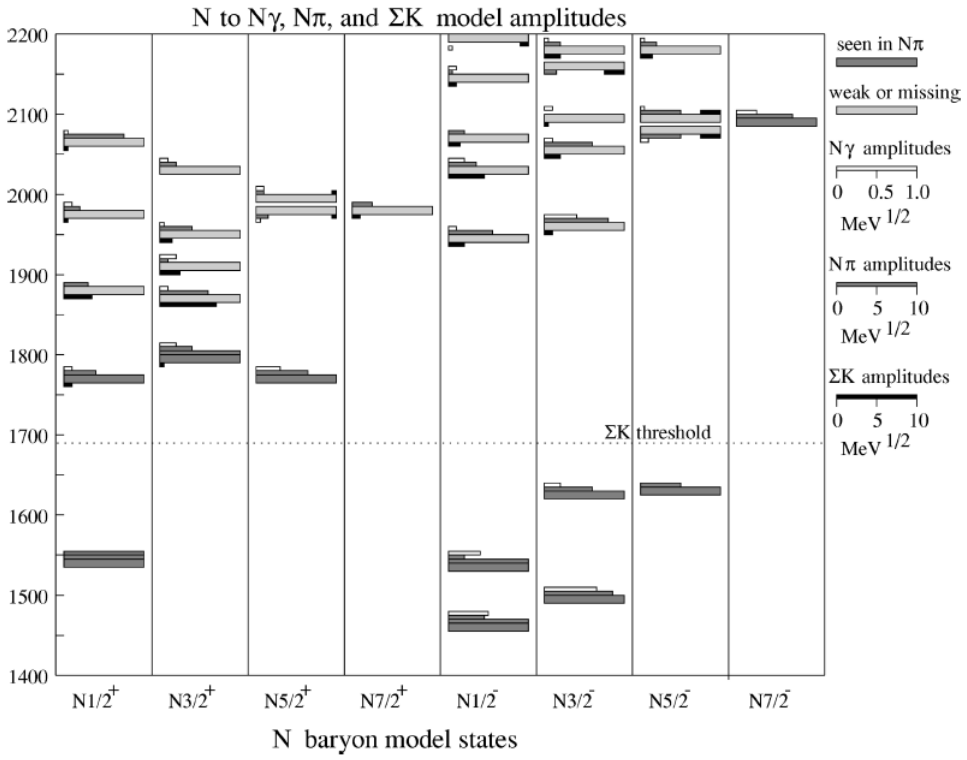

Figure 1.5: Mass predictions (in MeV) for Nγ, Nπ and KΣ final states from the relativised quark model of Capstick and Roberts [1].

1.3 Kaons and Hyperons

A Kaon is a strange meson where one of the two quarks is a strange or anti-strange quark. Hyperons, denoted by Y, are baryons where one up or down quark has been replaced by one strange quark. The Λ and Σ^0 particles belong to the hyperon group. Both the Λ and the Σ^0 particles share the same up, down, strange (uds) valence quark structure. However, the up, down (ud) in the Λ are a spin singlet state. In contrast, the up, down (up) in the Σ^0 are a spin triplet state. The Λ and Σ^0 are from the same baryon octet as the proton and neutron, as shown in Figure 1.3 and both have spin 1/2. The Λ has a mass of 1115.68 MeV/c^2 and a mean lifetime of 2.6 $\times 10^{-10}$s, whilst the Σ^0 has a mass of 1192.64 MeV/c^2 and a mean lifetime of 7.47 $\times 10^{-20}$s. An important difference between the two particles is their isospin. The Λ has isospin = 0 and the Σ^0 has isospin = 1. This is a very important property of baryon spectroscopy since a KΣ^0 final state can excite both N^* and Δ states whereas the KΛ final state can only involve intermediate isospin 1/2 N^* states, making the reaction easier to describe.

Both particles have very short lifetimes and as a result they will not travel far enough before decaying to be detected in the CLAS. They must be reconstructed

from their decay daughter products. The branching ratio for the Λ is:

$$\Lambda \rightarrow p\pi^{-}(63.9\%) \tag{1.1}$$

$$\Lambda \rightarrow n\pi^{0}(35.8\%) \tag{1.2}$$

The Σ^0 decays with a 99.9% branching ratio into:

$$\Sigma^0 \rightarrow \gamma\Lambda \tag{1.3}$$

where the decay γ has an energy of 77 MeV.

The Λ hyperon is self analysing, which means that it violates parity and decays weakly, therefore allowing its polarization to be measured. This parity violating property arises from quantum mechanical interference of a parity violating S-wave and a parity conserving P-wave amplitude [21]. A polarization component $P_{\Lambda i}$ can be defined, where i ϵ\{x,y,z\} is a given axis in space. The proton angular intensity distribution, I(cosθ^p_Λ) as a function of the proton polar angle in the hyperon rest frame is given by:

$$I(cos\theta^p_\Lambda) = \frac{1}{2}(1 + \alpha P_\Lambda cos\theta^p_\Lambda) \tag{1.4}$$

where α is the self-analysing power of the hyperon which has been measured experimentally in reference [18], to be 0.642. It is clear from this equation that one can extract the Λ polarization, P_Λ from the proton angular distribution. The Σ^0 polarization can also be measured through its self-analysing decay to its daughter Λ. Reference [22] provides a detailed mathematical proof of this. However, the basics are outlined here. A Σ^0 produced in the reaction will have some polarization P_{Σ^0} and as it decays to a Λ via a magnetic dipole transition some of the original Σ^0 polarization will be preserved by the Λ. When the direction of the Λ is not explicitly measured (see [22]), the polarization of the Λ is related to the polarization of the parent Σ^0 by:

$$P_\Lambda = -\frac{1}{3}P_{\Sigma^0} \tag{1.5}$$

It will therefore be possible to extract the polarization of both hyperons in this work through the weak decay of the Λ. However, the statistical uncertainty for the Σ^0 results will be almost three times as large as for the Λ.

1.4 Coherent Bremsstrahlung

In the Bremsstrahlung process an electron incident on a suitable radiator is decelerated by the electromagnetic field of the radiator's nuclei and emits an energetic photon. Bremsstrahlung has a continuous spectrum which becomes more intense when the energy of the accelerated particles is increased. When an amorphous radiator such as carbon is used, the Bremsstrahlung produced photons exhibit an energy spectrum that falls off with increasing photon energy (see chapter 3 Figure 3.4). If a radiator with a regular lattice structure, such as diamond is chosen and the diamond is orientated correctly with respect to the electron beam direction then one particular reciprocal lattice vector can be isolated in the crystal radiator [23]. The energy spectrum of these produced photons exhibit the characteristic coherent peak structure as shown in Figure 3.4. The photons under the coherent peak have a high degree of linear polarization.

1.5 Spin Observables in Pseudo-scalar meson Photoproduction

Spin observables have been shown to be more sensitive to the contributing resonances and underlying reaction dynamics than the traditional method of measuring cross sections. It is possible to combine spin observables to allow for a model independent analysis.

1.5.1 Formalism

Spin observables arise naturally from a study of the transversity amplitudes which can be related to the scattering amplitude of the reaction. The scattering amplitude for kaon photoproduction can be derived by writing down the s-matrix in the form:

$$S_{fi} = \frac{1}{(2\pi)^2}[\frac{M_n M_\Lambda}{4E_\Lambda E_K E_n E_\gamma}]^{\frac{1}{2}} M_{fi} \times \delta^{(4)}(p_n + p_\gamma - p_K - p_\Lambda) \tag{1.6}$$

where M, E and p are the mass, energy and 4-momenta of the reaction particles [24]. The Lorentz-invariant matrix M_{fi} element is given by:

$$M_{fi} = u(p_\Lambda, s_\Lambda) \sum_{j=1}^{4} A_j M_j u(p_p, s_p) \tag{1.7}$$

The amplitudes A_j contain information on the contributions of each state and

channel to the overall amplitude. Equation 1.7 can now be expressed in terms of the two component spinors χ , which gives an alternate representation of the amplitudes. The matrix element is now written as:

$$M_{fi} = [\frac{E_\Lambda + M_\Lambda}{2M_\Lambda}]^{\frac{1}{2}}[\frac{E_n + M_n}{2M_n}]^{\frac{1}{2}} < \chi(\Lambda)|F|\chi(n) > \tag{1.8}$$

where F can be given as a combination of the four Chew, Goldberger, Low and Nambu (CGLN) amplitudes [25]. These amplitudes can be written down as functions of scattering angle and energy [26]. The CGLN amplitudes can be subjected to a multi-pole analysis [27] in this formalism. However, it is convenient to change to a representation using transversity amplitudes when studying spin observables. Transversity amplitudes are denoted by b_i and are written in terms of the CGLN amplitudes as:

$$b_1 = -\frac{i}{\sqrt{2}}(F_1 - F_2 e^{-i\theta})e^{\frac{i\theta}{2}} \tag{1.9}$$

$$b_2 = -\frac{i}{\sqrt{2}}(F_1 - F_2 e^{-i\theta})e^{\frac{-i\theta}{2}} \tag{1.10}$$

$$b_3 = -b_1 - \frac{sin\theta}{\sqrt{2}}(F_3 + F_4 e^{-i\theta})e^{\frac{i\theta}{2}} \tag{1.11}$$

$$b_4 = -b_2 - \frac{sin\theta}{\sqrt{2}}(F_3 - F_4 e^{i\theta})e^{\frac{-i\theta}{2}} \tag{1.12}$$

Reference [26] shows that it is also possible to express the transversity amplitudes in terms of s-channel helicity flips N, S_1, S_2 and D. A negative flip amplitude is represented by N, S_1 and S_2 are single flip amplitudes and D is a double flip amplitude. The transversity amplitudes can now be written as:

$$b_1 = \frac{1}{2}[(S_1 + S_2) + i(N - D)] \tag{1.13}$$

$$b_2 = \frac{1}{2}[(S_1 + S_2) - i(N - D)] \tag{1.14}$$

$$b_3 = \frac{1}{2}[(S_1 - S_2) - i(N + D)] \tag{1.15}$$

$$b_4 = \frac{1}{2}[(S_1 - S_2) + i(N + D)] \tag{1.16}$$

The four amplitudes are complex and completely describe the photoproduc-

Table 1.2: Spin observables with their transversity representations and the type of observable. Table produced from reference [26].

Spin Observable	Transversity rep.	Type
Differential x-section, $d\sigma/dt$	$\|b_1\|^2+ \|b_2\|^2+ \|b_3\|^2+ \|b_4\|^2$	Single
Photon beam asymmetry,Σ	$\|b_1\|^2+ \|b_2\|^2- \|b_3\|^2- \|b_4\|^2$	Single
Target asymmetry, T	$\|b_1\|^2- \|b_2\|^2- \|b_3\|^2+ \|b_4\|^2$	Single
Hyperon recoil polarization, P	$\|b_1\|^2- \|b_2\|^2+ \|b_3\|^2- \|b_4\|^2$	Single
Polarization transfer, G	$2\ \mathrm{Im}(b_1b_3+ b_2b_4)$	Beam-Target
Polarization transfer, H	$-2\ \mathrm{Re}(b_1b_3- b_2b_4)$	Beam-Target
Polarization transfer, E	$-2\ \mathrm{Re}(b_1b_3+ b_2b_4)$	Beam-Target
Polarization transfer, F	$2\ \mathrm{Im}(b_1b_3- b_2b_4)$	Beam-Target
Polarization transfer, O_x	$-2\ \mathrm{Re}(b_1b_4- b_2b_3)$	Beam-Recoil
Polarization transfer, O_z	$-2\ \mathrm{Im}(b_1b_4+ b_2b_3)$	Beam-Recoil
Polarization transfer, C_x	$2\ \mathrm{Im}(b_1b_4- b_2b_3)$	Beam-Recoil
Polarization transfer, C_z	$-2\ \mathrm{Re}(b_1b_4+ b_2b_3)$	Beam-Recoil
Polarization transfer, T_x	$2\ \mathrm{Re}(b_1b_2- b_3b_4)$	Target-Recoil
Polarization transfer, T_z	$2\ \mathrm{Im}(b_1b_2- b_3b_4)$	Target-Recoil
Polarization transfer, L_x	$2\ \mathrm{Im}(b_1b_2+ b_3b_4)$	Target-Recoil
Polarization transfer, L_z	$2\ \mathrm{Re}(b_1b_2+ b_3b_4)$	Target-Recoil

tion process. Sixteen real numbers can be derived by taking bi-linear combinations and results from this work when combined with previous and future analyses will form a complete measurement of all sixteen spin observables. Table 1.2 shows the sixteen observables with their relations to the transversity amplitudes.

The authors of [26, 28, 29] have investigated how many observables are required to be measured to allow for the determination of the amplitudes without any discrete ambiguities. They concluded that a measurement of the differential cross-section ($d\sigma/dt$) , with the three single spin observables (Σ, P, T) and four appropriately chosen double spin observables (e.g. O_x, O_z, T_x, G) are sufficient to resolve all ambiguities. In the free proton case, there are data for $d\sigma/dt$, Σ, P, T, O_x, O_z,C_x,C_z [21,22,30,31] with data for the observables E, G, T_x, and T_z from a polarized target currently under analysis [32]. In the bound neutron case, this work provides measurements for five observables Σ, P, T, O_x, O_z. When these results are combined with the results from ongoing CLAS analyses using a circularly polarized photon beam [33] and future analysis on a polarized deuterium target [34], this will allow for a model-independent determination of the reaction amplitude.

The spin observables derived from the scattering amplitude imply an important correlation to the physics processes involved in strangeness photoproduction. Model calculations [2, 3] suggest that the spin observables measured in this anal-

ysis should be very sensitive to the underlying resonance contributions.

1.5.2 Experimental Extraction of Spin Observables

There are two main coordinate systems used in the literature. The primed system has the z-axis orientated along the direction of the outgoing K^0 particle. The unprimed system, which is used in this work, has the z-axis oriented along the incoming photon momentum axis, which leads to the quantization axis being defined as:

$$\underline{z} = \frac{\underline{k}}{|k|}, \underline{y} = \frac{\underline{k} \times \underline{q}}{|\underline{k} \times \underline{q}|}, \underline{x} = \underline{y} \times \underline{z} \tag{1.17}$$

where $\underline{k}$ is the momentum of the incoming photon and $\underline{q}$ is the momentum of the outgoing K^0. The unprimed system was a natural choice for this analysis as previous spin observable measurements have shown the polarization to be preferentially transferred along the z-axis in this system [22].

With the coordinate system defined, the extraction of spin observables can be done by analysing the angular distributions of the reaction decay products [35]. When using a linearly polarized photon beam and having the ability to measure the hyperon recoil polarization, the observables can be related as follows:

$$\begin{aligned} \rho_f \frac{d\sigma}{d\Omega} = \ & \tfrac{1}{2}\tfrac{d\sigma}{d\Omega}_{un} \ \Big\{1 - P_\gamma^{lin}\Sigma\cos 2\phi - \sigma_x\left(P_\gamma^{lin}O_x \sin 2\phi\right) \\ & +\sigma_y\left(P - P_\gamma^{lin}T\cos 2\phi\right) - \sigma_z\left(P_\gamma^{lin}O_z\sin 2\phi\right)\Big\} \end{aligned} \tag{1.18}$$

where $\frac{d\sigma}{d\Omega}$ is the differential cross section, Σ is the beam asymmetry, P is the recoil polarization, T is the target asymmetry and O_x and O_z are the double spin beam-recoil observables. The degree of linear beam polarization is P_γ^{lin} and the σ_i matrices are the hadron quantization axes of equation 1.17. Reference [24] shows that for an outgoing hyperon with arbitrary axis $\underline{\hat{n}}$ the differential cross-section is given by the trace:

$$P_f.\underline{\hat{n}}\frac{d\sigma}{d\Omega} = Tr\left[\sigma.\underline{\hat{n}}\rho_f\frac{d\sigma}{d\Omega}\right] \tag{1.19}$$

Equation 1.19 can then be substituted into 1.18 and by setting S = 1 - $P_\gamma^{lin}\Sigma\cos2\phi$, υ_x= $P_\gamma^{lin}O_x\sin2\phi$, υ_y= P - $P_\gamma^{lin}T\cos2\phi$, υ_z= $P_\gamma^{lin}O_z\sin2\phi$,

$$\rho_f \cdot \underline{\hat{n}} \frac{d\sigma}{d\Omega} = \frac{1}{2}\frac{d\sigma}{d\Omega}_{un} \left\{ S.Tr\left[\begin{pmatrix} 1 & 0 \\ 0 & 1 \end{pmatrix}\right] - \varphi_x.Tr\left[\sigma \cdot \underline{\hat{n}} \cdot \sigma_x\right] + \varphi_y.Tr\left[\sigma \cdot \underline{\hat{n}} \cdot \sigma_y\right] \right.$$
$$\left. -\varphi_z.Tr\left[\sigma \cdot \underline{\hat{n}} \cdot \sigma_z\right] \right\} \tag{1.20}$$

Polarization components can then be derived from the Pauli matrices:

$$P_x = -\frac{P_\gamma^{lin} O_x sin2\phi}{1 - P_\gamma^{lin} \Sigma cos2\phi} \tag{1.21}$$

$$P_y = \frac{P - P_\gamma^{lin} T cos2\phi}{1 - P_\gamma^{lin} \Sigma cos2\phi} \tag{1.22}$$

$$P_z = -\frac{P_\gamma^{lin} O_z sin2\phi}{1 - P_\gamma^{lin} \Sigma cos2\phi} \tag{1.23}$$

These three expressions allow for the extraction of the spin observables from the angular distributions of the polarization components. These relations can be substituted into equation 1.4, which gives the polarization of the recoiling hyperon. Furthermore, by using information from the two different polarization states of the photon beam, the three asymmetry relations can be derived from which the spin observables can be extracted.

1.6 Summary

The non-perturbative nature of QCD at intermediate energies means one has to rely upon phenomenological models to describe the structure of the nucleon. Baryon spectroscopy provides an opportunity to study the properties of a nucleon through its excited states. Quark models have thus far provided most of the theory on the baryon resonance spectrum, since chiral perturbation theory cannot be applied to resonance physics and lattice QCD calculations are still at an early stage. The key issue is to explain why the quark models predict a much richer resonance spectrum than has been observed experimentally. A large proportion of the world data is from $\pi N \rightarrow \pi N$ scattering experiments. However, quark model calculations have shown that some of these resonance states should couple strongly to $K^0\Lambda$ and $K^0\Sigma$ final states [1].

The work presented in this thesis will provide high quality, first time measurements of several polarization observables. The photoproduction of $K^0\Lambda$ and $K^0\Sigma$ will be studied at photon energies from 1.3 to 2.3 GeV with a linearly polarized

photon beam. This will give access to five observables: the photon asymmetry Σ, the target asymmetry T, the hyperon recoil polarization P, and the two double polarization observables O_x and O_z. The interpretation of these measurements will aim to provide some insight into the missing resonance problem, as well as giving a better understanding of the process of strangeness production. The results of this work and their theoretical interpretation should provide an insight into the strangeness production process. Combining the spin observable results in this study with those from previous CLAS analyses should give a model independent method of determining the overall amplitudes without any phase ambiguities. This will be a step towards understanding the "missing" resonance issue and in determining the degrees of freedom available in the non-perturbative energy region.

Chapter 2

Previous Experiments and Theoretical Background

This chapter will outline the motivation for the analysis and extraction of polarization observables in $K^0\Lambda$ and $K^0\Sigma^0$ photoproduction, starting with a review of previous experiments. The focus will then be on a number of the phenomenological models that are used in the energy range of non-perturbative QCD. A selection of coupled-channels, isobar and Regge models will be studied, noting their successes and limitations in describing the baryon spectrum.

2.1 Previous Experiments

The primary motivation is the lack of data for spin observables in the neutral decay channels from a quasi-free neutron target. Historically, the main focus of investigation for kaon photoproduction on the nucleon has been for the reactions $\gamma p \to K^+\Lambda$ and $\gamma p \to K^+\Sigma^0$ since there is a large amount of experimental data available in these channels. Unfortunately, this is not the case for the $\gamma n \to K^0\Lambda$ and $\gamma n \to K^0\Sigma^0$ channels since free neutron targets are not available. The deuteron can be used as an effective neutron target because it has a small binding energy and simple internal structure. Therefore, kaon photoproduction on the deuteron is the natural candidate for investigating kaon photoproduction on the neutron. Given the lack of data this section will therefore only mention a few previous experiments that show a relevant degree of similarity. For the proton there are several published results by groups at the Spectrometer Arrangement for Photon Induced Reactions (SAPHIR) [36, 37] and CLAS [21, 30, 38–40] collaborations. The published total cross-sections are shown in Figure 2.1. The C_x and C_z polarization transfer observables are shown in Figure 2.2. The results

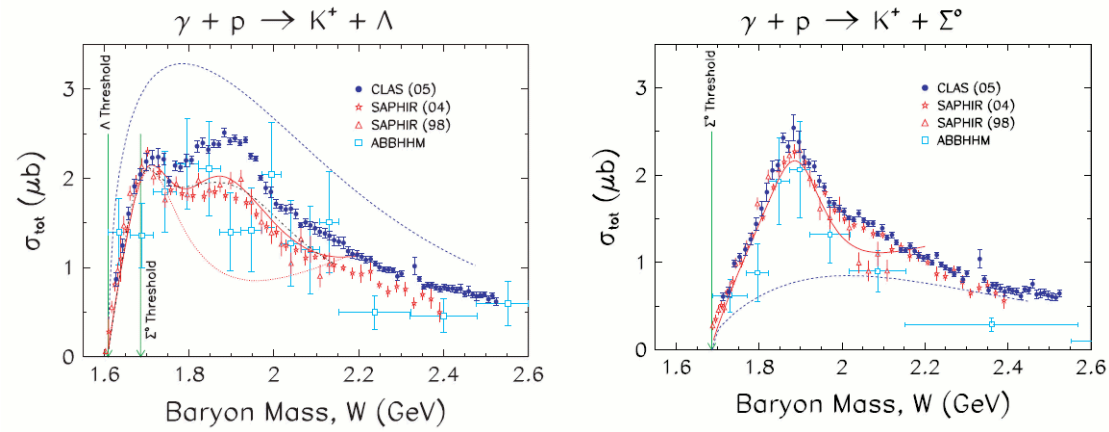

Figure 2.1: Total cross-sections for Λ and Σ photoproduction on the proton showing the latest CLAS data [21] with previous measurements from Bonn. In both plots the CLAS data are shown as blue dots with the SAPHIR 04 (red stars), SAPHIR 98 (red triangles) and ABBHM (blue squares) [36, 37]. The plots also display a comparison with several theoretical models: Regge model [43, 44] (dashed blue), Kaon-MAID [41] (solid red), Kaon-MAID with the $D_{13}(1895)$ resonance turned off (dotted red) and the model of Saghai et al [45] (dot-dashed black).

clearly show that the photon transfers almost all of its polarization to the hyperon along the z-axis for a broad range of kinematics. In contrast, there is a negligible amount of polarization transferred from the beam to the hyperon along the x-axis. The model calculations used for comparison in Figure 2.2 are: Kaon-MAID (dashed green) [41], partial wave analysis (blue) [42], Regge-plus-resonance (solid red) [43] and Gent (magenta) [44].

2.1.1 Deuteron Experiments at Jefferson Lab

Two real photon experiments have previously been undertaken at Jefferson Lab. The g10 experiment [46], which ran in the summer of 2003, utilised a high energy ($\sim$ 6 GeV) circularly polarized electron beam to produce a secondary unpolarized photon beam. The electron beam was run with a high current to produce a high number of statistics. Its aim was to measure excited and exotic pentaquark states. A total of ten billion events were recorded. Since the only part of the tagger covering photon energies above 4.5 GeV was in the trigger, the data are not suitable for resonance physics.

The g2 experiment [47] , run in the summer of 1999, accumulated far fewer statistics. Again the experiment used a circularly polarized electron beam to produce an unpolarized photon beam. Its main focus was on both inclusive and

exclusive measurements of the cross-sections for the six elementary strangeness production channels on the nucleon as well as the investigation of the hyperon-nucleon interaction. For linearly polarized photon beams, there are currently no CLAS data on the deuteron.

2.1.2 Deuteron Experiments at other facilities

Other photon facilities include the GRenoble Anneau Accelerateur Laser (GRAAL) in Grenoble and the Mainzer Mikrotron (MAMI) in Mainz. Both laboratories can achieve a maximum beam energy of 1.5 GeV. This is below the threshold for most of the third-tier N* resonances, including the $D_{13}(1900)$. This limits the reaction kinematics which these two facilities can study.

The Electron Accelerator and Stretcher (ELSA) facility in Bonn uses the same coherent Bremsstrahlung method to produce linearly polarized photon beams as employed at Jefferson Lab. However, its maximum electron energy is considerably lower at 3.5 GeV. The degree of linear photon polarization increases with the ratio of $\frac{E_\gamma}{E_e}$, so the facility in Hall B at Jefferson Lab is significantly better for higher photon energies. More importantly, the current detector configuration at ELSA is intended for neutral particle detection, and can therefore be seen as complimentary to the CLAS.

The Laser Electron Photon Spring-8 facility (LEPS) has highly polarized back scattered photon beams up to 2.4 GeV using a 351nm laser. Recently, beam polarization asymmetries for the γp $\rightarrow K^+\Lambda$ and γp $\rightarrow K^+\Lambda$ channels were published [48]. Preliminary results from an inclusive measurement of the differential cross-section and beam asymmetry in the $\gamma n \rightarrow K^+ \Sigma^-$ channel are now available (see Figures 2.3 and 2.4 respectively) [49]. In contrast to the CLAS, the LEPS detector acceptance is limited to very forward angles which is not suited to exclusive measurements and gives poor kinematic coverage. Therefore, polarization observables that involve the hyperon recoil polarization cannot be measured. Nor is it possible to separate re-scattering events from quasi-free ones.

Given the full angular coverage available in Hall B at Jefferson Lab and the limitations of the above mentioned photon facilities, it is the perfect location to study exclusive strangeness production on the deuteron.

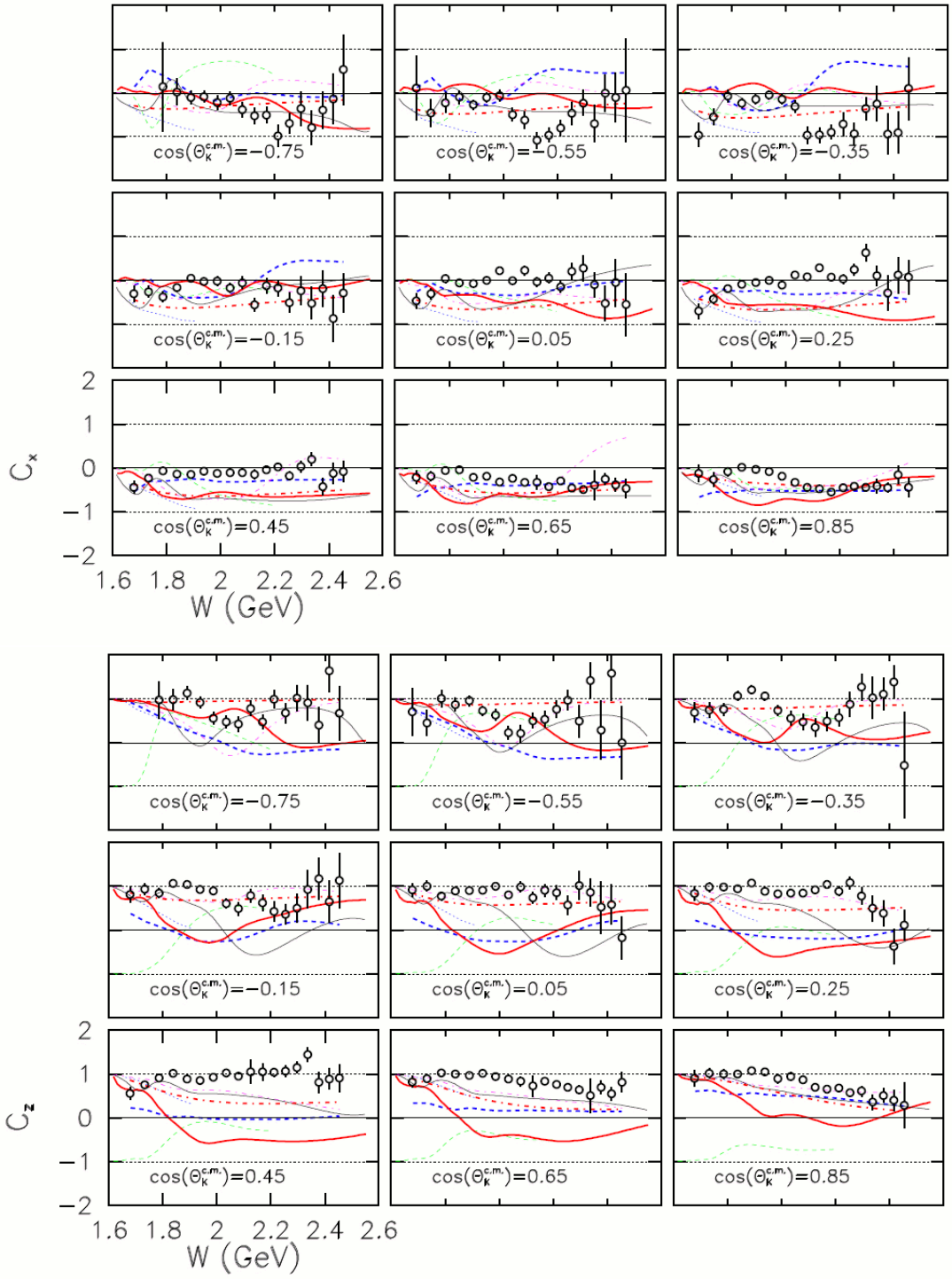

Figure 2.2: C_x (top) and C_z (bottom) double spin observables for the $\gamma p \to K^+\Lambda$ channel as measured at CLAS [22]. The model calculations used for comparison are: Kaon-MAID [41] (dashed green), partial wave analysis [42] (blue), Regge-plus-resonance [43] (solid red), Gent model [44] (magenta).

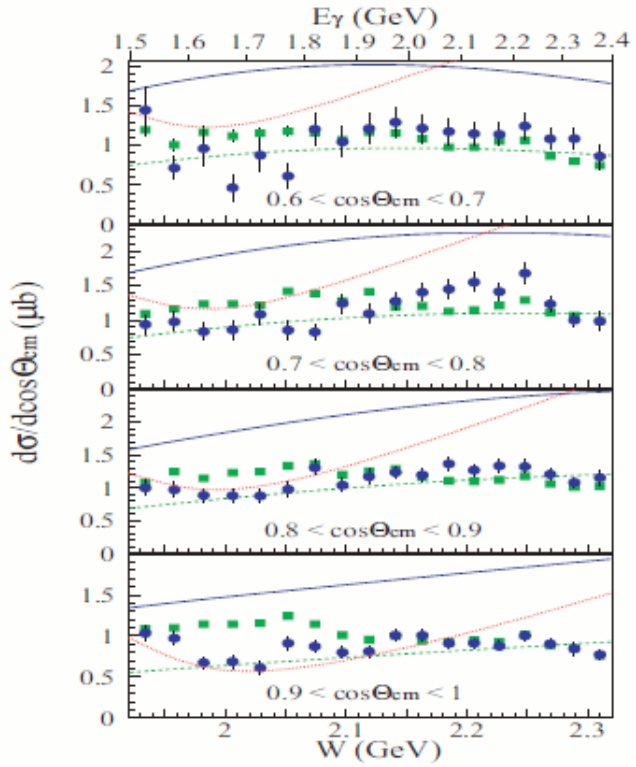

Figure 2.3: Differential cross-sections for $\gamma n \rightarrow K^+\Sigma^-$ (circle) and $\gamma p \rightarrow K^+\Sigma^0$ (squares). Only statistical error bars are shown. The solid and dashed curves are the Regge model calculations for the $K^+\Sigma^-$ and $K^+\Sigma^0$ respectively. The dotted curve is the Kaon-MAID model calculations for $K^+\Sigma^-$. Figure taken from reference [49].

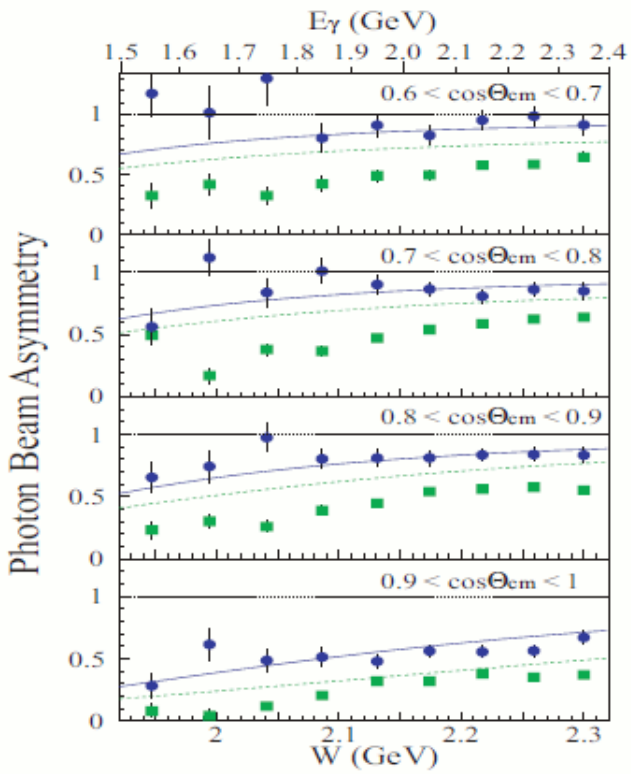

Figure 2.4: Photon beam asymmetries for $\gamma n \rightarrow K^+\Sigma^-$ (circle) and $\gamma p \rightarrow K^+\Sigma^0$ (squares). The solid and dashed curves are the Regge model calculations for the $K^+\Sigma^-$ and $K^+\Sigma^0$ respectively. Figure taken from reference [49].

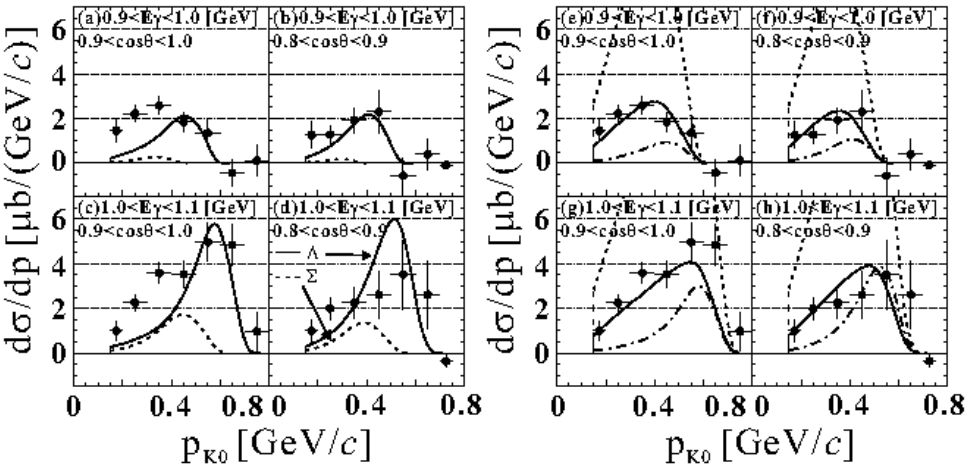

Figure 2.5: Momentum Spectra for K^0 with calculated cross-sections using the elementary amplitudes of Kaon-MAID [3] (a to d) and SLA [51] (e to h) models. Solid and dashed curves in (a to d) show contributions from n(γ,K^0)Λ process and sum of n(γ,K^0)Σ^0 and p(γ,K^0)Σ^+ processes, respectively. Dashed, solid and dot-dashed lines in (e to h) show contribution of n(γ,K^0)Λ process with r_{KK_l}= -0.447, -1.5, and -3.4, respectively.

2.1.3 K^0 Differential Cross-Section Results - Laboratory of Nuclear Science (LNS)

Differential cross-sections of the ^{12}C(γ,K^0) reaction at photon energies below 1.1 GeV have been measured by the authors of [50] and are shown in Figure 2.5. Neutral Kaons were identified by reconstructing the $K_s{}^0 \rightarrow \pi^+\pi^-$ decay. The authors found that the integrated cross-section is almost the same magnitude as that of ^{12}C(γ,K^+). Quasi-free spectra of the reaction were calculated using the elementary amplitudes given by the Kaon-MAID [3] and Saclay-Lyon A models [51]. It was found that both models described the spectra in the threshold region reasonably well, though the Saclay-Lyon A model can account better for the excess of the measured cross-section in the K^0 low momentum region compared with the Kaon-MAID calculation. The authors suggest that this may show the n(γ,K^0)Λ reaction to be more backward peaked in the centre-of-mass frame.

2.2 Polarization Observables

Polarization or spin observables have been shown to be amongst the most sensitive probes of a process. These spin observables are of particular interest in reactions that involve the photoproduction of strange mesons, as it is possible for a suitable

combination of the observables to allow for a model independent analysis. They arise naturally from a study of the production amplitudes which can be related to the scattering amplitude of the reaction as shown by the authors of reference [24].

Sixteen polarization observables can be defined which can be divided into two subgroups: single- and double-polarization observables as seen in Table 1.2.

The recoil observables can be measured by taking advantage of the fact that the Λ and Σ hyperons are self-analysing[1]. The observables are not independent but are related by a set of inequalities (2.1-2.2) [52] and six equations (equations 2.3 to 2.8) [24].

$$(P_y)^2 + (O_x)^2 + (O_z)^2 \leq 1 \tag{2.1}$$

$$(\Sigma)^2 + (O_x)^2 + (O_z)^2 \leq 1 \tag{2.2}$$

$$E^2 + F^2 + G^2 + H^2 = 1 + P^2 - \Sigma^2 - T^2 \tag{2.3}$$

$$FG - EH = P - \Sigma T \tag{2.4}$$

$$T_{x'}^2 + T_{z'}^2 + L_{x'}^2 + L_{z'}^2 = 1 + \Sigma^2 - P^2 - T^2 \tag{2.5}$$

$$T_{x'}L_{z'} - T_{z'}L_{x'} = \Sigma - PT \tag{2.6}$$

$$C_{x'}^2 + C_{z'}^2 + O_{x'}^2 + O_{z'}^2 = 1 + T^2 - P^2 - \Sigma^2 \tag{2.7}$$

$$C_{z'}O_{x'} - C_{x'}O_{z'} = T - P\Sigma \tag{2.8}$$

For example, if the recoil polarization P, the beam asymmetry Σ and the four beam-recoil observables are known, then one can calculate T. The eight observables of interest in this work can then be extracted from the expression for the polarized differential cross-section [24].

[1]This means it violates parity and decays weakly, therefore allowing its polarization to be measured.

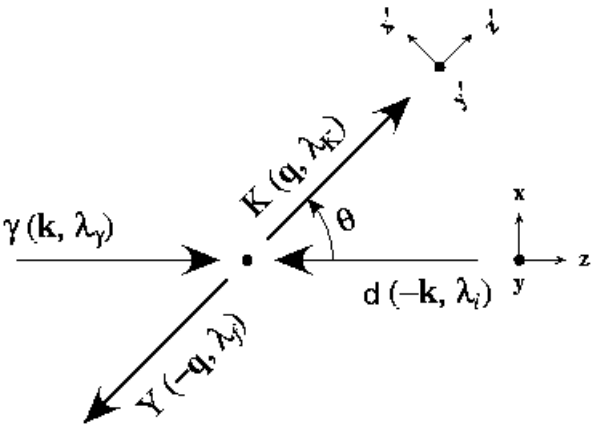

Figure 2.6: Definition of the unprimed and primed coordinate systems as used in the literature. In the unprimed system, the z-axis points along the direction of the incoming photon momentum, $\overrightarrow{k}$. In the primed system, the z' axis points along the kaon momentum, $\overrightarrow{q}$, the y' axis is perpendicular to the reaction plane and defined by $\overrightarrow{P_\gamma} \times \overrightarrow{P_K}$. The x' axis is in the reaction plane.

$$\frac{d\sigma}{d\Omega} = \sigma_0\{1 - P_{lin}\Sigma cos2\phi \tag{2.9}$$

$$+P_{x'}(-P_{lin}O_{x'}sin2\phi - P_{\odot}C_{x'})$$

$$-P_{y'}(-P + P_{lin}Tcos2\phi)$$

$$-P_{z'}(P_{lin}O_{z'}sin2\phi + P_{\odot}C_{z'})\}$$

Here P_{lin} and $P_{\odot}$ are the degrees of linear and circular polarization respectively and ϕ is the angle between the photon polarization vector and the reaction plane. The orientation of the unprimed and primed axes are shown in Figure 2.6.

In the circularly polarized case, the asymmetries for $C_{x'}$ and $C_{z'}$ are constructed using the beam helicity information rather than the ϕ dependence [38]. The target asymmetry T is the most problematic as it has the same ϕ dependence as Σ and the same $P_{y'}$ dependence as the recoil polarization P. Therefore, the uncertainties from Σ and P will propagate into the determination of T.

In order to perform a complete measurement determining all amplitudes up to an overall phase and eliminate the ambiguities, two additional double-polarization observables are required [26]. These are the beam-recoil polarization transfer observables O_x and O_z. Their method of extraction will be discussed in chapter 5.

2.3 Coupled-channels model

Coupled-channels models have the ability to account for multi-step intermediate processes and final state interactions. The multi-step process $\gamma N \rightarrow \pi N \rightarrow KY$ is thought to have a large effect in kaon photoproduction since the $\gamma N \rightarrow \pi N$ amplitudes are significantly larger than the direct KY production process.

Significant progress has been made by Waluyo and Bennhold in developing a coupled-channels Chiral-Symmetry-Inspired (CSI) model [53]. It is based on the work by Feuster and Mosel [54] but the driving terms of the original model, which are defined through traditional effective Lagrangians, have been replaced by ones with new background and resonance parts. The new background is obtained from a potential that takes into account the requirements of SU(3) chiral dynamics. This involves expanding the chiral Lagrangian to a given order and includes contact terms permitted to that order. The resonance contributions have been updated using the modern covariant resonance Lagrangians derived by Pascalutsa [55].

New background amplitudes are reconstructed from the standard s, t, and u Born terms, σ and a_0 scalar-meson resonances, ρ, ω and K^* vector meson resonances, as well as Weinberg-Tomozawa and higher order chiral contact terms. The new resonance amplitudes are constructed from the s- and u-channel pole diagrams where spin-$\frac{1}{2}$,$\frac{3}{2}$ and $\frac{5}{2}$ baryon resonances propagate in the intermediate states. This is the first coupled-channels model where baryon resonances are included using modern hadronic and electromagnetic interaction Lagrangians.

The CSI model includes five asymptotic states of πN, $2\pi N$, ηN, KΛ and KΣ. To ensure that the CSI model is gauge-invariant, the gauge-invariance restoration scheme of Davidson and Workman [56] has been implemented. The model is used to investigate baryon resonance states through meson photoproduction reactions, and is currently implemented in the energy region of W $<$ 2 GeV. The model uses input from recent high quality photoproduction data provided by the CLAS collaboration [21, 30, 57]. Figure 2.7 shows fits from the CSI model to the $\gamma p \rightarrow K^+\Lambda$ differential cross-section data at high W.

In the energy range of 1.8 $<$ W $<$ 2.0 GeV, four possible missing resonance states were investigated using the CSI model and the available proton data. They are the S_{11}, P_{11}, P_{13} and D_{13}. Each would constitute the third state in its respective partial wave. No evidence for the first three was found. A possible D_{13} state was found with a mass of 1961 MeV and a width of 313 MeV. Its properties and a comparison with the values from other analyses are shown in Tables 2.1 and 2.2.

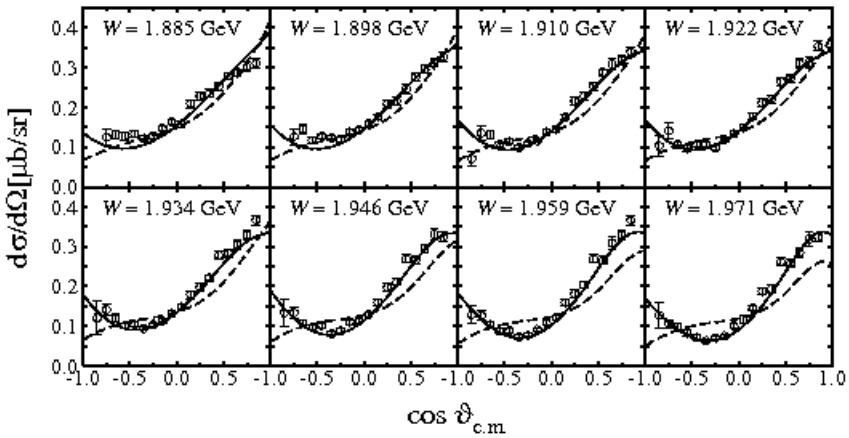

Figure 2.7: Differential cross-sections for $\gamma p \rightarrow K^{+}\Lambda$ at high W, given as a function of the kaon angle in the centre of mass system. The solid lines show the calculation using the CSI model with the D_{13} resonance and the dashed lines without the D_{13} resonance. Data are from reference [30].

Table 2.1: Preliminary properties of the $D_{13}(1900)$ resonance extracted from proton data. The mass and total width are given in MeV, and the decay ratios β are in %. CSI is the Chiral Symmetry Inspired model and P & M is the Penner and Mosul model of reference [16].

$D_{13}(1900)$	Mass (MeV)	Γ_{tot}(MeV)	$\beta_{\pi N}$	$\beta_{2\pi N}$	$\beta_{\eta N}$	$\beta_{K\Lambda}$	$\beta_{K\Sigma}$
CSI model	1961	313	7	48	0.5	15	31
P & M	1946	859	12	59	7	0.2	0.7
Vrana et al. [58]	1940	412	10	75	14	0	-

Table 2.2: Preliminary electromagnetic helicity amplitudes in $10^{-3}\mathrm{GeV}^{-1/2}$ for the D_{13} (1900) resonance extracted from proton data. The superscript p or n indicates the proton or neutron helicity amplitude. CSI is the Chiral Symmetry Inspired model and P & M is the Penner and Mosul model of reference [16].

$D_{13}(1900)$	$A^p_{1/2}$	$A^p_{3/2}$	$A^n_{1/2}$	$A^n_{3/2}$
CSI model	+21	-1	+130	+123
P & M model	+12	-10	+23	-9

If the existence of the missing D_{13} resonance is confirmed, it would fall into the PDG [10] two star category where a resonance state is found in different analyses with rough agreement of mass values, but with disagreement in other properties such as decay width of helicity amplitudes. Until neutron data becomes available all these parameters must be regarded as preliminary.

Recent evidence for the $D_{13}(1900)$ comes from the available KΛ and KΣ photoproduction differential cross-section data on the proton [30, 37, 40]. Current coupled-channels analyses [16, 53] give a reasonably good description of the proton data. However, most of the extracted properties of the missing $D_{13}(1900)$ resonance vary widely. New data are needed to provide a more stringent constraint for the resonance properties or to rule out its existence completely. A careful look at the helicity amplitudes of the $D_{13}(1900)$ resonance, shown in Table 2.2 suggests which new data are needed. The $A^n_{1/2}$ and $A^n_{3/2}$ values are large which indicates the presence of a large sensitivity to the $D_{13}(1900)$ in the neutron channel $\gamma n \rightarrow K^0\Lambda$ reaction.

The Σ channels are not sensitive to the D_{13} resonances due to the Σ having isospin 3/2. However, data are needed for KΣ^-, K$\Sigma^+$and KΣ^0 to exploit the isospin symmetry of the Σ. The first of these channels can only be studied with a neutron target. The isospin symmetry is important since the Σ channels also couple to Δ^*(I=3/2) states. The latest CSI model predictions[2] for the observables in the $\gamma n \rightarrow K^0\Lambda$ channel are shown in Figure 2.8, with and without the $D_{13}(1900)$ resonance.

2.4 Isobar Models

These models were pioneered by Thom [59] with the aim of describing the hadronic reaction by evaluating various tree-level Feynman diagrams for both resonant and

[2]The data will not be compared to this model as the authors of these calculations have not made them readily available for comparison.

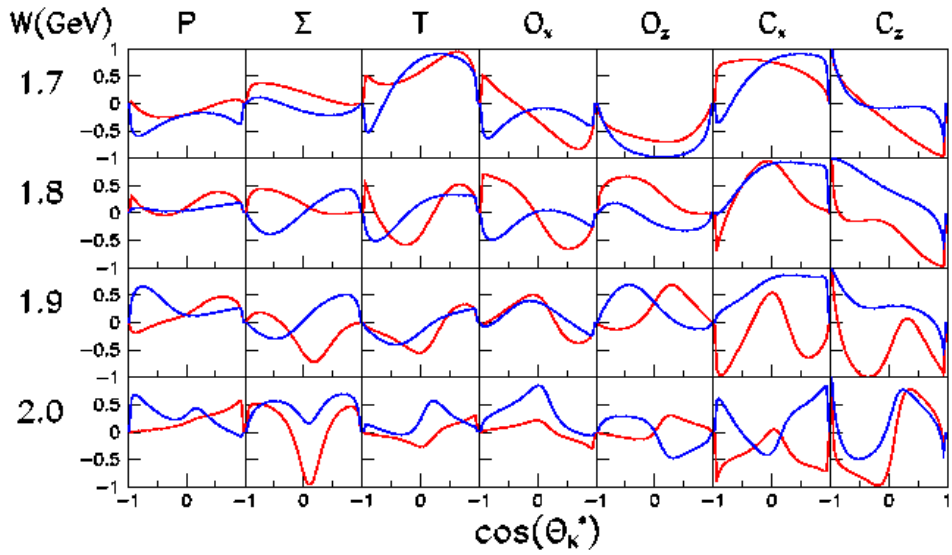

Figure 2.8: CSI model predictions for the seven spin observables in the $\gamma n \rightarrow K^0\Lambda$ channel as a function of kaon angle in the centre of mass reference frame. The red curve shows the calculation with the $D_{13}(1900)$ resonance included and the blue curve without the $D_{13}(1900)$.

non-resonant exchange of mesons and baryons. Isobar models assume that the particle production and decay proceed via resonances and all subsequent decays appear to be two-body reactions. For example, the decay A →B + C + D is actually A →X + D followed by X →B + C. The intermediate state X is a resonance state with mass and width. Effective Lagrangian isobar models at the order of the tree-level have been developed by different groups to try to unfold the nucleon resonance excitation spectrum [60–62]. In this formalism every particle in the reaction can be treated as an effective field with properties such as photo-coupling amplitudes, mass and strong decay widths. Although a tree-level approach does not account for the effects of channel coupling and final state interactions, it does reduce the complexity of the interaction and gives a reliable first order understanding of the resonance parameters. The Feynman diagrams contributing to the $\gamma n \rightarrow K^0 Y$ reaction are shown in Figure 2.9.

The Kaon-MAID isobar model [41] is an effective Lagrangian model where the hadrons are the degrees of freedom. This model bases its initial selection of amplitudes on the recommendations of numerous analyses [60–63], attempting to provide a description of kaon photoproduction based on the selection of a minimal number of reaction diagrams. The resonances selected for inclusion in this model are listed in Table 2.3. The Kaon-MAID model uses standard Born terms to describe the background as well as $K^*(892)$ and $K_1(1270)$ vector meson

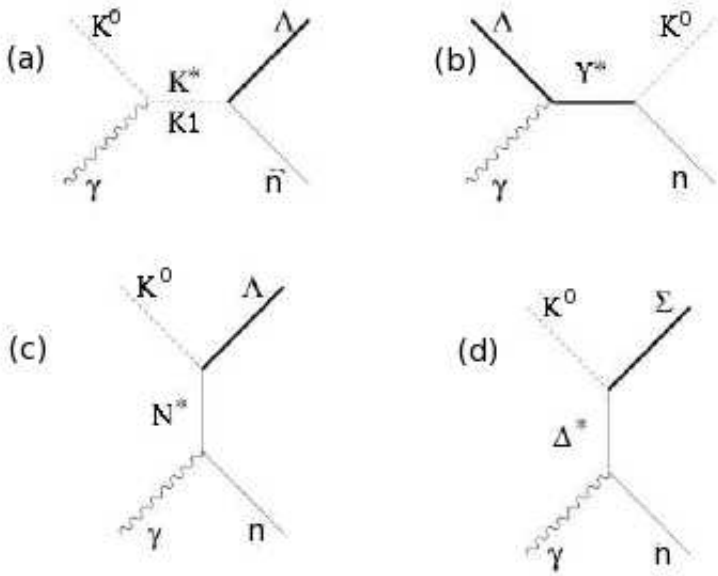

Figure 2.9: Feynman diagrams for the reaction γn $\rightarrow$K$^0\Lambda$ (a) to (c) with the additional diagram (d) for the reaction γn$\rightarrow$K$^0\Sigma^0$. The diagrams represent contribution in the t, u and s-channels respectively.

Table 2.3: Table showing the amplitudes included in the Kaon-MAID isobar model [41].

Resonance	KΛ	KΣ	Channel
$S_{11}(1650)$	X	X	s-channel
$P_{11}(1710)$	X	X	s-channel
$P_{13}(1720)$	X	X	s-channel
$D_{13}(1895)$	X		s-channel
$S_{31}(1900)$		X	s-channel
$P_{31}(1910)$		X	s-channel
K* (893)	X	X	t-channel
$K_1(1270)$	X	X	t-channel

poles in the t-channel. The gauge method developed by Haberzettl [64] was used to include hadronic form factors. It also included separate cut-off masses of 800 and 1890 MeV which were used to suppress the background and resonance sectors separately. Except for the $D_{13}(1895)$, the resonances in Table 2.3 were documented to contribute strongly to kaon photoproduction. Mart and Bennhold were one of the first to provide evidence for the $D_{13}(1895)$ state, a potential missing resonance in strangeness photoproduction [3]. Their model investigated $K^+\Lambda$ photoproduction, as its isospin structure allows only the excitation of N* states, whereas the $K^+\Sigma^0$ channel also allows Δ states to contribute making it more complicated to describe. Their work was guided by the coupled channels approach of Feuster and Mosel [54] which indicated that the three "core" resonant states $S_{11}(1650)$, $P_{11}(1710)$ and $P_{13}(1720)$, should dominate the $K^+\Lambda$ channel. The main reason for the development of this model was to try to reproduce the cross-section results from the SAPHIR collaboration [37] (Figure 2.1). The model describes the general trend of the data well but does not account for the structure at W=1900 MeV. This feature can be described by the constituent quark model of Capstick and Roberts [1] which predicts the existence of excited baryon states around W=1900 MeV. One such state predicted to exist was the $D_{13}(1960)$, which should have a large decay width into the $K\Lambda$ channel. This $D_{13}(1960)$ state was then entered into the model calculations. The subsequent results showed that the model agreed well with the cross-section measurements. Taking this result along with the good agreement between the partial widths for the core resonances with the quark model predictions, gave reassurance that the structure in the SAPHIR cross-section does reflect the $D_{13}(1960)$ state. Mart and Bennhold concluded that measuring the photon asymmetry would be a good way to examine the role of the $D_{13}(1960)$ missing resonance in kaon photoproduction.

Saghai [45] did a further investigation of the SAPHIR cross-section data in an effective Lagrangian approach and concluded that the cross-section could be equally well reproduced without the inclusion of the $D_{13}(1960)$ resonance. The background parameters were adjusted with the inclusion of two hyperonic resonances $P_{01}(1810)$ and $P_{03}(1890)$, to reproduce accurately the fitted data. This highlights the danger of using limited observables to draw conclusions about the existence of predicted missing resonances in an isobar prescription.

The Gent model, developed by Janssen et al [2,65,66] is an effective field theory which takes into account contributing tree-level diagrams only. In addition to the s-channel resonance diagrams, t-channel K^* and hyperon exchange is included as well as standard Born terms. Tree-level approaches are relatively simple. The

number of parameters required to be determined by fits to the data is usually much smaller than for coupled-channels approaches. Despite the reduction in fit parameters, it has been shown in reference [67] that the interpretation of current data using this approach is plagued by ambiguities.

Further developments to the Gent model have been made by Corthals et al [68]. They have included a new method of constraining the background in $\gamma p \rightarrow KY$ reactions. High energy data ($E_\gamma >$ 4 GeV) are used to fix the parameters of the background process and a Regge model approach is used to extrapolate this background to the resonance region. By definition, the Regge model cannot account for any features which appear as strong s-channel resonances and therefore a limited number of s-channel resonances are also included. This gives rise to a Regge-Plus-Resonance (RPR) model. Reference [68] argues that even though the notion of duality might suggest a problem with double counting in the kinematics of the resonance region, this is unlikely to be a significant problem. This new method of dealing with the background has many advantages over previous attempts that relied on heavy interference with Born terms and were not applicable at photon energies above 2 GeV. It also reduces the number of free parameters to a handful of coupling constants for the s-channel resonances.

2.5 Multi-pole and Partial Wave Analyses

The CLAS and SAPHIR cross-section results have been studied in a partial wave framework along with the CLAS recoil polarization and LEPS photon beam asymmetry results by Sarantsev et al [42]. Data from the $K^+\Lambda$ and $K^+\Sigma^0$ channels were combined with previous results on π^0 and η photoproduction [69, 70]. Both the CLAS and SAPHIR cross-section results were found to be incompatible and required an energy dependent normalization factor as is shown in Figure 2.10. This factor was introduced to account for the discrepancies between the CLAS and SAPHIR cross-section measurements.

The calculations from Sarantsev [42] are compared to the photon asymmetry and recoil polarization data in Figure 2.11. Both analyses suggest the possibility of including a baryon resonance with a P_{11} state observed in the region of 1840 MeV. The analyses also suggests the possible existence of four D_{13} resonances at energies of 1520, 1700, 1870 and 2170 MeV.

The CLAS, SAPHIR and LEPS data has also been studied using a multi-pole approach by the authors of [27], looking at possible contributions from higher spin states. Their study showed a mutual consistency between the SAPHIR

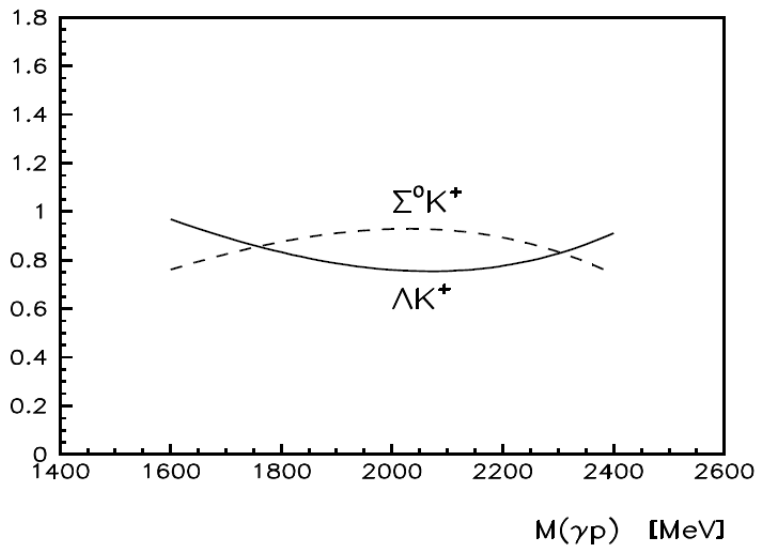

Figure 2.10: Energy dependent normalization factor from reference [42].

and CLAS data, while the LEPS data was shown to be more consistent with the CLAS results. Fitting their calculations to both the SAPHIR and CLAS data, they identified the $S_{11}(1650)$, $P_{13}(1720)$, $D_{13}(1700)$,$D_{13}(2080)$, $F_{15}(1680)$ and $F_{15}(2000)$ as the main resonances. Although the fits to the CLAS and LEPS data point towards the $P_{13}(1900)$, $D_{13}(2080)$,$D_{15}(1675)$, $F_{15}(1680)$ and $F_{75}(1990)$ as having the main contribution. This highlights the difficulty in having two mutually incompatible data sets from SAPHIR and CLAS. Figures 2.12 and 2.13 show results from three different fits compared to the published data for the photon and target asymmetries respectively.

The first fit is of LEPS and SAPHIR data, in the second fit LEPS and CLAS data was used and in the third fit all three LEPS, CLAS, SAPHIR data sets were used. The results appear to suggest that when applying the world database for kaon photoproduction, attempts to extract resonance parameters will be largely dependent on the data set. The multi-pole analysis shows the importance of including higher spin states in the calculation and highlights the need for high precision measurements of as many different observables as possible to allow for their parameter extraction. It is important to note that all models agree well where there are data but predict different trends where no data exists. The models presented here will be better tested with soon to be published data on the free proton [31].

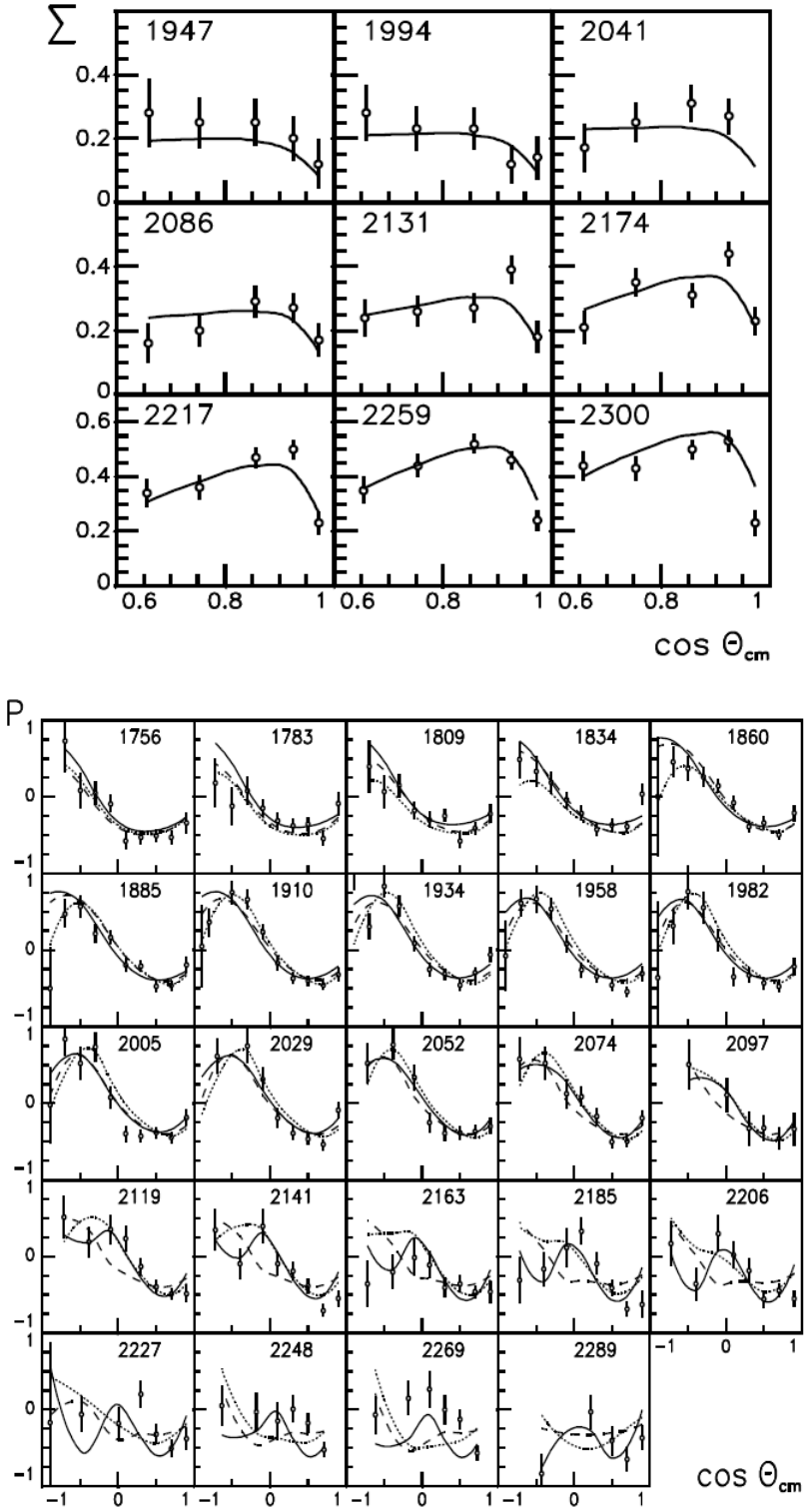

Figure 2.11: Beam asymmetries for various W bins for the $\gamma p \rightarrow K^{+}\Lambda$ reaction from LEPS [48] showing the partial wave analysis fits [42] (top plot). Recoil polarization results from CLAS [21] (bottom plot) with the solid line showing the partial wave fits, the dashed line is the fit with no N(2170) D_{13} included, and the dotted line is the fit with no N(1840) P_{11} included.

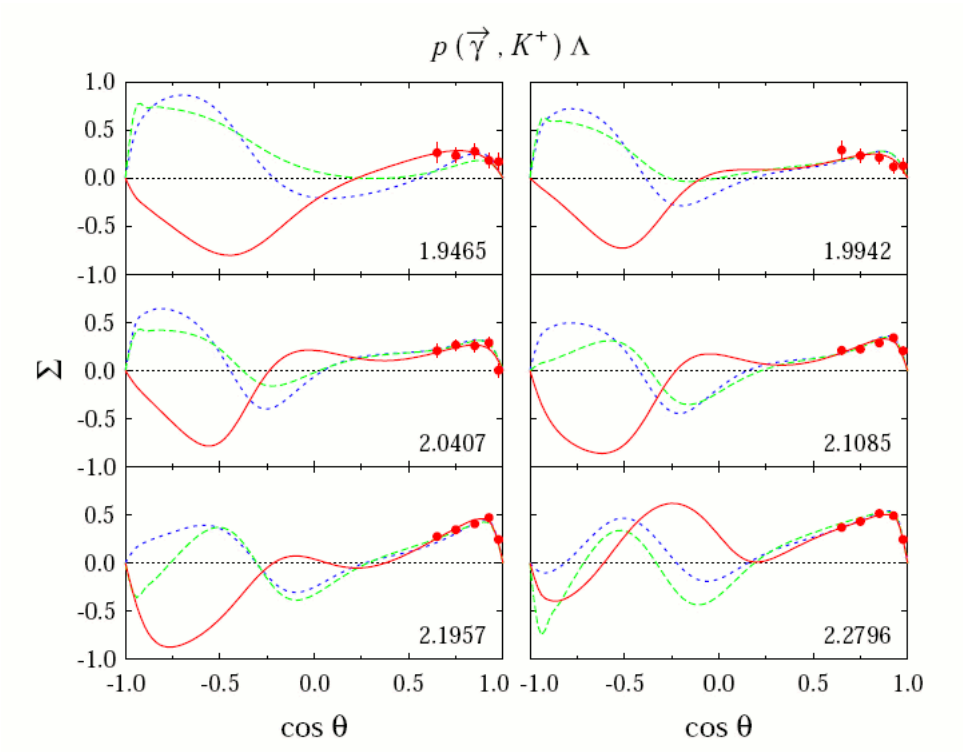

Figure 2.12: Multi-pole fits [27] to the photon asymmetry data from LEPS [48]. Solid red line is from fit 1, the blue dot-dashed line from fit 2 and the green dashed line from fit 3.

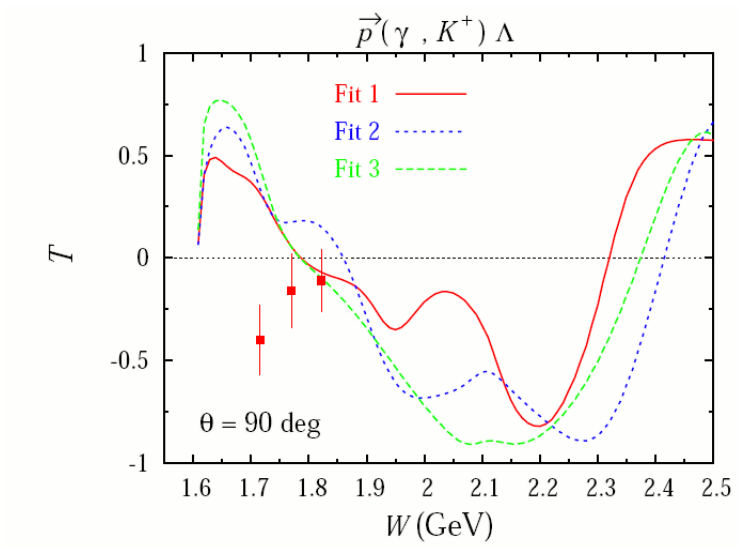

Figure 2.13: Multi-pole fits [27] to the target asymmetry data from reference [71]. Solid red line is from fit 1, the blue dot-dashed line from fit 2 and the green dashed line from fit 3.

2.6 Regge Models

In 1959, Regge introduced a new concept for dealing with scattering amplitudes [72]. When discussing solutions of the Schrodinger equation for non-relativistic potential scattering, he suggested to treat the angular momentum as a complex variable. Regge showed that an extension into the complex plane could help in determining the dispersion properties of the scattering amplitudes. It became clear that this technique was extremely useful in high energy particle physics, as it could account for poles in a partial wave decomposition when crossing symmetry is considered. The Regge formalism groups particles together with the same quantum numbers but different spin into "Regge trajectories". The idea is that at high energies ($>$ 4 GeV) where single resonances can no longer be identified, the photoproduction process is described by the exchange of Regge trajectories rather than individual particles. Although Regge models are most valid at high energies, recent studies have suggested that meson photoproduction in the resonance region can be fairly well described by a Regge approach.

The Regge model of references [43, 73] describes the exclusive electromagnetic strangeness production reactions $\gamma p \rightarrow K^+\Lambda$ and $\gamma p \rightarrow K^+\Sigma^0$ through the exchange of only two t-channel trajectories: K and K*. Their model did not use s-channel resonance excitations and the coupling constants at the [K, (Λ, Σ), N] and [K^*,(Λ, Σ),N] vertices were constrained to high energy photoproduction data.

The model calculations of [43, 73] are compared to cross-section results from SAPHIR [37] and CLAS [21] for both $K^+\Lambda$ and $K^+\Sigma^0$ channels in Figure 2.14. Two calculations are shown, one with both K$^+$and K* exchanges and one with only K^* exchange. Some agreement is achieved with the calculation including both the K and K*trajectories and the CLAS data, at forward angles and low centre of mass energy. However, the model does not account for the bumps seen in the cross-sections around W = 1.75 GeV and 1.95 GeV in the $K^+\Lambda$ channel. This is likely due to these structures being from the results of s-channel resonances and therefore not accounted for in a pure t-channel exchange model. The right plot in Figure 2.14 shows photon asymmetry results from LEPS compared against the model calculations. The model including both K and K*trajectories reproduces the general trend of the K$^+\Sigma^0$ data in the highest centre of mass energy bin. However, in the K$^+\Lambda$ channel the model with only the K trajectory does a better job at describing the data both in magnitude and trend. The results from this analysis should present an interesting test of the range of applicability of Regge models as they should become less valid at the kinematics of this experiment.

The Regge-plus-resonance (RPR) model [44] is a recent attempt at reproduc-

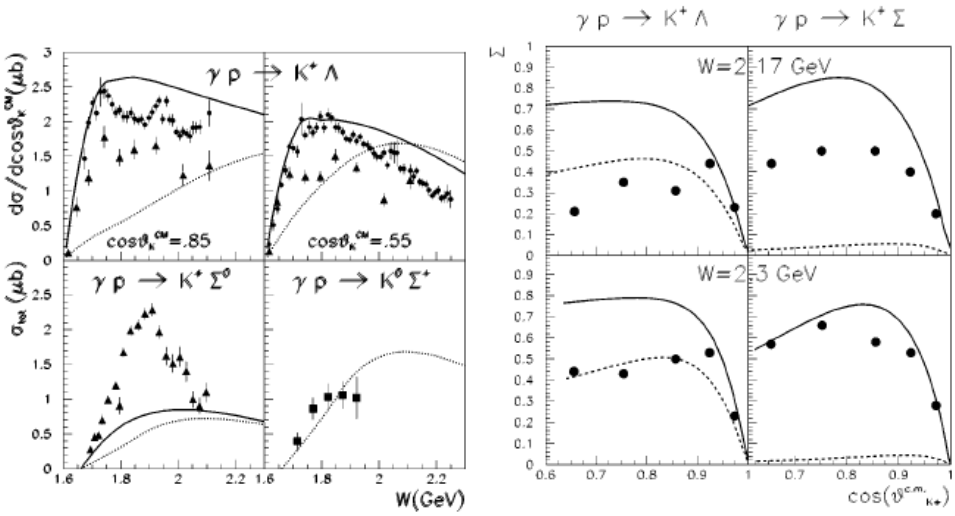

Figure 2.14: Regge model calculations from [43, 73] for cross-sections results (left plot) from reference [30] (circles), [37] (triangles) and [74] (squares). Regge model calculations from [43, 73] compared to the photon asymmetry results (right plot) from [48]. The solid line includes both K and K* trajectories, the dashed line includes only the K trajectory.

ing cross-sections and polarization measurements in hadronic reactions. It has been developed in a effective Lagrangian framework and differs from previous isobar models by using Regge trajectory exchange in the t-channel to describe the KY background. The model is evolved into the resonance region by adding in a number of s-channel resonances to fit existing data. These resonances must vanish at higher energies, hence one can constrain the background in high energy data. The major advantage of this approach over an isobar approach is that only the resonance couplings are left as free parameters in the resonance region. The need for strong hadronic form factors for background terms is reduced by using Regge propagators. This removes gauge invariance issues that prove problematic in the pure isobaric scheme. The Regge scheme can be visualised in Figure 2.15 where the photoproduction cross-section for hyperons is plotted against the various energy regions and both resonant and Regge effects are shown.

In the "high energy" region above 4 GeV the background is modelled by the exchange of Regge trajectories. In the resonance region (E<4GeV) s-channel resonances start to play a key role. The RPR model used K and K* Regge exchange to describe the background and included the well established core resonances to extrapolate into the resonance region. Effects of including a 2 star $P_{13}(1900)$ resonance were investigated as well as including contributions from the $D_{13}(1900)$ and $P_{11}(1900)$ resonances. Different RPR models are compared to photon asymmetry

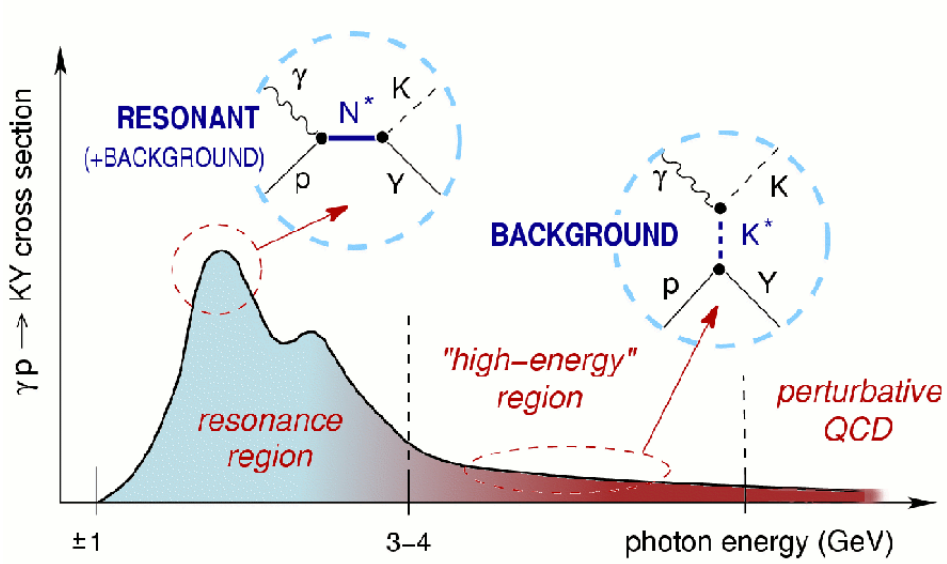

Figure 2.15: Energy scales used in the Regge-plus-resonance approach. Figure from reference [75].

and recoil polarization data respectively in Figures 2.16 and 2.17 . These results when taken with previous cross-section measurements provide some evidence for the inclusion of the 2 star $P_{13}(1900)$ state. As yet experimentally undetected, the $P_{11}(1900)$ state emerges from the calculation as a more likely candidate for a possible missing resonance than the $D_{13}(1900)$. It is stated in reference [68] that the authors are reluctant to claim strong evidence for the existence of either of these missing states. They show that a model using only the core set of resonances can give an equally valid description of the reaction dynamics. They conclude is that the structure seen in the observables at W $\sim$ 1900 MeV could be explained by fine tuning the background terms, rather than being evidence of a missing resonance.

A RPR scheme was developed for the Σ hyperons where the reactions $\gamma p \rightarrow K^+\Sigma^0$ and $\gamma p \rightarrow K^0\Sigma^+$ could be treated in a common isospin related description [75, 76]. This was possible because the Σ^+ and Σ^0 hyperons form part of the isotriplet and the strong coupling strengths are related via SU(2) Clebsch-Gordan coefficients. Reference [76] suggests the 2 star $P_{13}(1900)$ plays an important role along with the core resonances.

2.7 Summary

The last decade has seen a resurgence of interest in the field of strangeness photoproduction. High luminosity and large acceptance detectors have allowed high

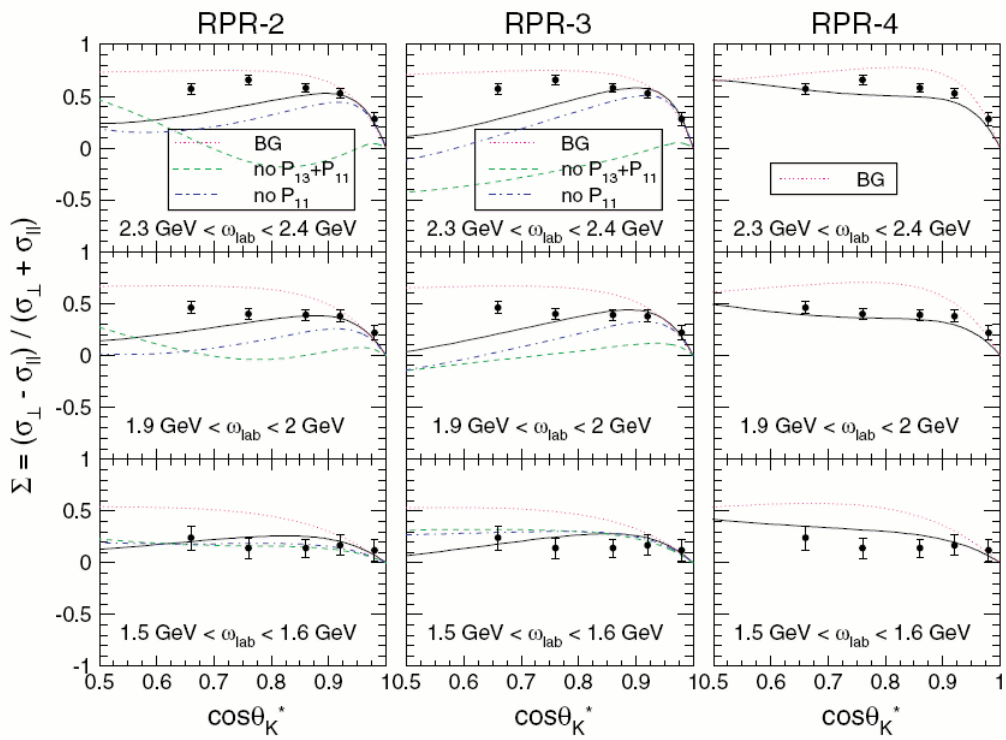

Figure 2.16: Regge-plus-resonance calculations [68] for the photon asymmetry for the KΛ channel compared to the LEPS data [48]. The RPR-2 and RPR-3 models contain the 2-star $P_{13}(1900)$ and the missing $P_{11}(1900)$, whereas the RPR-4 model contains only the "core" resonances.

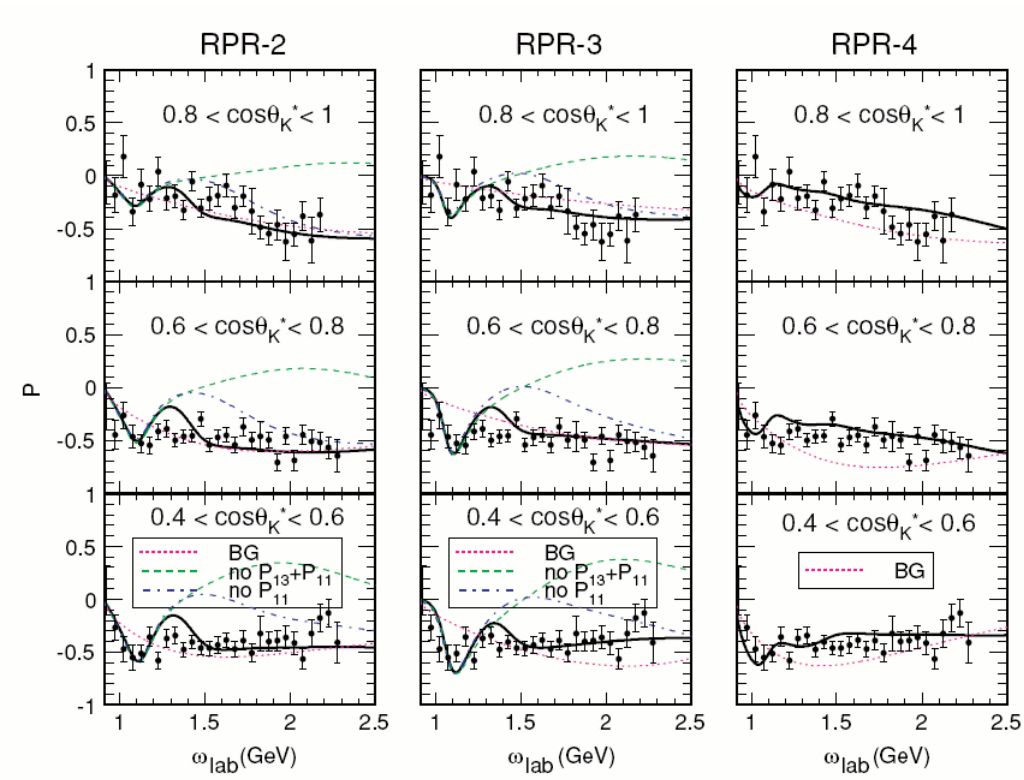

Figure 2.17: Regge-plus-resonance calculations [68] for the Λ recoil polarization compared to the CLAS data [30]. The RPR-2 and RPR-3 models contain the 2-star $P_{13}(1900)$ and the missing $P_{11}(1900)$, whereas the RPR-4 model contains only the "core" resonances.

precision data to be taken. When the data are analysed and compared to new model calculations, one may finally resolve the missing resonance issue, where the quark model predicts some states to exist that should couple strongly to KΛ and KΣ final states but have not yet been detected experimentally. Various models have been developed, one such model is an isobar model by Mart and Bennhold, which reproduces early cross-sections results from SAPHIR and appeared to show some evidence of one of the missing states. In contrast, recent model calculations were able to reproduce equally well the SAPHIR results by looking at different approaches to handling the non-resonant background terms, neglecting the need to include any missing states. The results from these analyses showed the difficulties in trying to extract resonance information from a limited data set. The possible inclusion of new higher spin states has also been highlighted by recent model calculations, and the need for new data on neutron channels to firmly establish their existence.

Recent analyses have shown there to be a serious lack of consistency between the cross-section results measured at CLAS and SAPHIR. Mart and Sulaksuno have provided multi-pole calculations which show a clear data set dependence in what specific resonances are predicted to couple to the KΛ channel. This situation requires new measurements to test the consistency of the two sets of cross-section data.

The work described in this thesis provides the worlds first polarization measurements for the $K^0\Lambda$ and $K^0\Sigma^0$ channels covering more than 1 GeV in photon energy and the full angular range. These measurements are predicted to be extremely sensitive to resonance contributions. The current theoretical models will be investigated using the results from single polarization observables and the results for the double polarization observables O_x and O_z.

Chapter 3

Experimental Set-up

3.1 Introduction

This chapter describes the detector used for the g13b experiment and all other apparatus used for particle identification. The g13b experiment was undertaken at the Thomas Jefferson National Accelerator Facility, Virginia, USA between March 2007 and June 2007, using the Continuous Electron Beam Accelerator Facility (CEBAF) [77]. The g13b experiment "Kaon Production on the Deuteron Using Linearly Polarized Photons" [33] was designed to provide data for polarization observables for a number of hadronic reactions.

The facility at Jefferson Lab is well suited to studying the electromagnetic structure of mesons, baryons and nuclei using either an electron or photon beam probe. There are three experimental halls where the beam is delivered simultaneously, Halls A, B and C. The g13b experiment was undertaken in Hall B using the CEBAF Large Acceptance Spectrometer and the photon tagger. Their layout is shown in Figure 3.1.

3.2 The Accelerator Facility

Jefferson Lab has a recirculating linear electron accelerator that can supply electron energies up to 6 GeV with a 100% duty cycle [78]. The primary beam can then be separated and sent simultaneously to the three experimental halls, A, B and C. The equipment in the experimental halls are complimentary and thus a wide range of physics issues can be addressed. The accelerator consists of two linear accelerators in parallel, which are connected by five recirculation arcs, shown in Figure 3.2. CEBAF is capable of delivering a "continuous wave" beam where the electrons are delivered in well defined 2.0005 ns bunches. Electrons

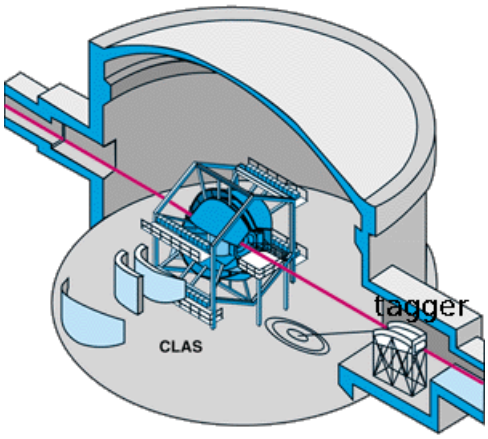

Figure 3.1: Representation of the layout of Hall B showing the locations of the CLAS detector and the photon tagging spectrometer in the bottom right of the picture. The red line shows the path of the photon beam through the CLAS detector and photon tagger.

of energies of approximately 67 MeV are produced via thermonic emission and are then injected into the first linac. They are then passed through a rotating disk which has three slits to produce the three different beam bunches before being accelerated by cryomodules through the linac. The electrons are then sent through the the recirculation arcs before being accelerated through the second linac. Each pass through the linac accelerates the electrons by approximately 550 MeV so a maximum of 5 passes will provide the maximum electron beam energy of approximately 6 GeV. The beam extractor/separator is then used to extract the accelerated electrons and send them to the three experimental halls.

The CEBAF accelerator can deliver beam currents sufficient enough to achieve luminosities of $10^{38} cm^{-2} s^{-1}$ to Halls A and C. The available beam current for Hall B is limited by the occupancies in the large acceptance detector components. Thus, the beam current to Hall B is frequently three orders of magnitude smaller than that to Halls A and C (e.g 10nA compared to 10 μA).

3.3 Coherent Bremsstrahlung Facility

A linearly polarized photon beam was used during the g13b experiment since it has been shown to enhance the study of photo-induced exclusive reactions [79]. A linearly polarized beam gives access to more single and double observables than is possible with a circularly polarized beam. These spin observables have also been shown to be very sensitive to the reaction amplitudes and the contributing nucleon resonances [2, 80]. The process of coherent Bremsstrahlung (see chapter

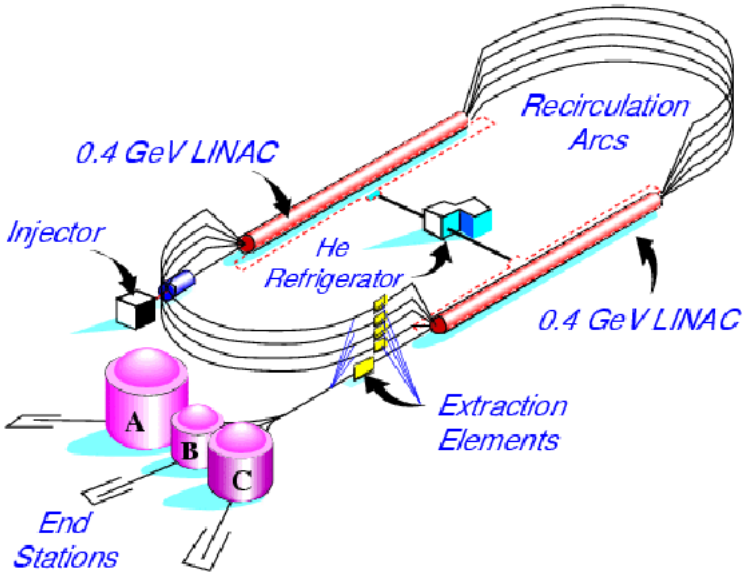

Figure 3.2: Racetrack configuration of the CEBAF at Jefferson Lab.

1 section 1.4) is used to produce the linearly polarized photon beam. The primary electron beam is incident on a suitably orientated diamond radiator [23]. A schematic layout of the Hall B coherent Bremsstrahlung facility is shown in Figure 3.3. The mixed electron and photon beams then pass through the photon tagger where the photon beam continues undeflected whilst the energy degraded electrons are steered out of the beam using the magnet and onto the tagger hodoscope where the energy of the electron can be measured and subsequently the energy of the photon can be determined. A detailed description of the coherent Bremsstrahlung process can be found in reference [23], with its specific use at Jlab given in references [81,82].

As discussed in section 1.4, if an amorphous radiator is used the photons will be produced with an energy spectrum that falls off with increasing photon energy, $\frac{1}{E_\gamma}$ as shown in the top plot of Figure 3.4. When using a diamond radiator, its regular lattice structure gives rise to photons with fractional energies, corresponding to specific momentum transfers of the electrons to the crystal nuclei. This energy spectrum gives a characteristic "coherent peak" structure, which can be seen in the middle plot of Figure 3.4. The fluctuations in the incoherent and coherent spectra are not statistical but are due to E-counter efficiencies and the overlapping widths of the counters. These effects are removed by making an enhancement spectrum. This is done by dividing the coherent spectrum by the incoherent spectrum as shown in the bottom plot of Figure 3.4.

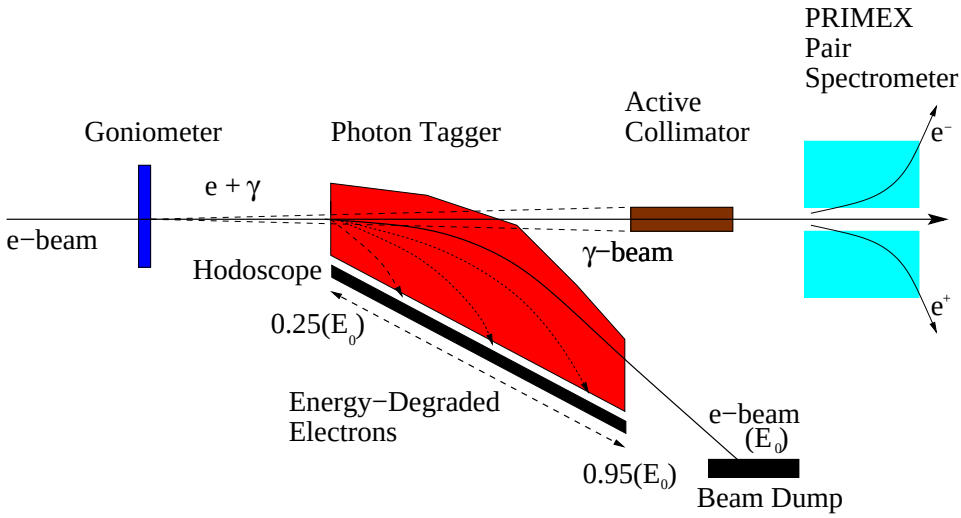

Figure 3.3: Schematic layout of the coherent Bremsstrahlung facility in Hall B.

Diamond Radiator and Goniometer

The quality and stability of the linearly polarized photon beam is largely determined by the quality of the diamond radiator. Defects in the crystal can adversely affect the coherent Bremsstrahlung process because the background production of unpolarised photons becomes significant. This can give rise to a less stable beam with a lower degree of relative polarization.

There are various requirements for a radiator for coherent Bremsstrahlung. It should have a regular crystal lattice structure because the primary electron beam has to be scattered on a radiator that allows the recoil momentum to be taken up by the crystal as a whole and not by the individual atoms [23]. To achieve this, the crystal must be positioned with respect to the electron beam in such a way that the recoil momentum is equal to one of the crystal reciprocal lattice vectors. This satisfies the Laue condition $\overrightarrow{q} = \overrightarrow{g}$, where $\overrightarrow{g}$ is the reciprocal lattice vector of the crystal. Diamond is also chosen as it has a small lattice constant and relatively high Debye temperature. This Debye temperature means that the amplitude of the thermal motion of the atoms in the lattice is small and the lattice structure is relatively unaffected by thermal effects [83]. When an electron passes through the diamond radiator there is a spread in the direction of the electrons due to multiple scattering effects, crystal defects in the lattice and divergence of the incident electron beam. It is therefore important to use the correct thickness of diamond. For g13b a 50 micron diamond was used. To enhance the coherent spectrum this angular variation must be kept smaller than the characteristic opening angle for coherent Bremsstrahlung,

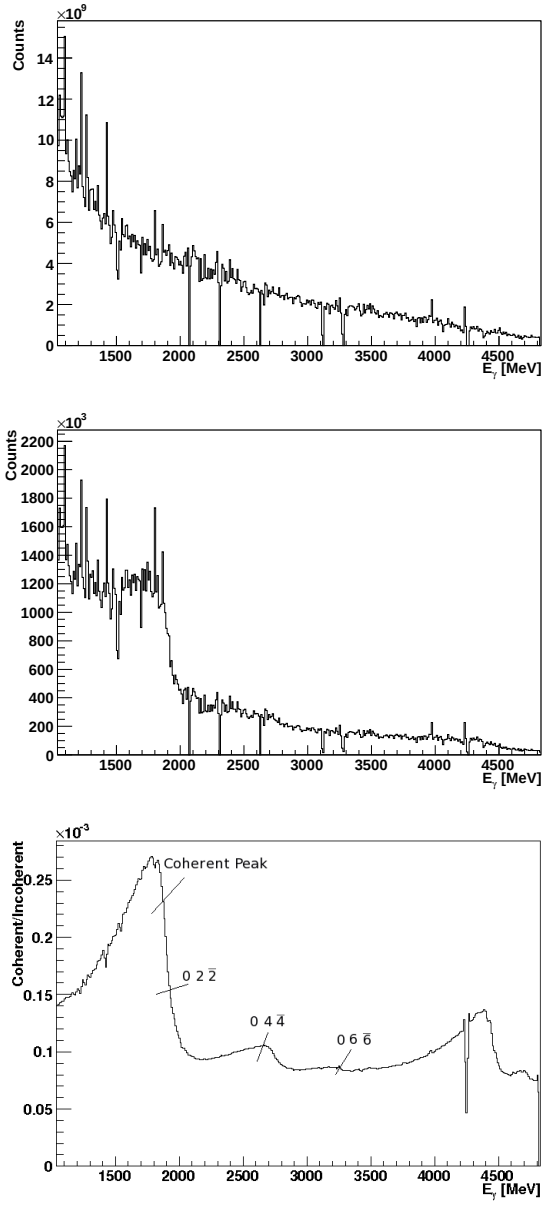

Figure 3.4: Energy spectrum of incoherent Bremsstrahlung photons produced from an amorphous radiator (top). Energy spectrum of coherent Bremsstrahlung photons produced from a diamond radiator (middle). Enhancement spectrum of coherent/incoherent spectra. Relevant reciprocal lattice vectors are labelled (bottom).

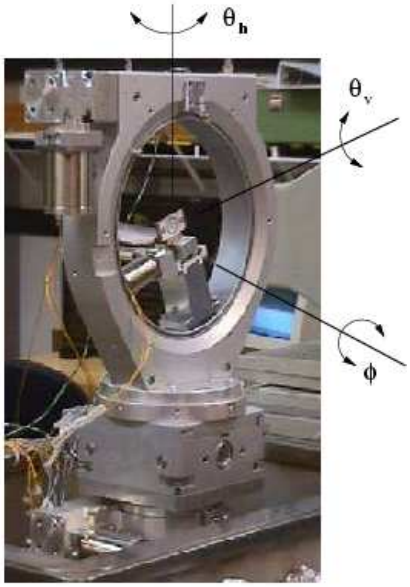

Figure 3.5: The George Washington Universities Goniometer in test condition. The target ladder can be seen in the centre of the device.

$$\theta_{br} = \frac{mc^2}{E_0} \tag{3.1}$$

where E_0 is the primary electron energy and m is the electron mass. Reference [23] provides an in depth explanation of this relation and its importance.

The goniometer is a device developed by the George Washington University that is responsible for controlling the orientation of the diamond [84]. It allows the positioning of the diamond crystal to a precision of better than 10 μrad. Up to six radiators can be held on the target ladder at any one time and it can move the diamond through three rotational and two translational axes. The goniometer is placed approximately 10 cm upstream of the photon tagger and is maintained in vacuum conditions. The goniometer is controlled with its dedicated software. The degrees of freedom of the goniometer are labelled on the picture of the goniometer in Figure 3.5. The target ladder with the different radiators is shown in Figure 3.6 .This allows the type of radiator to be changed remotely as well as the orientation of the linearly polarized beam.

Active Collimator

The active collimator is located downstream of the photon tagging spectrometer and is displayed under test conditions in Figure 3.7. The aperture of the colli-

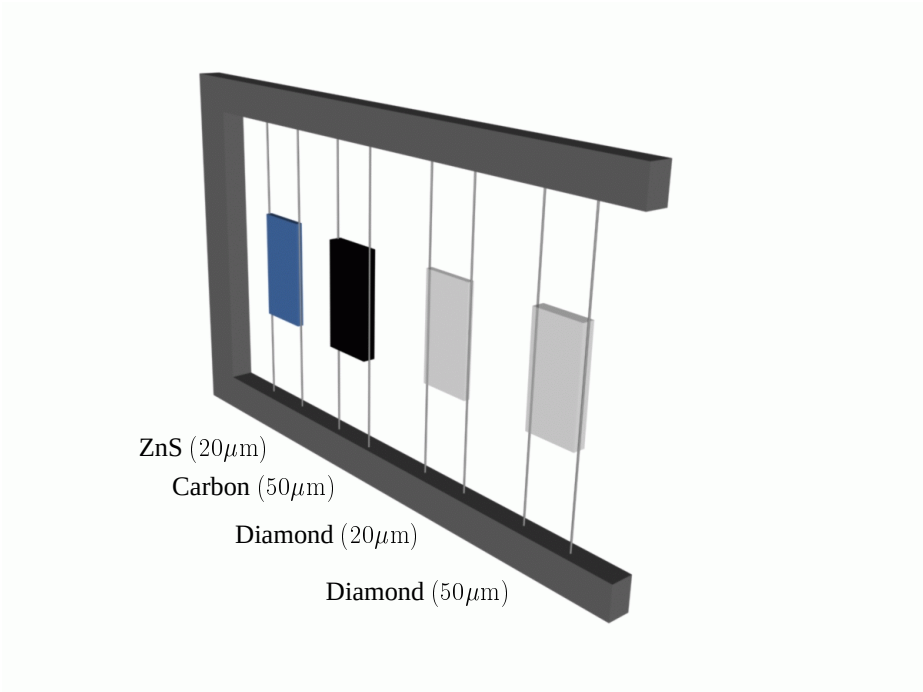

Figure 3.6: Goniometer target ladder. The different radiators and their thickness are shown.

mator is 2 mm in diameter and is located 22.9 m downstream of the diamond radiator. It is composed of 13 nickel disks, each with an outer diameter of 50 mm and a thickness of 15 mm. Each disk has a small aperture bored through its centre and they are stacked into a cylindrical sheath of stainless steel with a 4 mm cubic scintillator sandwiched between them. This measures the rate of e^+e^- pairs produced by photons outside the 2 mm core incident on the first nickel disk. This makes online monitoring of the count rates in the scintillator possible, which can be translated into shifts in beam position. These shifts are identified as asymmetries in the measured rates from the photomultiplier tubes located at different positions around the scintillator.

The main purpose of the active collimator is to enhance the degree of linear polarization within the coherent peak. The natural emission angle of coherent Bremsstrahlung decreases with increasing photon energy, as outlined in reference [23]. The angular distribution for incoherent Bremsstrahlung is independent of photon energy. Therefore, by tightly collimating the photon beam, it is possible to enhance the relative contribution of coherent Bremsstrahlung and thus enhance the relative degree of linear polarization.

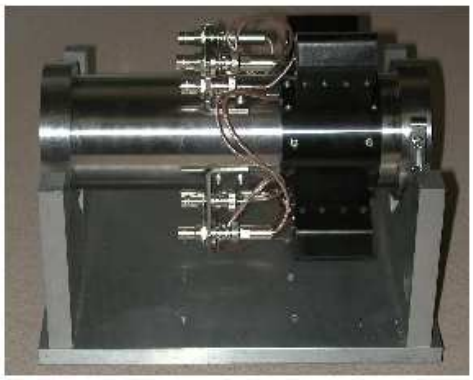

Figure 3.7: The active collimator shown under test conditions.

Photon Tagger

Bremsstrahlung photons produced in Hall B within the energy range of 20-95% of the incident electron energy are tagged using the photon tagger [85]. The tagger is based around the principle of the electron Bremsstrahlung process in which the energy transferred to the scattering nucleus is extremely small. The reaction obeys the energy conservation relation:

$$E_\gamma = E_0 - E_e \tag{3.2}$$

where E_γ is the energy of the Bremsstrahlung photon, E_0 is the incident electron energy and E_e is the energy of the deflected electron. The incident electron energy is determined by the accelerator, so the measurement of the deflected electron energy allows an accurate measurement of the photon energy provided the electron can be associated with the photon that caused the trigger. The detected photon is then said to be "tagged".

Photons produced in the Bremsstrahlung process pass through the tagger magnetic field continuing undeviated towards the CLAS. When electrons that have produced a photon enter the tagger they are focused towards the tagger hodoscope by the uniform dipole magnetic field. Electrons that did not produce a photon retain enough energy to be bent into the beam dump. The hodoscope consists of two scintillator planes known as the energy plane and the timing plane, which allows for the determination of the degraded energy of the electron and hence the energy of the photon. The layout of the photon tagger is shown in Figure 3.8.

The hodoscope has three main requirements: It should provide accurate momentum information for the detected electron to allow the photon energy to be calculated to the required resolution. It should provide timing information ac-

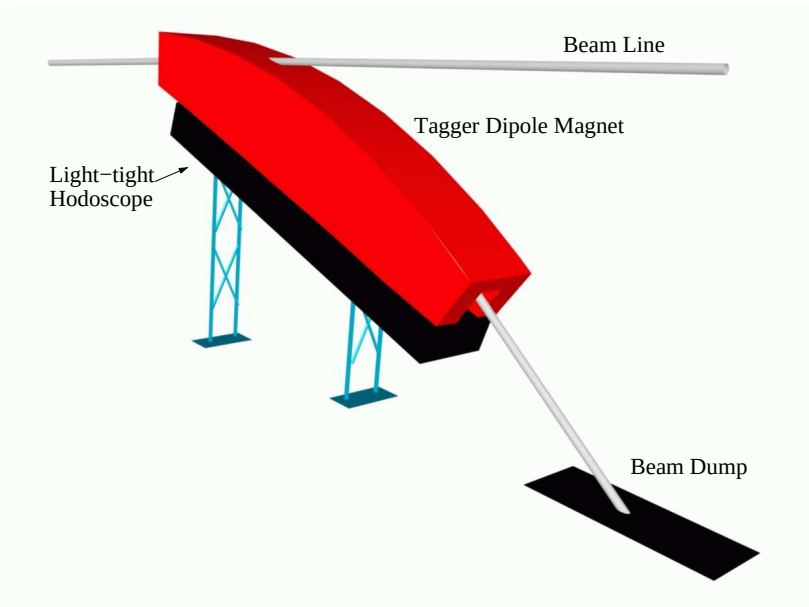

Figure 3.8: Schematic diagram of the photon tagger.

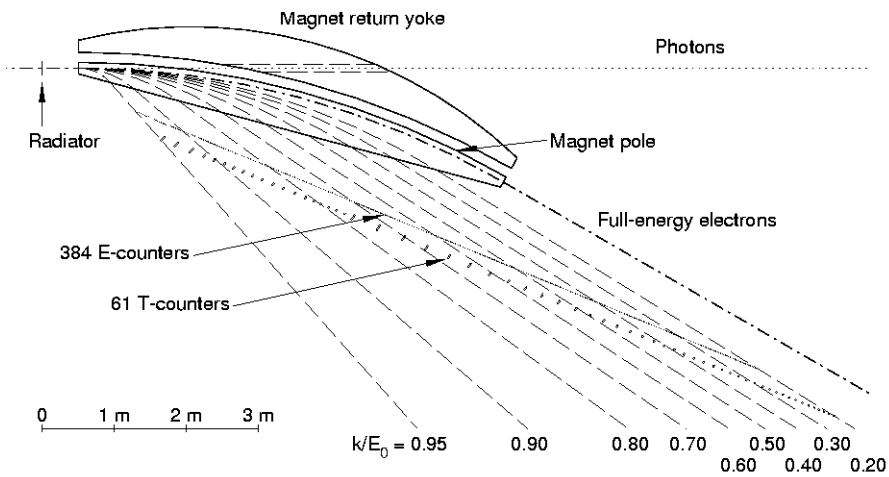

Figure 3.9: Schematic representation of the photon tagger, showing the relative positions of the T and E-counters.

curate enough for coincidences to be made with any subsequent events triggered by the photon in a downstream detector. The final requirement is that it should provide sufficiently good timing resolution to allow for the identification of the 2 ns beam bucket from which an event occurred. The energy and timing planes are highly segmented and have their working surface normal to the beam trajectory, which allows the beam bucket to be determined. The hodoscope consists of 61 overlapping T-counter scintillators for timing measurements. Each T-counter is then divided into 121 T-bins including the original T-counters and the overlaps between them. The overlaps are used to provide a higher resolution. The T-plane resolution has to be better than 300 ps to be able to associate a tagged photon with the correct 2 ns beam bucket. The scintillators are 2 cm thick and can provide a timing resolution of approximately 50 ps, ten times better than the 500 ps timing resolution of the E-counters. This is achieved by making them thicker and placing them further from the dipole magnet than the E-counters, shown in Figure 3.9. The T-paddles were also arranged into two separate groups with the first 19 paddles covering the photon energy range 75% to 95% of the incident electron energy being narrower than the remaining 42 paddles covering the remainder of the photon energy range [85]. The paddle array was built to be orthogonal to the electron trajectory so as to reduce the effects from back-scattered particles.

The T-counter scintillators each have two photomultiplier tubes (PMTs) and a pipeline multi-hit time-to-digital convertor (TDC). The multi-hit TDCs allow each T-counter to register many photons for each trigger. Since most of the photons have similar energies, it can be difficult to "tag" the correct one if two or more arrive within the same 2 ns beam bucket. These events are easily identified. A valid tagger event is only registered if there is a coincidence between a T-counter and its associated E-counters. T-counter signals are read out from both ends using fixed light guides and PMTs.

There are 384 E-counters, each of which is 4 mm thick. They are used to determine the energy of the photon and are divided into 767 E-bins. The overlaps in this case are of the order of one third of a paddle, again being used to provide a higher resolution. The widths of each of these scintillators vary between 6 mm and 18 mm depending on position so as to produce constant momentum bins of around $0.003E_0$. They are 20 cm long and 4mm thick. The E-plane lies above the T-plane, with the E-plane lying close to the exit flange of the magnet vacuum box. This minimises the effect of multiple electron scattering as they pass through the exit window and helps to optimise resolution. The paddle array was also built to be orthogonal to the electron trajectory as it passes through the focal plane,

Figure 3.10: The 40cm long g13b target cell.

thereby reducing any effect from back-scattered particles. Each E-counter has one PMT and a standard TDC. Signals from one end of the E-counter are read out via a light guide connected to an optical fibre, which is connected to the PMT. The outputs of each of the tagger TDCs are grouped together in blocks of four. These blocks are then grouped together in a module known as the tagger master OR. This signal then goes on to form part of the CLAS trigger.

3.4 Target

A 40 cm long cylindrical cell containing liquid deuterium was used as the target for the g13b experiment. Liquid deuterium was used to optimize the density of atomic neutrons and protons for the study of strange decay channels. Figure 3.10 shows a picture of the target cell used during g13b.

3.5 The CEBAF Large Acceptance Spectrometer (CLAS)

The CLAS detector design is based on a toroidal magnetic field, with six superconducting magnets which naturally divide the detector into six regions.

The near full solid angle coverage allows for the ability to detect exclusive multi-particle final state reactions with good momentum resolution. There are some small regions of zero acceptance where the magnetic coils lie. The CLAS tracks the azimuthal and polar angle distributions of the various reaction products. It is composed of six independent detectors, each of which provide complimentary information on the particles detected. Particle properties such as mass, momentum, charge and velocity can all be determined from the subsystems. The

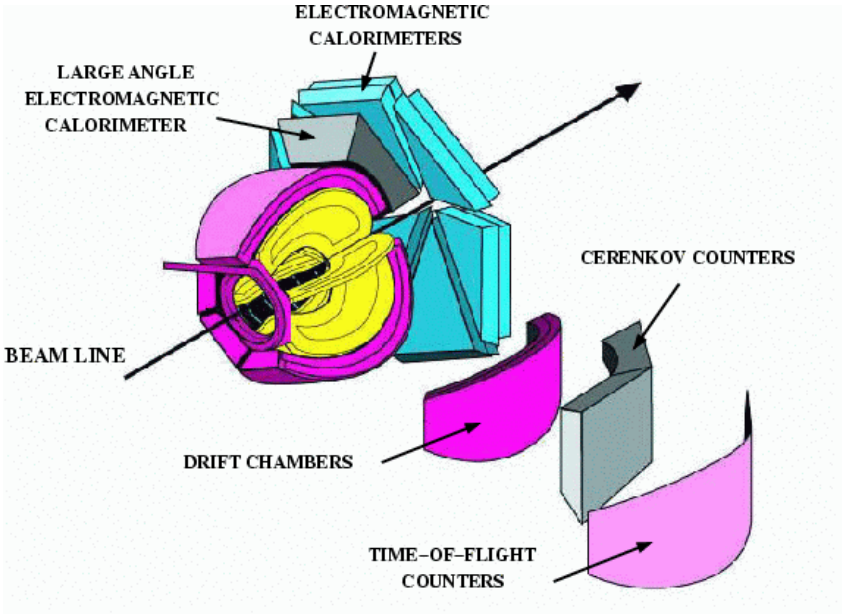

Figure 3.11: Schematic diagram of the CEBAF Large Acceptance Spectrometer with the subsystem components peeled away.

region around the centre of CLAS where the target is placed is magnetic field free to allow for the use of a dynamically polarized target. A schematic diagram of the CLAS, which shows its layered structure is shown in Figure 3.11. Figure 3.12 shows a photograph of the detector.

At the centre of CLAS lies the target cell which is a 40 cm long liquid Deuterium target. This is surrounded by a segmented start counter which allows for the determination of the hadronic reaction time. Further out are the drift chambers which provide tracking and momentum information, then the time of flight scintillators and at the outermost edge of CLAS the Cerenkov counter and Large Angle Calorimeter. The detection sequence for a charged particle is as follows. After production in the target cell, the particle passes through the start counter, where the start time is recorded. The charged particle then travels through the three drift chamber regions. Upon entering (Region 1) and leaving (Region 3) the drift chambers the initial and final direction of the particle can be calculated. Region 2 is situated in the region of maximal toroidal field strength and hence the curvature of the track as it passes through this region determines its momentum. After traversing the drift chambers the particle then enters the time of flight system. The time of flight determines the particles velocity by combining the information from the particles start time and the time that it hit a TOF scintillator. This calculated velocity and the momentum as determined from the drift chambers can be combined to calculate the particle mass. The following

Figure 3.12: Photograph of the CLAS detector in Hall B with the Time of Flight system removed.

sections describe, in detail, the sub systems of CLAS with the exception of the Cerenkov Counters as they were not used during the g13b experiment.

Superconducting Torus Magnet

Six superconducting magnetic coils provide the toroidal magnetic field within CLAS [77]. These coils are mounted around the beam line to create six 60° sectors. The acceptance of CLAS is reduced to about 75% of 4π solid angle due to the presence of the coils. The configuration of the magnet can be seen in Figure 3.13.

The magnetic field is always transverse to the momentum of the particle. The maximum intensity of the field is 2T. Data for g13b was taken with a field setting of -1500A. The negative polarity and the relatively low field setting gave negatively charged particles a greater acceptance as less would be lost down the beam line hole at forward angles.

Start Counter

The start counter is crucial for real photon experiments. It surrounds the target within CLAS and is used to provide a reference start time for the hadronic interaction. This is done by selecting the correct electron beam bucket that produced the Bremsstrahlung photon that caused the hadronic interaction in CLAS. This

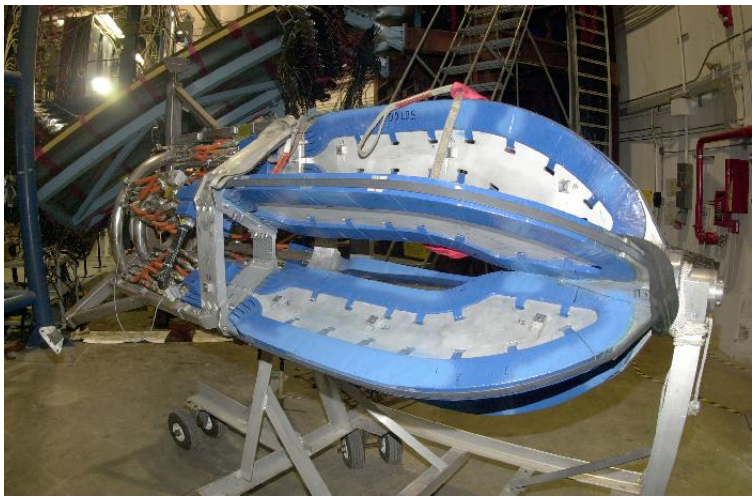

Figure 3.13: Photograph of the six magnetic coils of CLAS

information is then combined with the tracking through the drift chambers and the time of flight information which ultimately allows particle identification to be carried out.

The design of the start counter allows for full azimuthal and polar angle acceptance and completely surrounds the target. The device has twenty four paddles and maintains the electromagnetic background within acceptable limits by requiring that the hit multiplicity in the paddles be equal to or greater than two. Six pieces of scintillator joined in a coupled paddle configuration surround the target cell, which can be seen in Figure 3.14. The scintillators in each paddle have a 502 mm long straight section with a tapered end called the "nose".

A signal that is produced from a charged particle hitting the scintillator is read out via a light guide and a photomultiplier tube (PMT) attached at the backward direction. This results in six channels each corresponding to the six sectors of CLAS. The PMT's each contain a charge-to-digital converter (QDC) and time-to-digital converter (TDC) which provide energy and timing information of the interaction in the scintillator. The timing resolution of the start counter is approximately 260 ps when well calibrated and the angular coverage is the same as that of the time of flight system, except in the forward direction. Having a well defined start time for the interaction allows the for the easy identification of the RF beam bucket from which the event photon was produced.

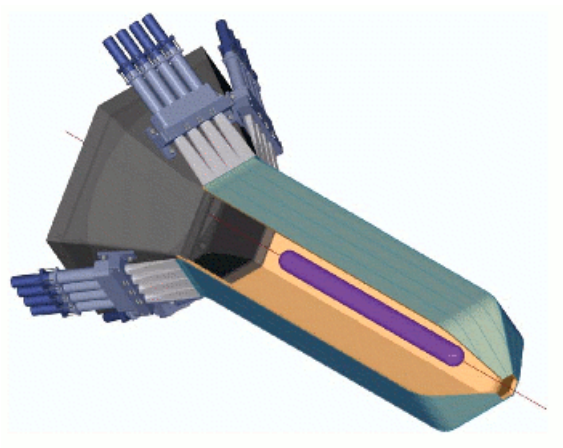

Figure 3.14: Schematic layout of the Start Counter at CLAS.

Drift Chambers

The CLAS drift chambers, shown in Figure 3.15, are used to measure charged particle momentum. Charged particles in CLAS are tracked by drift chambers which are arranged in three regions. Region 1 is located closest to the target, within the (nearly) field free region inside the Torus bore and is used to determine the initial direction of charged particle tracks. Region 2 is located between the Torus coils, in the region of strong toroidal magnetic field and is used to obtain a second measurement of the particle track at a point where the curvature is maximal, to achieve good energy resolution. Region 3 is located outside the coils, again in a region with low magnetic field and measures the final direction of charged particles headed towards the outer Time-of-Flight counters, Cerenkov counters and the Electromagnetic Calorimeters. Each region within a given sector contains one axial superlayer with up to 1200 sense wires in six layers (four layers in the case of Region 1) and one stereo superlayer with sense wires in six layers at an angle of 6 degrees with respect to the axial wires. The wires are arranged into a hexagonal pattern with up to 192 sense wire in each layer. Each superlayer is surrounded with a row of guard wires to minimize edge effects. The cells are constructed to produce six field wires around a single sense wire in a repeating hexagonal pattern. The resolution of each cell varies between 310-380μm.

The chambers are filled with the same gas mixture which consists of 90% argon and 10% carbon dioxide. A high voltage is supplied to the field wires and as a charged particle enters the chamber it will ionise the gas molecules with the ejected electrons then drifting to the sense wire. The drift time for the electrons to arrive on the sense wire is then measured to determine the drift distance of the particle to the sense wire. The particle's trajectory can be tracked using this

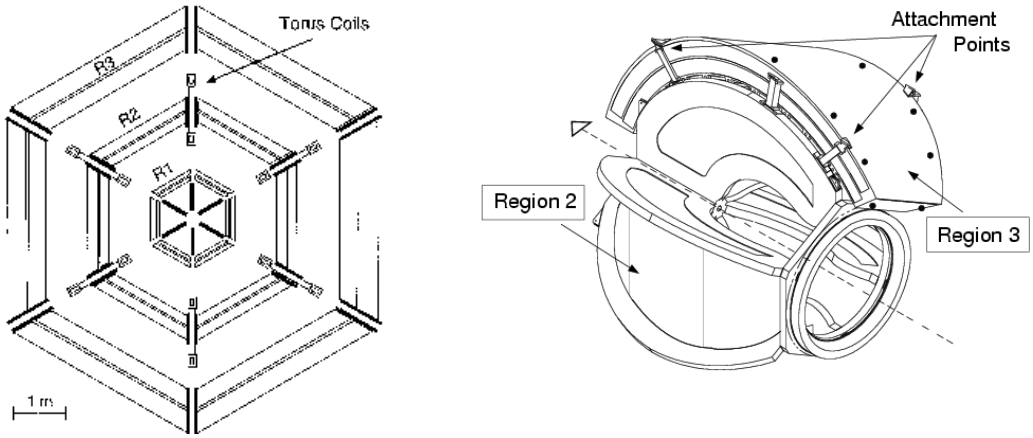

Figure 3.15: Cross section of the Drift Chambers (left) and regions 2 and 3 of the drift chamber shown in their installed positions on the torus cryostat (right).

method throughout all three regions.

Time of Flight

The time of flight (TOF) system [86] consists of 57 plastic scintillator paddles per sector and covers the entire active azimuthal angle and a polar angle of 8° to 142 °. A total area of 206 m^2 is covered by the time of flight. Each scintillator is 5.08 cm in thickness although their lengths and widths vary depending upon their position. The lengths vary from 32 cm at forward angles (∼8°) to 445 cm at a lab angle of approximately 76°. Their widths vary from 15 cm at forward angles or 22 cm at large angles. These dimensions were chosen to satisfy both the consideration of spatial coverage and achievable timing resolution. Figure 3.16 shows a schematic view of the time of flight scintillators in a single sector. The scintillators are grouped into a four panel configuration which allows for the required polar angle coverage.

The scintillators all have a PMT attached at both ends and the signal is read out by a Charge to Digital Converter (QDC) and a Time to Digital Converter (TDC). For any charged particle passing through CLAS, the flight time, which is measured from the target to the time of flight system, is used to calculate the particles velocity. Combining the velocity along with the measured momentum from the drift chambers allows the mass of the particle to be determined via the relation $\beta = \frac{p}{E}$. The TOF mass is used for initial particle identification in this analysis.

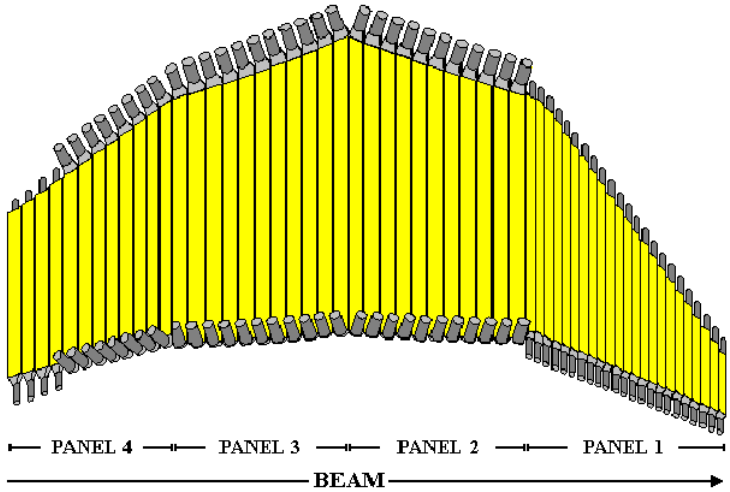

Figure 3.16: A Schematic view of a single sector of the time of flight system.

Electromagnetic Calorimeters

The electromagnetic calorimeters (EC) [87] are used for the detection of neutral particles such as photons with energies greater than 0.2 GeV and also for detecting neutrons. They can also be used to detect electrons with energies above 0.5 GeV. The six sectors of CLAS have an EC with a polar angle coverage of $8^o < \Theta < 45^o$ and consist of thirty nine layers of scintillator and lead in a sandwich composition.

Each scintillator is 10mm in thickness and the lead is 2.2mm thick. Figure 3.17 shows a schematic layout of the EC scintillator-lead composition. Each layer has the form of an equilateral triangle in order to cover the hexagonal geometry of CLAS. Also apparent is the successive 120 degree rotation in the orientation of the scintillator strips in each layer, labeled as u, v and w planes. This recurring three plane configuration gives rise to stereo information on the position of the deposited energy in the scintillator.

As a particle enters the EC it will interact with the scintillator-lead layer and lose energy by radiating a Bremsstrahlung photon. This photon then induces the production of a e^+e^- pair which leads to more Bremsstrahlung, thus producing an energy shower. The energy information is used in conjunction with positional information to identify the interacting particle.

The Large Angle Calorimeter (LAC) is primarily used as an extension of the EC to allow particle detection at more backward angles in sectors 1 and 2 only. The LAC covers an azimuthal angle of 120°, but only covers the range $45^0 < \Theta < 75^0$ in polar angle. It is favourable to use the LAC in experiments where there is a desire to detect neutral particles at very backward angles. Particle detection in the LAC is similar to that in the EC, scattered electrons and neutral

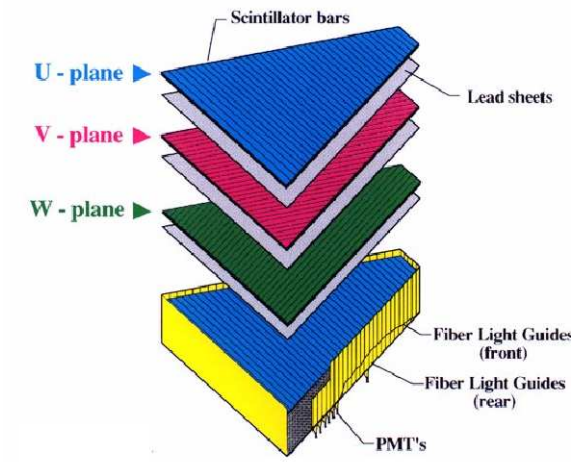

Figure 3.17: Diagram showing the three different views of the electromagnetic calorimeter.

particles such as photons coming from radiative processes are detected in the lead-scintillator sandwiches. The lead has a thickness of 2mm and the scintillator a thickness of 15mm. In total, the LAC contains 33 layers successively orientated at 90^0 to each other.

3.6 Beamline Devices

Beam Position Monitors

The Beam Position Monitors (BPMs) are used to monitor any shift in direction of electrons and/or photons along the beam line. Since g13b used a diamond radiator to produce photons, the BPMs were very important in ensuring the electrons were correctly incident on the diamond and that the photons passed efficiently through the collimators. There are three BPMs along the beam line, 2C21A is just upstream of the goniometer, 2C24A is just upstream of the tagger and 2H01A is downstream of the tagger [77]. The electron beam produces an induced current in wires adjacent to the beam line, which is measured by the BPM. The current varies with the position of the electrons and this allows the BPM to determine and record the position of the electron beam. This information is recorded into the data stream every two seconds.

Total Absorption Shower Counter

The total absorption shower counter (TASC) is located downstream of CLAS and is primarily used to measure the photon flux. The TASC uses four lead glass

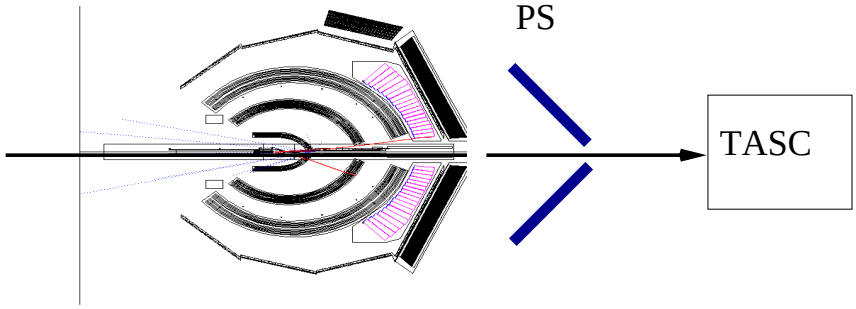

Figure 3.18: The relative positioning of the pair spectrometer and total absorption shower counter downstream of CLAS.

blocks to give an accurate determination of the beam line efficiency, therefore allowing for the calculation of the number of Bremsstrahlung photons that hit the target. Each block has a length of approximately 17 radiation lengths and is coupled to a phototube, providing nearly 100% efficiency. The TASC can only operate effectively at beam currents of approximately 100 pA which means that special TASC data runs have to be taken periodically during the experiment. Each time there was a change in running configuration for the coherent peak, these normalisation runs were taken.

Pair Spectrometer

The Pair Spectrometer (PS) is a backup device to measure the full beam intensity. It operates on the principle that when a photon interacts with the aluminium foil converter it will produce an e^+e^- pair. The magnetic field sweeps these pairs out of the beam line and into the spectrometer scintillator and microstrip detectors. The energy of the e^+e^- pair can then be calculated from their hit positions in the PS, which in turn is used to calculate the energy of the interacting photon. The PS can also be used to measure the photon flux at higher beam intensities than is possible with the TASC and can provide a way to check the beam position. From measuring the rate of e^+e^- pairs detected it is possible to infer if there is any shift in beam position.

3.7 Trigger System

The trigger system in CLAS is vital in deciding when a particular event will be recorded into the data stream for future physics analysis. The configuration of the trigger is set up to maximise the proportion of triggers from events of interest (which vary in each experiment) and minimise those from accidentals such as

cosmic rays passing through the detector and electronic noise. CLAS has a two level trigger system (level 1 and level 2) which records events or ignores them based on the configuration. The level 1 trigger processes digital signals via a memory look up from the outer detector subsystems, e.g the time of flight or electromagnetic calorimeters. The level 2 trigger has a more stringent constraint for the acceptability of an event, it utilises tracking information from the drift chambers.

The level 1 trigger [88] utilises logic signals from the time of flight, electromagnetic calorimeters and the start counter (which is used in photon experiments) subsystems along with the tagger master-OR. This trigger is constructed from a coincidence between each of these detector subsystems. The g13b experiment used a level 1 trigger which was configured to require one charged particle per event. This was chosen to allow a very open ended trigger to accommodate all the reactions being studied as part of g13b. Sector based signals from each of the subsystems act as inputs for the level 1 trigger which consists of a three stage memory look up.

Memory look up 1 takes each of the pre-trigger inputs (62 bits) and maps them into four bits per input. Look up 2 then reduces these further into four trigger words, each 3 bits per sector. The final memory look up, makes correlations between sector events based upon geometrical considerations which account for events with hits in different sectors of CLAS. At this final stage of the level 1 trigger, the tagger master-OR is checked for coincidence before the level 1 trigger is passed to the trigger supervisor, which issues all start/stop and clear signals, as well as gates and resets for the detector electronics. It also places events on the data acquisition queue.

Data Acquisition

The data acquisition (DAQ) system at CLAS processes events into a format that can be used for physics analysis using the CLAS Online Data Acquisition (CODA) system [89]. Data from the various subsystems are received at the DAQ where it is digitised by VME and FASTBUS creates in the experimental hall before it is collected by VME readout controllers [77]. The digitised values are then tabulated in a way that each event is associated with a unique identity number. These data arrays are buffered and sent to an online acquisition computer. At this point the event builder assembles the fragments and converts them into a Bank Operating System (BOS) format [90]. The event builder then passes the completed events on to the event transporter which transfers them to shared

memory where they can be used for data monitoring or online analysis. Finally, the event recorder saves all the events for permanent storage on the RAID array. From here the data can be transported to the Jlab tape silo where it becomes available for offline analysis. For g13b the event rate was 8kHz with a livetime of approximately 85%.

3.8 Summary

Superconducting technology is utilised at CEBAF to deliver a high luminosity, high quality electron beam to three experimental halls simultaneously. With the halls set up to be complimentary to one another, this allows for a broad range of physics research to be undertaken at the lab. Having the coherent Bremsstrahlung facility in Hall B allows the production of a secondary linearly polarized photon beam by scattering the electrons off a suitably orientated diamond radiator. The pair spectrometer and active collimator are beamline devices which are used to monitor and improve the beam quality. Combining this setup with the CLAS detectors high acceptance for charged particles makes Hall B the world's premier facility to study polarization observables in strangeness photoproduction. After the data has been collected, the attention then turns to the process of data reconstruction and calibrations.

Chapter 4

Data Processing and Calibrations

4.1 Data Processing and Run Conditions

Before performing the physics analysis of the experimental data, acquired during the run period, the raw signal information from the detector subsystems must be converted into meaningful physical values. These physical values come in the form of timing, position, energy and momentum of the detected particles. The first stage of this conversion process is done by undertaking two tasks in parallel. One task being the data reconstruction, also known as *"cooking"* and the second is the calibration of the individual detector subsystems. Each detector subsystem has a offline software package designed to produce calibration constants which are used by the *cooking* process. Many iterations of these parallel tasks are required in order to refine the data into the final form necessary for physics analysis.

The following is a summary of the run conditions for the g13b experiment:

Table 4.1: Table summarising the g13b running conditions.

Running Conditions	Linear Polarization
Torus Current	-1500 A
Trigger	two-sector, no tagger
Beam Current	10 nA
Tagged Photon Energy Range	$1.3 - 2.3$ GeV
Radiator	diamond (50 μm)
Target	LD_2 and (LH_2 for calibration use only)
Target Length and Diameter	40 cm and 40 mm (max diameter)
Target Position	20 cm upstream of CLAS centre

Table 4.2: Electron beam and photon beam settings with total triggers for each polarization plane setting and mean polarizations.

		Triggers		Mean Pol.	
E_e (GeV)	E_γ (GeV)	PARA	PERP	PARA	PERP
3.302, 3.914 and 4.192	1.3	3.7×10^8	4.3×10^8	0.75	0.71
4.065 and 4.475	1.5	1.9×10^9	1.7×10^9	0.70	0.74
4.065 and 4.748	1.7	2.2×10^9	1.8×10^9	0.71	0.73
5.057	1.9	3.6×10^9	2.7×10^9	0.74	0.78
5.057 and 5.157	2.1	3.0×10^9	2.6×10^9	0.70	0.70
5.157	2.3	2.8×10^9	2.9×10^9	0.71	0.71

The g13b experiment used a number of electron beam energies to produce different energies of polarized photon beam (1.3 to 2.3 GeV, in steps of 200 MeV). This meant that different electron beam energies (and thus polarizations) could have contributed to the same coherent peak setting. This then required the calculation of a weighted mean polarization of each coherent peak and polarization plane setting. The polarization plane depends on the diamond orientation in the goniometer and is defined to be either parallel (PARA) or perpendicular (PERP). The PARA or PERP refers to the orientation of the Bremsstrahlung photon's electric field vector with respect to the lab floor. Where an amorphous radiator was used the polarization plane is defined as AMO (for amorphous). The polarized data were acquired by taking the ratio 2:2:1 of PARA, PERP and AMO data.

Given the running conditions above, $\sim$ 120 TB of data were collected, satisfying the required targets given in the proposal [33]. The data are summarised in Table 4.2 for production on an LD_2 target.

Data Reconstruction

The process of data reconstruction or *"cooking"* converts the raw information into reconstructed Bank Operating System (BOS) banks. A reconstructed BOS bank is a collection of data words containing detector subsystem information which is now in a physical format (e.g. position, time, momentum).

This process utilises a software package called RECSIS (REConstruction and analySIS package). The raw data are first calibrated appropriately, depending upon the detector subsystem, resulting in a set of calibration constants. Each of these constants is stored in a centralised MySql [91] database and linked to RECSIS via an experiment-specific run index. Once a set of calibration constants is deemed to be adequate they are used to adjust the reconstructed physical

information in the BOS banks and one iteration of the data *"cooking"* is complete. This adjustment of the bank information accounts for factors such as detector position, trigger times and offsets of each detector subsystem with respect to the others.

For the g13b experiment there were two overall passes of the *cooking*, each consisting of multiple versions, before the data were finally decided to be of high enough quality for physics analysis. Pass refers to the current iteration of the overall process, while version refers to the current status of the calibrations. Data processing in this fashion is very computationally intensive and took $\sim$ 12 months of constant running on the JLab computing farm with $\sim$ 30000 raw input and $\sim$ 80000 subsequent output files.

4.2 Subsystem Calibrations

Timing calibrations are of particular importance with CLAS, since timing is the basis for all particle identification (PID) and the determination of particle momenta. It is also very important to determine the correct beam bucket to correctly identify the event photon. In this section brief overviews of the calibration principles and methods for each of these subsystems will be presented. More detail will be given in relation to the calibration of the time of flight system, for which the author was responsible.

4.2.1 Start Counter Calibration

The start counter calibration is performed in two stages. The first stage of the calibration process involves internally aligning each pair of coupled paddle scintillators, whilst the second stage aligns the three pairs with respect to each other.

When a hit is registered in a pair of coupled paddles, two TDC timings result (T_1 and T_2). For real physical events, the time difference between these two timings should be a constant. These real events are then selected and the time difference ($T_1 - T_2$) distribution is plotted. By adjusting a constant associated with each paddle, the time difference can be centred on zero. This internal alignment procedure is carried out for all three coupled paddle scintillator pairs.

The next stage requires alignment of the now internally aligned paddle pair with respect to each other. In order for this to be done, an external reference time is required with which to compare the start counter time of each paddle pair. This external reference time is provided by a tagger T-counter, and so for each coupled paddle pair the start counter time is subtracted from the T-counter

time. At this point, the constants for each coupled paddle pair are adjusted (but now by the same amount) so as to align the the main peak of this time difference distribution with the main peaks of the distributions from the other pairs. This timing difference alignment however, need not be centred on zero as this is simply an internal calibration of the start counter subsystem and will be accounted for in the photon tagger time and time of flight calibrations.

The final stage in the calibration of the start counter is to determine a constant time offset, known as $st2tof$. It is necessary to align the start counter time with the time of flight subsystem in order to obtain accurate time of flight measurements, since the start counter provides the event start time. Aligning of the start counter to the time of flight is achieved by subtracting the vertex time of a track as measured by the time of flight, from the vertex time of the track as measured by the start counter, and aligning the resulting distribution's offset to be centered on zero. The final evaluation of $st2tof$ cannot be done until both the drift chamber and time of flight calibrations are completed.

4.2.2 Photon Tagger Calibration / Beam RF

The calibration procedures for the photon tagger and beam RF are detailed in References [85,92]. The concept of the photon tagger calibration can be described as follows. The TDC values from the E-counter and T-counter PMTs are required to be converted into times. This is done by calculating and storing some calibration constants for each TDC. These values are then used to convert the TDC channels into times. Once these times have been determined, geometrical matching between E-counter hits and T-counter hits is performed. This matching is only performed if the E-counter and T-counter hits represent a certain combination, based on the overlap of the E and T focal planes in relation to typical electron trajectories. This combination must be one in which the electron did not scatter after interacting with the radiator foil. At this same stage of geometrical matching, a timing coincidence between the E-counter hit and T-counter hit is also required. Determination of the final timing involves using the T-counters, which are individually corrected for offsets, to identify the 2 ns beam bucket. Finer (< 2 ns) corrections to this timing are achieved using the RF machine time.

The tagger calibration process can be done in several discrete stages, each of which produces constants for use in the reconstruction process. These stages will now be briefly discussed.

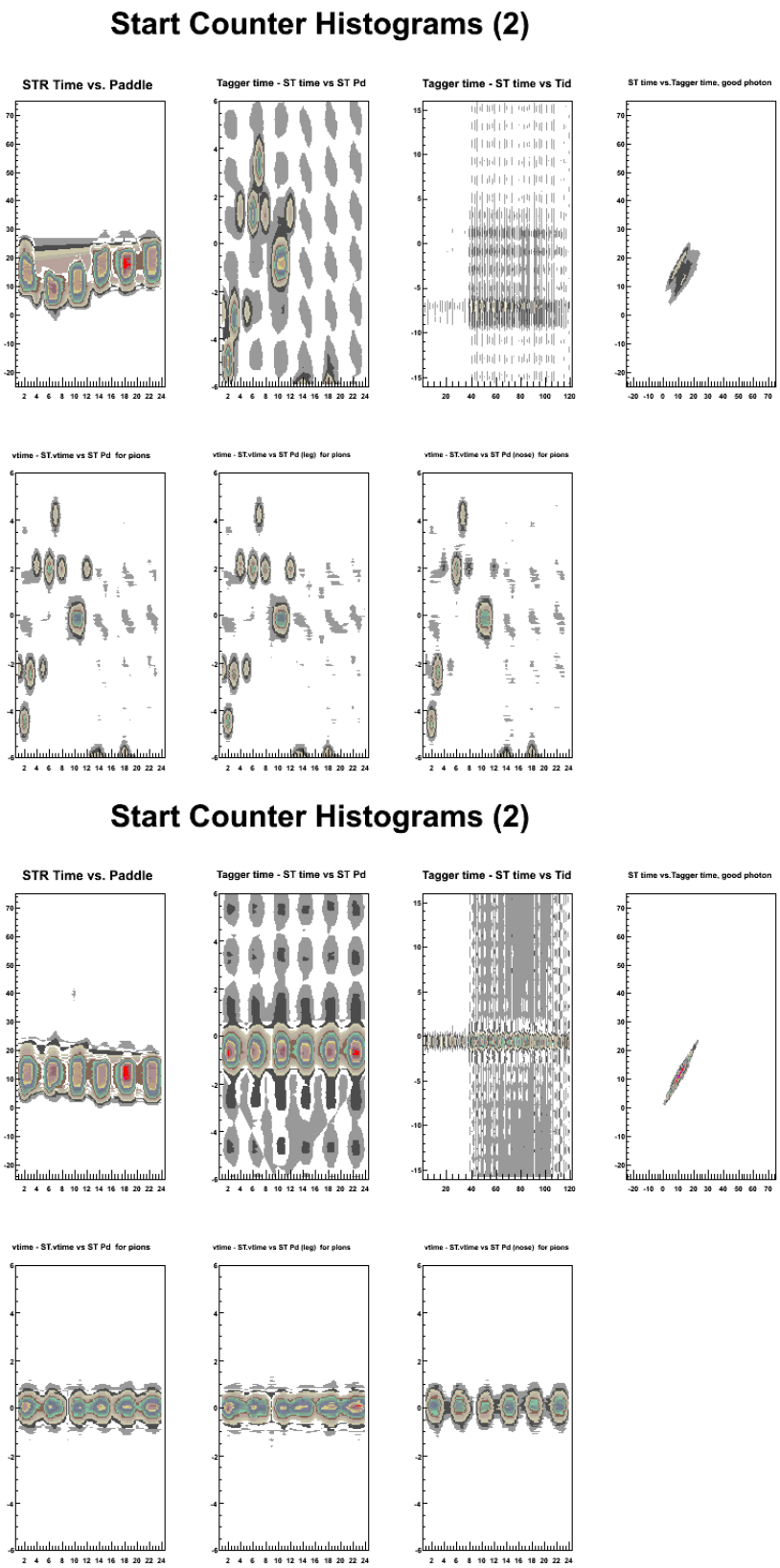

Figure 4.1: Start counter calibration plots showing before calibration (top) and after (bottom).

T-counter TDC Left-Right Slope Calibration

The timings from the left and right TDCs from each T-counter need to be corrected. This is done by comparing the times calculated by both TDCs and then correcting them relative to each other and the RF, on a counter by counter basis. The calibration software for the photon tagger measures and plots two slopes, β_{LR} and β_{RF}, from which the correction can be determined. These slopes are defined in reference [92].

A well calibrated set of TDC slopes are shown in the top left of Figure 4.2. All T-counter slopes are shown using an arbitrary scale, the times are in ns.

Base Peak Calibrations

The TDCs in the tagger operate in what is known as common-start self-triggered mode. This means that they will start to measure time when either the CLAS level 1 trigger fires (common-start) or when a hit is recorded on a T-counter (self-triggered). Since either the left or right TDC will register the first time and become the trigger, the base peak calibration constant is the mean position of the TDC peak. As a result of this, the actual time measured by the T-counter TDCs is the TDC time with the base peak constant subtracted, and therefore corrected for the signal delay. For details of the equations used to determine these constants see reference [92].

RF Timing Adjustments

The correct RF beam bucket from which the reconstructed hit was obtained must now be identified. The available RF time is actually given relative to the trigger time. The information it provides is related to the phase shift between the machine RF time, with a period of 2.004 ns and the trigger.

To improve the timing alignment from the base peak calibrations, a reference detector is decided upon. For experiments involving photon running this is the start counter. The start counter is typically chosen as this is the first subsystem which will detect reaction products in CLAS. By using a reference time from the chosen reference detector, the T-counter mis-alignment at the trigger level can be determined and corrected for. This is done by the application of a constant for each T-counter, defined in reference [92].

This stage has used the start counter for a reference time, but a better solution would be to utilise the accelerator RF timing as a reference as this is more accurate and has a resolution of $\sim$ 80 ps. However, to be able to use the RF

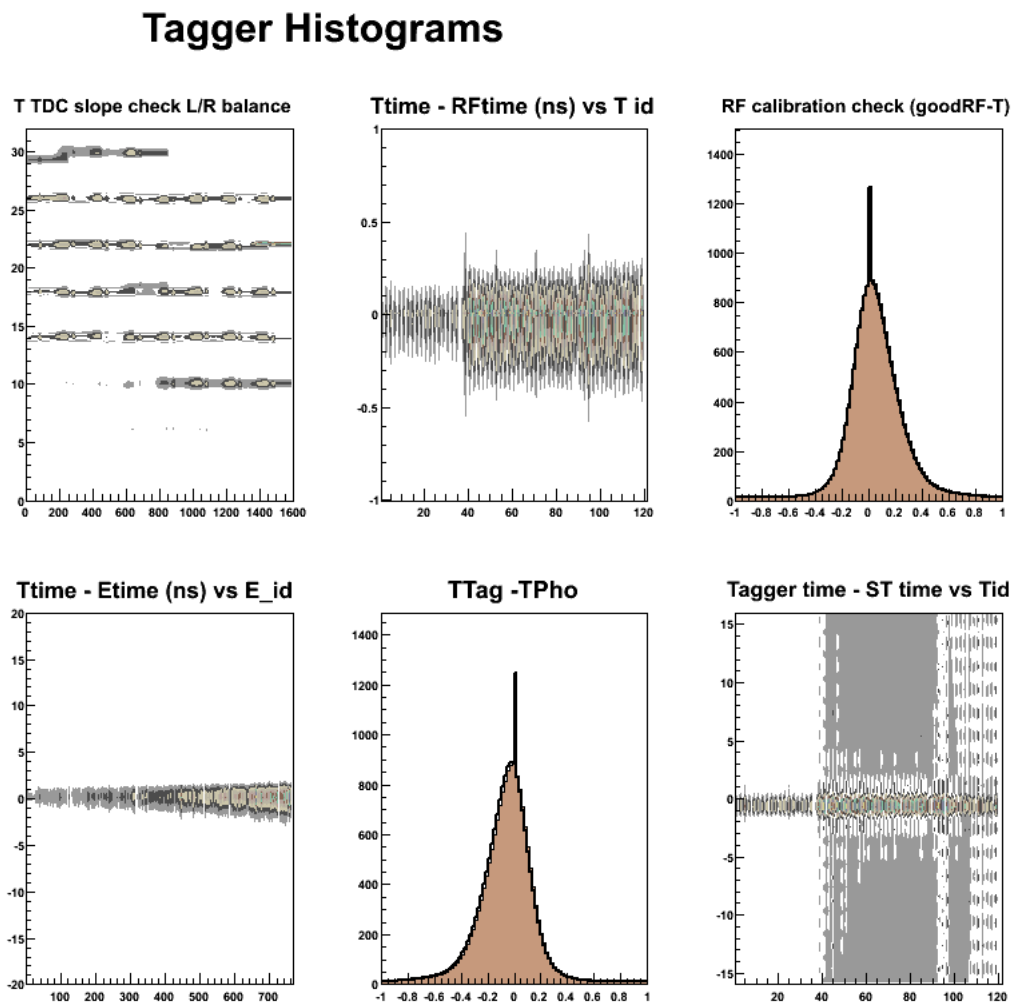

Figure 4.2: Tagger calibration plots for a well calibrated run. Plots are of the LR balance alignment (top left), tagger t-counter time minus RF time versus T-counter (top middle), RF calibration check (top right), tagger t-counter time minus e-counter time versus E-counter (bottom left), tagger time minus RF corrected tagger time (bottom middle) and tagger time minus start counter time versus T-counter (bottom right).

as a reference, the RF phase shift for each T-counter has to be determined and accounted for. The top middle plot of Figure 4.2 shows the tagger time minus RF time distribution across all T-counters.

Once the procedures described above have been completed, two times for an event are now available in the TAGR bank, which (after the tagger has been aligned to the time of flight subsystem) can now be used in further physics analysis. The first is the tagger time reconstructed on an event by event basis and the second is RF bucket real time, considered to be the actual photon time. These are defined in reference [92]. The photon tagger timing and the beam RF timing are now considered to be calibrated and aligned.

Tagger to Time of Flight Offset

The time attributed to the tagged photon should be defined to be the time it takes the photon to reach the centre of the CLAS target, which is the assumed interaction point. This time is relative to the CLAS detector subsystems and can be defined, since the RF timing and the T-counter signal are now independent of each other. The principles and methods used to determine this tagger to time of flight offset, known as $tag2tof$, are the same as those for $st2tof$, explained in section 4.2.1.

4.2.3 Time of Flight Calibration

The time of flight calibration [86] is an essential part of determining the quality of the charged particle identification and the mass resolution. It is at this point in the overall calibration process where the start counter, photon tagger and time of flight timings are aligned relative to each other. The author was responsible for the TOF calibration so a more detailed description of the calibration will be given below. There are several stages in the TOF calibrations process each of which will be outlined.

Status & Pedestals

The raw data is scanned and the status of each of the 288 scintillator paddles is flagged with a number between 0 and 5 which refers to the state of the scintillator (0 - counter is ok, 1 - No ADC, 2 - No TDC, 3 - No ADC and TDC, 5 - Any other reconstruction problem).

The ADC pedestals were measured by a special pulser run. A typical ADC value is 100 therefore the pedestals calibration is deemed satisfactory when the

fluctuation in ADC channel is less than 5 for each counter when compared to previous values.

TDC & Time-walk Calibration

The TDC calibration takes the form of a channel to time (ns) conversion. Pulser data is also used in this calibration. The resulting TDC channel vs. time distribution is fitted with the following function:

$$t = c_0 + c_1 T$$

where c_0 and c_1 are the determined calibration constants, T is the TDC channel number and t is the time in ns. The c_0 constants were set during the initial calibration of the TDC's. The c_0 constant is an overall offset relative to the trigger timing and, as long as the cable length doesn't change, this number should not change.

Time-walk is an instrumental shift in the measured time when using leading edge discriminators. It is essentially the dependence of the trigger time on the signal peak height that comes from triggering on the edge of the signal. The calibration to determine the time-walk correction is based on special laser data. A laser pulse of fixed energy is delivered to each scintillator and simultaneously to a diode, which provides timing information. As no special laser runs were taken during g13b, the constants from the previous experiment were used.

Left-right Alignment

The left-right alignment of each scintillator is the next stage of the TOF calibration. This alignment and the resulting left-right time offsets allow for the determination of hit position within the scintillator. The hit position from the TDC left and TDC right are then plotted for each scintillator on a sector-by-sector basis. This sector based distribution should be symmetric around zero, that is to say the x-projection of the left and right edges ($edge_L$ and $edge_R$, respectively), for each scintillator, should be symmetric around zero. Any left-right time offset, Δt, arising is calculated via the following relation:

$$\Delta t = (edge_L + edge_R)/v_{eff},$$

where v_{eff} is the effective velocity in the scintillator material with a nominal value of 1.6×10^8 ms^{-1}.

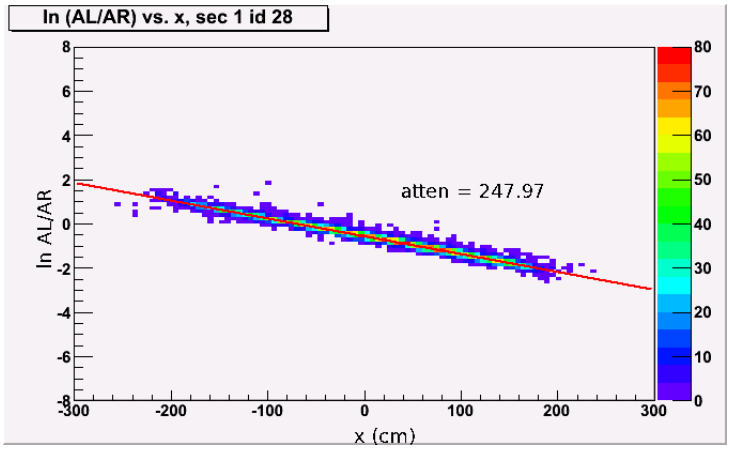

Figure 4.3: Example of the attenuation length calibration with the fit shown in red.

Attenuation Length

The attenuation length calibration is a measure of the energy attenuation in each scintillator. Good timing calibrations are required for this stage in order to select pions for the energy loss calibration. The geometric mean position of the Minimum Ionising Particle (MIP) is measured for each scintillator using the pulse height outputs of the left and right ADCs. The MIP pulse heights are then normalised such that a particle incident normally at the centre of a scintillator bar has a pulse height equivalent to 10 MeV. The attenuation length is then calculated by determining the relation between the amount of light arriving at each PMT and the hit position along the scintillator. An example of a distribution from this calibration is shown in Figure 4.3 where AL and AR are the left and right ADC's respectively.

Geometric Mean

The geometric mean calibration accounts for the dE/dx (energy loss) in the scintillator. The geometric mean in ADC channels of the minimum ionising peak for every counter must be known. It is a position independent handle on the energy deposition in the counter. It is given by:

$$GMEAN = \sqrt{(ADC)_L (ADC)_R}$$

where $(\mathrm{ADC})_{L/R}$ are the left/right ADC values. An example distribution of this step is shown in Figure 4.4.

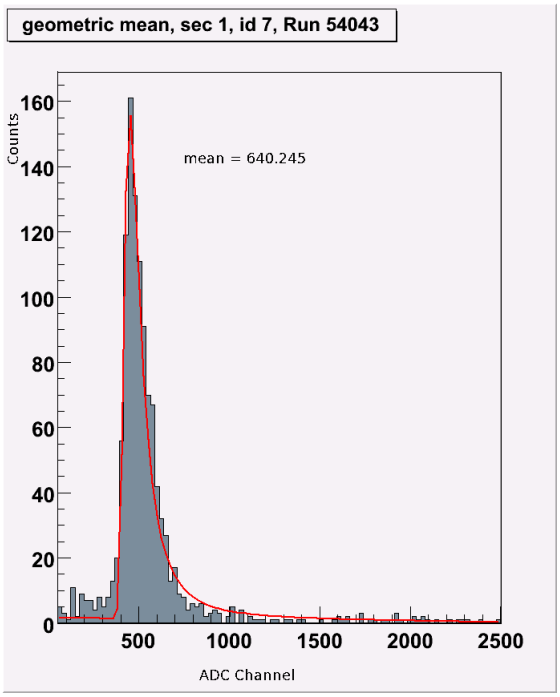

Figure 4.4: Example of the geometric mean distribution with the Gaussian plus 2nd order polynomial fit shown in red.

Effective Velocity

The effective velocity of light in the scintillator plastic has to be calibrated for each counter. An example distribution with fit is shown in Figure 4.5. Nominally this value is 16 cm/ns, however, it can vary by ±3 cm/ns over the detector area. The hit position along a scintillator with respect to the centre, y, is determined using timing information from both ends of the scintillator. Moreover, position y can be determined from tracking information. Therefore, a fit to the difference between the left and right timings (t_L and t_R) vs. y, can be used to determine v_{eff} and the position offset, y_{offset}, for each scintillator, using the relation:

$$y = \frac{v_{eff}}{2}(t_L - t_R - y_{offset}),$$

where t_L and t_R are the adjusted times from the left and right PMTs respectively.

Paddle-to-paddle delay

The final stage of the TOF calibration is the paddle-to-paddle delay. Each of the time of flight subsystems 288 scintillator counters must have their timing aligned with the start counter and photon tagger subsystems. Pions are selected

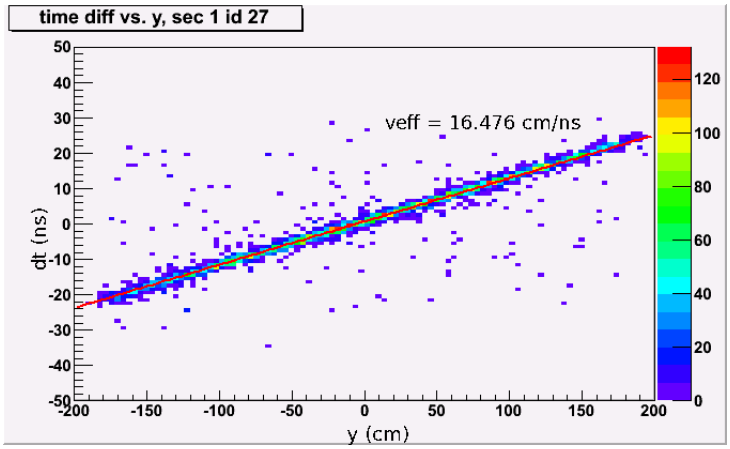

Figure 4.5: Example effective velocity distribution with the fit shown in red.

by cutting on the energy deposited in each scintillator and a distribution of vertex time from time of flight minus vertex time from the start counter/photon tagger is produced. The main peak of this distribution is then fitted, and an offset can be determined which centres the peak on zero.

4.2.4 Drift Chamber Calibration

The drift chamber calibration [93] accurately reconstructs the path a particle travelled through CLAS. This track reconstruction is based upon the measurement of the position of a particle within the drift chamber cells and is performed in two stages. The first stage is Hit Based Tracking (HBT) and the second, Time Based Tracking (TBT).

Stage one, the hit based tracking is based upon a least squares fit of a track to hit wire position and is calculated when at least three out of five superlayers register a hit. The track segments resulting from the HBT are then linked across all superlayers in a region and all three regions in order to reconstruct the particle's track. However, HBT has poor momentum resolution ($\sim 3-5\%$ for a 1 GeV/c track) due to the radially increasing diameters of the cells and the possibility of holes in the drift chamber. Holes are defined to be areas in a chamber with dead wires and they result in less than the maximum 34 layers registering track hits.

Stage two, the time based tracking requires a measurement of the drift time. Here, information about the particle's flight time from the target to the time of flight scintillators is used to augment the drift time. A look up table is then used to convert these augmented drift times into drift distances within the cells, then, within each cell, these positions are fitted in order to determine the track parameters. The drift time, t_{drift}, is defined as:

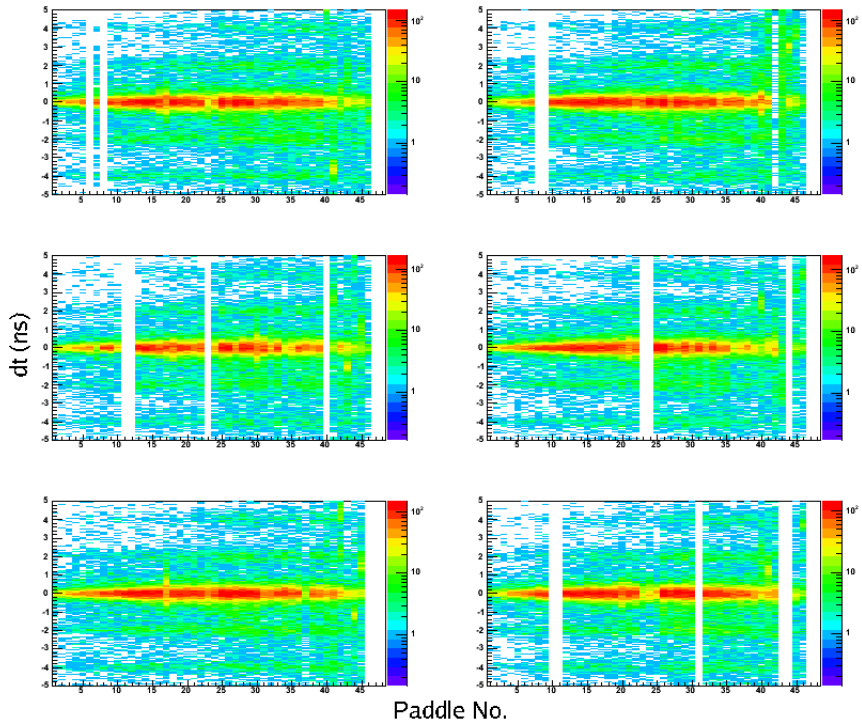

Figure 4.6: Paddle-to-paddle calibration showing all paddles in all sectors aligned to zero.

$$t_{drift} = t_{start} + t_0 - t_{TDC} - t_{flight} - t_{prop} - t_{walk},$$

where t_{start} is the start time of the event, t_0 is the time delay of the wire, t_{TDC} is the raw measured time of the TDC, t_{flight} is the flight time of the particle to travel from the reaction vertex to the wire, t_{prop} is the propagation time of the signal along the wire, and t_{walk} is a time-walk correction made for short drift times differences in ionisation of slow and fast moving particles. The implication of this last term is simply that minimum ionising particles produce smaller signals, resulting in larger time smearings. It should be pointed out that t_{start} is constructed based upon coincident signals from the photon tagger, start counter and time of flight subsystems for photon experiments such as g13b. Time based tracking improves the momentum resolution for a 1 GeV/c track to $\sim 0.5\%$.

4.2.5 Electromagnetic Calorimeters Calibration

The electromagnetic calorimeter calibration [94] aims to find an agreement between the vertex time of a track measured by the electromagnetic calorimeter and an independent vertex time of a track as measured by the time of flight subsystem. This means that the EC vertex time minus the TOF vertex time

distribution should be centred on zero. It is necessary that the EC time is well defined as this is essential in discriminating between photons and neutrons where detected particle's velocity is what identifies one from the other. It should be noted that not the entire energy of the neutron is deposited in the calorimeters. The calibration of the large angle electromagnetic calorimeters is done in a similar fashion.

4.3 Photon Polarization

The position of the coherent edge and the relationship between photon energy and photon polarization must be known to accurately determine the degree of linear photon polarization. The edge is defined to be the part of the slope of the peak that has the most negative gradient and is found by fitting a 4th order polynomial in the region of the coherent peak. An example of this is shown in Figure 4.7.

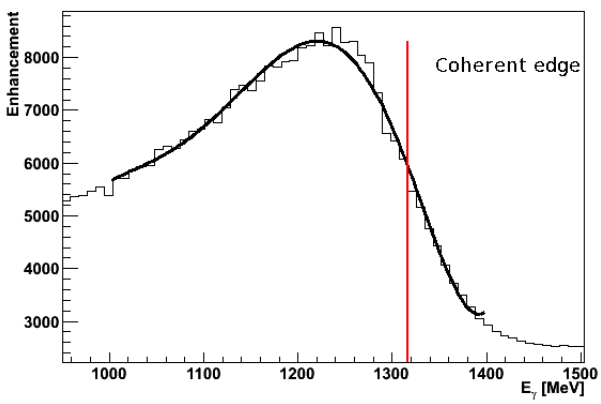

Figure 4.7: Enhancement plot zoomed in on coherent peak region. Solid black line is the polynomial fit to the coherent edge. Red vertical line denotes coherent edge position.

Prompt and random photons will contribute to the tagger scalers so a random background subtraction must be done first to both the polarized and amorphous data, which allows for the removal of photons that did not cause a trigger. An enhancement is produced by dividing the scalers for the polarized data by the scalers for the amorphous data. It is then compared to the analytic Bremsstrahlung (ANB) calculation [95] which allows the user to account for beam divergence and

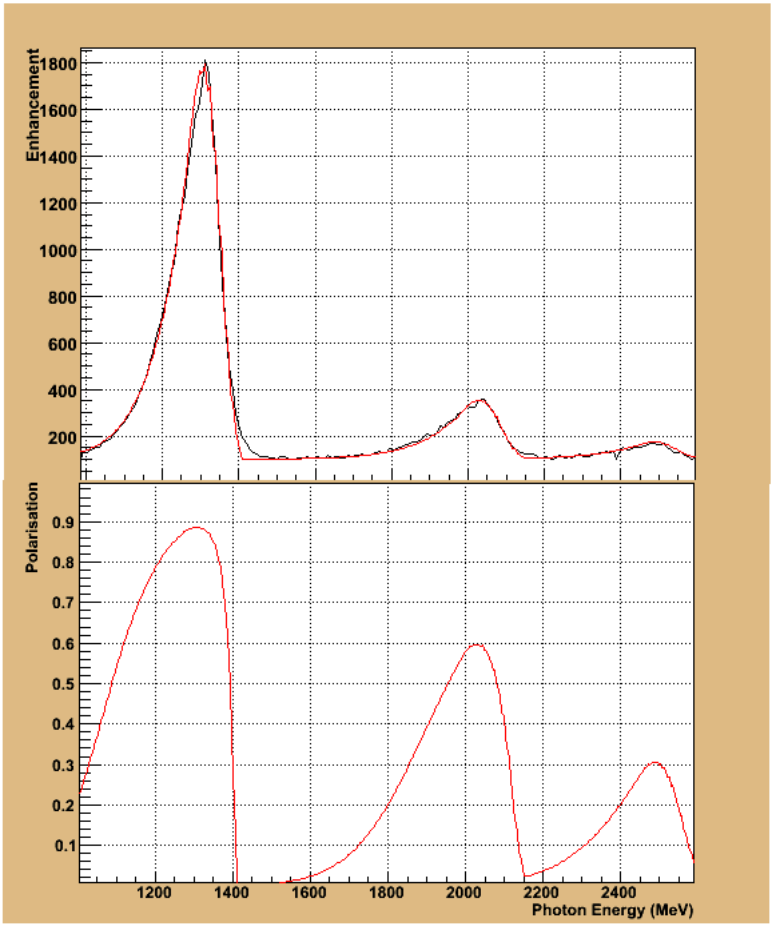

Figure 4.8: Enhancement of tagger scaler spectra (top) compared to the ANB calculation for the 1300 MeV coherent peak position. Resultant photon polarization (bottom) as a function of photon energy. The black line is the data and the red line shows the ANB calculation.

spot size, alongside numerous other parameters such as beam energy, radiator thickness or collimator geometry, upon which the beam polarization depends. A detailed treatment of these parameters is given in [81]. The calculation is performed several times and the parameters are adjusted until a good agreement is found with the enhancement plot. An optimised output from this calculation is shown in Figure 4.8.

During the experimental run, the coherent peak was not stable and hence the ANB calculation had to be performed for a range of energies around the coherent peak position as shown in Figure 4.9. Look up tables are generated for each different coherent edge position which allows an event by event determination of the photon polarization. The enhancement spectrum is regenerated for every 2 ns of data and is fitted with a 4th degree polynomial to determine the position of the coherent edge. The correct look up table is then selected for that event.

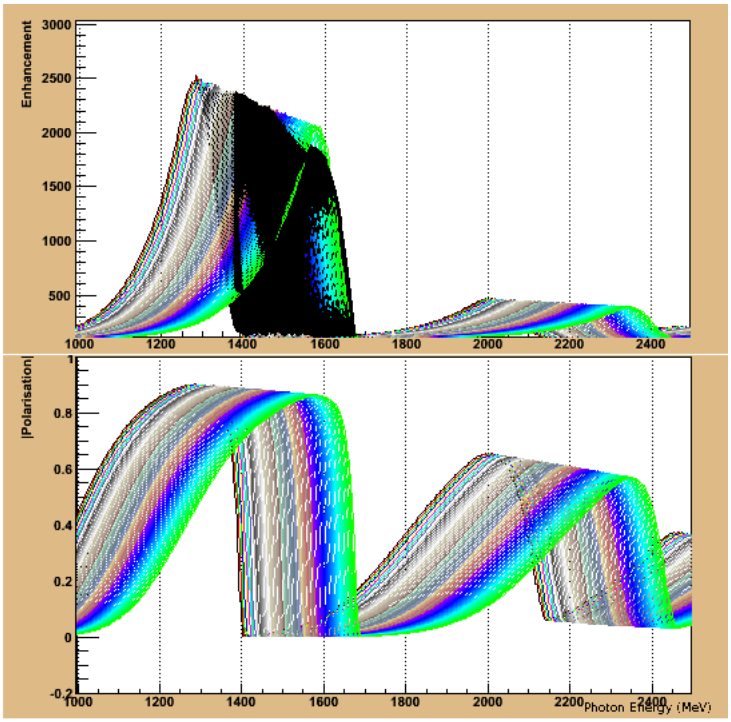

Figure 4.9: Enhancement of tagger scaler spectra (top) compared to the ANB calculation for the 1500 MeV coherent peak position over a range of photon energies. Resultant photon polarization (bottom) as a function of photon energy.

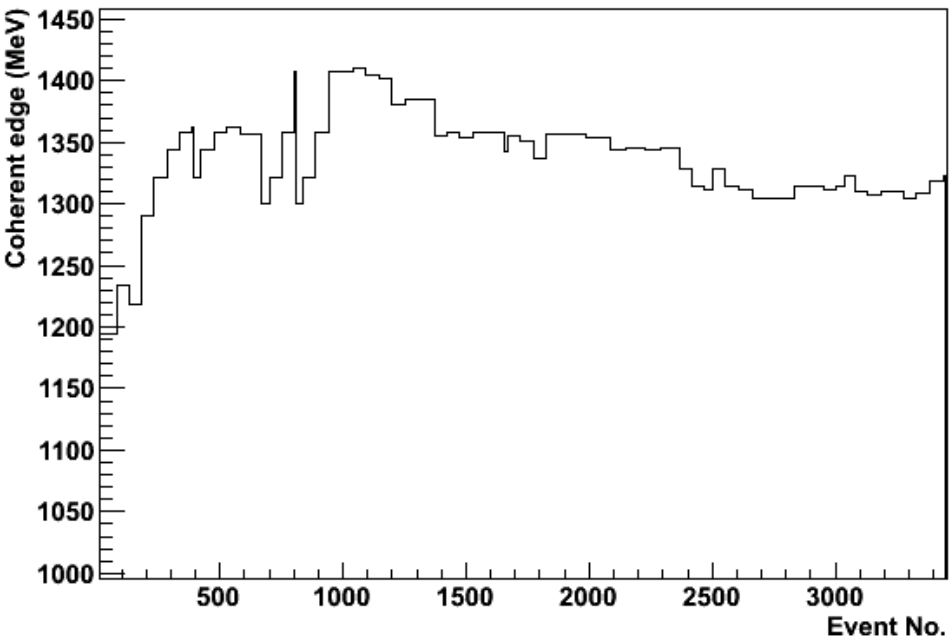

Figure 4.10: Coherent peak stability over one run. Fluctuations in coherent peak position around the nominal value of 1300 MeV are clearly shown.

With mean polarization values for each combination of electron beam, photon beam and plane setting now determined, the polarizations were then scaled according to the number events for each plane setting at each electron beam energy. This resulted in an overall weighted mean value of the linear photon polarization for g13b. The range in degree of linear polarization for the various coherent peaks was between 70 - 78%. These were the final values that were used to extract all the polarization observables for this analysis.

Systematic Uncertainty

The sources of systematic uncertainty in calculating the photon polarization come predominantly from the stability of the coherent peak. The stability of the peak over one run can be seen in Figure 4.10.

There is a small error from the ANB calculation itself. It can be split into four components: The dependence of the polarization on the tagger E-plane, the varying height of the coherent peak, the theoretical and data comparison limits and the uncertainty from the TDC spectra normalization.

In the tagger E-plane case, this effect is due to the fact that up to six E-bins can be associated with each T-bin for which the polarization is calculated. This introduces uncertainties in the true position of the coherent edge which can

change the value of the mean polarization. The instability of the position of the electron beam is what gives rise to the varying height of the coherent peak. The third effect is a result of there being an equally valid range of parameters that can give rise to good comparisons between the data and the calculation. The final case arises from the signal noise in the TDC spectra that may cause errors in the normalisation procedure.

These effects were considered in reference [81] which found the combined systematic uncertainty in the photon polarization to be 5% and this shall be the systematic error used for this analysis.

4.4 Summary

Once the processes described in this chapter have been completed, the data are then considered to be fully calibrated and in a format which can now be used for physics analysis. The information contained within the data is used for initial particle identification and the construction of 4-vectors. These particle 4-vectors allow for the physics analysis of events of interest within the data. The initial particle identification and event selection, along with the results of the data analysis, are presented in the following chapters.

Chapter 5

Data Analysis

5.1 Data Skim and Event Selection

The g13b data set was accumulated to allow for the study of various reaction channels. Any event that had a single charged particle track was recorded in the output stream. Output from the CLAS detector subsystems is transferred and collated on an event-by-event basis within a dynamic memory structure known as BOS (Bank Operating System) [90, 96]. Each detector subsystem within CLAS has at least one BOS bank containing the relevant raw output. These banks are then accessed using the appropriate function calls when required for calibration or *cooking*. Typically, the output of each data run is split into files of ~ 2 GB in size, and one standard data run (~ 2 hours for g13b) gave rise to $\sim 50 - 60$ data files. During uninterrupted production running it was possible to take $\sim 10 - 12$ runs per day. This resulted in a data set of approximately 30,000 files totaling 120 TB of disk space, of which $K\Lambda/\Sigma^0$ events contribute only a small percentage. The data was stored on the JLab tape silo, where all experimental data is stored. Retrieving the data from the tape silo in its original form would be very time consuming and would require large amounts of disk space. The solution was to filter the data or skim it, using the ROOTBEER software package [97], into Data Summary Tapes (DSTs) that contained candidate events from the $K^0\Lambda$ and $K^0\Sigma^0$ reaction channels. The main bank within a DST file is the EVNT bank which contains particle information such as energy, momentum, charge, mass and position. The skims were based on charge and loose mass cuts and, for this analysis, they required 4 or 5 particles to be recorded from the same event. The skims dramatically reduced the size of the data set down to approximately 2% of its original size. At this point the data was transferred over to Glasgow for permanent storage on local disks, where it was easily accessed for analysis.

The reduction in size of the data meant that the computing time required to do analysis was greatly reduced.

The remainder of this chapter will describe the event selection procedure used to identify the reactions

$$\gamma \mathrm{n} \rightarrow K^0 \Lambda \rightarrow \pi^+ \pi^- \mathrm{p}\ \pi^-(p_s)$$

$$\gamma \mathrm{n} \rightarrow K^0 \Sigma^0 \rightarrow \mathrm{K}^0 \gamma\ \Lambda \rightarrow \pi^+ \pi^- \gamma\ \mathrm{p}\ \pi^-(p_s)$$

in the CLAS detector. The Λ in these reactions decays into a proton and a π^- with a branching ratio of 64%, and into a neutron and a π^0 with a branching ratio of 36%. The Σ^0 undergoes a radiative decay into a Λ and a photon. For this analysis, only the pπ^- decay mode will be analysed since the CLAS has a low efficiency for neutral particle detection. The methods used to correctly identify the particles in CLAS will be described, focusing on an exclusive determination of the reactions through the identification of the π^+,π^-, p and π^-. All procedures and cuts used in particle identification will be discussed in the order in which they were used in the event selection.

The analysis of the g13b data set was carried out on six different photon energy settings along with amorphous data which was taken at regular intervals throughout the experimental run. The following sections describe, in detail, the analysis of the 1.9 GeV linearly polarized photon data set. The cuts and procedures used for this analysis are the same for all photon energy settings.

Time of Flight Mass Cuts

As shown above, both the hyperon channels being investigated result in π^+, π^-, π^-, p in the final state. In the Λ case this is exclusive and in the Σ^0 case there is a 77 MeV photon, which is below the 200 MeV detection threshold. Therefore the first step in the initial selection requires the identification of events with these 4 charged particles in the final state. However, the the possibility of detecting a photon was retained although not explicitly required for the identification of the Σ^0 from its radiative decay. The negative polarity field used during g13b meant that the acceptance for negatively charged pions was higher than for positively charged pions.

The filtering began with accepting events where only four particles were recorded in CLAS in coincidence with a valid tagger hit. At this stage loose mass cuts were implemented to refine the particle identification. These cuts are made on the mass squared as calculated by the time of flight subsystem and are dependent upon particle charge. The criteria are as follows:

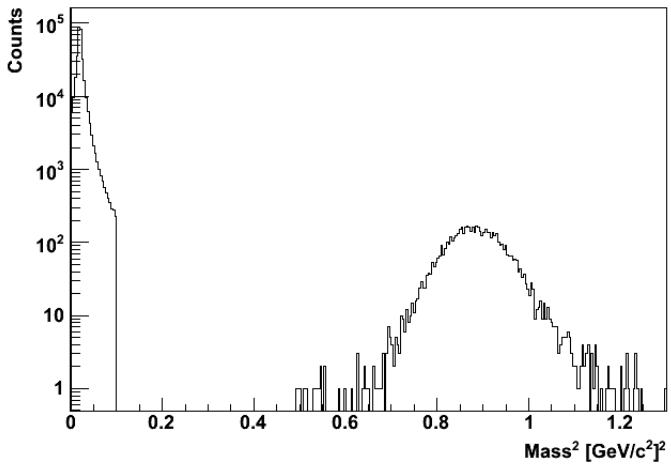

Figure 5.1: TOF mass^2 of protons and pions as detected in CLAS. The sharp cutoff regions indicate where the cuts were placed to identify each particle.

- Particles with zero mass and zero charge were identified as photons
- Particles with non-zero mass and zero charge were rejected
- Non-zero mass charged particles, were required to have a valid drift chamber track and either a valid time of flight hit or electromagnetic calorimeter hit
- The TOF mass^2 ranges used for initial identification are as follows:
  - $0.0 < M^2 < 0.1$ GeV$/c^2$: either π^-or π^+, dependent on charge
  - $0.49 < M^2 < 1.44$: proton

Events which contained one proton, one positively charged pion and two negatively charged pions were retained for further stages of event selection. This allows for the exclusive search for the $K^0\Lambda$ channel and the semi-exclusive search for the $K^0\Sigma^0$ channel, where the decay photon is not detected. The TOF mass^2 for the protons and pions can be seen in Figure 5.1, which shows that at this early stage, the protons and pions can be well identified with a simple mass cut.

Best Photon Selection

The next stage in the event selection process is to identify the photon that caused the event. Timing information for charged particles detected by the TOF was extrapolated backwards to provide the event reaction time. If an event has multiple photons (hits in the tagger), then the actual event photon is identified as

the photon with its time closest to the event vertex time. This procedure requires the difference between the π^+ vertex time and the photon vertex time to be minimised:

$$\Delta = (TOF^{\pi}_{time} - (\frac{TOF^{\pi}{}_{path}}{c\beta^{\pi}_{c}}) - (\gamma_{time} + \frac{z^{\pi}}{c})) \tag{5.1}$$

where,

$$\beta^{\pi}_{c} = \frac{p_{\pi}}{\sqrt{p_{\pi}{}^{2} + m^{2}_{PDG(\pi)}}} \tag{5.2}$$

using the PDG mass for the π^+ and the π^+ measured momentum.

Where,

$TOF_{time}{}^{\pi}$= π^+ flight time

$TOF_{path}{}^{\pi}$= π^+ path length

γ_{time}= event photon vertex time

z^{π}= z-vertex position of the π^+

c= speed of light

The timing difference Δ for the π^+ and best photon can be seen in Figure 5.2. If an event had more than one photon in the same 2 ns beam bucket (minimal vertex timing difference window) then it was rejected. This occurs less than 1% of the time so the loss in statistics is negligible.

Missing Mass/Momentum Cuts - $d(\gamma,p\pi^+\pi^-\pi^-)X$

A cut was applied to the $d(\gamma,p\pi^+\pi^-\pi^-)X$ missing mass to select events that were consistent with a missing proton (X=proton) from $K^0\Lambda$ events and a missing proton plus a low energy decay photon (X=proton+γ) from $K^0\Sigma^0$ events. The missing mass MM($p\pi^+\pi^-\pi^-$) calculated from the 4-vectors of the proton, π^+, and two π^- should correspond to the mass of a spectator proton plus some broadening from the decay photons. This step was carried out before extracting the hyperon yields or looking at invariant masses. Figure 5.3 shows missing mass distribution for $d(\gamma,p\pi^+\pi^-\pi^-)X$. Since the distribution is asymmetric, a Gaussian was fitted over the symmetric top half of the distribution in order to get loose cuts. A 3σ cut was taken at the lower end, however in order not to lose $K^0\Sigma^0$ events, the cut at the upper end was extended to a 5σ cut. The asymmetric loose cut is given below and is indicated by the red lines.

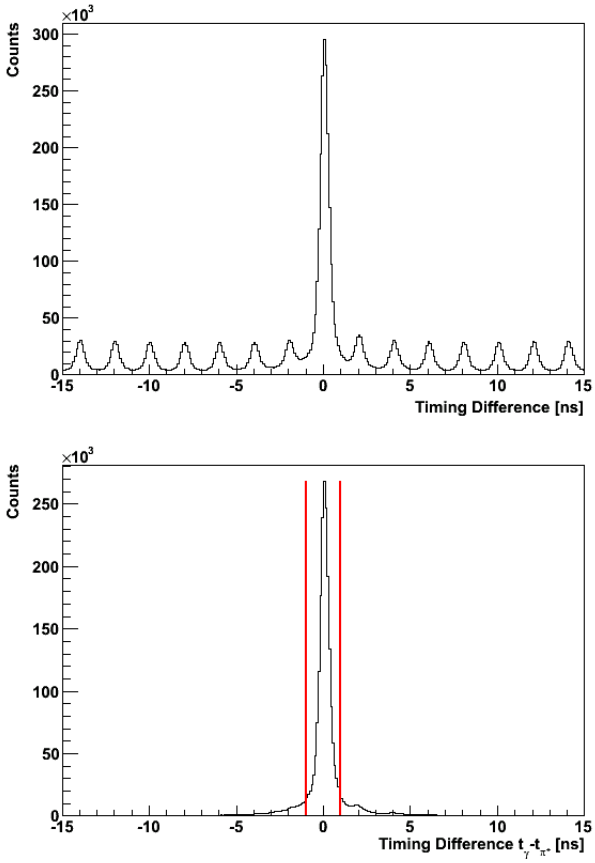

Figure 5.2: Tagger vertex time subtracted from the TOF vertex time for all photons (top). This shows the 2 ns beam bucket structure. Tagger vertex time subtracted from the TOF vertex time when the best photon has been selected (bottom). Red lines show $\pm 3\sigma$ cuts.

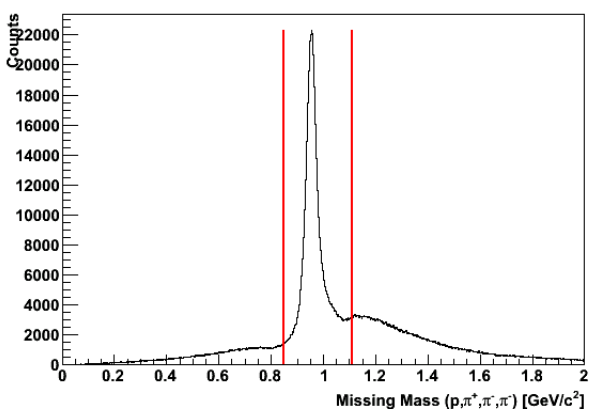

Figure 5.3: Missing mass of the reaction d(γ,p $\pi^+\pi^-\pi^-$)X. Red line at the lower end is the 3σ cut and at the upper end is 5σ.

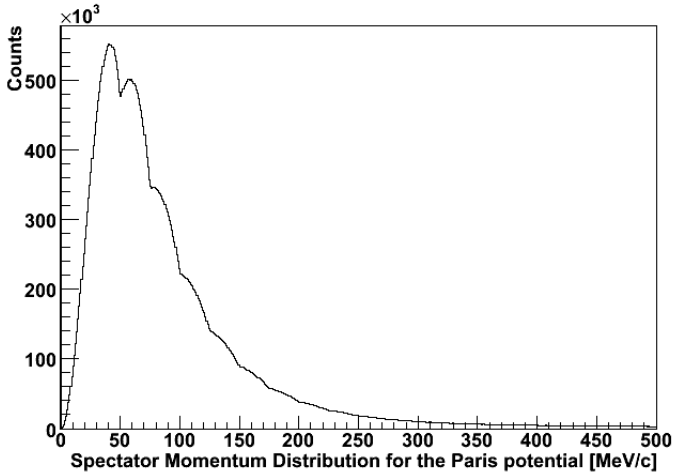

Figure 5.4: Spectator momentum distribution from a deuteron using the Paris potential.

$$0.894 \text{ GeV} < \text{MM}(p\pi^+\pi^-\pi^-) < 1.091 \text{ GeV}$$

There are a significant number of protons with high momentum, which are not consistent with the fermi momentum distribution of spectators. An example of the spectator momentum distribution for the Paris potential in a deuteron is shown in Figure 5.4.

In order to get to the subset of quasi-free events and reduce the initial background, the spectator proton momentum was cut at 300 MeV/c as shown in Figure 5.5. This cut will be refined later in the analysis, it is only intended to reduce background at this stage.

Spectator protons from re-scattering events can be better seen in a two dimensional plot (Figure 5.6) of missing momentum versus the cos θ distribution of the spectator proton. The distribution of low momentum spectators is isotropic in the lab frame for exclusive $K^0\Lambda$ events. The undetected photon emitted from forward moving Σ^0's makes the missing protons from those events appear to be forward peaked. It should be noted that the events in Figure 5.6 also include background and Final State Interaction events.

Minimum Momentum Cut

At this stage a cut was made on the minimum momentum of any detected proton from the Λ decay that was considered to be an event in the particle selection process. The cut was placed at 300 MeV/c as this is the minimum detection momentum for protons in CLAS.

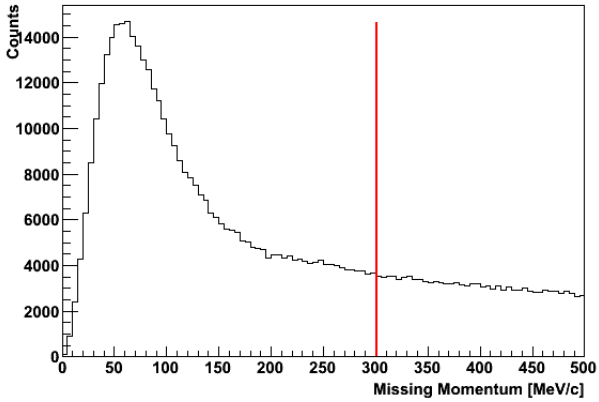

Figure 5.5: Missing momentum of the reaction d(γ,p $\pi^+\pi^-\pi^-$)X. The red line shows the cut placed at 300 MeV/c to reject high momentum spectator protons.

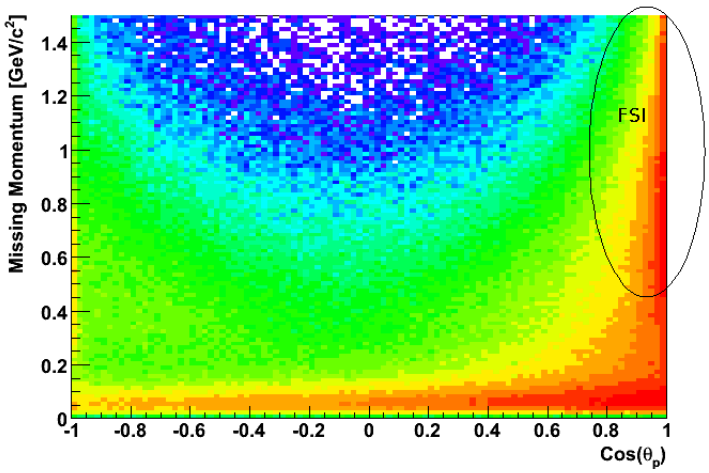

Figure 5.6: Missing spectator momentum versus the cos(θ_p) spectator angular distribution in the lab frame. The Final State Interaction (FSI) events are circled on the plot.

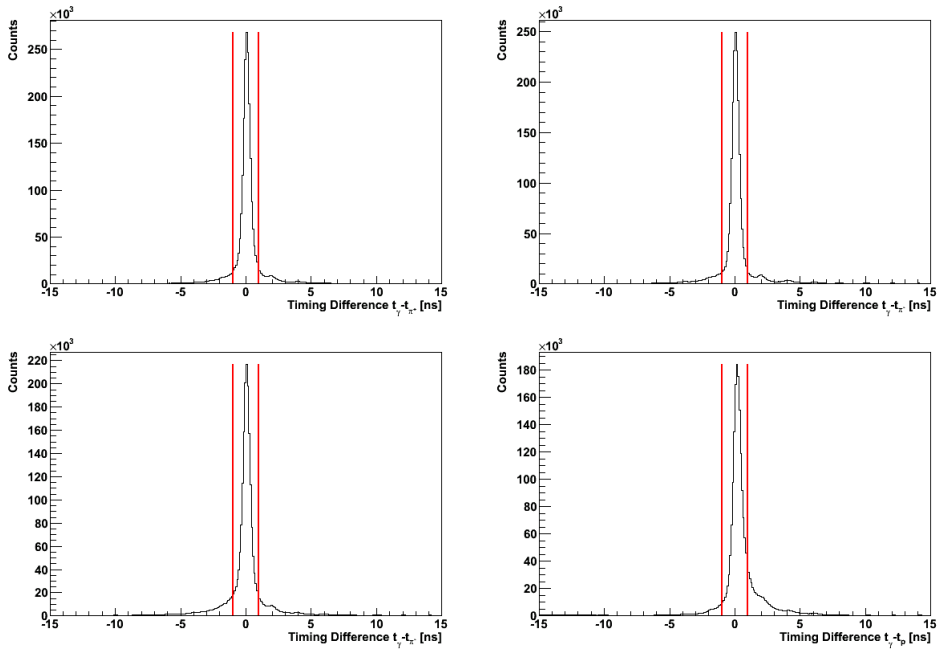

Figure 5.7: Vertex timing difference between the photon and π^+, after best photon selection (top left). Vertical lines on all plots indicate $\pm 3\sigma$ cuts. Vertex timing difference between the photon and π^-, after best photon selection (top right). Vertex timing difference between the photon and π^-, after best photon selection (bottom left). Vertex timing difference between the photon and proton, after best photon selection (bottom right).

Hadron - Photon Vertex Timing Cuts

If the timing calibrations of the detector subsystems are, in general, well defined, then the vertex time of the hadron would be the same as that of the photon (their difference would be centered on zero). Figure 5.7 shows that the hadron-photon vertex time distribution for all particles with $\pm 3\sigma$ cuts shown by the vertical lines, where the cuts were determined from a Gaussian fit to the peak. The slightly asymmetric shape of the distributions comes from the fact that the detected protons and pions have a detached vertex. This arises due to the parent hyperon travelling approximately 7 cm before decaying into a proton and a π^-.

Invariant Mass Cuts

The final step in identifying the correct reaction particles is to reconstruct the Λ and K^0 invariant masses. A problem arises due to there being two negatively charged pions in the final state. The π^- that decayed from the Λ must be distinguished from the π^- that decayed from K^0. All particle combinations are reconstructed and the pair that reconstruct closest to the PDG Λ/K^0 mass are

Table 5.1: PDG and fitted masses of the K^0 and Λ particles.

	PDG Mass (GeV)	Fitted Mass (GeV)
Λ	1.115 ± 0.150	1.115 ± 0.006
K^0	0.497 ± 0.024	0.496 ± 0.015

taken to be the correct pair. There will be ambiguity in this process, so when there is no clear distinction between the pions then they are rejected from the analysis. This occurs for less than 1% of events. To further clean up the invariant masses, a 3σ cut can be placed on the Λ and K^0 and the other particle plotted as a result of this. Figure 5.8 shows the K^0 invariant mass (top plot) reconstructed from the best π^+ and π^- combination. The K^0 peak is fitted with a Gaussian plus a third degree polynomial. Similarly, the Λ invariant mass reconstructed from the proton and π^- is shown in the bottom plot of Figure 5.8. The lambda peak is fitted with a Gaussian plus a third degree polynomial. The 3σ cuts are shown on both plots by the vertical red lines. The fitted K^0/Λ masses agree well with the PDG masses as shown in Table 5.1.

Figure 5.9 shows the invariant K^0 mass before (green histogram) the 3σ cut on the Λ and after the 3σ cut (yellow histogram). Figure 5.10 shows the invariant Λ mass before (green histogram) and after (yellow histogram) with the 3σ cut on the K^0 mass. The background contribution before the 3σ cuts is 20%, whereas after the cuts this is reduced to 8%. This background is discussed along with other systematic uncertainties later.

The quality of event selection and vertex reconstruction can be judged by how well the K^0 and Λ lifetimes are reproduced for lifetimes above the range dominated by the CLAS resolution. To do this the primary and secondary vertices must be reconstructed. The first step was to reconstruct the decay vertices using a technique called Distance of Closest Approach (DOCA). Using position and momentum information allows one to find a point along the line which connects the two particle trajectories. Thus, the momenta of the decaying particles can be calculated from their 4-vectors and the decay vertex from the DOCA routine. This information can now again be fed into the DOCA calculation and will give a line along the DOCA between the two reconstructed tracks. A point along this line is the event vertex. The event vertex should, if reconstructed properly, lie within the target cell (target limits are +40 cm to 0 cm). Figure 5.11 shows the event vertex z-distribution, which is consistent with the expected target z-distribution.

The simplest choice is to pick the point in the middle. Once all three points

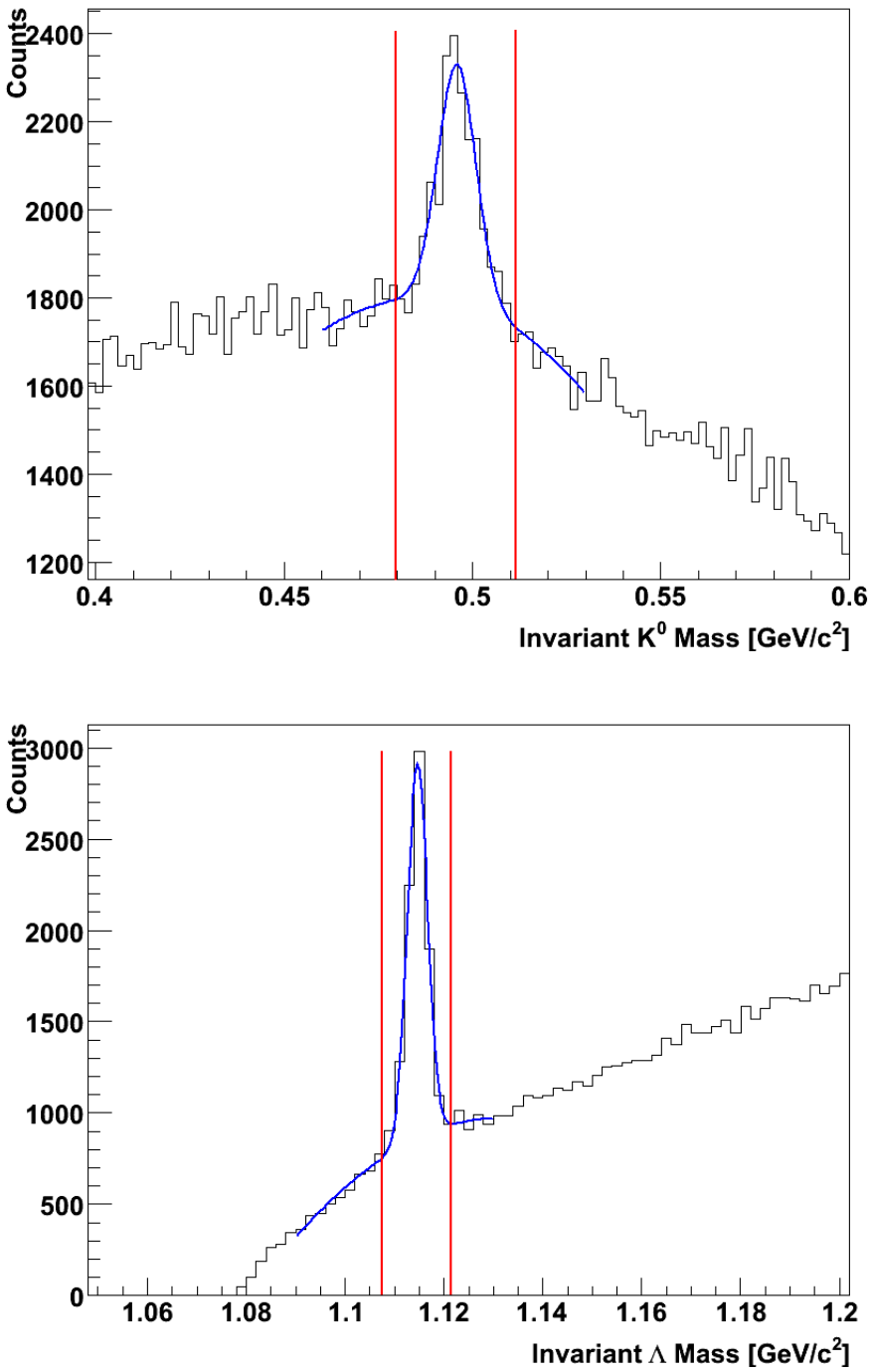

Figure 5.8: Fit to the K^0 invariant mass reconstructed from the correct π^+ and π^- combination (top). Fit to the Λ invariant mass reconstructed from the correct proton and π^- combination (bottom). Red lines indicate $\pm 3\sigma$ cuts.

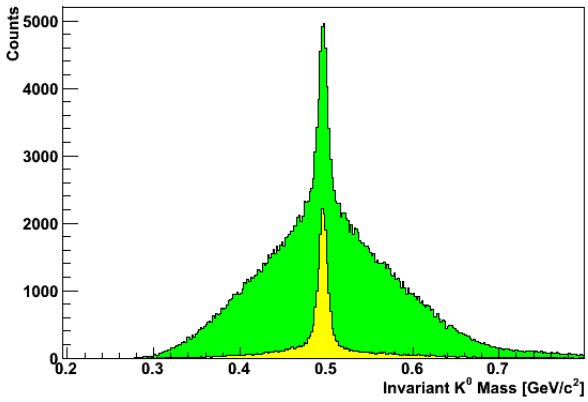

Figure 5.9: Invariant K^0 mass with (yellow) and without (green) 3σ cuts on the Λ particle.

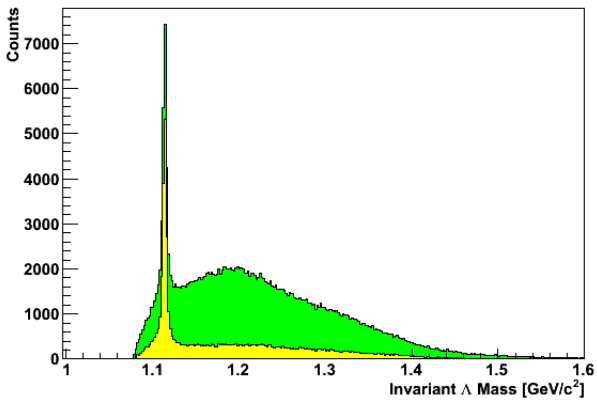

Figure 5.10: Invariant Λ mass with (yellow) and without (green) 3σ cuts on the K^0 mass.

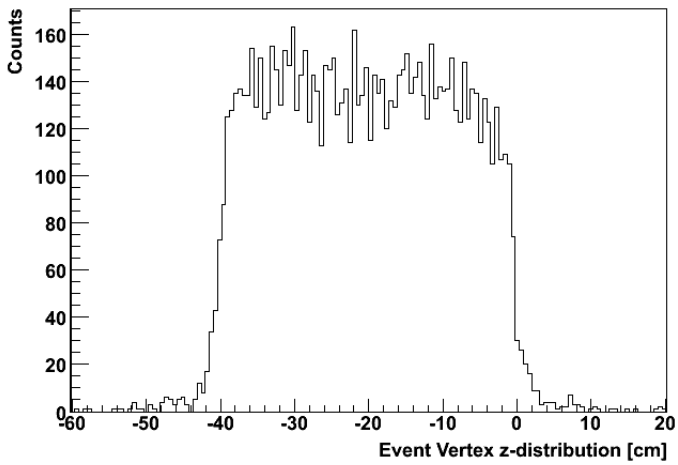

Figure 5.11: Primary z-vertex distribution. This shows most particles primary z-vertex was within the target volume.

Table 5.2: Table showing the PDG and measured decay constants ($\frac{1}{\tau}$, where τ is the particle lifetime) for the K^0 and the Λ.

	PDG - Decay Constant	Measured - Decay Constant
K^0	11.2 $ns^{-1} \pm$ 0 ns^{-1}	10.96 $\pm$ 0.17 ns^{-1}
Λ	3.8 $ns^{-1} \pm$ 0 ns^{-1}	3.993 $ns^{-1} \pm$ 0.069 ns^{-1}

are known, the distance, d from the primary vertex to the secondary one can be calculated. Then, the particle lifetime (in its rest frame) can be calculated from the simple expression:

$$\Gamma = \frac{m \times d}{p \times c} \tag{5.3}$$

where m is the (PDG) mass, p is the momentum, and c is the speed of light (in the same units as d). The K^0 lifetime is fitted over the range 0.02 ns - 0.38 ns in Figure 5.12, where the majority of events fall and where the CLAS resolution does not dominate. Similarly, the fit to the Λ lifetime over the range 0.02 ns - 1.0 ns in Figure 5.13 shows that the decay constant shows good agreement with that of the PDG value. Table 5.2 displays the PDG and measured decay constant values. The good agreements of these values with the PDG values indicate a good vertex reconstruction and event selection.

At this point in the analysis, all the particles required for the $\gamma d \rightarrow K^0\Lambda/\Sigma^0$ (p_s) reactions have been identified and will now be used in further analysis.

Energy Loss Corrections

Energy loss corrections are required in this analysis because a charged particle's momentum at its production vertex will be larger than that which is measured in the drift chambers. When the particle travels through the target cell, target walls and the start counter it will deposit some of its energy in these structures. The amount of energy lost (ELOSS) must now be accurately determined and the measured momentum appropriately corrected. A routine called ELOSS [98], is used, which tracks the particle through the materials of the target cell and start counter. It requires as input the particles 4-momentum and vertex position, as well as the geometry of the g13b target cell and returns the corrected particle 4-momentum. The energy loss distributions for the detected charged particles in this analysis can be seen in Figure 5.14 .

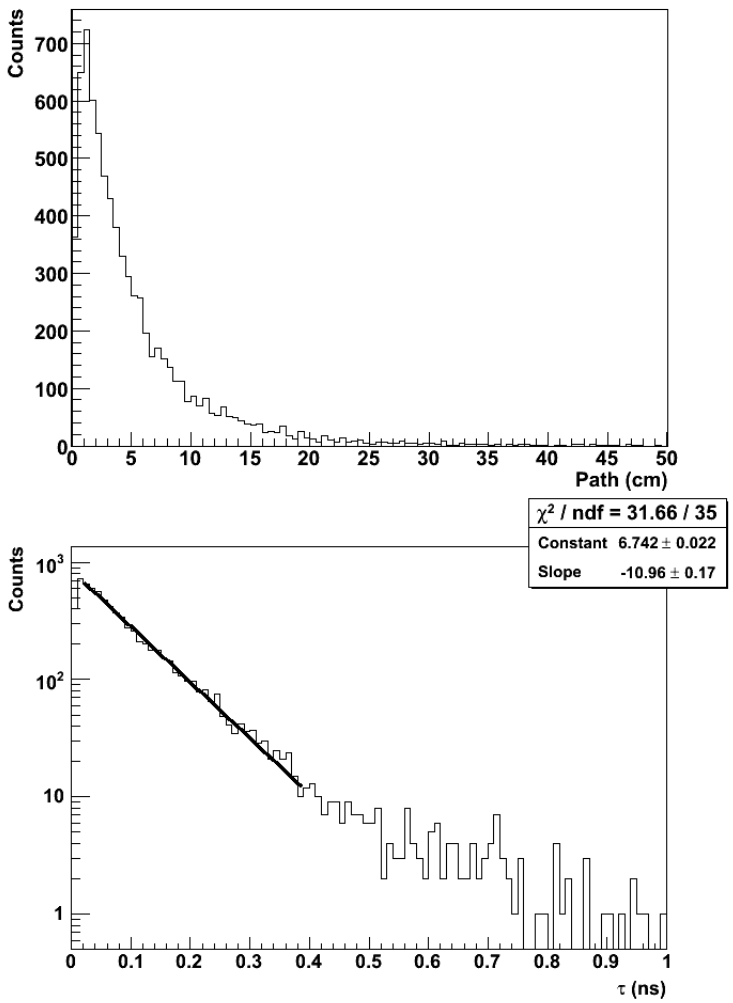

Figure 5.12: K^0 path length (top). There is a small deficit of events at small path lengths due to the CLAS resolution. K^0 lifetime (bottom). The K^0 lifetime is fitted over the range 0.02 ns - 0.38 ns, out with the range dominated by the CLAS resolution and background contamination.

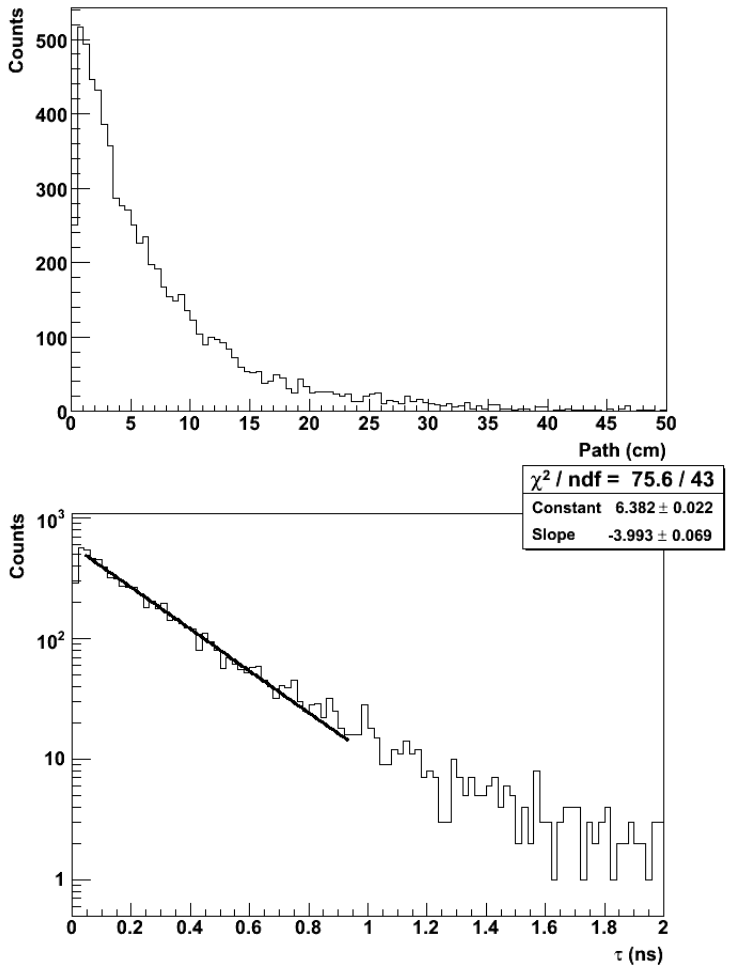

Figure 5.13: Λ path length (top). There is a small deficit of events at small path lengths due to the CLAS resolution. Λ lifetime (bottom). The fit to the Λ lifetime over the range 0.02 ns - 1.0 ns, out with the range dominated by the CLAS resolution and background contamination.

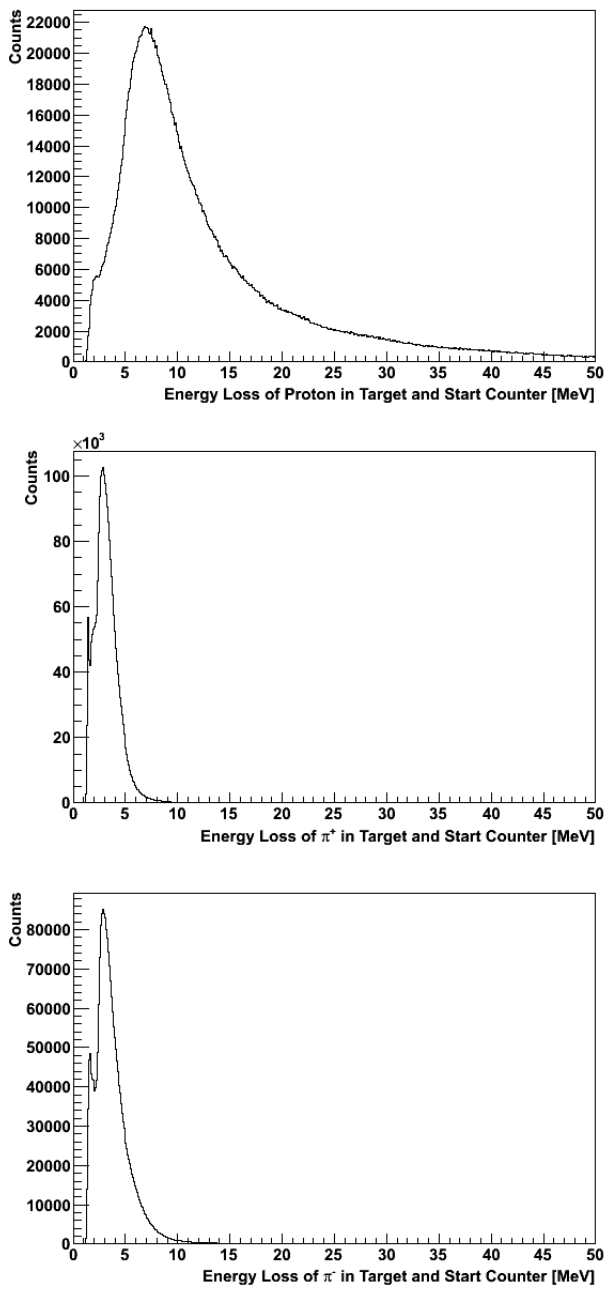

Figure 5.14: Energy loss of proton (top), π^+(middle) and π^-(bottom).

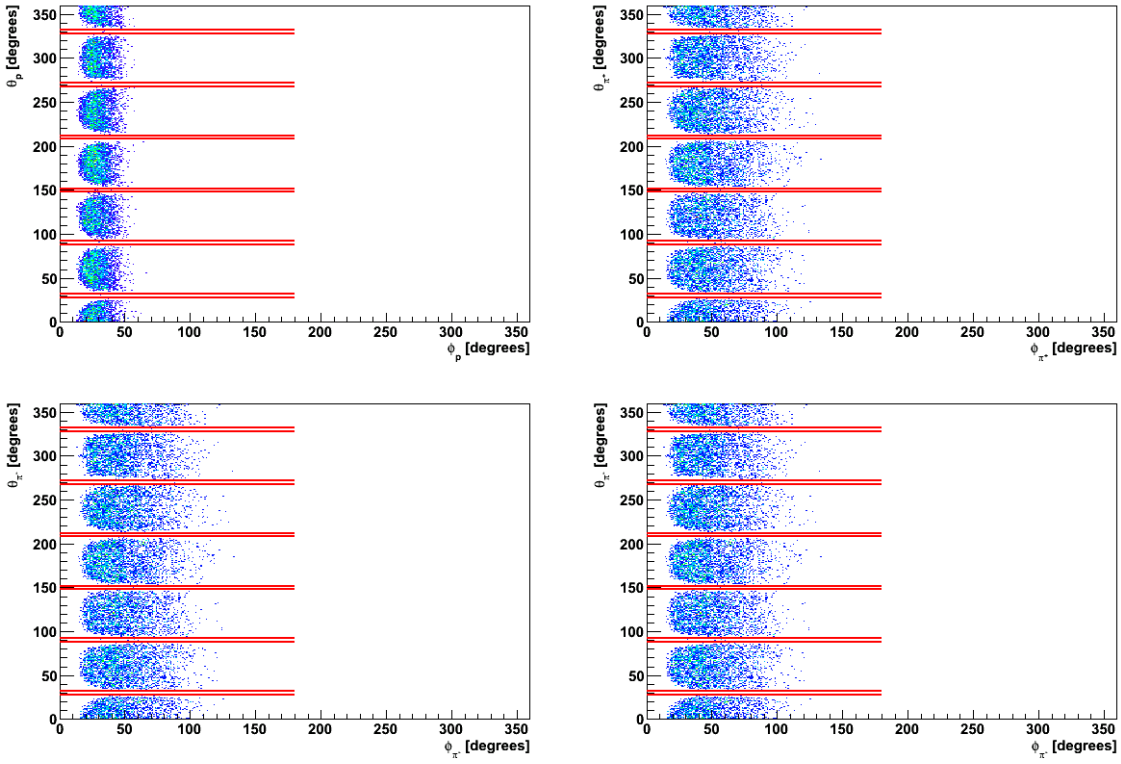

Figure 5.15: Proton, π^+, π_1^-, π_2^- θ versus ϕ distributions in the lab frame from top left to bottom right respectively. Red lines show where fiducial cuts are applied.

Fiducial Cuts

The CLAS detector has a non-uniform acceptance due to its segmented nature which makes modelling particle acceptance very difficult. This is of particular concern when extracting the hyperon recoil polarization as it requires a correction of the detector acceptance to be made. The areas of non-uniform acceptance are found at the edges of the drift chamber sectors and in regions where particles could interact with the torus magnet coils. The cuts chosen here are the same for all sectors of CLAS and are dependent on azimuthal angle and charge. In this analysis, fiducial cuts on the azimuthal distributions of $\pm 5^o$ at each sector division are used. This cut was chosen to be the same for both protons and pions, Figure 5.15 shows the distributions with cuts superimposed.

Hyperon Separation

The Σ^0 hyperon decays into a $\Lambda\gamma$ with a branching ratio of 100%, so it essential to separate a Λ from a Σ^0 decay from one produced directly. When using a proton target this can be done using the kaon missing mass. Fermi motion in the deuteron smears the hyperon masses meaning this method is no longer possible.

One can never completely separate the hyperons produced on a deuterium target, there will always be some overlap, however some separation can be made using a process which will be described in detail below.

If one combines the kaon missing mass as it would appear in a $\gamma n \rightarrow K^0 Y$ free neutron case (where Y is either a Λ or Σ hyperon), with the missing mass of a $K^0\Lambda$ produced from a $\gamma d \rightarrow K^0 Y$ deuterium case, then one can see that the Λ and Σ^0 are clearly separated (top plot of Figure 5.16) . Taking a projection on the $K^0\Lambda$ axis, as seen in the middle plot of Figure 5.16, clearly shows there is a significant background which has to be accounted for in the analysis.

The projection onto the $K^0\Lambda$ axis (middle plot of Figure 5.16 shows the missing mass of the spectator proton (main peak) plus some additional missing mass (flat broader peak) from $K^0\Sigma^0$ reactions. The spectator peak is positioned around 0.939 GeV, which agrees well with the PDG mass of a proton. The broad peak associated with $K^0\Sigma^0$ events arises from there being an undetected photon coming from the decay of the $\Sigma^0 \rightarrow \Lambda\gamma$. The decay photon has an energy of 77 MeV which is below the photon detection threshold in CLAS. The peaks are 77 MeV apart, which corresponds to the mass difference between a Λ hyperon and a Σ^0 hyperon. In order to determine where the cut between the hyperons should be placed, a further plot to examine the hyperon separation is shown in the bottom row of Figure 5.16. Here the MM($K^0\Lambda$) is plotted against the incident photon energy, where the separation of the two peaks can be seen more clearly. Combining information from the plots in Figure 5.16 justified a cut at 0.965 GeV/c^2 to separate the hyperons initially. Limits are placed on the hyperon ranges by performing a Gaussian fit to the spectator proton peak. A lower limit is chosen by taking a 3σ cut, which gives 0.894 GeV/c^2. There is a complication in defining an upper limit, as a Gaussian fit to the proton plus photon peak is unreliable, so a cut at 1.1 GeV/c^2 was placed, as it was felt this would incorporate all $K^0\Sigma^0$ events while minimising contamination from higher mass excited states. These cuts are denoted by the vertical and horizontal lines on the plots.

With a satisfactory separation of the hyperons, the next stage involves taking a projection onto the y-axis of the top plot in Figure 5.16. This axis shows the K^0 missing mass as if it were detected inclusively from a free neutron target, hence showing the Λ and Σ^0 hyperon masses. Projecting everything between the first two vertical cuts and the last two vertical cuts, gives the reconstructed missing mass distributions for each of the hyperons. These projections can be seen in Figure 5.17. By fitting the Σ^0 peak with a Gaussian one can take a $\pm 3\sigma$ cut around the peak, which will give the horizontal cuts that complete the box cut

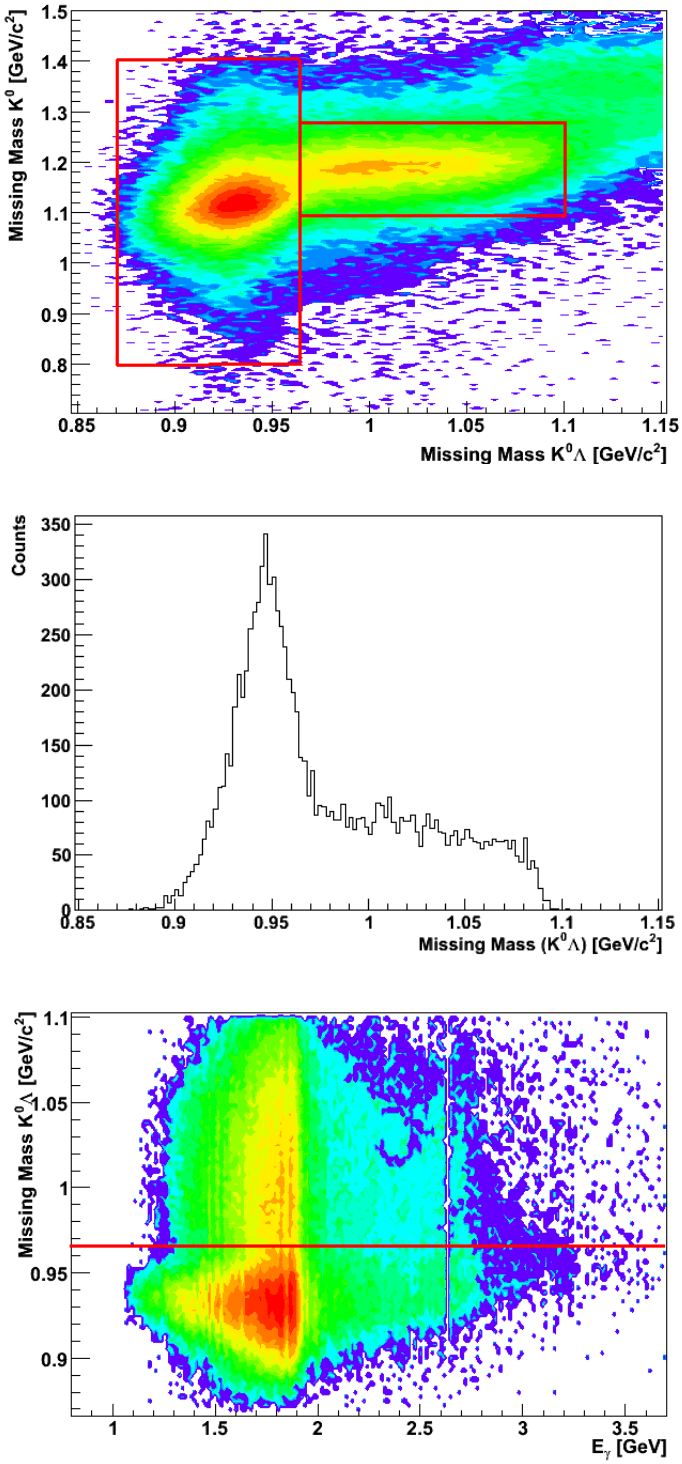

Figure 5.16: Hyperon separation where the x-axis is the MM($K^0\Lambda$) from the deuteron while the y-axis has MM(K^0) from a free neutron target (top). The lines indicate where cuts have been placed. A 1-D x-projection of the top plot showing the MM($K^0\Lambda$) (middle). MM($K^0\Lambda$) vs E_γ with line denoting where cut was placed (bottom).

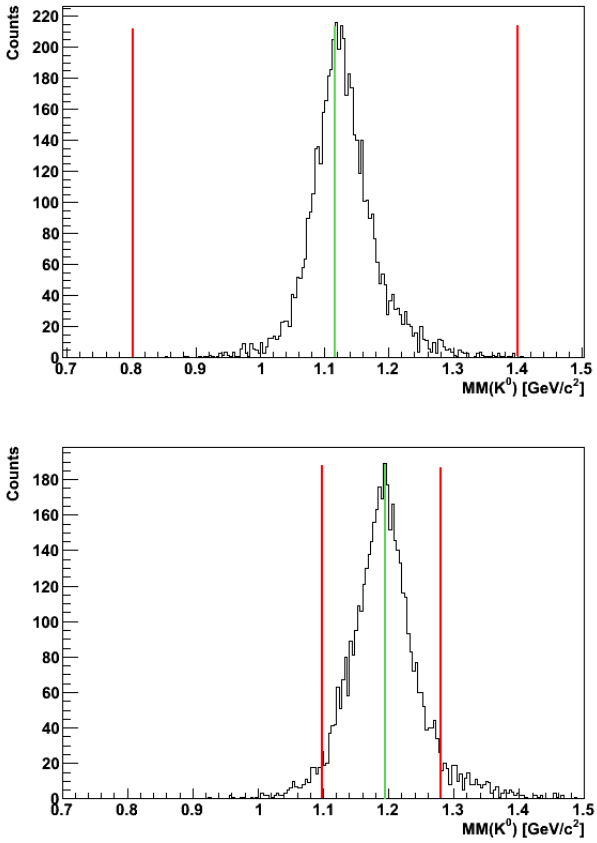

Figure 5.17: MM(K^0) in the range $0.87 < \mathrm{MM}(K^0\Lambda) < 0.965$ for Λ events (top). MM(K^0) in the range $0.965 < \mathrm{MM}(K^0\Lambda) < 1.1$ for Σ^0 events (bottom). Red lines in both plots indicate the cuts and the green lines indicate the PDG mass of the Λ and Σ^0.

around the Σ^0 hyperon. The same procedure can be applied to the Λ, however, a $\pm 3\sigma$ cut proves to be too narrow in this case and a wider 5σ cut has been implemented instead. Choosing too narrow a cut removes too much of the tails at either side of the peak and can affect the reliability of the fitting algorithm. A wider cut is required in the Λ case to account for the combined widths of each hyperon. Also, later in the analysis, the Λ peak will be fitted with a more appropriate function to extract yield and contamination information.

Spectator Momentum Cut

A cut on the spectator proton momentum is required to access the subset of quasi-free events in the data. A study on the bound proton [99] compared final photon asymmetry results with those on the free proton. It was found that with a cut of 200 MeV/c on the spectator momentum, the results overlapped well indicating that final state interactions were negligible. It was decided to

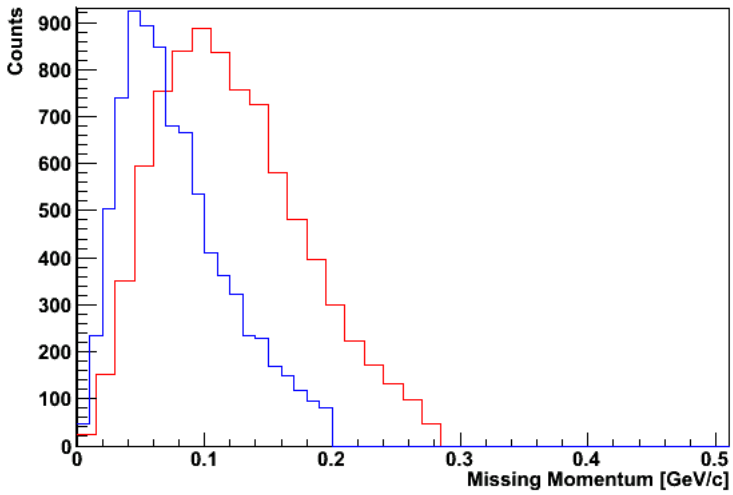

Figure 5.18: Missing momentum of spectator proton for Λ events (blue) cut at 200 MeV/c and for Σ^0 events (red) cut at 277 MeV/c.

place the cut at 200 MeV/c for $K^0\Lambda$ events and 277 MeV/c for $K^0\Sigma^0$ events from studying the distribution of spectator momentum against spectator proton angular distribution, plotted in Figure 5.6. Figure 5.18 shows the momentum distribution for the proton for each of the hyperons.

Hyperon Yield Extraction

Extracting the hyperon yields is the last stage in the event selection process. The yields were extracted after kaon identification and all other PID cuts. It is clear from the top plot of Figure 5.16 that there is a significant contribution from the Σ^0 under the Λ peak since it is broader due to the smearing from the undetected $\gamma's$. Conversely, the Λ resonance contributes negligibly to that of the Σ^0 and is thus not a problem. To be able to account for this contamination effect, the y-projections of the Λ are fitted with a Voigtian function (Breit-Wigner convoluted with a Gaussian) in a way that the overall Voigtian function fits the distribution by summing to smaller Voigtian functions that should describe the individual hyperon resonance contributions. A Voigtian function was used because the Breit-Wigner part best describes the shape of a resonance and the Gaussian part takes into account the detector resolution. Each Voigtian function has four parameters; the resonance width; the Gaussian width; the peak position and the height scaling factor. These parameters could be fixed or allowed to vary within some tight constraints. The resonance and Gaussian widths were allowed to vary very slightly in the first instance to get some nominal values. The values

Table 5.3: Table of all major analysis cuts.

Applied cut	Details of cut
Raw events skimmed	4 charged particles with associated masses
Identify $K^0\Lambda/\Sigma^0$ reaction	4 charged particles must be a π^+,π^-,π^-, p
Detected P_{proton}	$>$ 300 MeV/c
$\gamma - hadron$ vertex	$\pm 3\sigma$
MM(p,π,π,π) & $P_{spectator}$	-3σ, $+5\sigma$ and $<$ 300 MeV/c
Invariant Mass K^0/Λ	$\pm 3\sigma$
Fiducial	$\pm 5^0$ around fiducial region
$P^{K^0\Lambda}_{spectator}$	$<$ 200 MeV/c
$P^{K^0\Sigma^0}_{spectator}$	$<$ 277 MeV/c
Λ/Σ^0 separation	based mainly on Gaussian fit $\pm 3\sigma$

provide the tight constraints that the fit may vary around the nominal values. This ensured that any detector resolution or smearing effects can be accounted for in the final distributions. The peak positions were also tightly constrained, however the condition that the hyperon masses had to be 77 MeV apart was always fulfilled. The height scale factor was allowed to roam over a wider range than the other parameters. The same procedure is also done for the Σ^0 state. These two Voigtian functions are then summed to fit the y-projection of the Λ/Σ^0 admixture, which in turn gives the amount of Σ^0 events which lie below the Λ event peak. The distributions were fitted in each of the six angular bins per coherent peak setting, hence allowing one to determine the contribution to the measured Λ asymmetry from the Λ and Σ^0 events. Once this is known a true value for the Λ asymmetry can be obtained. An example of this fitting routine is shown in Figure 5.19.

The fitting routine was the final step before extracting the beam asymmetry for each of the hyperon channels. A summary of all analysis cuts is shown in Table 5.3.

5.2 Extraction of Σ

The extraction of Σ can be done now that the event selection process has identified the reactions γn $\rightarrow K^0\Lambda$ and γn $\rightarrow K^0\Sigma^0$ within CLAS. This section will discuss the methods used to extract the photon asymmetry from the data set. The results will be extracted for as wide a E_γ and $\cos\theta^{K^0}_{cm}$ range as the statistics allow and the final choice of bin width will be discussed. The methods used to determine the degree of photon polarization and the estimation of the systematic uncertainty associated with this measurement are also discussed in this section.

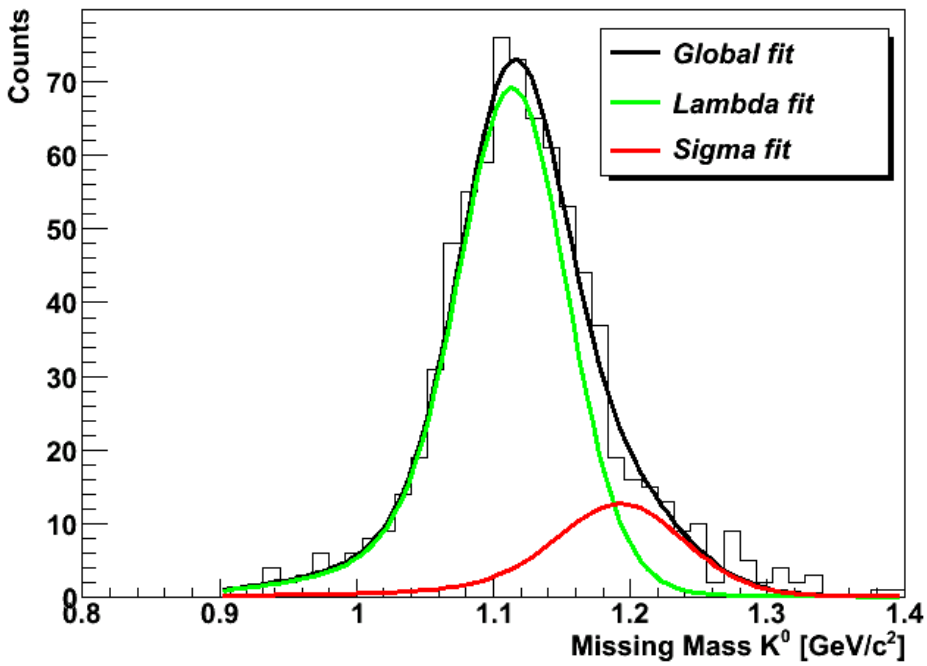

Figure 5.19: Voigtian fitting routine for one angular bin to extract Λ and Σ^0 yields for Λ beam asymmetry correction.

The coordinate systems and kinematics of the reactions are illustrated in Figures 8 and 9 in chapter 2. The unprimed coordinate system[1], where the z-axis is taken to be along the momentum direction of the incident photon beam, was chosen to present the photon asymmetry results in. This allows for consistency and comparison with previous work which has indicated that most of the hyperon polarization is preferentially transferred along $\hat{z}$, hence the reason this system was chosen.

Kinematic Bin Selection

The bin widths for each kinematic variable used in the measurement of Σ were chosen to maximise the information extracted as a function of both E_γ and cos $\theta^{K^0}_{CM}$. The logical choice would be to have an equal number of bins for each variable, however a complication arises when binning in E_γ as there are different discrete energy settings for the coherent edge. Both the luminosity and degree of photon polarization decrease rapidly when one moves away in energy from the coherent edge. Due to the limited statistics in this analysis, it was decided that

[1] A transformation between the unprimed and primed coordinate systems can be done using the standard rotation matrix $O_x = O_{x'}\cos\theta$ - $O_{z'}\sin\theta$, $O_z = -O_{x'}\sin\theta + O_{z'}\cos\theta$.

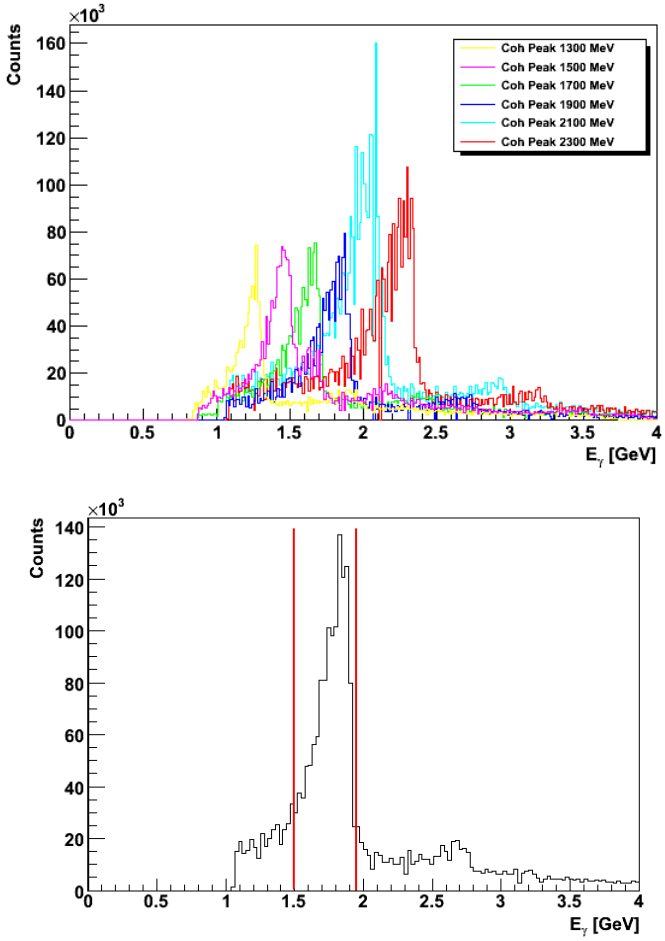

Figure 5.20: Photon energy distributions from all six coherent peak positions (top). This demonstrates the overlap in photon energy between settings. Photon energy bin superimposed on the 1.9 GeV coherent energy spectrum (bottom).

one large E_γ bin of 450 MeV width, which covers the region of highest photon polarization would be needed per coherent peak setting. An illustration of this bin selection is shown in the bottom plot of Figure 5.20 for the 1.9 GeV coherent peak position.

Six different coherent peak settings were used during the experiment, each separated by 200 MeV. The six coherent peak distributions are shown in the top plot of Figure 5.20. This resulted in six overlapping E_γ bins in total covering a continuous range in photon energy. To compliment this, six bins in $\cos(\theta_{cm}^{K^0})$ were chosen as shown in the top plot of Figure 5.21, ranging from -0.8 to +0.98. The majority of events detected in CLAS are forward angled which results in lower statistics at the backward angles. In order to best minimise the statistical uncertainty and accounting for the low statistics, the six non-uniform bins should contain an equal number of counts. The bin size was selected based on an having

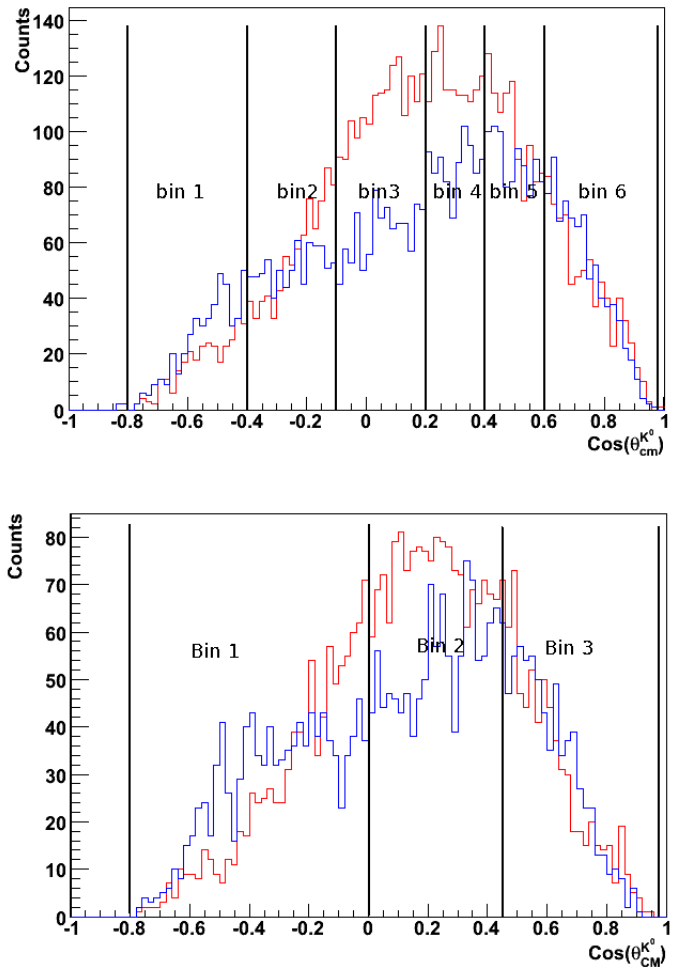

Figure 5.21: Top plot shows the non-uniform angular bins for photon asymmetry and recoil polarization extraction, superimposed on the $\cos(\theta^{K^0}_{cm})$ spectrum. Red distribution is for $K^0\Sigma^0$ events and the blue distribution for $K^0\Lambda$ events. Bottom plot shows non-uniform angular bins for O_x, O_z and Target extraction, superimposed on the $\cos(\theta^{K^0}_{cm})$ spectrum.

an approximate equal number of statistics in each bin balanced with good angular coverage. In total, there are 36 kinematic bins for which the photon asymmetry Σ was measured.

The Photon Beam Asymmetry Σ

The extraction of the photon asymmetry, along with the double polarization observables requires a measurement of the x and z-components of the hadron polarization. Details of their derivation can be found in chapter 1, equations 1.21 to 1.23. The photon beam had two polarization settings, offset by 90 degrees and producing almost equal statistics. The easiest way to extract Σ and the double polarization observables is to construct an asymmetry, A, as a function of θ and Φ as shown in equation 5.4. Using this method has the advantage that the CLAS detectors acceptance is independent of the initial photon polarization state. This means any acceptance effects will cancel out and removes the need to do an acceptance calculation to extract the observables which may potentially result in a large systematic uncertainty. There is one instance where the acceptance would not cancel, when their is a difference in the track reconstruction efficiency due to differences in the beam intensity between the two photon polarization states. This method depends on having identical running conditions for the parallel and perpendicular settings and flipping regularly between the two states, which was done during g13b.

$$A(\Phi, cos\theta_i) = \frac{N^{\parallel}(\theta_i, \Phi) - N^{\perp}(\theta_i, \Phi)}{N^{\parallel}(\theta_i, \Phi) + N^{\perp}(\theta_i, \Phi)} = -P_{\gamma}^{lin}\Sigma cos(2\Phi + \Phi_0) - \alpha\nu P_{\gamma}^{lin} O_i sin2\Phi cos\theta_i \tag{5.4}$$

The photon beam asymmetry, Σ can be measured by applying a two dimensional fit of the functional form of equation 5.4 to the asymmetry over θ and Φ. However, by integrating over all kaon polar angles θ one can derive a one dimensional asymmetry as a function of Φ only.

$$A(\Phi) = \frac{N^{\parallel}(\Phi) - N^{\perp}(\Phi)}{N^{\parallel}(\Phi) + N^{\perp}(\Phi)} = P_{\gamma}^{lin}\Sigma cos(2\Phi + \Phi_0) \tag{5.5}$$

The asymmetry is measured for all kinematic bins in E_{γ} and $\cos\theta_{CM}^{K^0}$. By performing a fit of the form of equation 5.5 over each distribution, the photon asymmetry can be extracted. The Φ_0 parameter accounts for any phase shift in the cos2Φ distribution. This was measured to be zero from higher statistics data [100] and was fixed in this analysis. The g13b parallel and perpendicular

data sets do not in general have the same number of events or mean polarization. This is a complication but can be accounted for by scaling the differences in yield and polarization. Scaling is done by taking weighted means of the yields and polarizations for each configuration. Equation 5.5 is then modified to become:

$$A(\Phi) = \frac{N^{||}(\Phi) - N^{\perp}(\Phi)}{N^{||}(\Phi) + N^{\perp}(\Phi)} = \frac{P^{||} - P^{\perp}}{P^{||} + P^{\perp}} + \frac{2P^{||}P^{\perp}}{P^{||} + P^{\perp}}\Sigma cos2(\Phi + \Phi_0) \tag{5.6}$$

where $P^{||}$ and $P^{\perp}$ are the mean polarizations for the parallel and perpendicular photon polarization settings.

The photon beam asymmetry Σ was extracted by fitting the function from equation 5.5 to each Φ distribution on a bin by bin basis. The Φ distributions for the parallel and perpendicular data sets can be seen in Figure 5.22. They are integrated over all $\cos\theta_{cm}^{K^0}$ angles. The bottom plot in Figure 5.22 shows the asymmetry of the two polarized data sets with statistical error bars. This clearly shows the powerful nature of the asymmetry technique in removing any acceptance effects, and providing a clean $\cos 2\Phi$ distribution.

Figures 5.23 and 5.24 demonstrate the fits to the kaon Φ distributions for one E_γ and one $cos\theta_{cm}^{K^0}$ bin for the $K^0\Lambda$ and $K^0\Sigma^0$ channels respectively. The reliability of the fits can be inspected by looking at the χ^2 per degree of freedom for each fit, which are shown in Figure 5.28.

Obtaining a clean beam asymmetry from the $\vec{\gamma}d \rightarrow K^0\Sigma^0(p)$ channel is the first step as this is an undiluted, reliable measurement. When extracting the beam asymmetry from the $\vec{\gamma}d \rightarrow K^0\Lambda(p)$ channel, there is the added complication of the contribution from the Σ^0 beam asymmetry to account for before a reliable measurement for the Λ can be obtained. In Figure 5.25 the uncorrected photon asymmetries are plotted against the corrected values. This is where a correction is made to account for the dilution from the Σ^0 as described previously.

The dilution corrected photon asymmetry for the $K^0\Lambda$ channel is then plotted as a function of $\cos\theta_{cm}^{K^0}$ in Figure 5.26. The photon asymmetry for the $K^0\Sigma^0$ channel is shown in Figure 5.27.

5.3 Extraction of Recoil Polarization

In order to extract the hyperon recoil polarization, a measurement of the y-component of the hadron polarization must be made. The y-component is defined as:

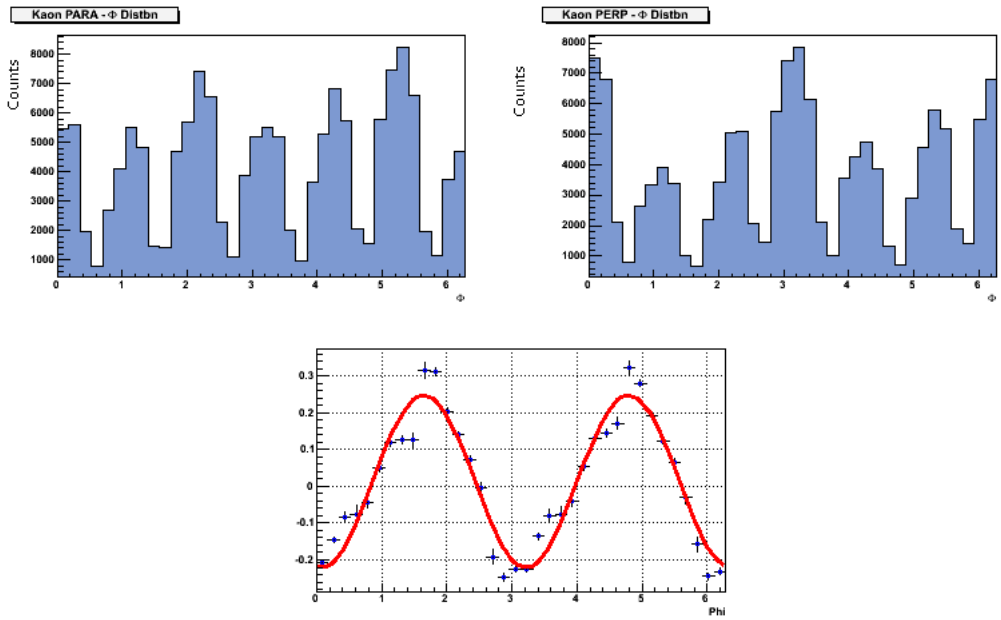

Figure 5.22: Top left: ϕ-yield of kaons for the parallel polarization setting integrated over the full angular range. Top right: ϕ-yield of kaons for the perpendicular polarization setting integrated over the full angular range. In both the parallel and perpendicular ϕ distributions, the regions of low acceptance correspond to the locations of the torus magnetic coils and are evident in the distributions. These regions are cut out with fiducial cuts as the statistics are low and unreliable. Bottom: Asymmetry of the two polarization settings with a cos2ϕ fit. This removes any acceptance issues since the detector acceptance e is independent of the photon polarization state.

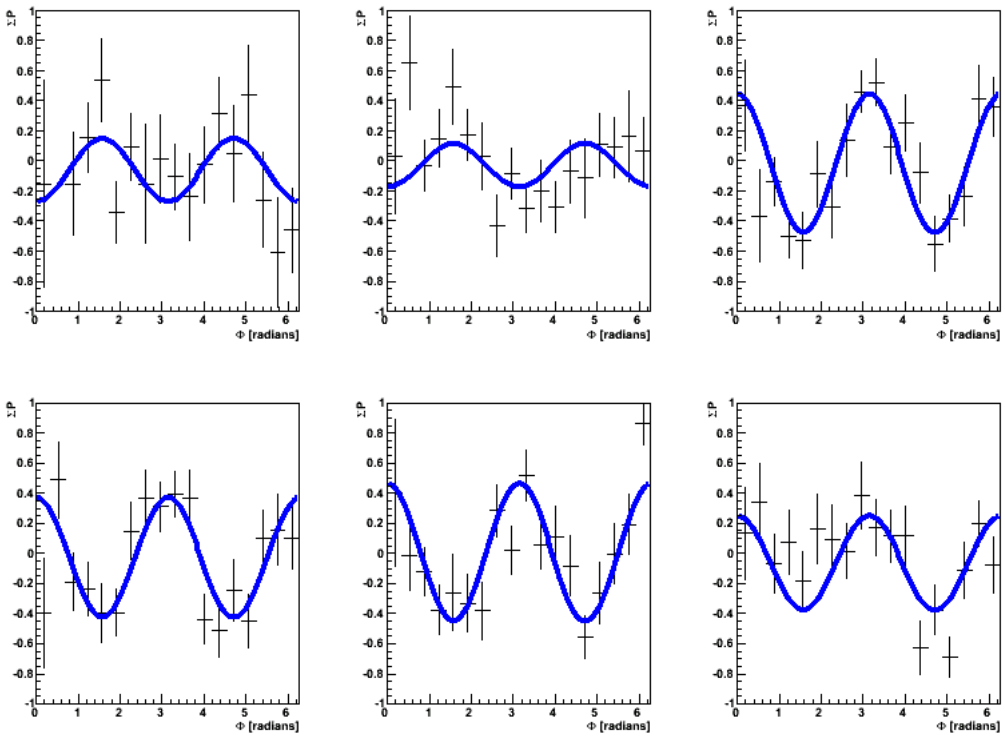

Figure 5.23: Cos2Φ fits of the $K^0\Lambda$ beam asymmetry for E_γ= 1.9 GeV. The histograms proceed from $\cos(\theta_{cm}^{K^0})$ = -0.6 in the upper left to $\cos(\theta_{cm}^{K^0})$ = 0.76 in the bottom right.

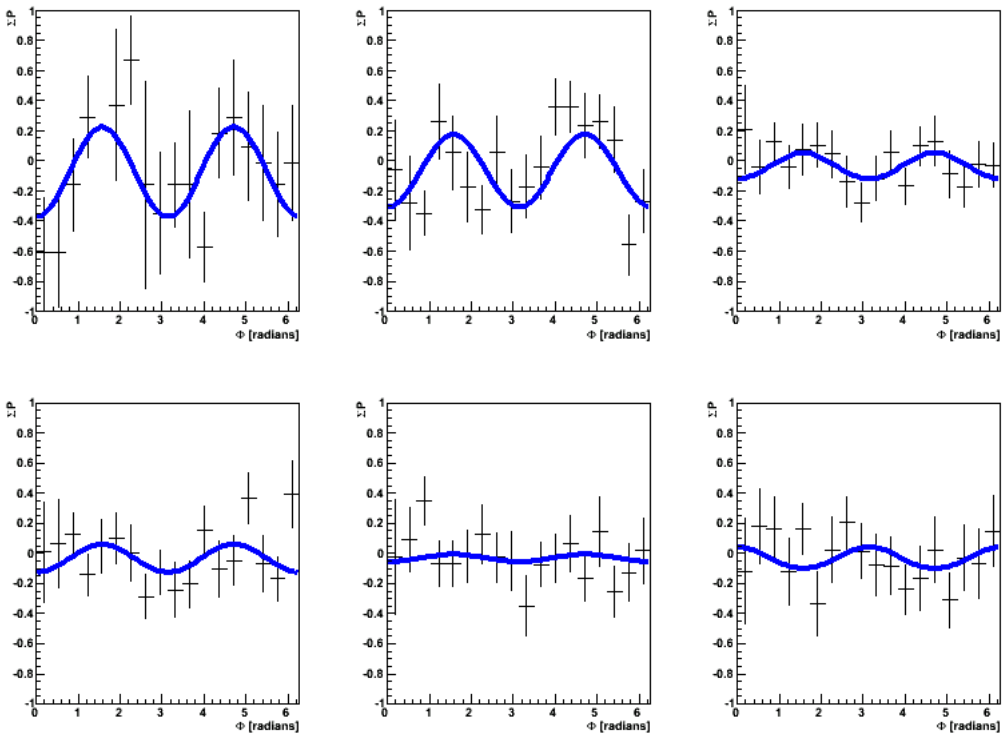

Figure 5.24: Cos2Φ fits of the $K^0\Sigma^0$ beam asymmetry for E_γ= 1.9 GeV. The histograms proceed from $\cos(\theta_{cm}^{K^0})$ = -0.6 in the upper left to $\cos(\theta_{cm}^{K^0})$ = 0.76 in the bottom right.

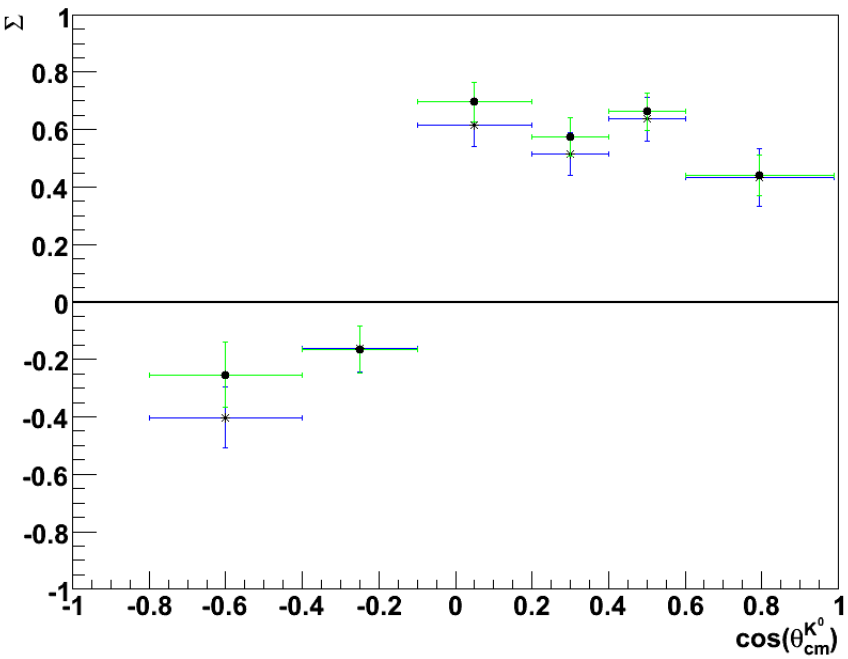

Figure 5.25: Photon asymmetry as a function of $\cos(\theta^{K^0}_{cm})$ at E_γ=1.9 GeV for the $K^0\Lambda$ channel. Uncorrected values are plotted in blue and corrected values are shown in green. All error bars are statistical and no systematic uncertainties are considered at this stage.

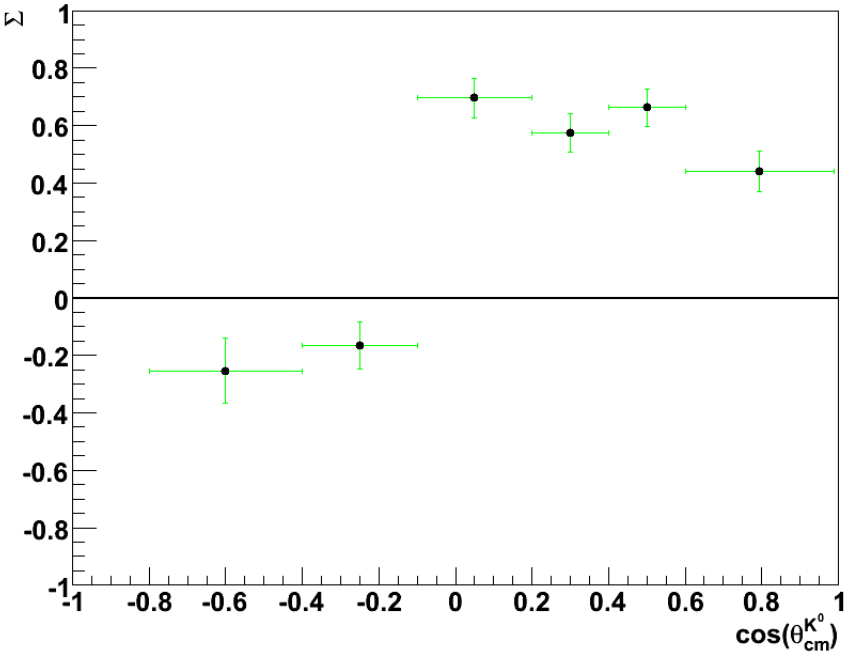

Figure 5.26: Photon asymmetry for the $K^0\Lambda$ channel as a function of $\cos\theta^{K^0}_{cm}$ for E_γ= 1.9 GeV. All error bars are statistical and no systematic uncertainties are considered at this stage.

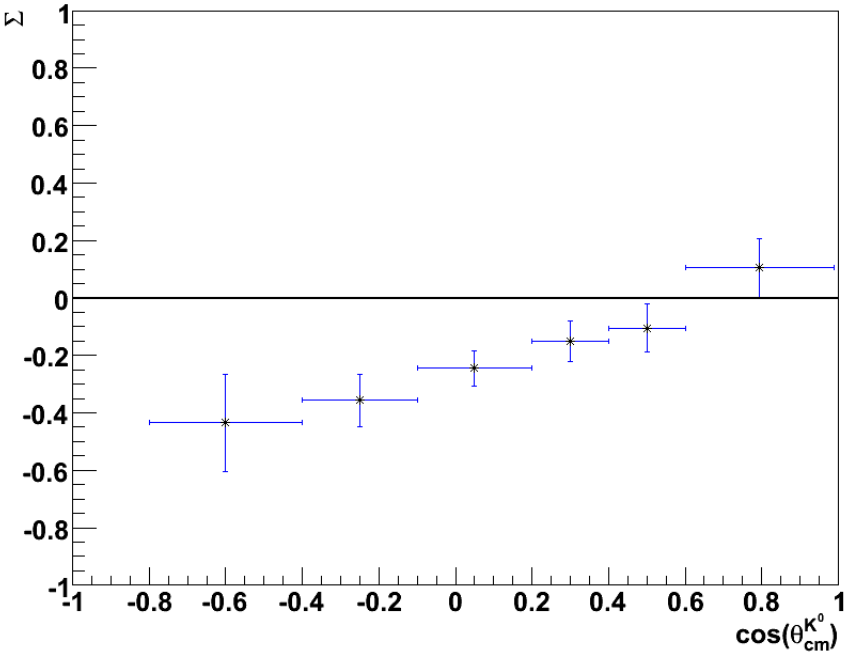

Figure 5.27: Photon asymmetry for the $K^0\Sigma^0$ channel as a function of $\cos\theta^{K^0}_{cm}$ for E_γ= 1.9 GeV. All error bars are statistical and no systematic uncertainties are considered at this stage.

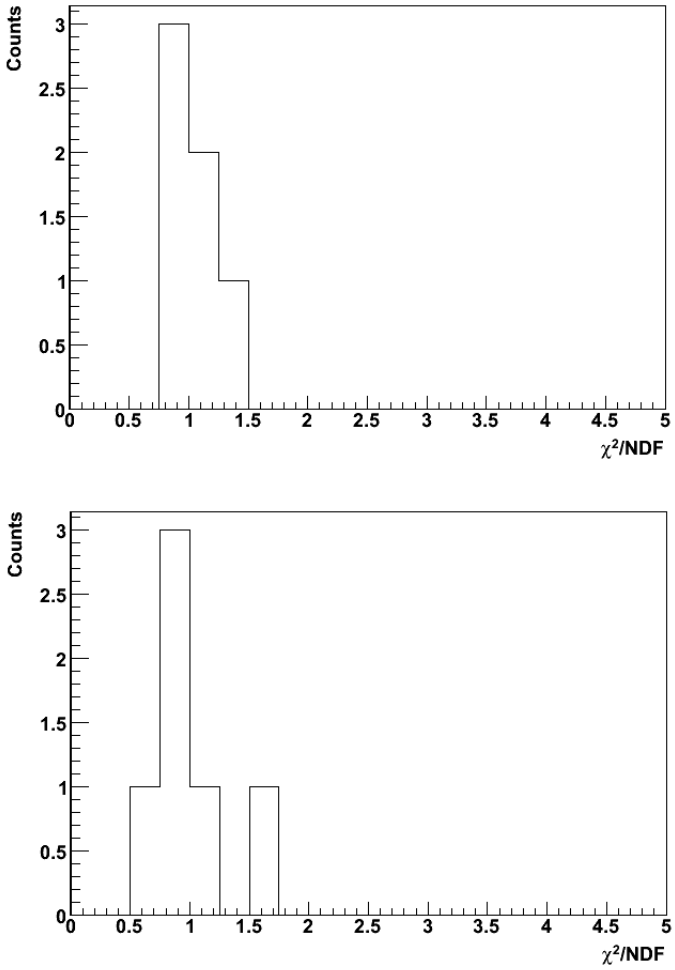

Figure 5.28: χ^2 values per degree of freedom for the $K^0\Lambda$ (top) and $K^0\Sigma^0$ (bottom) channels. These values are from fits for all beam asymmetry measurements over the full kinematic range.

$$P_y = -\frac{P - P_\gamma^{lin} T cos2\phi}{1 - P_\gamma^{lin} \Sigma cos2\phi} \tag{5.7}$$

where P_γ^{lin} is the degree of linear polarization, T is the target polarization, and ϕ is the kaon azimuthal angle. The same procedure that was used for the x and z-components of the polarization can be applied to the relation above to give the asymmetry in equation 5.8:

$$A(\Phi_i, cos\theta_y) = \frac{N^{||} - N^{\perp}}{N^{||} + N^{\perp}} = \frac{-P_\gamma^{lin} \Sigma cos(2\Phi) - \alpha P_\gamma^{lin} T cos(2\Phi) cos(\theta_y)}{1 + \alpha P cos(\theta_y)} \tag{5.8}$$

where P is the hyperon recoil polarization, T is the target asymmetry and the other variables are as defined previously. It is therefore possible to extract P and T from a two dimensional fit over Φ and θ_y. However, limited statistics meant that the two dimensional fit to this distribution was not stable when P was allowed to be a free parameter in the fit. The recoil polarization, P was therefore measured independently before fixing it in the two dimensional fit to allow for the extraction of the target asymmetry, T. Using an asymmetry technique to measure P is not possible, so a full detector simulation was necessary to provide an acceptance correction of the decay proton's angular distribution.

5.3.1 Detector Simulation

The CLAS acceptance must be measured in order to extract the hyperon recoil polarization. This requires the generation of events that can be passed through the detector simulation and are then reconstructed and analysed using the same analysis algorithm as the real data. Events from the reactions $K^0\Lambda$ and $K^0\Sigma$ must first be generated and decayed as they are in reality. These generated events are then passed through the CLAS detector simulation GSIM which is a GEANT3 [101] based simulation. They are then time smeared before being reconstructed and analysed. The flow chart in Figure 5.29 displays the full simulation process.

5.3.2 Phase Space Event Generator

The first stage in the simulation process is to generate 36 million $K^0\Lambda$ and $K^0\Sigma^0$ events, with 6 million for each coherent peak position. Since no reliable event generator packages existed for these reactions, one was written [102] which would include the input of spin observables. Events were generated pseudo-randomly

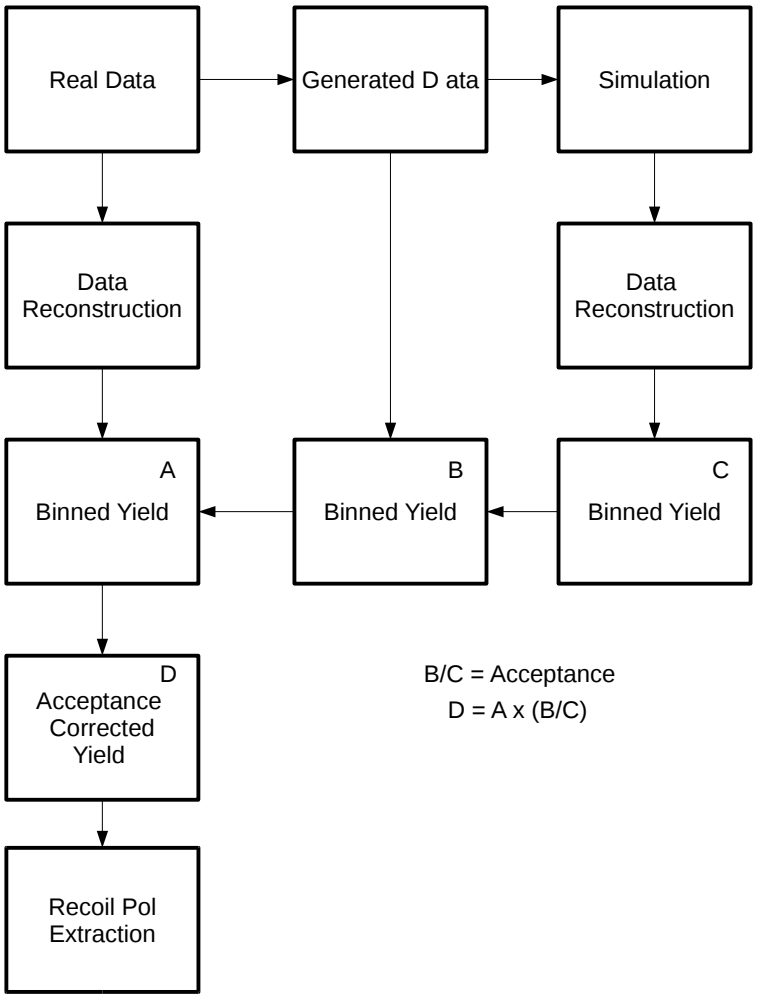

Figure 5.29: Flow chart displaying the steps used for the analysis and simulation that are needed to extract the hyperon recoil polarization.

with a flat 4-body phase space. The generator allowed the input of values for six spin observables, namely: the beam polarization, the photon beam asymmetry, recoil polarization, target polarization and the two double spin transfer observables. A realistic linear photon beam spectrum was also included, where the generator sampled from a histogram containing real data. This meant that the generated Monte Carlo data had the same characteristic coherent peak structure for the photon energy spectrum as the real data.

5.3.3 GSIM and GPP

An accurate simulation of the CLAS detector is provided by using the GSIM software package. Particles from a generated event are propagated through the simulated detector hence producing hits in the various detector subsystems. GSIM calculates the effects of particle decays, multiple-scattering and secondary interactions as the particles pass through the detector.

GSIM however, only produces events with perfect timing resolution for each detector subsystem, which does not give a realistic representation of the real detector resolution. Therefore, after each event is simulated it has to be passed through a program called GPP [103], which smears the timing output of the Time of Flight scintillator paddles and drift chambers to give a more realistic representation of the true CLAS timing resolution. The smearing is achieved by adding a pseudo-random time from a Gaussian distribution to the timing resolution of each subsystem. The GPP package also removes dead drift chamber cells to allow for the rejection of charged particle tracks where the trajectory passes through a known hole in the drift chamber. The accuracy of the simulation can be tested by comparing angular distributions from simulated events to those from the data. Figure 5.30 displays the comparison of the ϕ distributions for the four detected charged particles, where blue indicates the data and red for the simulation. Figure 5.31 shows the θ distributions for the data and simulated events. The data and simulated distributions agree well which demonstrates a good detector simulation and gives us faith that the acceptance calculation will be very accurate.

5.3.4 Measuring Detector Acceptance

The detector acceptance for the reactions $\gamma d \rightarrow K^0\Lambda(p)$ and $\gamma d \rightarrow K^0\Sigma^0(p)$ can be calculated from the ratio of simulated accepted events to thrown (generated) events. Extracting the hyperon recoil polarization requires the acceptance of the

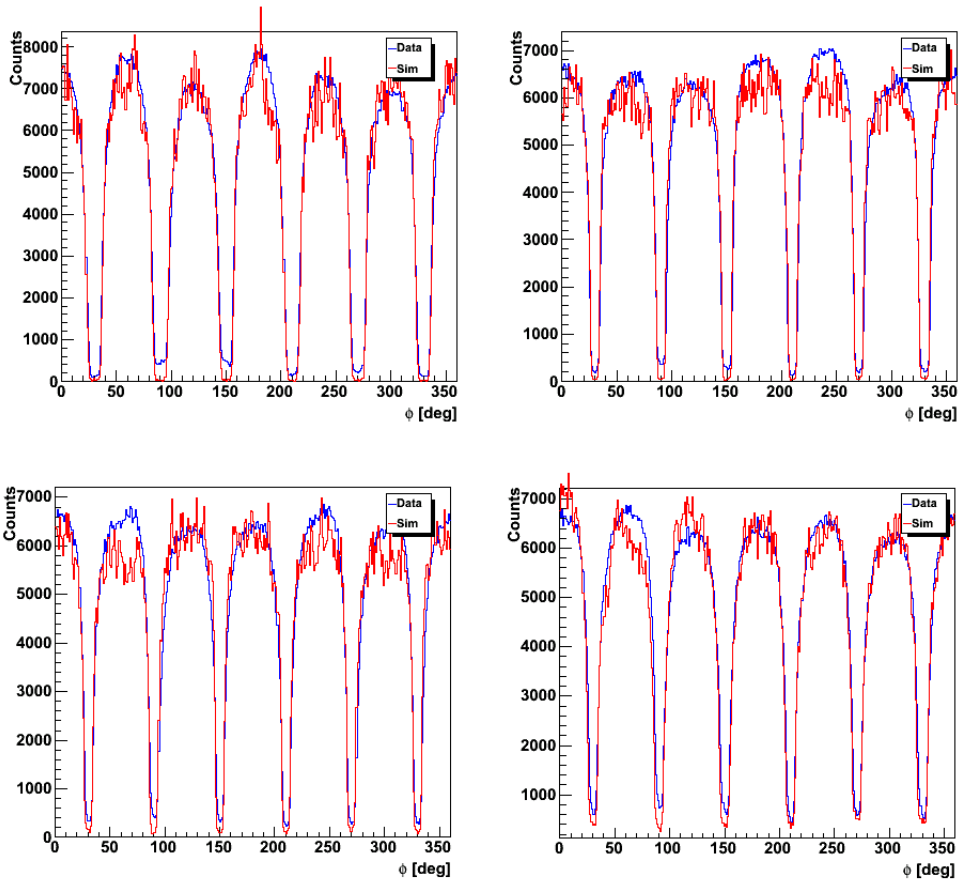

Figure 5.30: ϕ distributions from real data (blue) and simulation (red) for the proton (top left), π^+ (top right), π_1^- (bottom left) and π_2^- (bottom right).

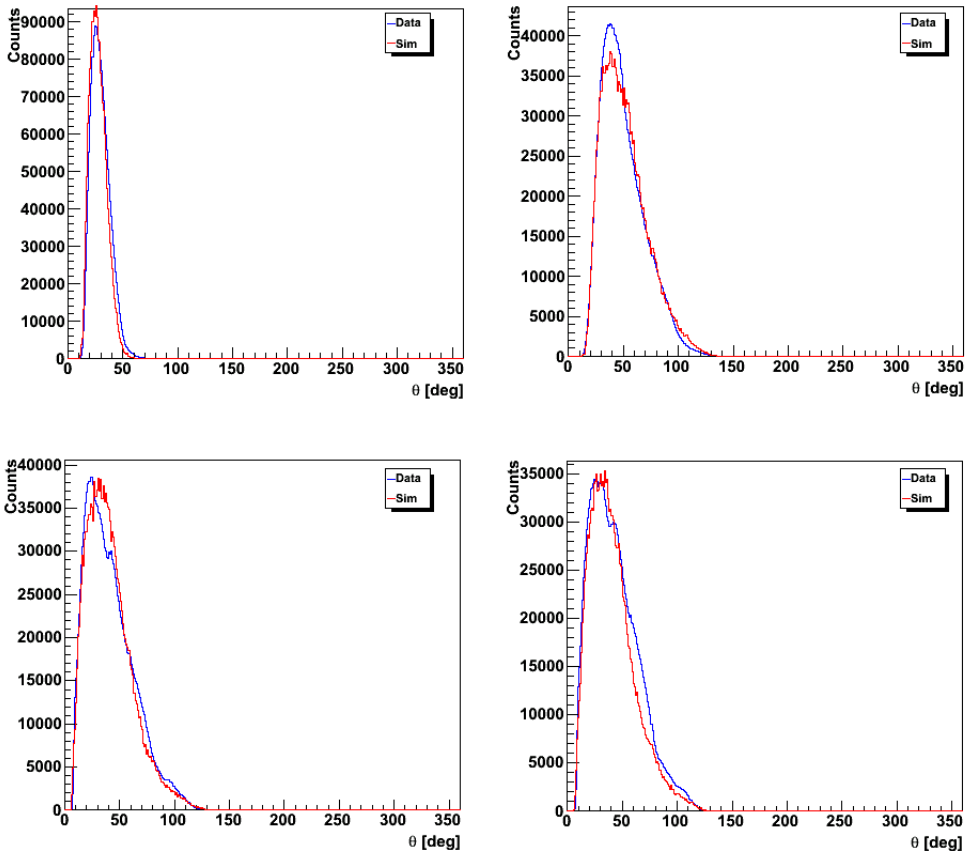

Figure 5.31: θ distributions from real data (blue) and simulation (red) for the proton (top left), π^+ (top right), π_1^- (bottom left) and π_2^- (bottom right)

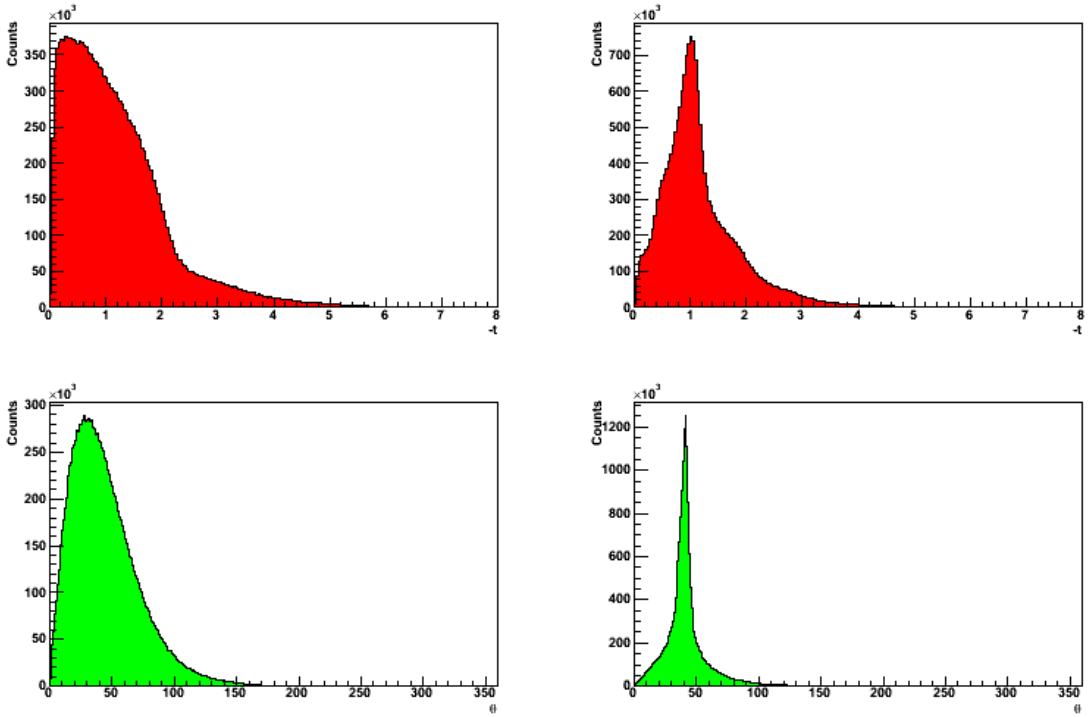

Figure 5.32: t-distributions for the generated events are shown on the top line for the original flat phase space (left) and for the modified phase space (right). The corresponding θ distributions are shown on the bottom line for the original phase space (left) and modified phase space (right).

proton angular decay distribution θ_y to be corrected. This acceptance was studied as a function of the kaon polar angle $\cos(\theta_{cm}^{K^0})$ and was measured over the full photon energy range of g13b. The same analysis cuts that were used for the real data (as described in Chapter 5) were used to determine the accepted events from the simulation.

Possible systematic uncertainties in the simulation were studied by generating events with different kinematic distributions. By changing the $\cos\theta$ distribution from flat phase space to various raised powers one could study the effect this had on the final acceptance. The final modified phase space was chosen to be $\cos^2\theta$. Modifying the θ distribution would cause a change in the t-dependence (four momentum transfer) of the proton. The results of this modification are shown in Figure 5.32.

The acceptance was corrected for both $\cos\theta_y$ and $\cos K_{cm}^0$ simultaneously in a two dimensional histogram. The acceptance corrected yield as a function of $\cos\theta_y$ was then projected out of the histogram. Figure 5.33 displays the results for the two generated distributions. When the acceptance is corrected as a function of

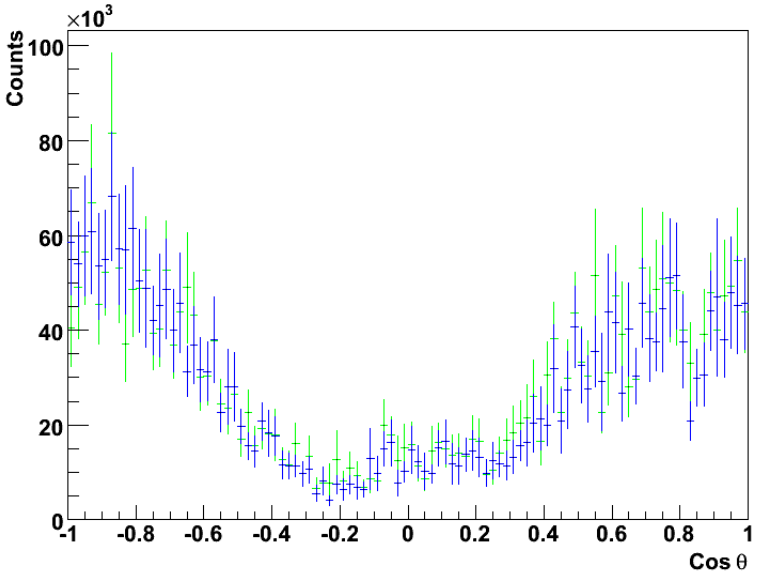

Figure 5.33: Plot showing the effect of correcting the acceptance as a function of both cosθ_y and cos$\theta_{cm}^{K^0}$ simultaneously on the final proton yield for the original flat phase space and the modified phase space. This shows the two distributions on the same plot (blue lines indicate flat phase space and green lines modified phase space).

its dependent variables simultaneously, the final corrected yields are the same regardless of the kinematics of the generated events.

Several different generated data sets each with different kinematic distributions were studied and it was found that the final corrected yields were always the same. This shows that for the reactions studied in this analysis, unfolding the detector acceptance is independent of the initial kinematic distributions. The final acceptance corrected proton yields could now be used to extract the hyperon recoil polarization.

5.3.5 Hyperon Recoil Polarization

The polarization of a recoiling hyperon can be measured through its parity-violating weak decay to a proton and a pion, as discussed in chapter one. This is measured in the hyperon rest frame, where its decay is preferentially orientated in the direction of its polarization. The polarization can be related to the decay proton angular distribution, I$_i$(cosθ_i) through equation 5.9.

$$I_i(cos\theta_i) = \frac{1}{2}(1 + \nu\alpha P_{Y_i} cos\theta_i) \tag{5.9}$$

where i ϵ\{x,y,z\} is one of the three axes in the specified unprimed coordinate

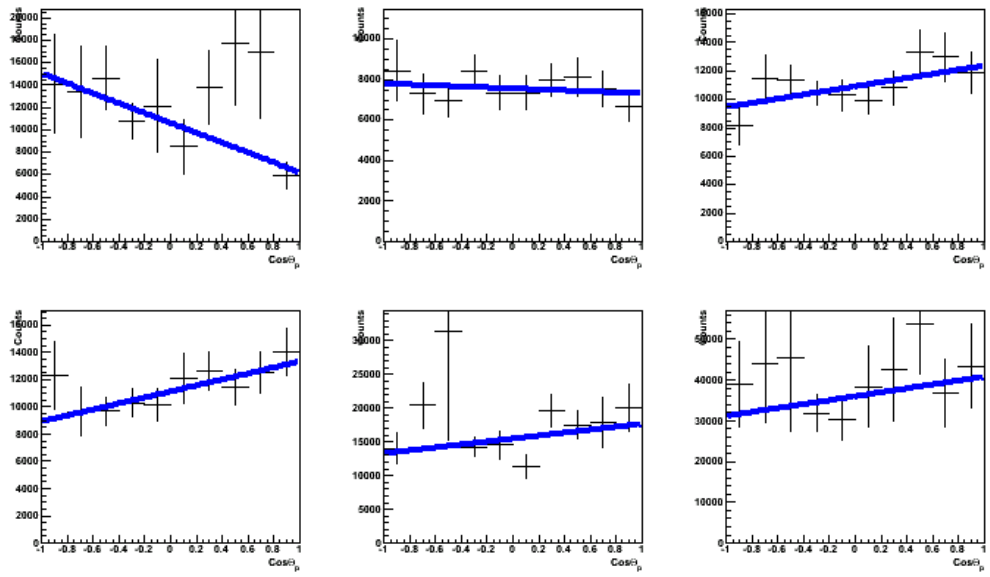

Figure 5.34: Linear fits of the acceptance corrected proton yield $\theta^{P}_{\Lambda_{RF}}$ for E_{γ}= 1.675 GeV. The range in angle is from $\cos(\theta^{K^0}_{cm})$ = -0.8 in the upper left to $\cos(\theta^{K^0}_{cm})$ = 0.9 in the bottom right.

system. Defining θ_i to be the polar angle between the proton and the corresponding axis in the hyperon rest frame and α is the weak decay asymmetry with a well established value of 0.642 $\pm$ 0.013 [18]. The ν term results from the dilution of the self analyzing power in the Σ^0 case, where its decay to a Λ and a photon gives a ν value of $-\frac{1}{3}$. This is effectively saying that the Λ preserves $-\frac{1}{3}$ of the Σ^0 original polarization [21]. In the $K^0\Lambda$ case ν is equal to $+1$. The dilution of the Σ^0 polarization means that the uncertainties in its measurement will be approximately three times larger than they are for the Λ.

The recoil polarization results are presented with an angular bin range similar to the photon asymmetry but with a smaller photon energy bin size of 125 MeV. The recoil polarization is independent of the initial photon polarization state, giving an approximate increase of a factor of two in statistics which allowed for the finer binning in energy. The linear fits of the proton angular distribution for one E_{γ} bin and the full $\cos(\theta^{K^0}_{cm})$ range are shown in Figure 5.34. The recoil polarization as a function of $\cos(\theta^{K^0}_{cm})$ is displayed in Figure 5.35.

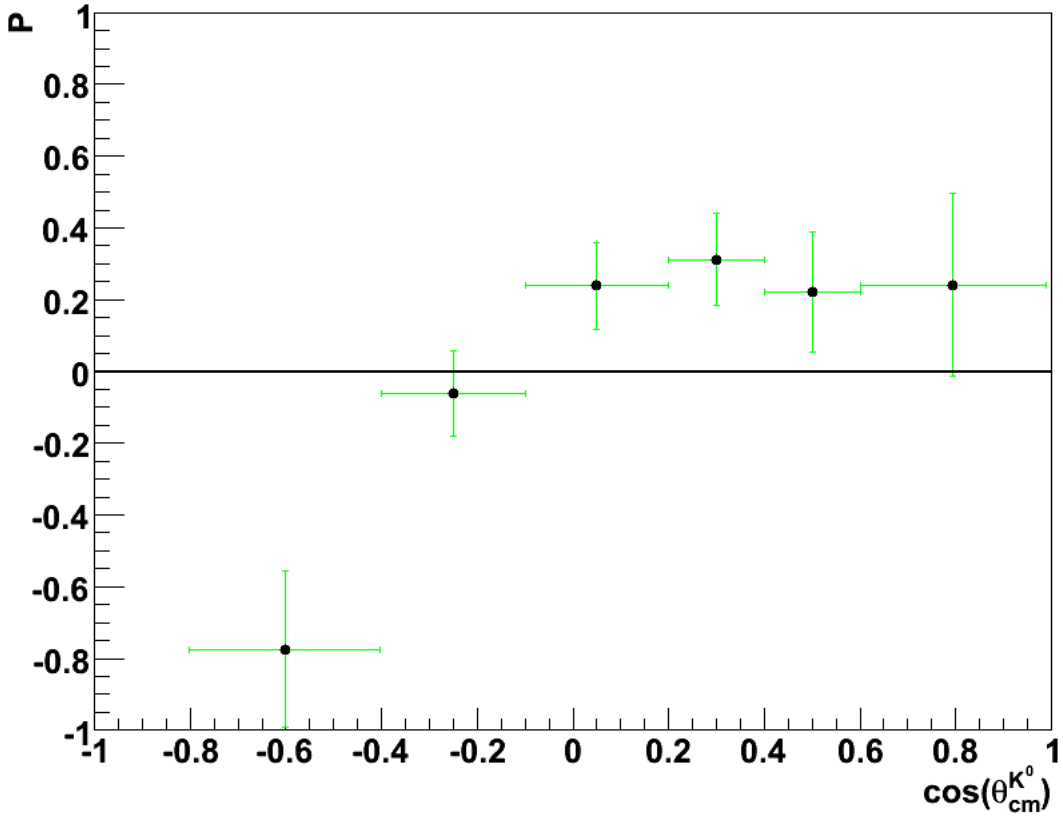

Figure 5.35: Recoil Λ polarization plotted as a function of $\cos(\theta_{cm}^{K^0})$ for the energy range $1.6 < E_\gamma < 1.75$ GeV. All error bars are statistical, systematic errors will be considered later.

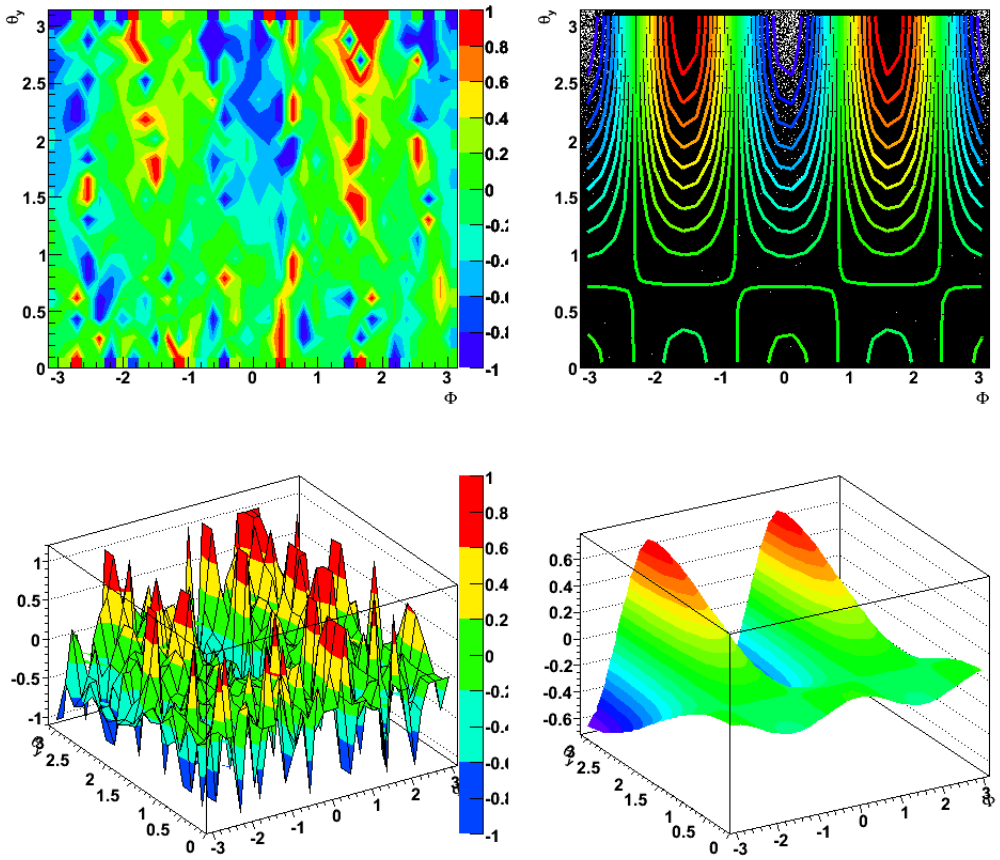

Figure 5.36: Two dimensional distribution over Φ and θ_y (top left) with the resultant two dimensional fit superimposed (top right). The two dimensional asymmetry distribution is then shown as a surf plot (bottom left) with the resultant fit (bottom right). These plots are for a photon energy of 1.8 GeV, integrated over the angular range $\cos(\theta^{K^0}_{CM})$ = -0.8 to 0.98.

5.4 Target Asymmetry

The target asymmetry, T can be extracted now that the hyperon recoil polarization, P is known. This is done by forming a two dimensional asymmetry of the form of equation 5.8. The statistics for the target polarization will be comparable to those for the double polarization observables, so the same bin sizes for E_γ and $\cos(\theta^{K^0}_{cm})$ are used to present the results.

The two dimensional fit for the $K^0\Lambda$ channel is plotted in Figure 5.36 for one E_γ and one $\cos(\theta^{K^0}_{cm})$ bin. The χ^2 values from the two dimensional fit, for all kinematics are displayed in Figure 5.37. The good values gives confidence in the overall stability of the extraction method.

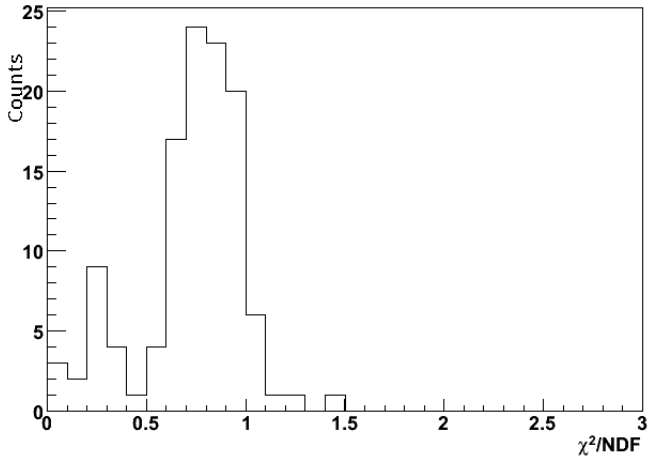

Figure 5.37: χ^2 values from the two dimensional fits used to extract the target asymmetry. These values are from fits over the full kinematic range.

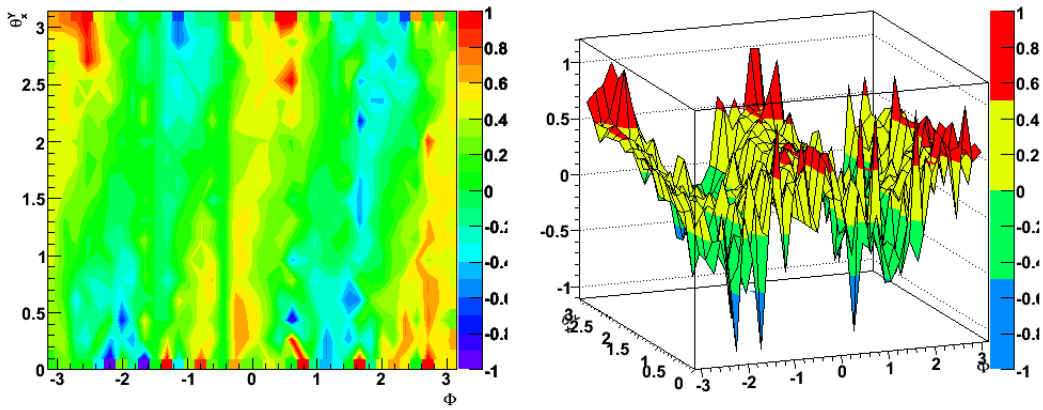

Figure 5.38: The 2-dimensional asymmetry over Φ and θ_i plotted for the x-component of the recoil polarization. These plots are for a photon energy of 1.9 GeV, integrated over the angular range $\cos(\theta_{cm}^{K^0}) = 0.4$ to 1.0.

5.5 Double Polarization Observables O_x and O_z

A 2-dimensional asymmetry over Φ and θ_i of the form of equation 5.4 is used to extract the double polarization observables. Some typical distributions are shown in Figure 5.38. The binning for O_x and O_z for both channels had to be reduced due to the decrease in statistics in the double polarization observables. Three angular bins, shown in the bottom plot of Figure 5.21 cover the range -0.8 to 0.98 in $\cos(\theta_{CM}^{K^0})$.

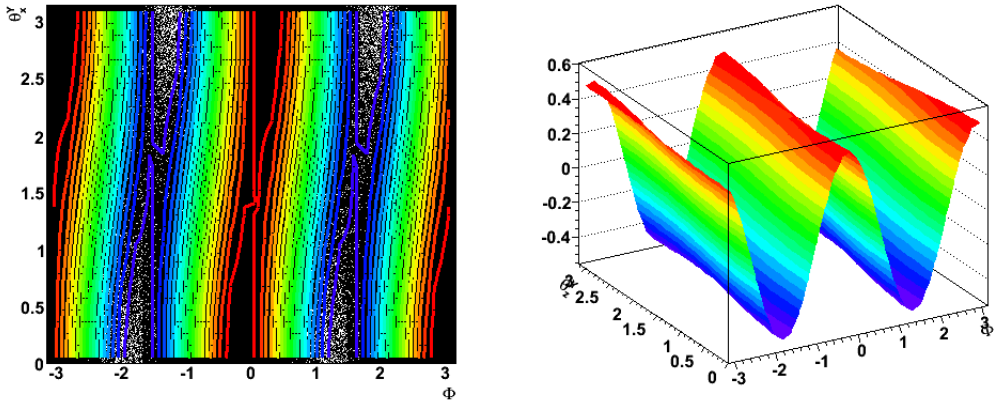

Figure 5.39: Example of the two dimensional fit for one E_γ and one $\cos(\theta^{K^0}_{CM})$ bin for the x-component of the hyperon polarization. Plots for the z-component are similar.

5.5.1 2-Dimensional Fit

This method involved a direct 2-dimensional minimum chi-square fit to the asymmetry distribution integrated over all Φ and θ_i angles. This fit was of the form of equation 5.4. Resulting plots from this extraction method for one E_γ and one $\cos\theta^{K^0}_{cm}$ bin are shown in Figure 5.39. The chi-squared values from the 2-dimensional fitting routine for both O_x and O_z are displayed in Figure 5.40. These good values give confidence in the fitting algorithm. The resulting values for O_x and O_z are then plotted in Figures 5.41 and 5.42 as a function of $\cos(\theta^{K^0}_{CM})$ for the $K^0\Lambda$ and $K^0\Sigma^0$ channels respectively. The values of O_x and O_z for the $K^0\Lambda$ have been corrected for using the same method described previously.

5.6 Systematic Uncertainties

The systematic uncertainty from the event selection process was studied by varying the cuts and analysing the effect this had on the final polarization results. These studies estimate a systematic uncertainty of 3%. The background from the initial K^0 and Λ identification must also be accounted for. Assuming the worst case, where the background would be fully polarized then this would dilute the final polarization results by 8%. It is anticipated that this background is unpolarized and will not have an effect on the final polarization results. It is therefore combined with the uncertainty from the event selection process. An accurate measurement of the photon beam polarization was required, which introduced a further systematic uncertainty of 5% into the results.

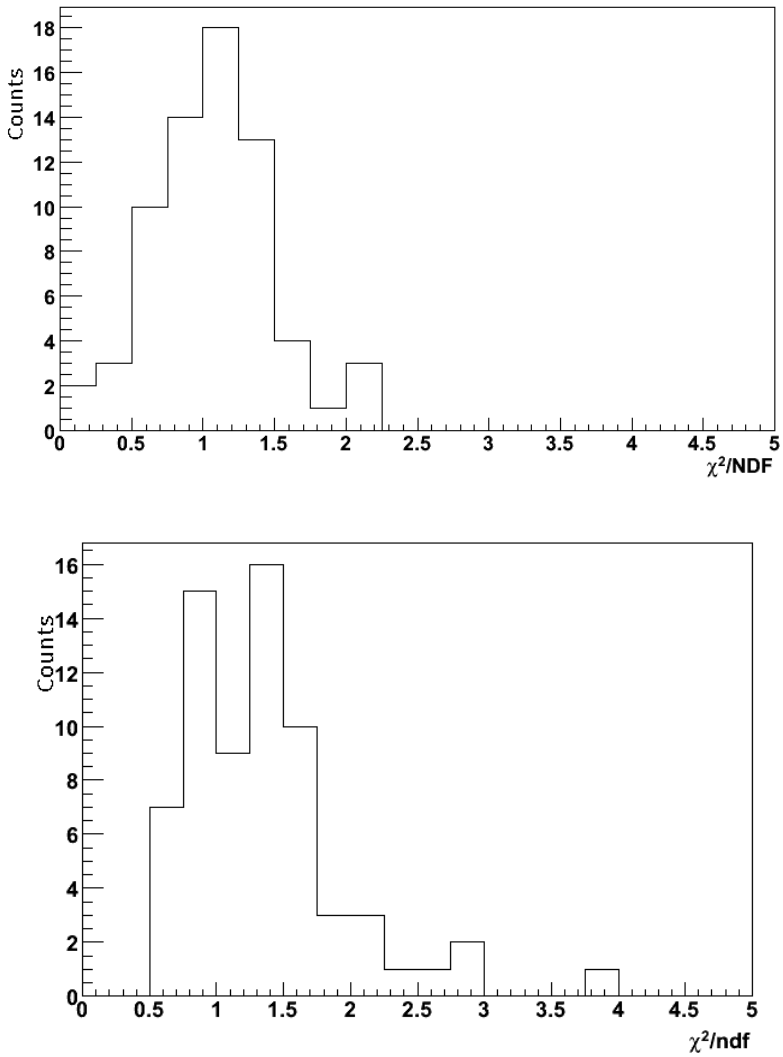

Figure 5.40: χ^2 per degree of freedom values from the two dimensional fits used to extract the O_x (top) and O_z (bottom) double polarization observables for the $K^0\Lambda$ channel. These values are from all fits over the full kinematic range.

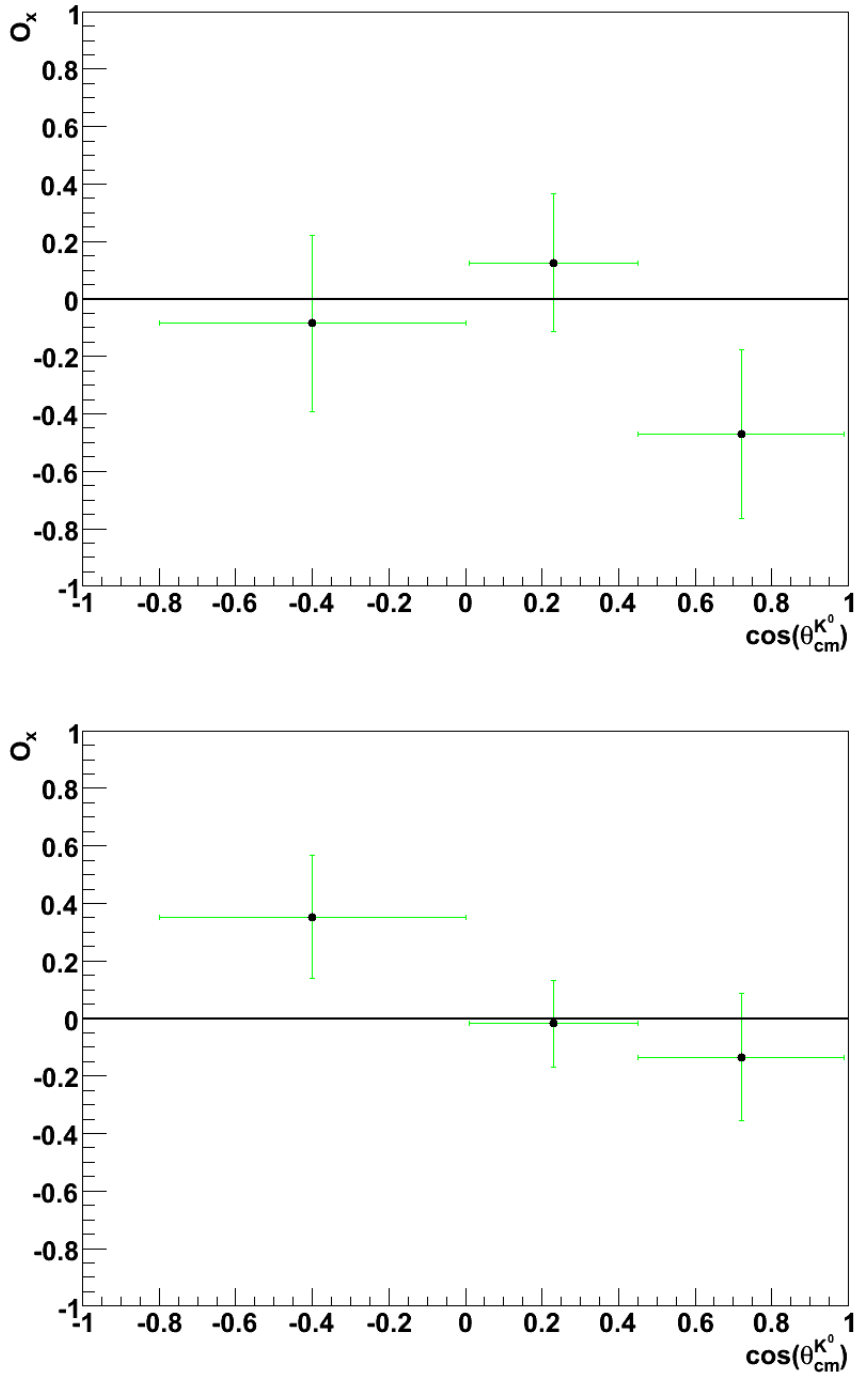

Figure 5.41: O_x observable for the $K^0\Lambda$ channel (top) and for the $K^0\Sigma^0$ channel (bottom). O_x is plotted as a function of $\cos(\theta_{cm}^{K^0})$ for E_γ= 1.9 GeV. All error bars are statistical and no systematic uncertainties are considered at this stage.

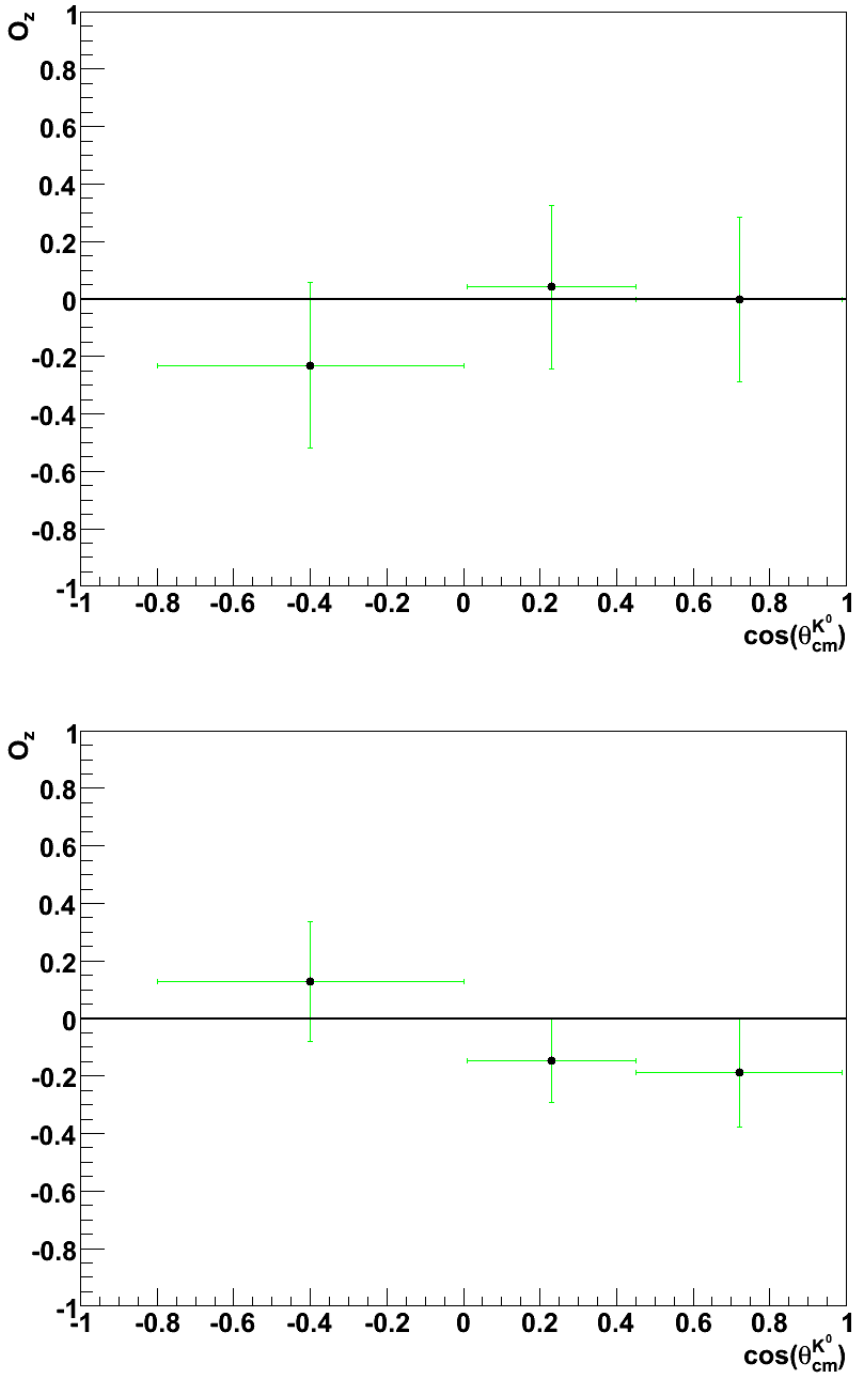

Figure 5.42: O_z observable for the $K^0\Lambda$ channel (top) and for the $K^0\Sigma^0$ channel (bottom). O_z is plotted as a function of $\cos\theta_{cm}^{K^0}$ for E_γ= 1.9 GeV. All error bars are statistical and no systematic uncertainties are considered at this stage.

Table 5.4: Systematic uncertainties for the Σ, O_x, O_z, P and T polarization observables.

Polarization Observable	Systematic Uncertainty
Σ	10%
O_x and O_z	10%
P and T	10%

The main sources of error for the hyperon recoil polarization and target asymmetry will come from the methods used to extract the hyperon yields, the photon polarization calculation and the uncertainty associated with the acceptance correction. As previously discussed, the systematic uncertainty due to the yield extraction was measured to be approximately 11% (including background contamination). The uncertainty related to the photon polarization was 5%. When extracting the recoil polarization, the proton angular distribution has to be acceptance corrected, adding a further source of uncertainty. Previous CLAS analyses have determined the systematic uncertainty to be of the order 5-10%. However, in this analysis the systematic uncertainty was studied by changing the kinematic distributions of the generated events. When the acceptance is corrected simultaneously as both a function of $\cos\theta_y$ and $\cos\theta_{CM}^{K^0}$, the final calculated acceptance is almost the same, regardless of the kinematics of the generated events. It is worth noting that when the acceptance was corrected as a function of $\cos\theta_y$ only, the overall magnitude of the acceptance changed but the shape remained unchanged. Since the hyperon recoil polarization is given by the gradient of a linear fit to the acceptance corrected proton distribution, then it remained unchanged. Therefore, the overall systematic uncertainty from the acceptance correction is found to be of the order of 1%. The final systematic uncertainties for the polarization observables are summarised in Table 5.4.

5.7 Summary

A complex analysis algorithm has been developed to identify the particles of interest in the reactions $\gamma d \rightarrow K^0\Lambda(p)$ and $\gamma d \rightarrow K^0\Sigma^0(p)$. The initial filtering of events was based on simple TOF mass cuts which reduced the data set down to a manageable size for storage on local disks. A number of cuts were then implemented to reduce the background and correctly identify K^0's and Λ's, without discarding too many good events. The final invariant mass plots of the K^0 and Λ show that the cuts are successful in suppressing most of the background. Clean separation of hyperons is not possible due to the Fermi motion of the nucleon's

in the deuterium target, so a method of estimating how much contribution there is from one hyperon to the other on the final beam asymmetries was developed.

By analysing the x and z-components of the hyperon polarization, the double polarization observables O_x and O_z were measured along with the photon beam asymmetry Σ. Extracting the photon beam asymmetry was done by constructing a 1-dimensional fit to an asymmetry over the kaon azimuthal angle. The double polarization observables required a two dimensional fit to an asymmetry over both the kaon azimuthal angle and the proton polar angle in the hyperon rest frame. An acceptance correction was not needed since both methods used asymmetries of the parallel and perpendicular data sets in each kinematic bin.

A linear fit to the decay proton's angular distribution in the hyperon rest frame allows for the hyperon recoil polarization to be extracted. The hyperon recoil polarization is independent of the initial photon polarization state, so doing an asymmetry measurement was not possible. This introduced the need for an acceptance correction. This was done using an event generator to generate $K^0\Lambda/\Sigma^0$ events, then running these events through the GSIM simulation of CLAS to obtain the detector's acceptance as a function of both the proton polar angle θ_y and the kaon production angle $\cos(\theta_{CM}^{K^0})$. After measuring the hyperon recoil polarization, the target asymmetry was then extracted from a two dimensional fit to an asymmetry over the kaon azimuthal angle ϕ and the y-component of the proton polar angle θ_y.

Chapter 6

Results and Discussion

The methods used to extract the final hyperon yields and to measure the polarization observables have been discussed in the previous chapter. The attention now focuses on the presentation of the final results. The preceding chapter discussed the systematic uncertainties associated with these results, as well as the choice of binning. It should be noted that the error bars in all final results plots only take the statistical uncertainty into account. For the photon asymmetry and the double polarization observables O_x and O_z there is a systematic uncertainty of 10% with a corresponding uncertainty of 10% for the recoil polarization and target asymmetry.

This chapter will present the final results for the first measurement of the photon asymmetry, the double polarization observables O_x and O_z, the hyperon recoil polarization and the target asymmetry. There are no previous measurements for $K^0\Lambda$ and $K^0\Sigma^0$ on the neutron and therefore the model calculations used to compare the results with have not been constrained by any data and are purely predictive. The two models used to compare results with are the Kaon-MAID isobar prescription [41] and the Regge-plus-resonance (RPR) approach of Corthals [68, 76]. The Kaon-MAID and RPR models used for comparison will first be compared to highlight their differences in predicting the data and any missing resonances. Each model's calculations are based on data fitted from the $K^+\Lambda$ and $K^+\Sigma^0$ channels. In both cases, the electromagnetic coupling constants of the resonances included in the calculations are the same as those for the $K^+\Lambda$ and $K^+\Sigma^0$ channels from the free proton and isospin independence is assumed. The final results of this analysis will then be compared to both models but no strong physics conclusions will be interpreted from these comparisons in the light of there being much more theoretical work required to develop these models for the neutron. The models will have to be constrained by the new neutron data be-

fore any firm comparisons between the model calculations and data can be made. Finally, the results of this analysis for the photon beam asymmetry and hyperon recoil polarization will be compared to those from the free proton analysis [31] to look for any differences in the production mechanism between KΛ/Σ production on the neutron and on the proton. This is only done for the photon asymmetry and hyperon recoil polarization as the statistics are at their greatest for these observables.

6.1 Preview of Model Comparisons

The Kaon-MAID and RPR models differ in the way they describe the background and resonance terms. A more detailed account of both models and their differences is given in chapter 2. It is very difficult to make a claim of finding a missing resonance without there being some model dependence. For this reason the 1.9 GeV energy bin has been selected for all observables to look at the different predictions made by the Kaon-MAID and RPR models and to highlight the difficulty in finding a new state. Figure 6.1 shows the photon beam asymmetry, Σ plotted against the full calculations (includes missing resonances) from the Kaon-MAID and RPR models as well as the core calculations (without missing resonances). It should be noted that the full calculations for the Kaon-MAID and RPR models do not include exactly the same resonances. The RPR model includes the $P_{13}(1900)$ and $D_{13}(1900)$ states, whereas only the latter is included in the Kaon-MAID model. This highlights the internal difference between the calculations including only the core states and those including missing states. Similar plots are shown in Figure 6.2 through 6.5 for the P, T, O_x and O_z spin observables respectively. It is clearly evident from these plots that making a claim of a finding a missing resonance is highly model dependent. In most cases the predictions from the models will vary not only in magnitude but also in sign. This also shows that the models calculate the background and core resonance contributions differently.

Overall, it is clear that by comparing the two different models to the data, there will be some model dependence of the final physics conclusions. Therefore the next section will show the data for each measured spin observable compared separately with the Kaon-MAID and RPR models but no physics conclusions will be drawn from this until better theoretical models have been developed.

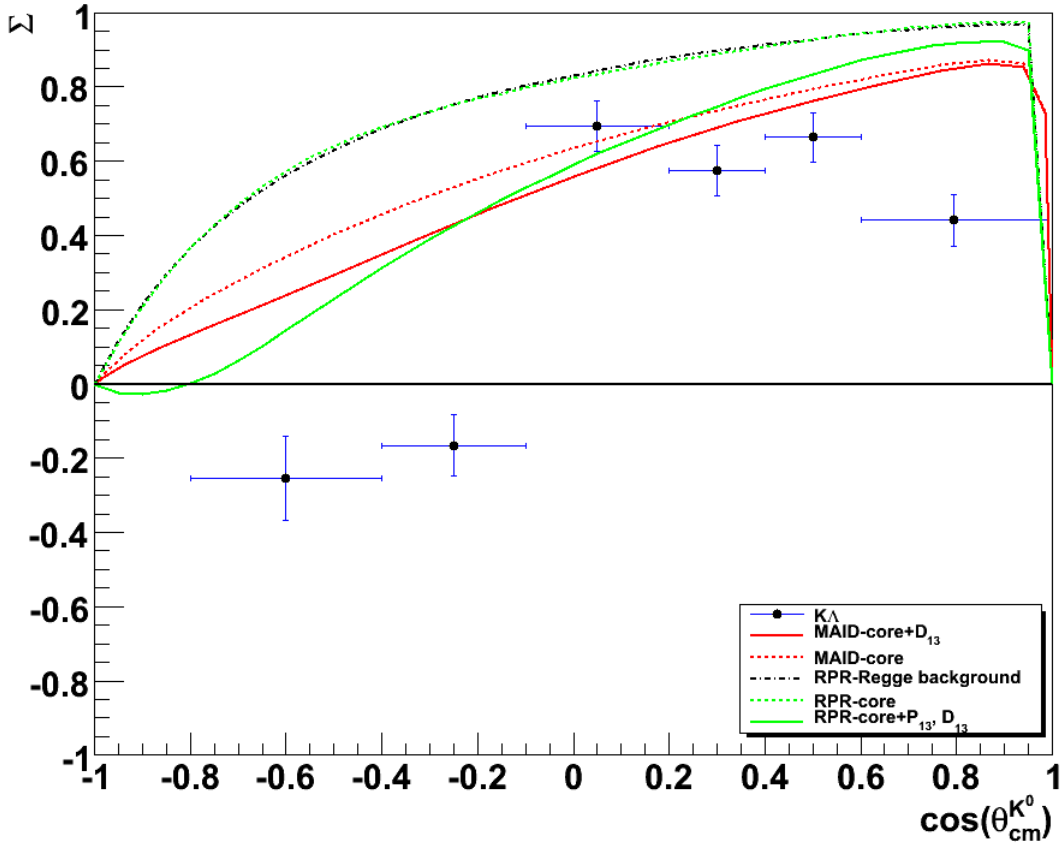

Figure 6.1: Model comparisons for the photon asymmetry for the $K^0\Lambda$ channel at 1.9 GeV. The photon beam asymmetry, Σ is plotted against the calculations (solid and dashed red lines) from the Kaon-MAID and RPR (solid and dashed green lines) models. This highlights the difference between the models and their predictions of any missing states.

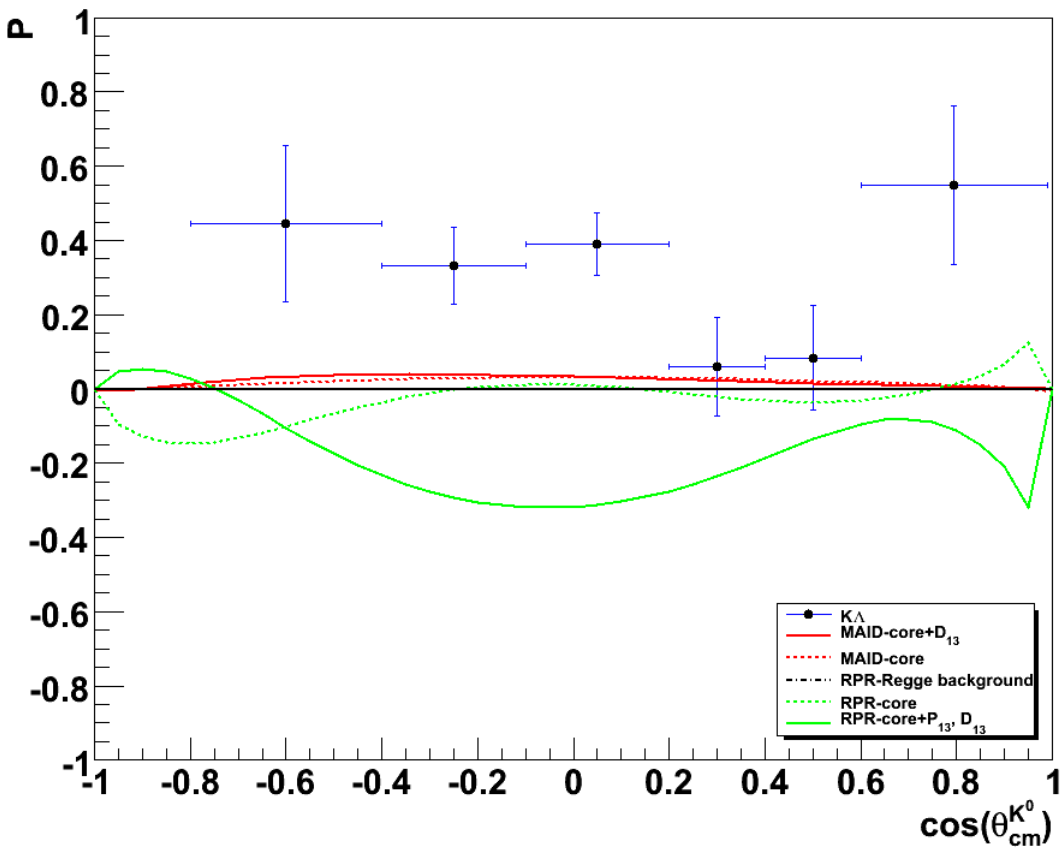

Figure 6.2: Model comparisons for hyperon recoil polarization for the $K^0\Lambda$ channel at 1.9 GeV. The hyperon recoil polarization, P is plotted against the calculations (solid and dashed red lines) from the Kaon-MAID and RPR (solid and dashed green lines) models. This highlights the difference between the models and their predictions of any missing states.

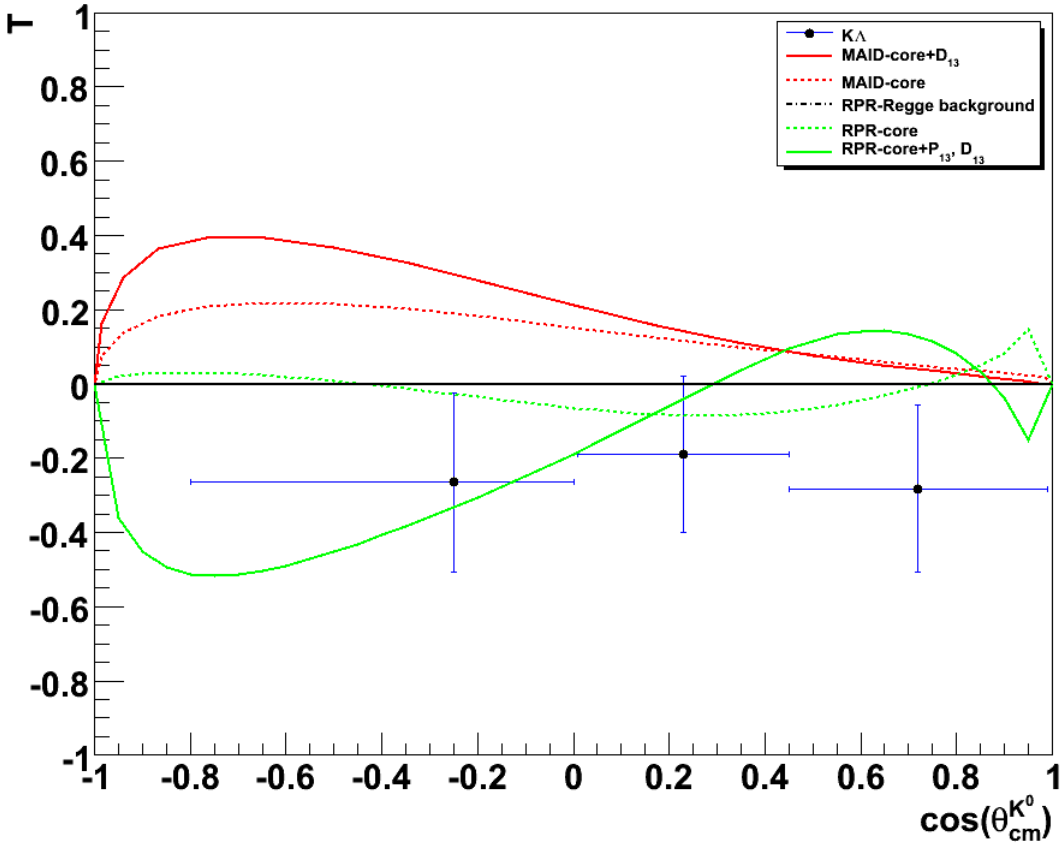

Figure 6.3: Model comparisons for hyperon recoil polarization for the $K^0\Lambda$ channel at 1.9 GeV. The target asymmetry, T is plotted against the calculations (solid and dashed red lines) from the Kaon-MAID and RPR (solid and dashed green lines) models. This highlights the difference between the models and their predictions of any missing states.

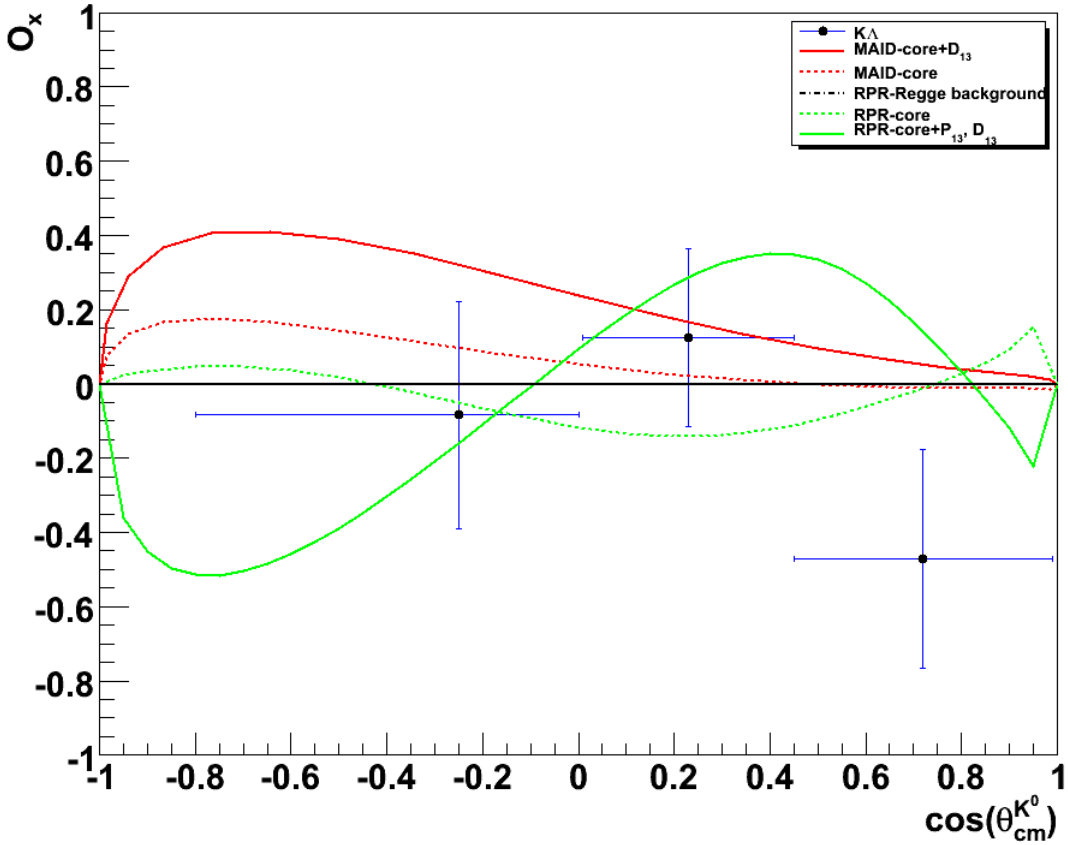

Figure 6.4: Model comparisons for the double polarization observable O_x for the $K^0\Lambda$ channel at 1.9 GeV. The double polarization observable, O_x is plotted against the calculations (solid and dashed red lines) from the Kaon-MAID and RPR (solid and dashed green lines) models. This highlights the difference between the models and their predictions of any missing states.

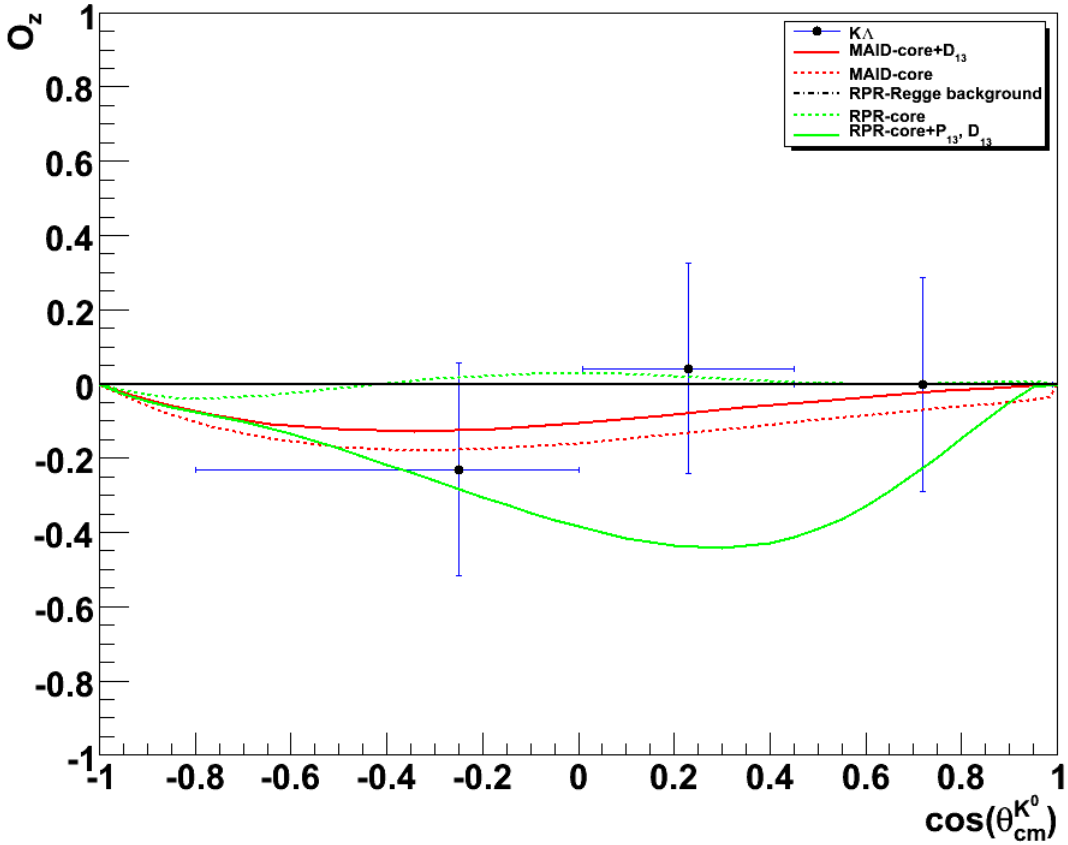

Figure 6.5: Model comparisons for the double polarization observable O_z for the $K^0\Lambda$ channel at 1.9 GeV. The double polarization observable, O_z is plotted against the calculations (solid and dashed red lines) from the Kaon-MAID and RPR (solid and dashed green lines) models. This highlights the difference between the models and their predictions of any missing states.

6.2 Photon Asymmetry

The results for the photon asymmetry for the $K^0\Lambda$ channel are shown compared to the Kaon-MAID and RPR calculations in Figures 6.6 and 6.7 respectively. They are plotted as a function of the centre of mass kaon angle $\cos(\theta_{cm}^{K^0})$. In Figures 6.10 and 6.11they are plotted as a function of the photon energy $E_\gamma$for the $K^0\Lambda$ and $K^0\Sigma^0$ channels respectively. The statistical error bars for photon energies above 1.9 GeV are on average larger due to the fewer statistics at these energies. Additionally over all photon energies, at extreme backward angles, data are missing due to the limited statistics. Similar plots are shown for the $K^0\Sigma^0$ channel in Figures 6.8 and 6.9.

6.2.1 Photon asymmetry results $K^0\Lambda$

The first feature to notice about the $K^0\Lambda$ results is that for all energies, the mid to forward angle bins have a positive photon asymmetry. The backward angles show a negative photon asymmetry at energies above 1.5 GeV. The photon asymmetry remains flat for energies up to 1.5 GeV, where it then begins to show a peak at approximately $\cos(\theta_{cm}^{K^0}) \simeq 0$ for photon energies between 1.5 GeV to 1.9 GeV. At photon energies greater than 1.9 GeV, the asymmetry rises at forward angles, exhibiting a very strong signal at forward angles at energies between 2.1 GeV and 2.3 GeV.

A comparison of the $K^0\Lambda$ photon asymmetry with calculations from the Kaon-MAID model are shown in Figure 6.6. The Kaon-MAID model uses an isobar prescription that includes the core $S_{11}(1650)$, $P_{11}(1710)$ and $P_{13}(1720)$ resonances along with the missing $D_{13}(1900)$. In all plots, the black dashed curve represents calculations where only the core set of resonances are included and the red solid line includes the core resonances plus the $D_{13}(1900)$ resonance. The two model variants do not differ significantly to allow for any real physics in the data to be interpreted. The models predict the correct sign of the asymmetry for mid to forward angles but differ in sign at backward angles at the higher energies. There are no Kaon-MAID calculations available for the 2.3 GeV energy setting.

The photon asymmetry results are also compared to calculations from the Regge-plus-resonance model of Corthals et al [68, 75], as described in chapter 2. The background in this scheme is modelled by t-channel Regge-trajectory exchange, in this case it consists solely of a K* (892) Regge-trajectory. The inclusion of the $S_{11}(1650)$, $P_{11}(1710)$ and $P_{13}(1720)$ core resonances evolve the calculations into the resonance region. The weakly established $P_{13}(1900)$ and the

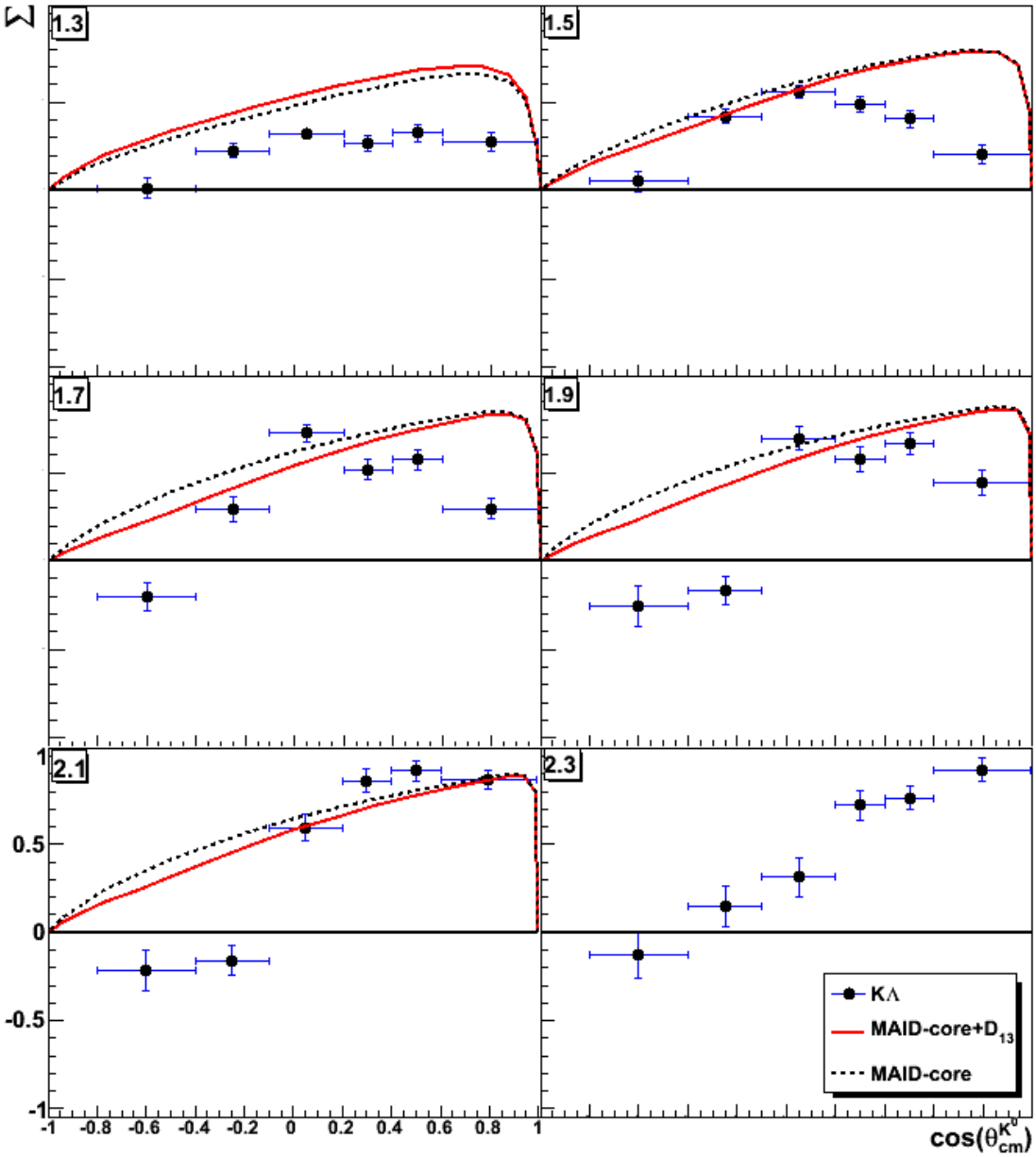

Figure 6.6: Photon asymmetries for the reaction $\gamma n \rightarrow K^0\Lambda$ as a function of $\cos(\theta^{K^0}_{cm})$ ranging from E_γ= 1.3 GeV (top left) to 2.3 GeV (bottom right). Data are compared to model calculations from the Kaon-MAID model: core resonances (black dashed line), inclusion of D_{13}(1900) (solid red line).

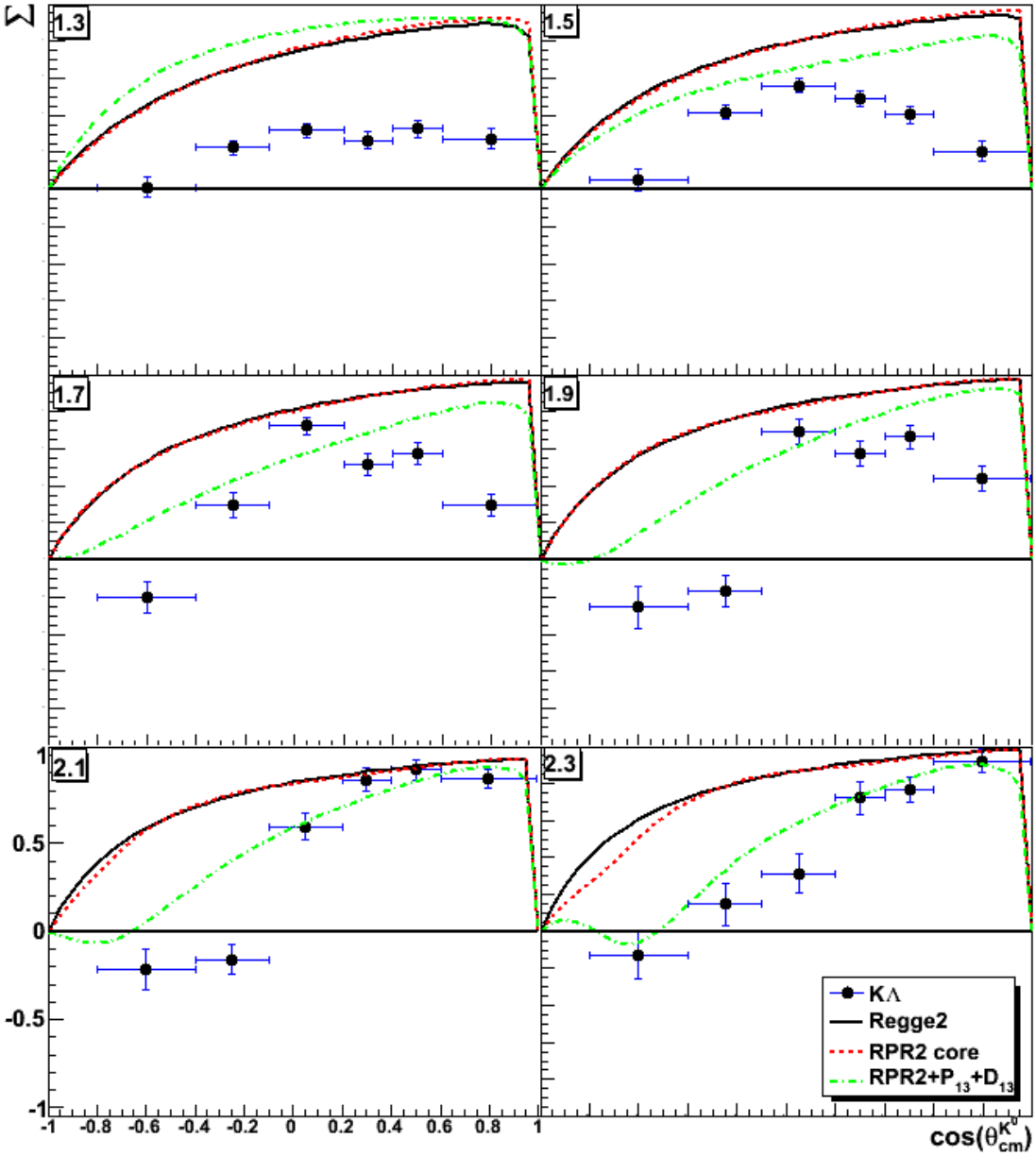

Figure 6.7: Photon asymmetries for the reaction $\gamma n \rightarrow K^0\Lambda$ as a function of $\cos(\theta^{K^0}_{cm})$ ranging from $E_\gamma = 1.3$ GeV (top left) to 2.3 GeV (bottom right). Data are compared to model calculations from the Regge-plus-resonance approach: Regge background (solid black line), core resonances (red dashed line) core resonances plus the inclusion of $D_{13}(1900)$ and $P_{13}(1900)$ states (green dot-dash line).

missing $D_{13}(1900)$ states are also included in the calculations to investigate their importance. The black solid line in the plots corresponds to calculations where only the Regge background is modelled, the dashed red line includes the core set of resonances and the dot-dashed green line includes the $P_{13}(1900)$ and $D_{13}(1900)$ states.

The results are finally plotted as a function of E_γ and compared with Kaon-MAID calculations in Figure 6.10. Apart from the backward angles the model calculations and data agree on the sign but the general trend is not well reproduced.

6.2.2 Photon asymmetry for $K^0\Sigma^0$

The photon asymmetry for the $K^0\Sigma^0$ channel is largely negative over all energies except at extreme forward angles. At 1.3 GeV, the asymmetry is relatively flat till 1.5 GeV where it gradually rises to a positive value at forward angles. From 1.7 GeV to 1.9 GeV, the asymmetry has a stronger signal at backward angles with it tending to small values close to zero at mid to forward angles. The 2.1 GeV setting again shows a strong asymmetry at backward angles with it rising to a positive value at a forward angle. There is a mid to forward angle peak forming at the 2.3 GeV setting with it then rising to a positive value at the forward angles.

The results of the photon asymmetry are compared to the Kaon-MAID model calculations in Figure 6.8 where an isobar framework based on the inclusion of the $S_{11}(1650)$, $P_{11}(1710)$, $P_{13}(1720)$, $S_{31}(1900)$ and $P_{31}(1910)$ resonances is used. The calculations for the lower energies, 1.3 GeV and 1.5 GeV, reproduce the general trend of the data very well. The data at 1.7 and 1.9 GeV are not well described by the model. For the 2.1 GeV data there is a sign difference between the model and data at backward and forward angles with mid angles predicted to have a larger asymmetry than is measured. There are no calculations available for the 2.3 GeV data.

Figure 6.9 shows the results compared to calculations from the Regge-plus-resonance approach. For $K^0\Sigma^0$ production, four different model schemes are used. The background in this scheme is modeled by t-channel Regge-trajectory exchange. For this channel there are two variations of this. One model consists of a K* (892) and a K*(1410) Regge-trajectory. The other only includes a K*(892) Regge-trajectory. This is because there are no data available to determine if the K*(1410) Regge-trajectory is required to describe the reaction. It should be noted that the K*(1410) trajectory is needed to describe the $K^0\Sigma^+$ channel from the proton. The inclusion of the $S_{11}(1650)$, $D_{33}(1700)$, $P_{11}(1710)$, $P_{13}(1720)$,

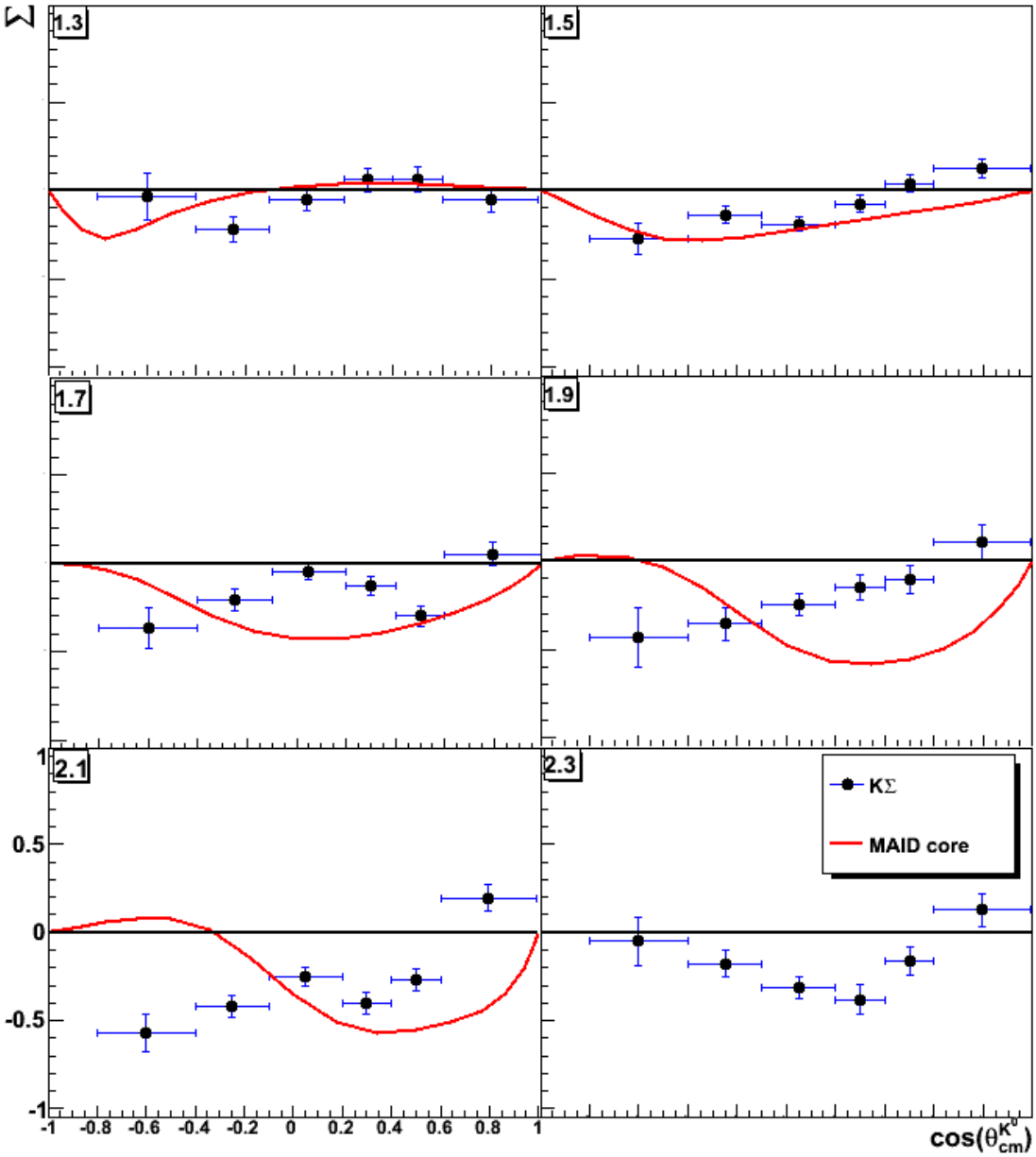

Figure 6.8: Photon asymmetries for the reaction $\gamma n \rightarrow K^0\Sigma^0$ as a function of $\cos(\theta^{K^0}_{cm})$ ranging from E_γ= 1.3 GeV (top left) to 2.3 GeV (bottom right). Data are compared to model calculations from the Kaon-MAID model: core set of resonances (solid red line).

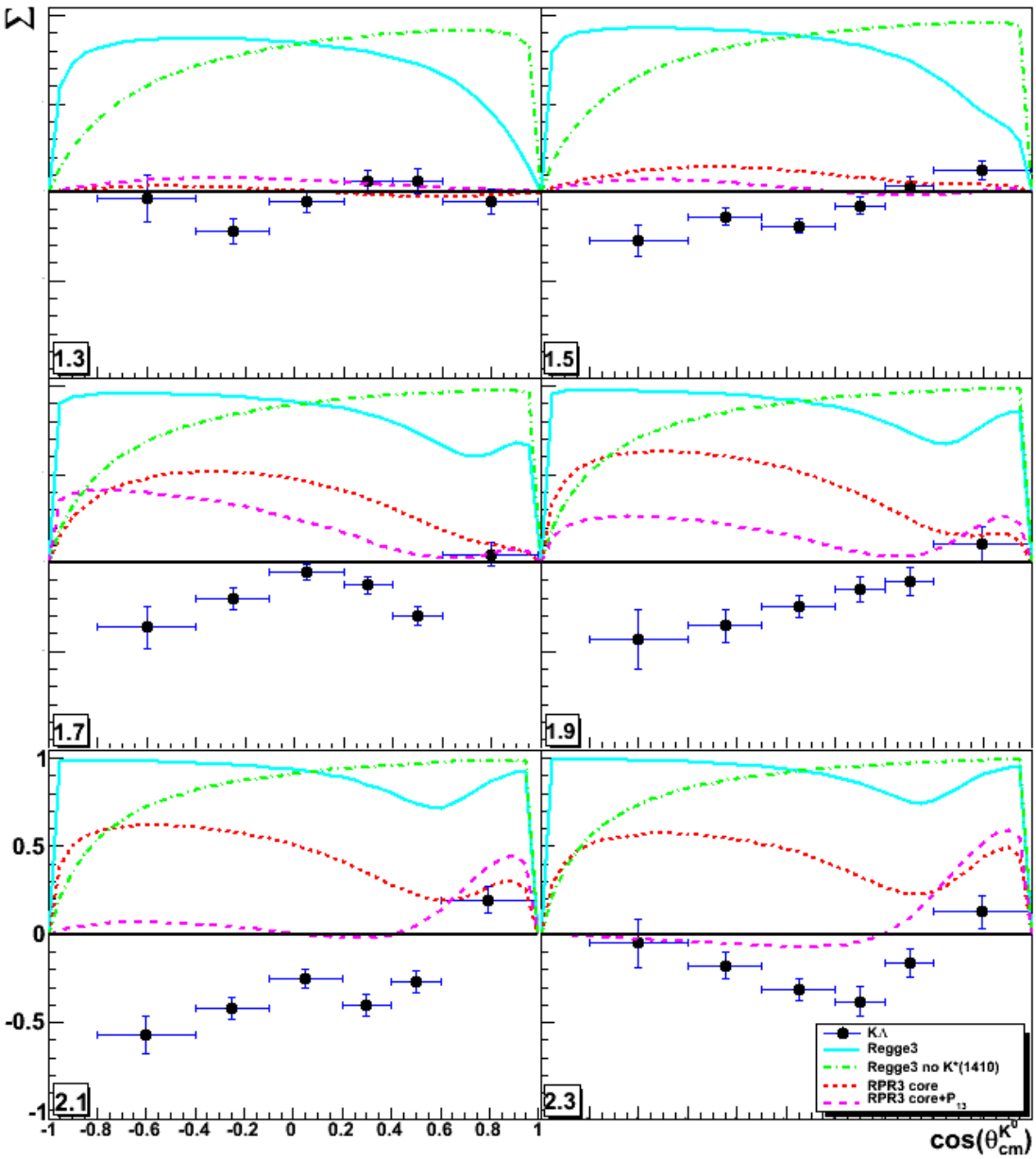

Figure 6.9: Photon asymmetries for the reaction $\gamma n \rightarrow K^0\Sigma^0$ as a function of $\cos(\theta^{K^0}_{cm})$ ranging from E_γ= 1.3 GeV (top left) to 2.3 GeV (bottom right). Data are compared to model calculations from the Regge-plus-resonance approach: Regge background with K*(892) and K*(1410) trajectories (solid blue line), Regge background with K*(892) trajectory only (green dot-dashed line), core resonances (red dashed line), core resonances plus inclusion of P_{13}(1900) (pink dashed line).

$S_{31}(1900)$, $P_{31}(1910)$ and $P_{33}(1920)$ core resonances evolve the calculations into the resonance region. The weakly established $P_{13}(1900)$ state is also included in the calculations to investigate its role in this reaction.

The solid blue line is the Regge-3 model which takes into account the K*(892) and K*(1410) trajectories. The green dot-dashed curve encompasses the Regge-3 model but only including the K*(892) trajectory. The red dashed curve represents the RPR-3 model with the following core resonance $S_{11}(1650)$, $D_{33}(1700)$, $P_{11}(1710)$, $P_{13}(1720)$, $S_{31}(1900)$, $P_{31}(1910)$ and $P_{33}(1920)$ included. The pink dashed curve represents the RPR-3 model with the core resonances and the inclusion of the $P_{13}(1900)$. All these resonances are established in the PDG except for the $P_{13}(1900)$ which is a 2-star resonance and the $D_{13}(1900)$ which is a 'missing' resonance.

The results are then plotted as a function of E_γ and compared with Kaon-MAID core calculations in Figure 6.11. The model does not reproduce the data well.

6.3 Recoil Polarization

The recoil hyperon polarization for the $\gamma n \rightarrow K^0\Lambda$ channel is compared to Kaon-MAID calculations in Figure 6.12. Results are then also compared to the Regge-plus-resonance approach as a function of $\cos(\theta_{cm}^{K^0})$ in 150 MeV E_γ bins in Figure 6.13. The recoil polarization is plotted as a function of E_γ in Figure 6.14. Similar plots are shown for the $K^0\Sigma^0$ channel in Figures 6.15 through 6.17.

6.3.1 Discussion of recoil polarization results for $K^0\Lambda$

The first observation of the recoil polarization is that for energies between 1.225 GeV and 1.525 GeV the recoil polarization is positive over the full angular range. For energies between 1.675 GeV and 2.275 GeV the recoil polarization becomes negative at backward angles and positive at mid to forward angles.

A comparison of the $K^0\Lambda$ recoil polarizations with calculations from the Kaon-MAID model are shown in Figure 6.12. Over all kinematics there is very little distinction between the different Kaon-MAID calculations. There are no Kaon-MAID calculations available for the 2.275 GeV data.

The recoil polarizations are also compared to the RPR model calculations in Figure 6.13. The first observation is that the Regge-2 model has a zero contribution over all kinematics. The data are in general not well described by the RPR models.

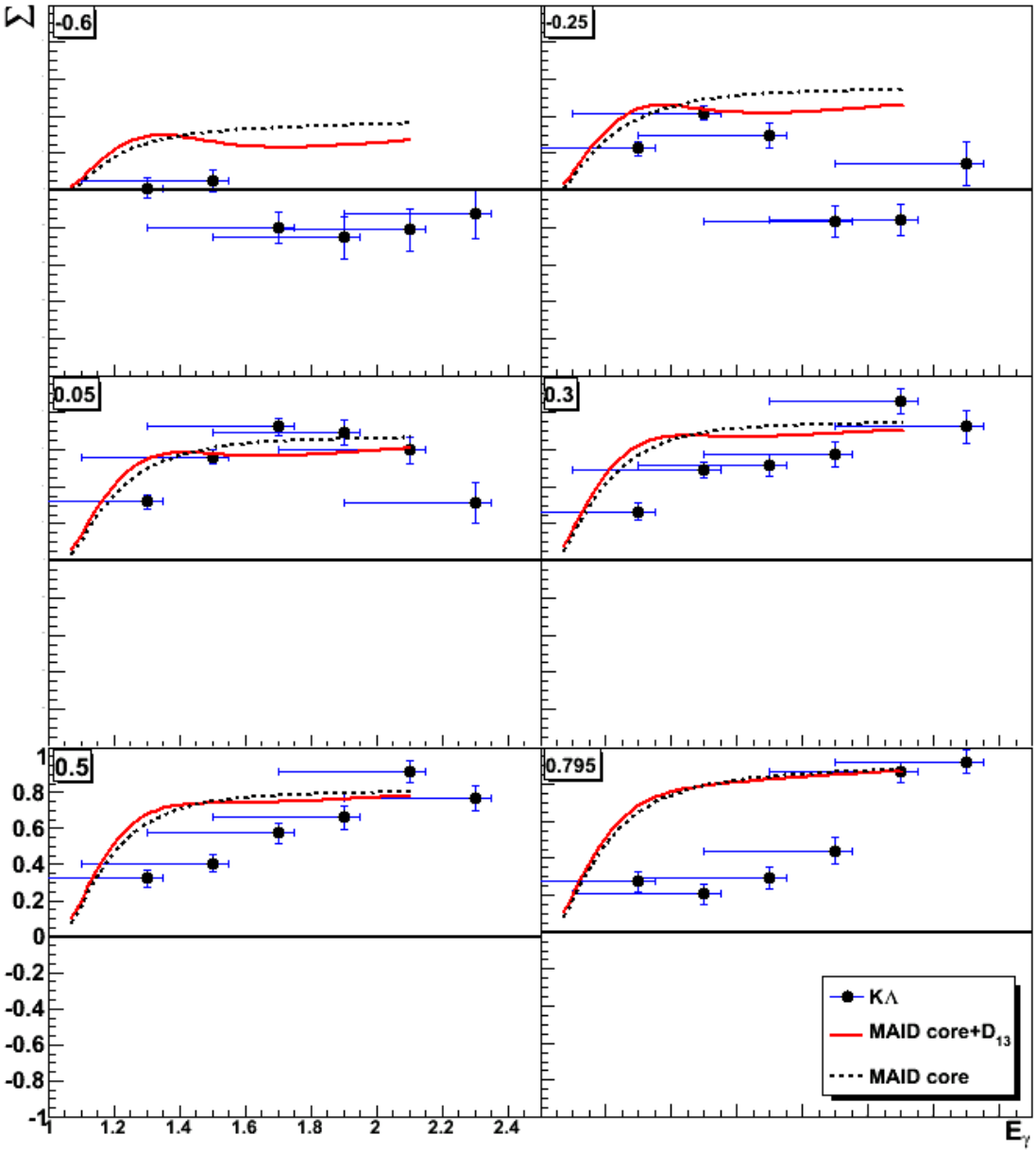

Figure 6.10: Photon asymmetries for the reaction $\gamma n \rightarrow K^0\Lambda$ as a function of E_γ ranging from $\cos(\theta_{cm}^{K^0})$= -0.6 (top left) to 0.795 (bottom right). Asymmetric error bars are a result of the wide and overlapping binning in photon energy.

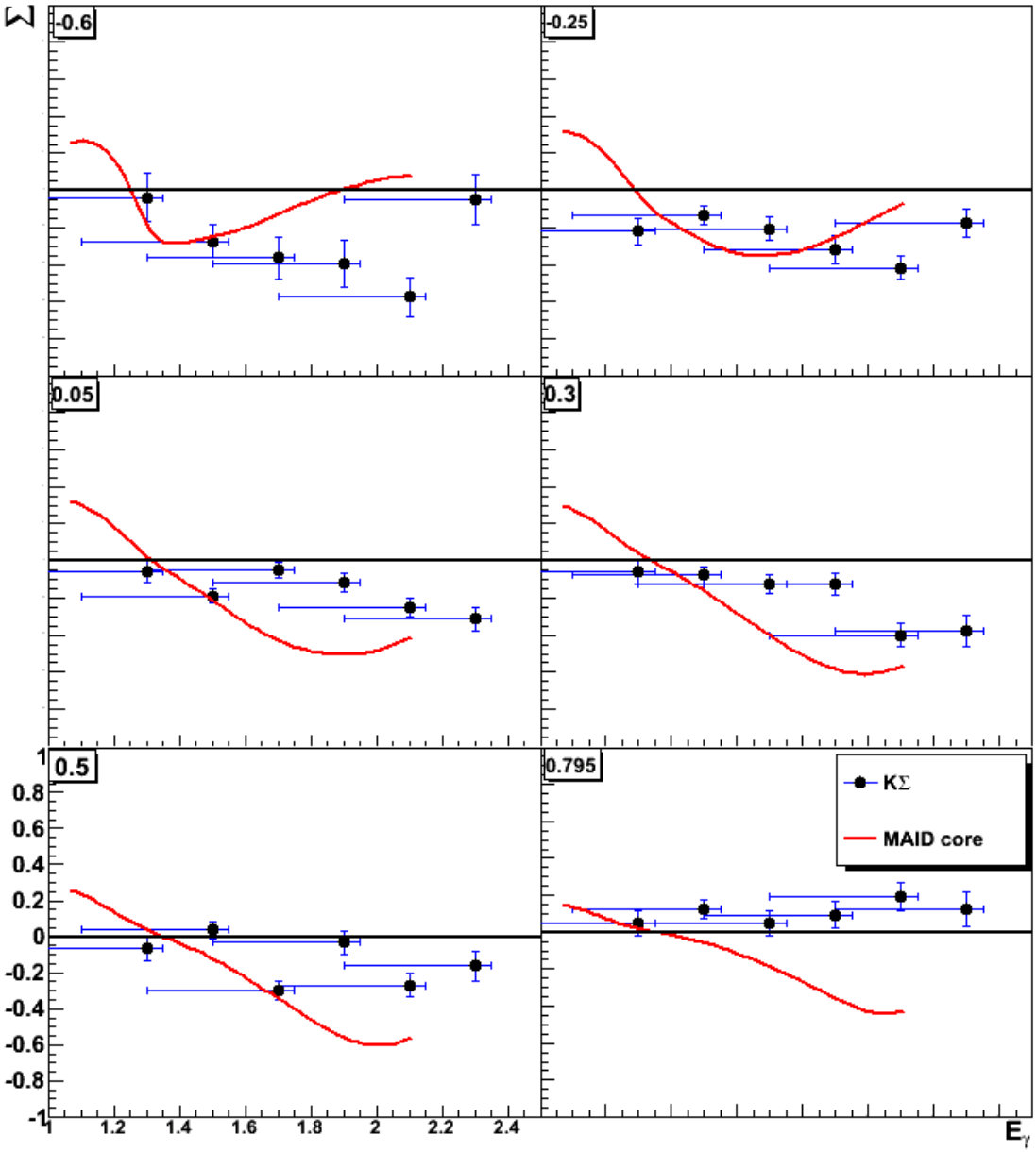

Figure 6.11: Photon asymmetries for the reaction $\gamma n \rightarrow K^0\Sigma^0$ as a function of E_γ ranging from $\cos(\theta^{K^0}_{cm})$= -0.6 (top left) to 0.795 (bottom right). Asymmetric error bars are a result of the wide and overlapping binning in photon energy.

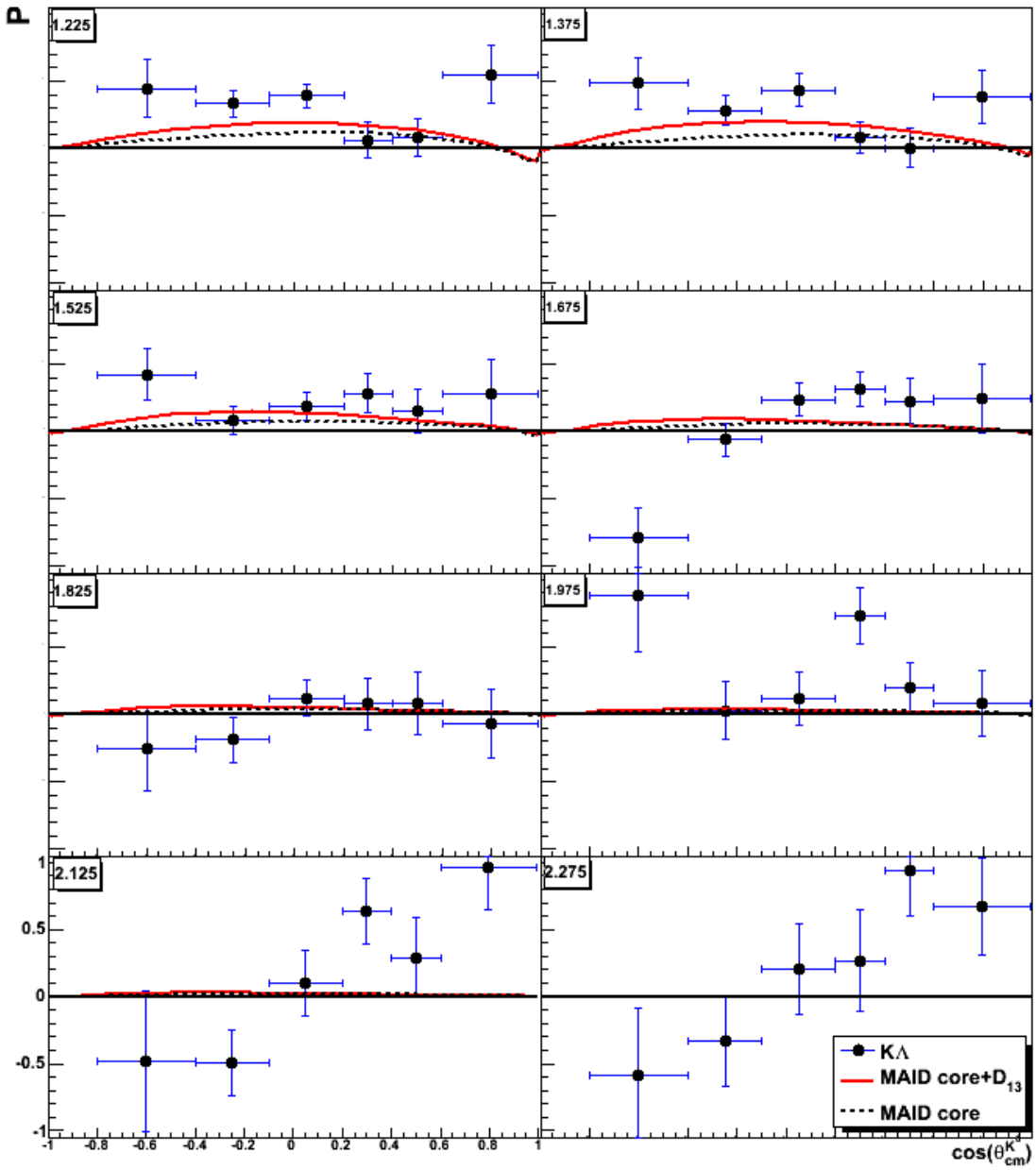

Figure 6.12: Hyperon recoil polarization for the reaction $\gamma n \rightarrow K^0\Lambda$ as a function of $\cos(\theta^{K^0}_{cm})$ ranging from E_γ= 1.225 GeV (top left) to 2.275 GeV (bottom right). Data are compared to model calculations from the Kaon-MAID model: core resonances (black dashed line), inclusion of $D_{13}(1900)$ (solid red line).

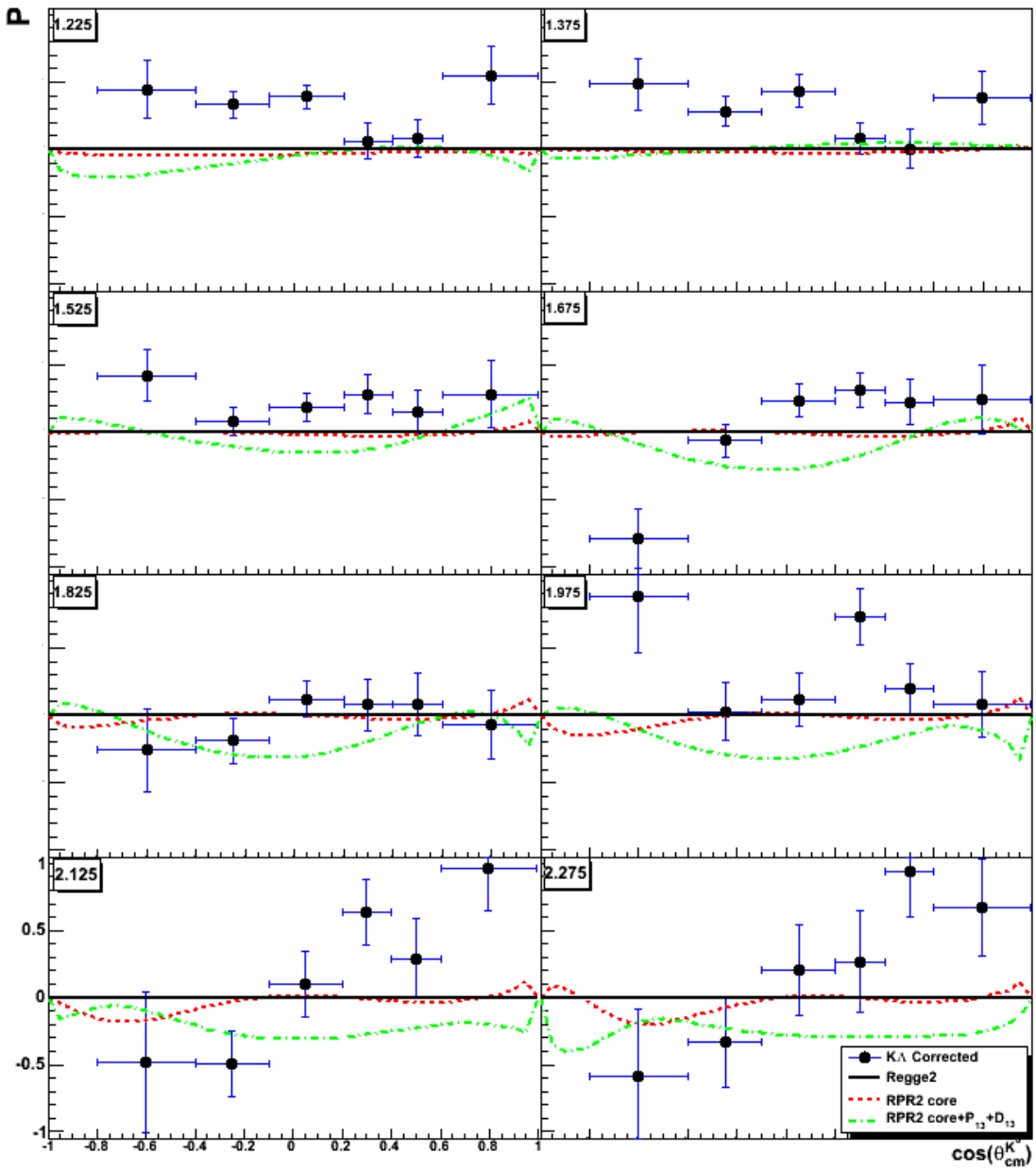

Figure 6.13: Hyperon recoil polarization for the reaction $\gamma n \rightarrow K^0\Lambda$ as a function of $\cos(\theta^{K^0}_{cm})$ ranging from E_γ= 1.225 GeV (top left) to 2.275 GeV (bottom right). Data are compared to model calculations from the Regge-plus-resonance approach: Regge background (solid black line), core resonances (red dashed line) core resonances plus the inclusion of $D_{13}(1900)$ and $P_{13}(1900)$ states (green dot-dash line).

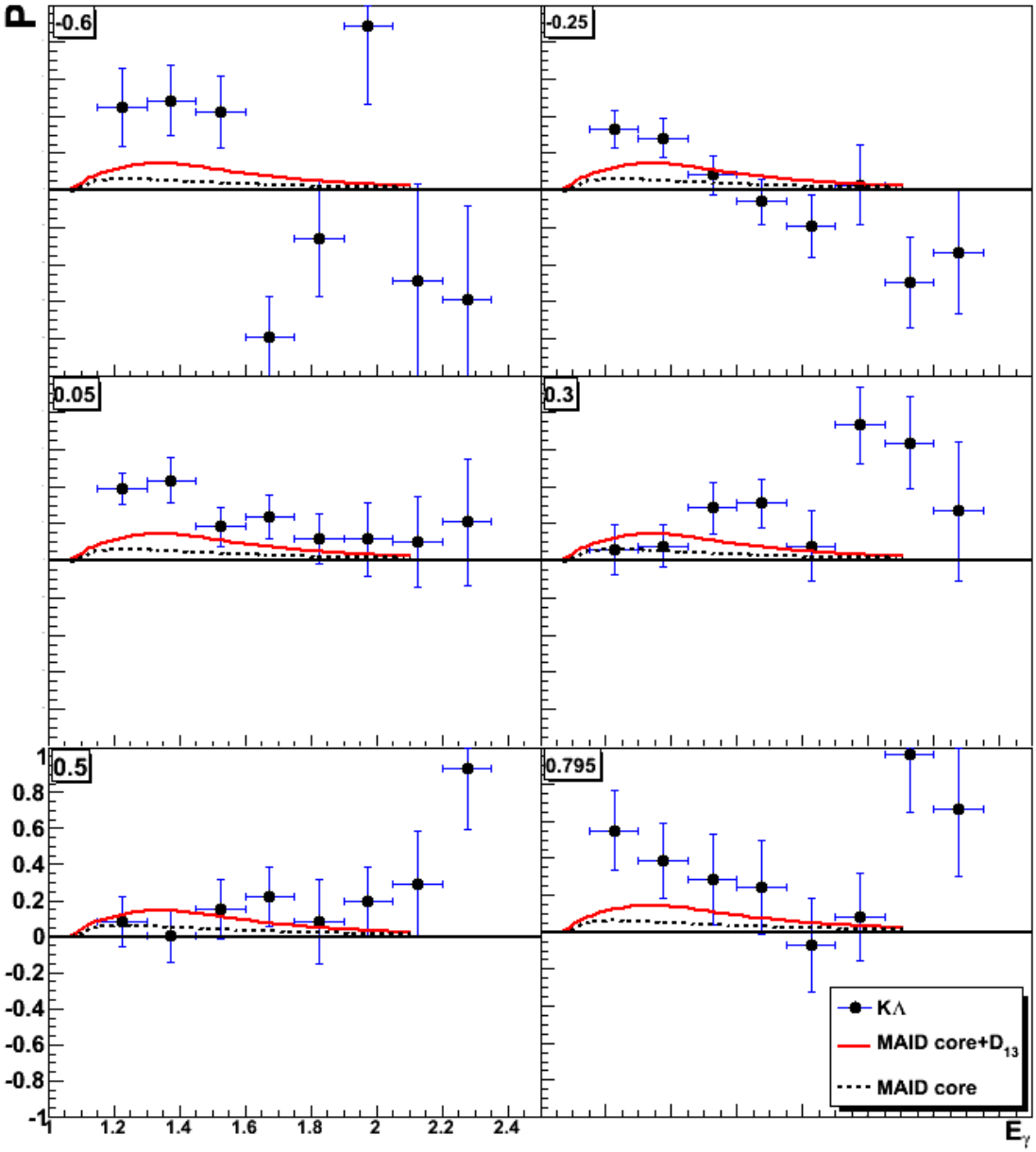

Figure 6.14: Hyperon recoil polarization for the reaction $\gamma n \rightarrow K^0\Lambda$ as a function of E_γ ranging from $\cos(\theta^{K^0}_{CM})$ = -0.6 (top left) to 0.795 (bottom right).

The recoil results are plotted as a function of E_γ and compared with the Kaon-MAID calculations in Figure 6.14. Neither model describes the data well.

6.3.2 Discussion of recoil polarization results for $K^0\Sigma^0$

The recoil polarizations for the $K^0\Sigma^0$ channel are predominantly positive except at back to mid angles at 1.525 GeV and the backward angles in the 1.825 and 2.125 GeV data.

The recoil polarizations are then compared to the Kaon-MAID approach in Figure 6.15. In the two lowest energy bins, 1.225 and 1.375 GeV the model differs in sign to the data. At 1.525 GeV the data at backward to mid angles agrees with the model well. However, the large positive polarization at extreme backward angles is not accounted for by the model. The general data trend at 1.675 GeV is well described by the model except at extreme backward angles. The model predicts lower polarizations than are measured. The 1.825 GeV data trend is well described by the model except for the very backward angles where a high polarization is measured but is not predicted. Data at 1.975 GeV are not well described by the model. The 2.125 GeV data trend is reasonably well described except at backward angles. The model under predicts the recoil polarizations over the full angular range. There are no calculations available for the 2.275 GeV data.

The RPR model predictions are compared to the data in Figure 6.16. Generally, over all kinematics the models do not describe the data well.

- The Kaon-MAID core calculations are compared to the data which are plotted as a function of E_γ in Figure 6.17. The general trend is not well reproduced.

6.4 Target Asymmetry

The results for the target asymmetry are compared to Kaon-MAID calculations for the $\gamma n \rightarrow K^0\Lambda$ channel as a function of $\cos(\theta_{cm}^{K^0})$ in Figure 6.18. They are also compared to the Regge-plus-resonance model in Figure 6.19. In Figure 6.20, the results are plotted as a function of E_γ. Similar plots for the $\gamma n \rightarrow K^0\Sigma^0$ channel are shown in Figures 6.21 through 6.23.

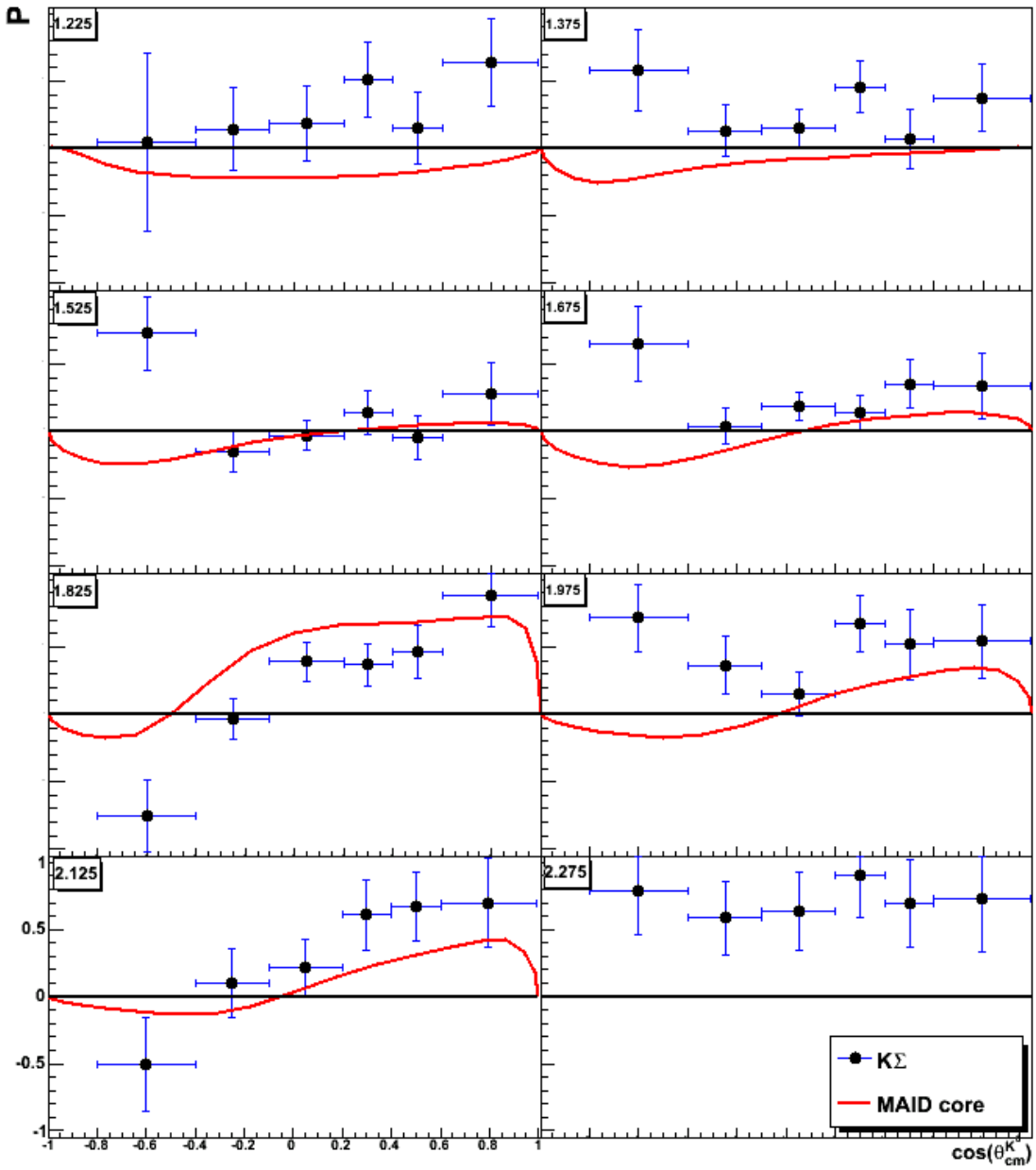

Figure 6.15: Hyperon recoil polarization for the reaction $\gamma n \rightarrow K^0\Sigma^0$ as a function of $\cos(\theta^{K^0}_{cm})$ ranging from E_γ= 1.225 GeV (top left) to 2.275 GeV (bottom right). Data are compared to model calculations from the Kaon-MAID model: core set of resonances (solid red line).

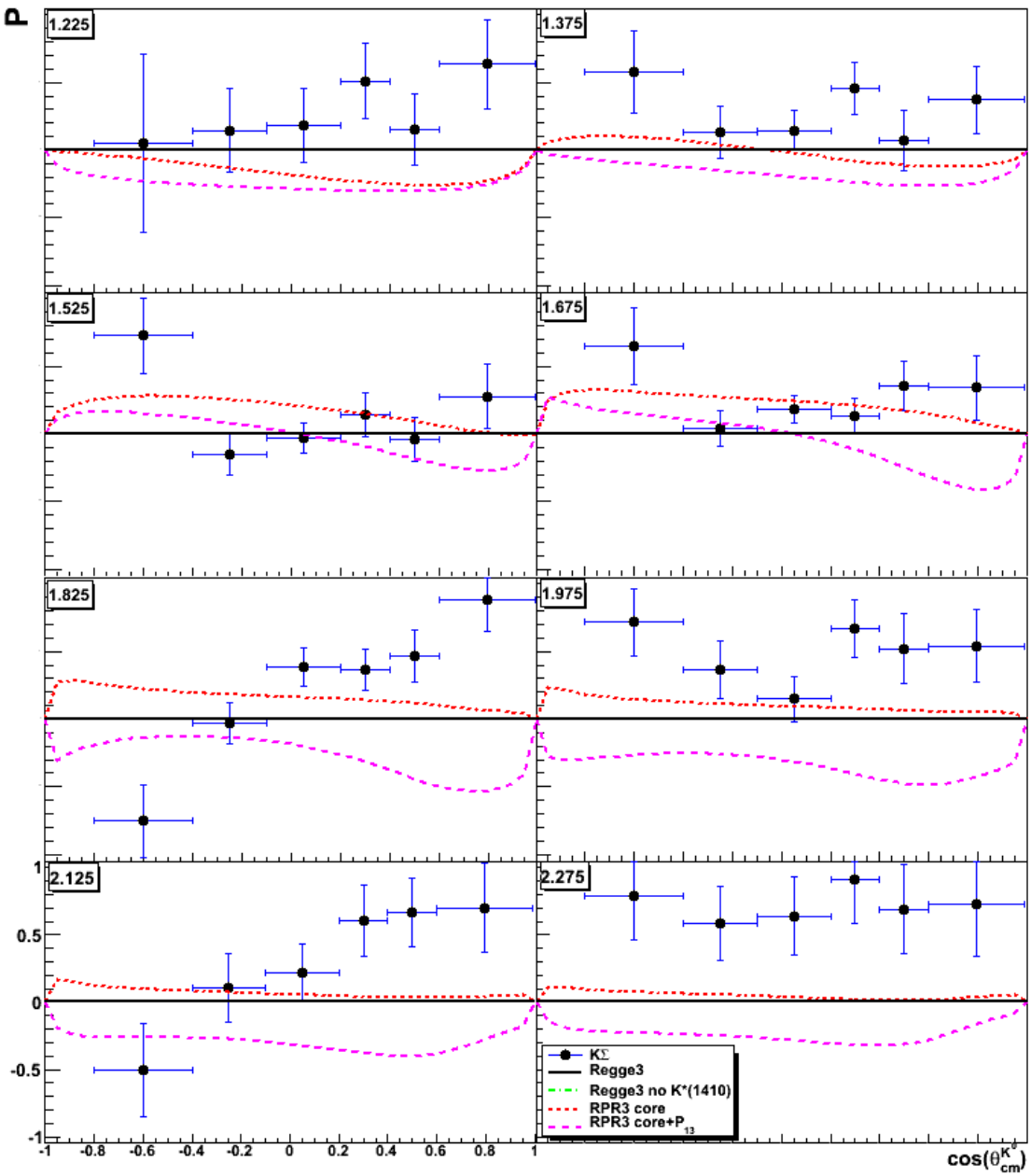

Figure 6.16: Hyperon recoil polarization for the reaction $\gamma n \rightarrow K^0\Sigma^0$ as a function of $\cos(\theta^{K^0}_{cm})$ ranging from E_γ= 1.225 GeV (top left) to 2.275 GeV (bottom right). Data are compared to model calculations from the Regge-plus-resonance approach: Regge background with K*(892) and K*(1410) trajectories (solid black line), Regge background with K*(892) trajectory only (green dot-dashed line), core resonances (red dashed line), core resonances plus inclusion of P_{13}(1900) (pink dashed line).

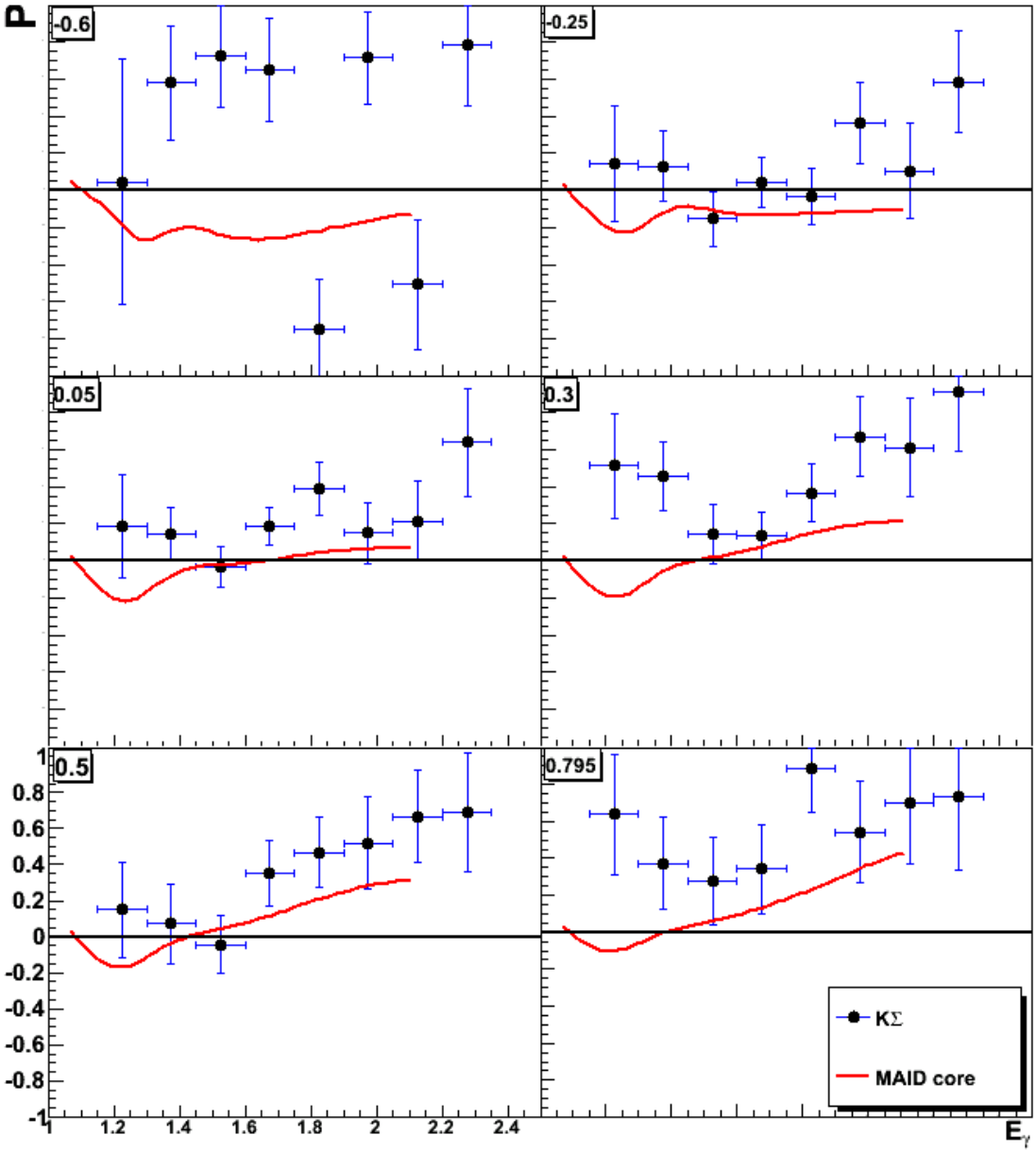

Figure 6.17: Hyperon recoil polarization for the reaction $\gamma n \rightarrow K^0\Sigma^0$ as a function of E_γ ranging from $\cos(\theta^{K^0}_{CM})$ = -0.6 (top left) to 0.795 (bottom right).

6.4.1 Discussion of target polarization results for $K^0\Lambda$

Target asymmetry results are compared to Kaon-MAID calculations in Figure 6.18. The target asymmetry results at 1.2 GeV show a strong positive signal. The Kaon-MAID models over predict the magnitude of the asymmetry. At 1.4 GeV, there is better agreement between the data and model at mid to forward angles, with any distinction between the models impossible. The 1.6 GeV and 1.8 GeV data show a change in sign of the asymmetry and are in general flat. The models do not predict a sign change as they remain positive. At 2.0 GeV the data could be consistent with either model. At mid to forward angles any distinction between the models becomes impossible. There are no model calculations available for the 2.2 GeV data.

Calculations from the RPR model are compared to the data in Figure 6.19. The data at 1.2 GeV are all positive, no model calculations describe the data well. In general there is no good agreement between the data and the models from 1.4 GeV to 2.2 GeV.

The results are plotted as a function of E_γ and compared with Kaon-MAID calculations in Figure 6.20. The general trend is reasonably well reproduced at mid angles and low photon energies, however, the model does not predict negative asymmetries.

6.4.2 Discussion of target polarization results for $K^0\Sigma^0$

The target asymmetry results are compared to the Kaon-MAID model in Figure 6.21. The data are almost all consistent with zero over all kinematics. There are no model calculations available for the 2.2 GeV data.

The results are then compared to the RPR approach in Figure 6.22. It is difficult to say whether any model shows agreement with the data over all kinematics since the large error bars make discrimination between models very difficult. In general, the models do predict the correct sign of the asymmetry but always over predict the magnitude.

The target asymmetry results are plotted as a function of E_γ and compared with Kaon-MAID core calculations in Figure 6.23. The models do not reproduce the data

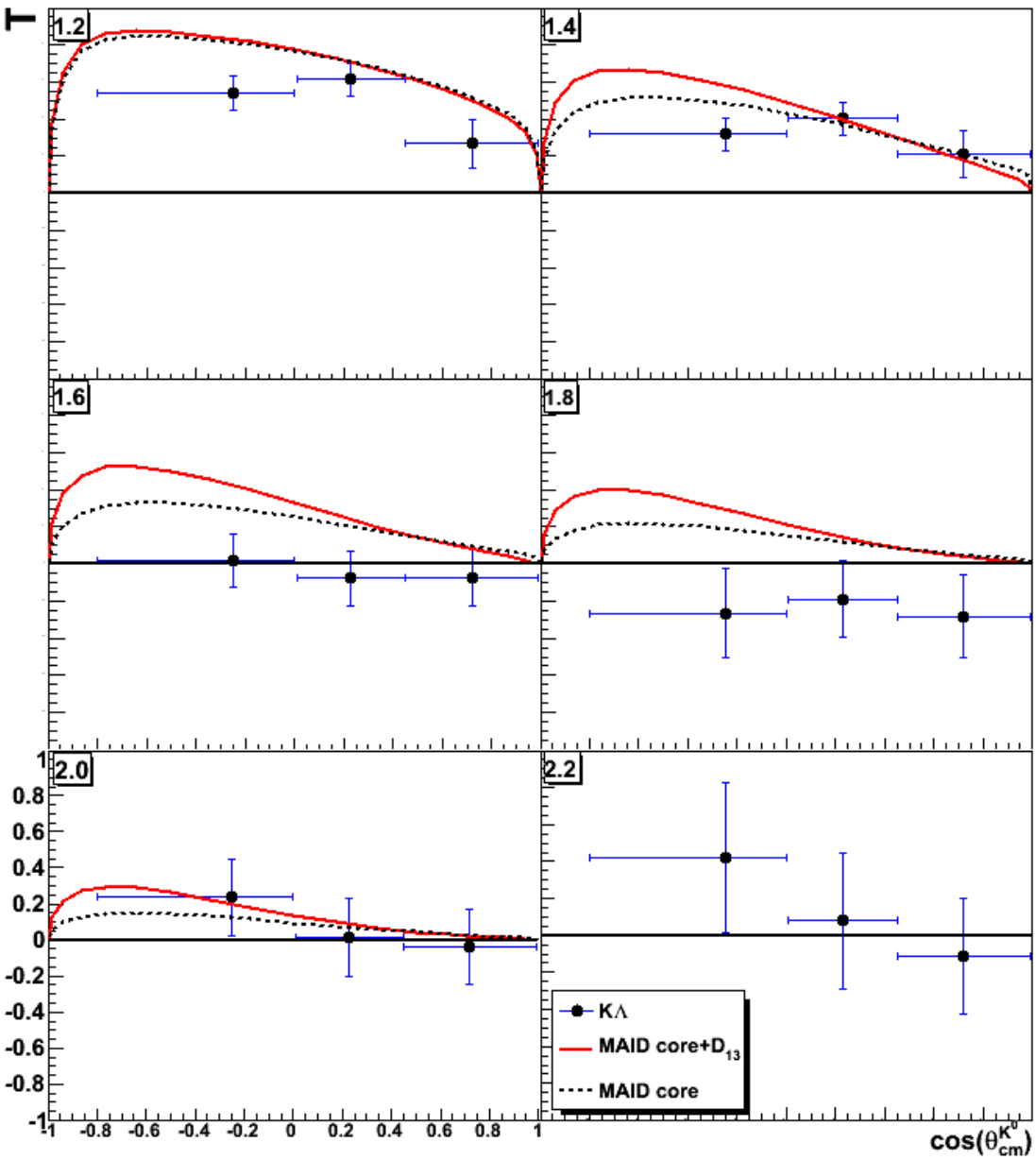

Figure 6.18: Target asymmetry for the reaction $\gamma n \rightarrow K^0\Lambda$ as a function of $\cos(\theta_{cm}^{K^0})$ ranging from E_γ= 1.2 GeV (top left) to 2.2 GeV (bottom right). Data are compared to model calculations from the Kaon-MAID model: core resonances (black dashed line), inclusion of $D_{13}(1900)$ (solid red line).

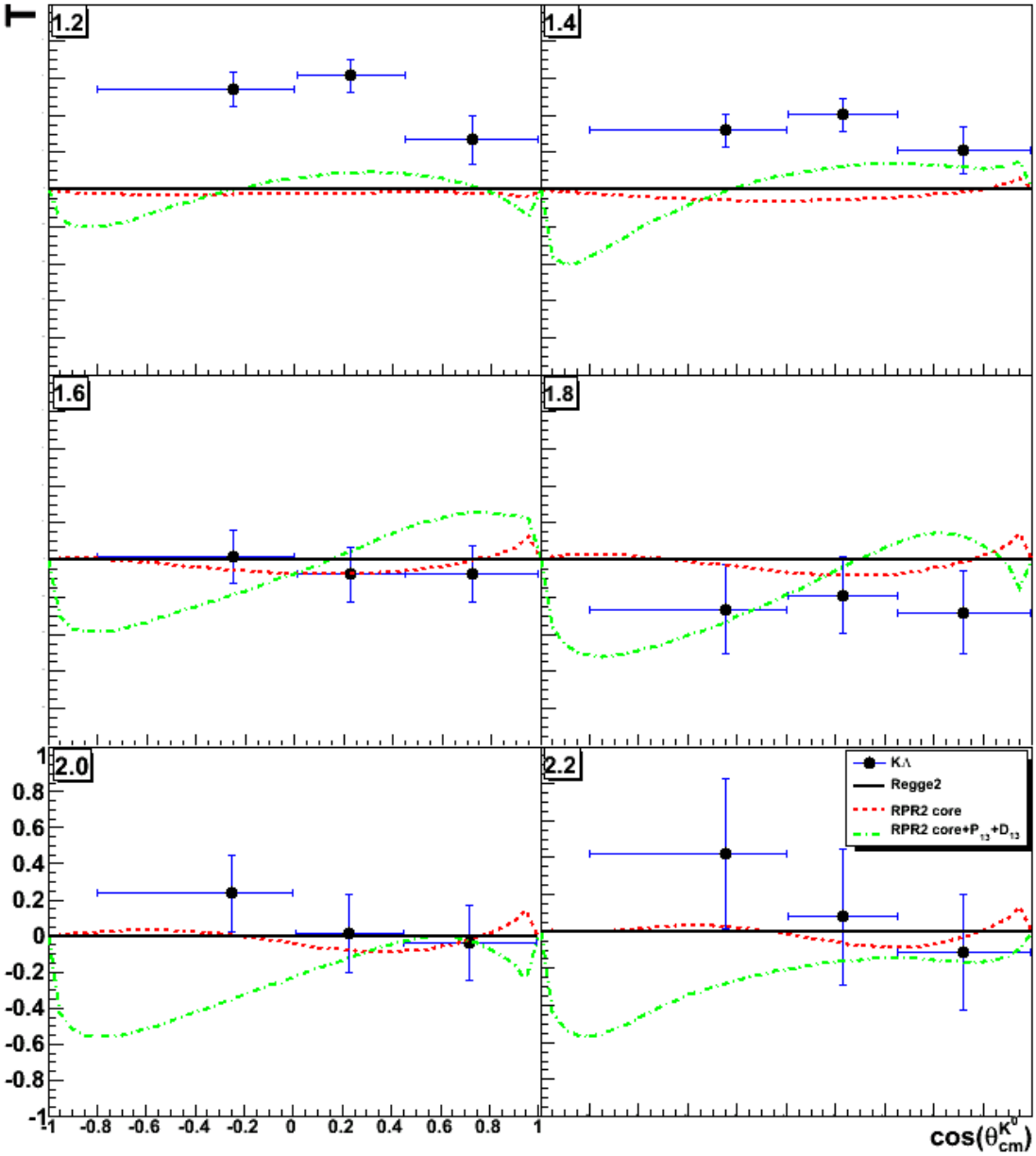

Figure 6.19: Target asymmetry for the reaction $\gamma n \rightarrow K^0\Lambda$ as a function of $\cos(\theta_{cm}^{K^0})$ ranging from E_γ= 1.2 GeV (top left) to 2.2 GeV (bottom right). Data are compared to model calculations from the Regge-plus-resonance approach: Regge background (solid black line), core resonances (red dashed line) core resonances plus the inclusion of $D_{13}(1900)$ and $P_{13}(1900)$ states (green dot-dash line).

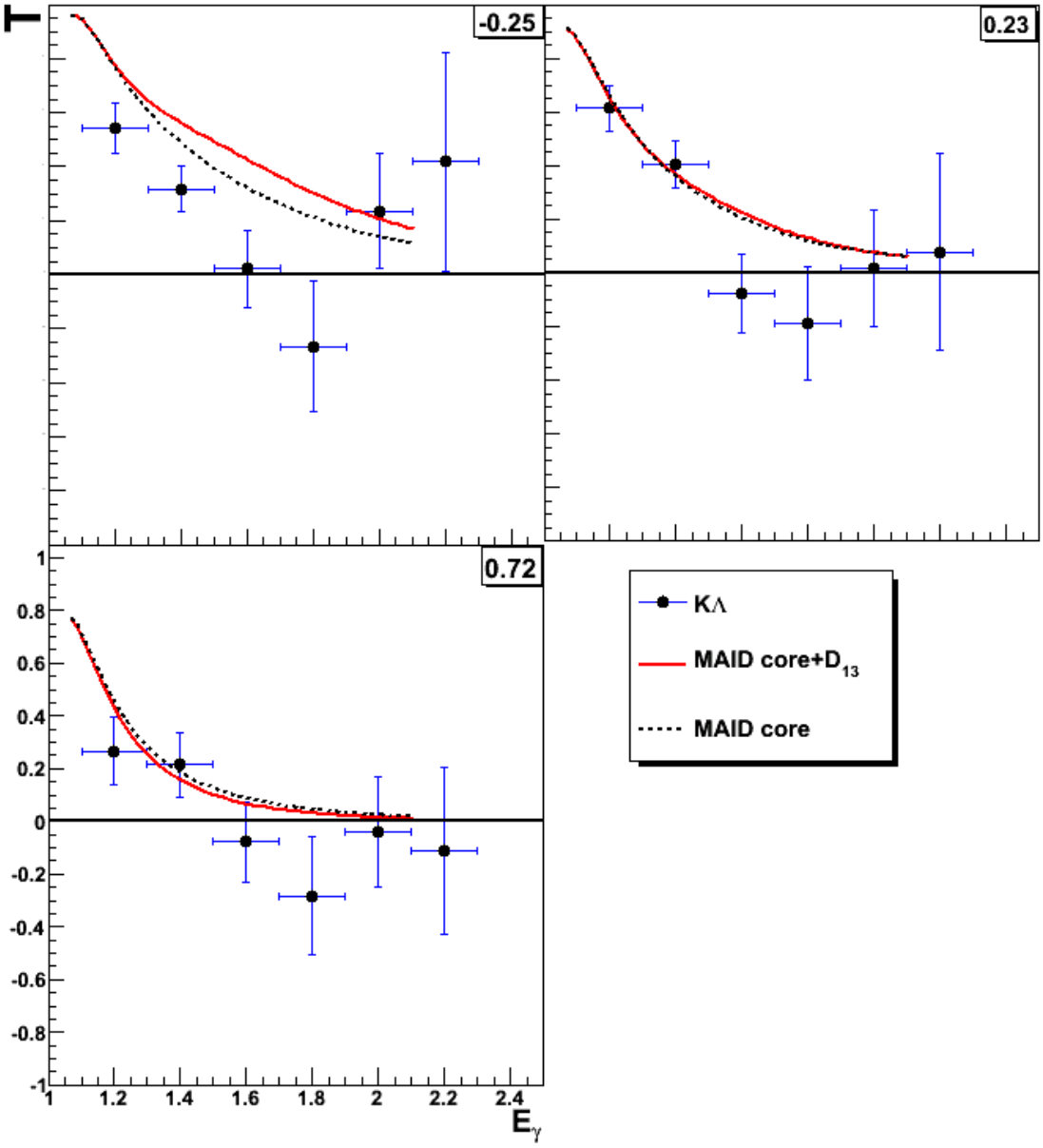

Figure 6.20: Target asymmetry for the reaction $\gamma n \rightarrow K^0\Lambda$ as a function of E_γ ranging from $\cos(\theta_{CM}^{K^0})$ = -0.4 (left) to 0.72 (right).

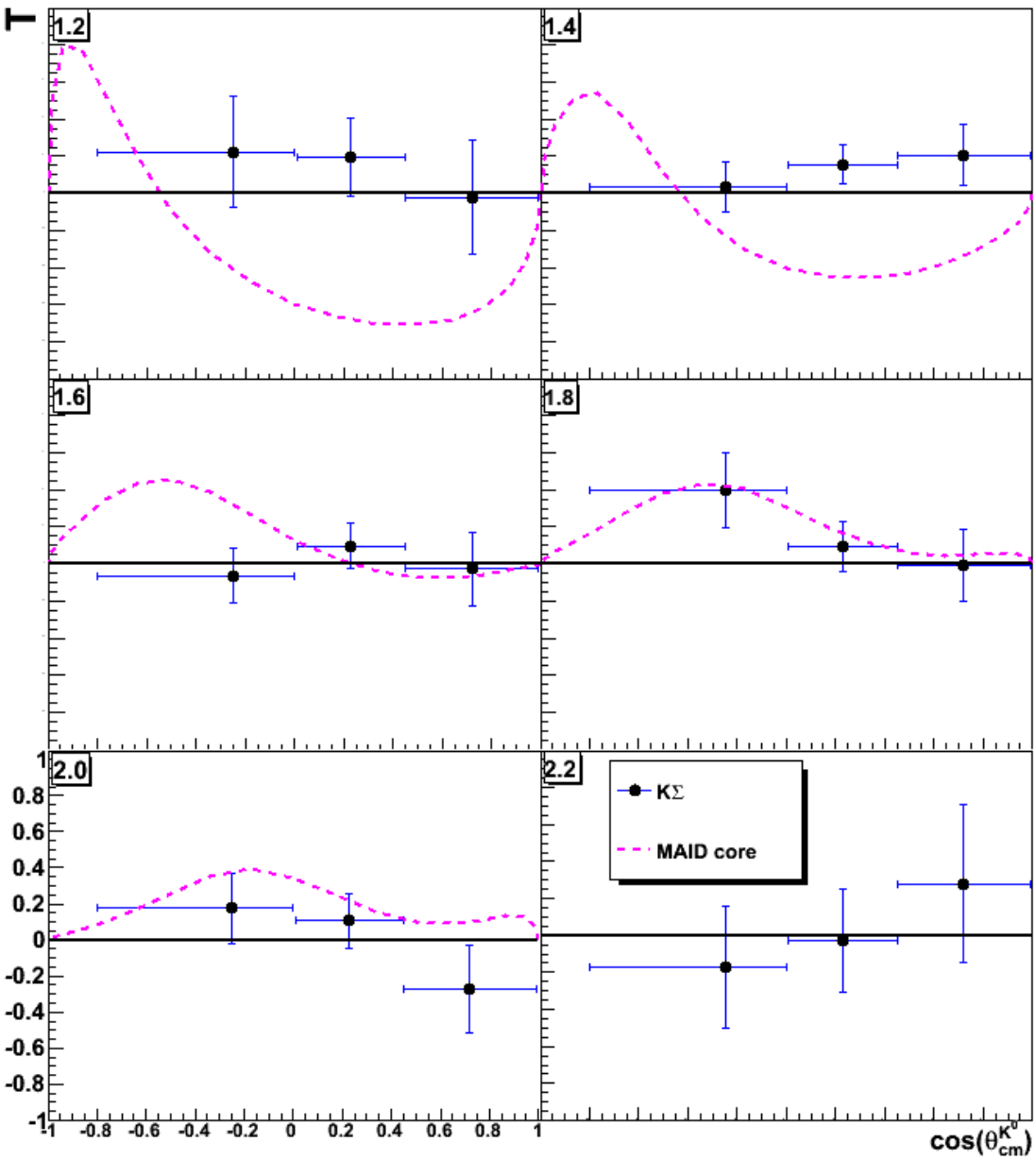

Figure 6.21: Target asymmetry for the reaction $\gamma n \rightarrow K^0\Sigma^0$ as a function of $\cos(\theta^{K^0}_{cm})$ ranging from E_γ= 1.2 GeV (top left) to 2.2 GeV (bottom right). Data are compared to model calculations from the Kaon-MAID model: core set of resonances (dashed pink line).

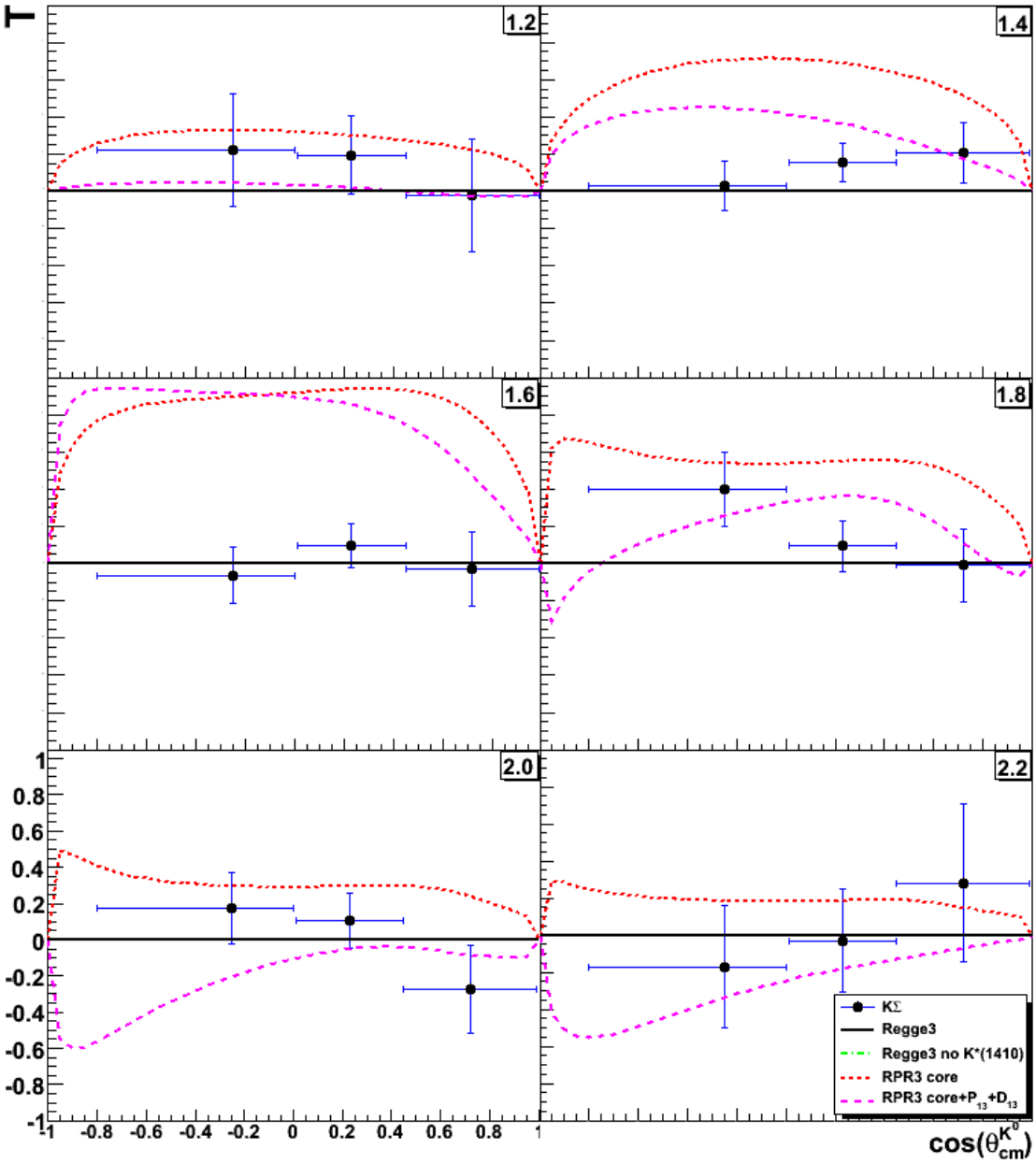

Figure 6.22: Target asymmetry for the reaction $\gamma n \rightarrow K^0\Sigma^0$ as a function of $\cos(\theta^{K^0}_{cm})$ ranging from E_γ= 1.2 GeV (top left) to 2.2 GeV (bottom right). Data are compared to model calculations from the Regge-plus-resonance approach: Regge background with K*(892) and K*(1410) trajectories (solid black line), Regge background with K*(892) trajectory only (green dot-dashed line), core resonances (red dashed line), core resonances plus inclusion of P_{13}(1900) (pink dashed line).

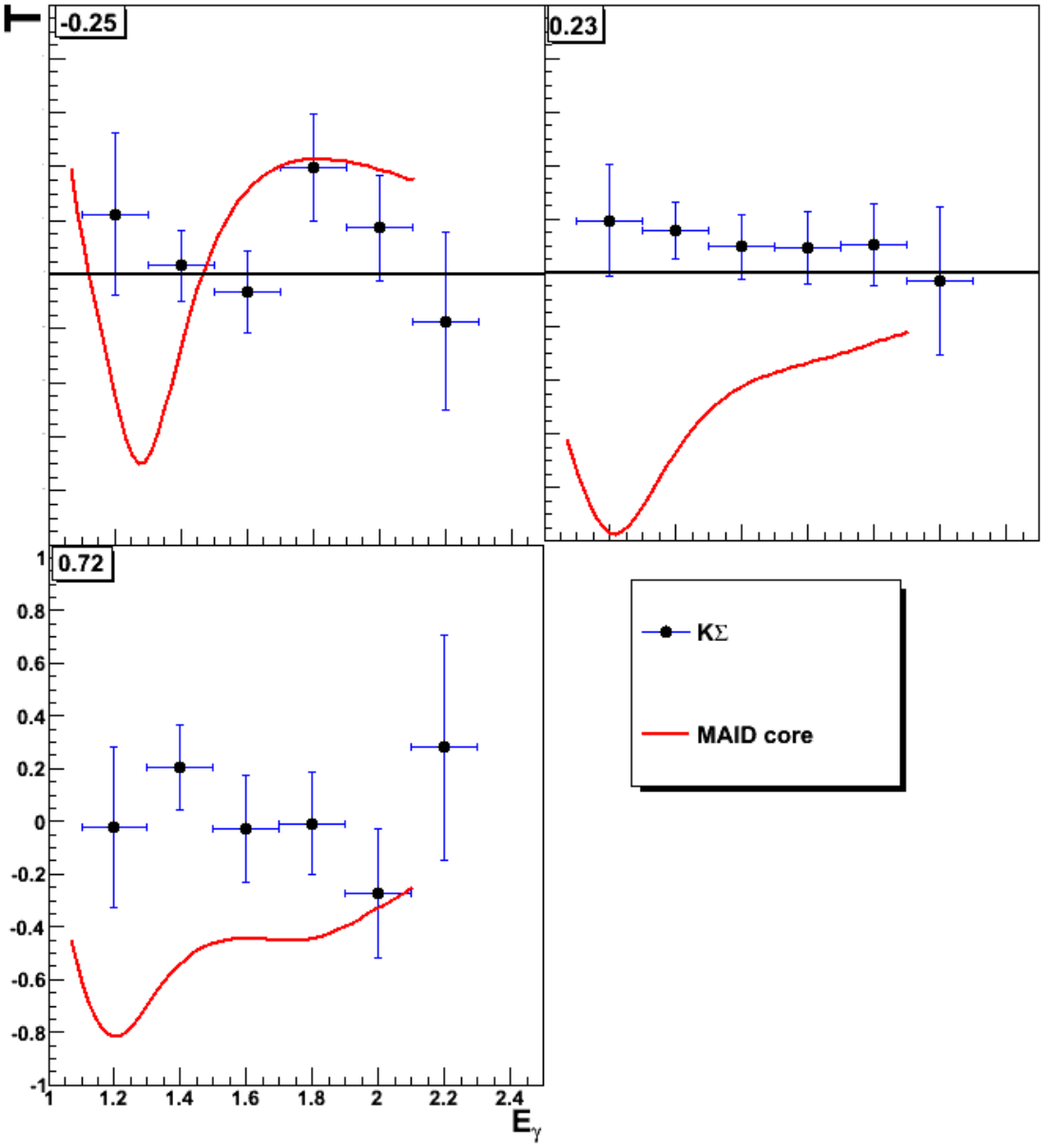

Figure 6.23: Target asymmetry for the reaction $\gamma n \rightarrow K^0\Sigma^0$ as a function of E_γ ranging from $\cos(\theta^{K^0}_{CM})$ = -0.4 (top left) to 0.72 (bottom left).

6.5 Double Polarization Observables, O_x and O_z

The double polarization observables O_x and O_z are compared to model calculations from the Kaon-MAID framework for the $K^0\Lambda$ channel as a function of $\cos(\theta_{cm}^{K^0})$ in Figures 6.24 and 6.25. They are then compared to the Regge-plus-resonance approach in Figures 6.26 and 6.27. The results are then shown as a function of E_γ in Figures 6.28 and 6.29. Similar plots for the $K^0\Sigma^0$ channel are shown in Figures 6.30 through 6.35. Although the statistics are limited this is a first measurement and offers some discrimination between the model calculations.

6.5.1 Discussion of O_x/O_z results for $K^0\Lambda$

The O_x results are compared to the Kaon-MAID model in Figure 6.24. At the lowest energy, 1.2 GeV there is a strong polarization signal over all $\cos(\theta_{cm}^{K^0})$ angles for O_x. For energies beyond 1.6 GeV, the polarization becomes negative in most angular bins, which differs to the predictions from the Kaon-MAID calculations. There are no calculations available for the 2.2 GeV energy data.

The O_z results are compared to the Kaon-MAID model in Figure 6.25. The preliminary calculations in general do not produce an accurate description of the data. Again, there are no calculations available for the 2.2 GeV energy data.

The results for O_x are compared to the RPR approach in Figure 6.26. The data between 1.2 GeV to 1.4 GeV are positive over all angles where as the models predict negative polarizations at backward angles. The data between 1.6 GeV and 2.2 GeV have a very small polarization transfer or are consistent with zero. Results for O_z are compared to the RPR calculations in Figure 6.27. The data for energies between 1.2 and 1.8 GeV are within error consistent with zero. The data at 2.0 GeV have negative polarizations and at 2.2 GeV the statistics are too low to make any comparison.

The results are plotted as a function of E_γ and compared with Kaon-MAID calculations in Figures 6.28 and 6.29. The calculations do not reproduce the data.

6.5.2 Discussion of O_x/O_z results for $K^0\Sigma^0$

The results for O_x are compared to the Kaon-MAID calculations in Figure 6.30. The first observation for O_x is that the Kaon-MAID calculations describe the general trend and magnitude of the data well up to an energy of 1.4 GeV. At energies beyond 1.6 GeV, the models do not describe the data well. They differ in sign and either under or over predict the magnitude of the polarization. There are no calculations available for the 2.2 GeV energy data.

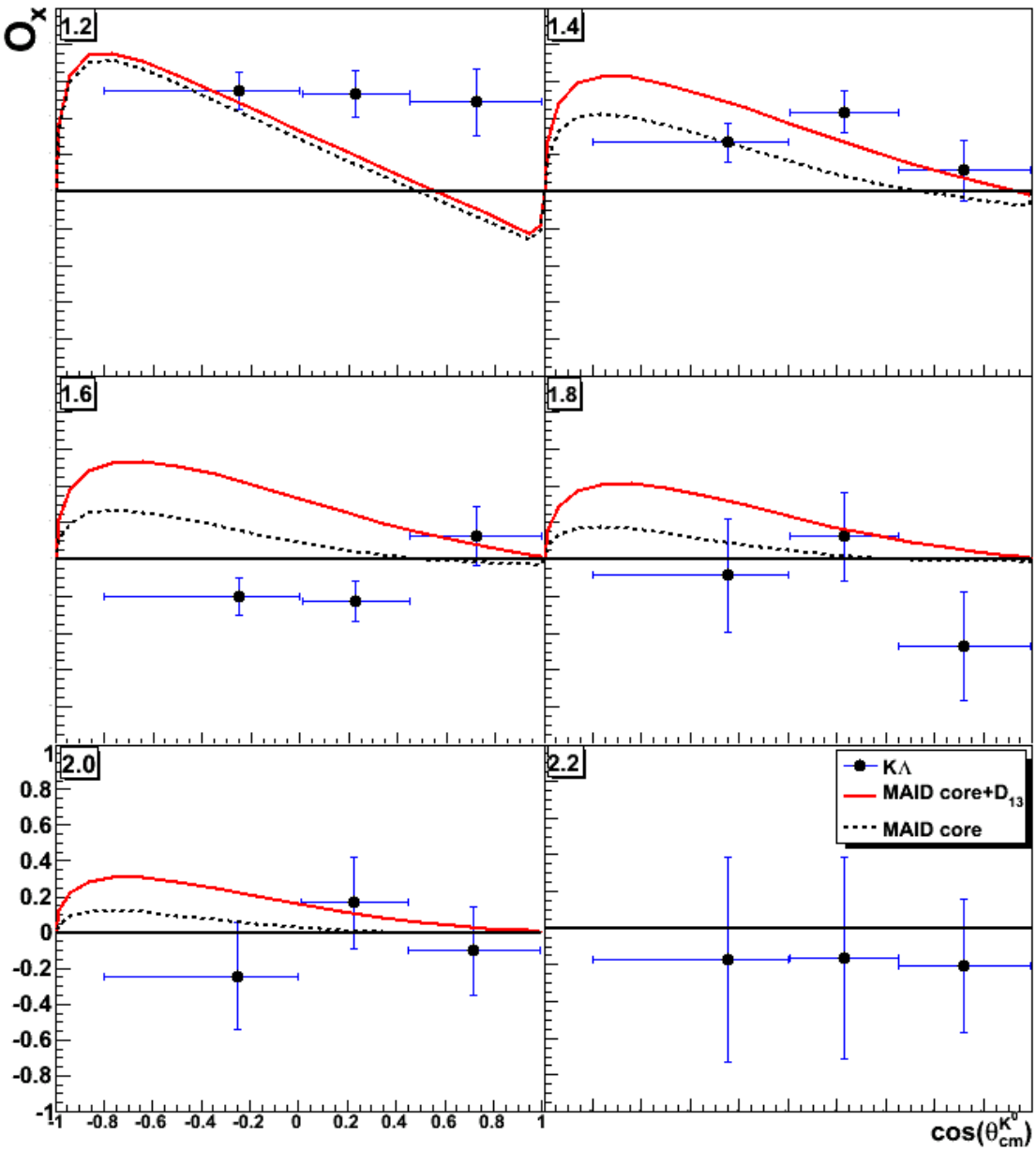

Figure 6.24: O_x double polarization observable for the reaction $\gamma n \rightarrow K^0\Lambda$ as a function of $\cos(\theta_{cm}^{K^0})$ ranging fr$_{x_x}$om E_γ= 1.2 GeV (top left) to 2.2 GeV (bottom right). Data are compared with model curves from the Kaon-MAID isobar model: core resonances (black dashed line) and including $D_{13}(1900)$ (solid red line).

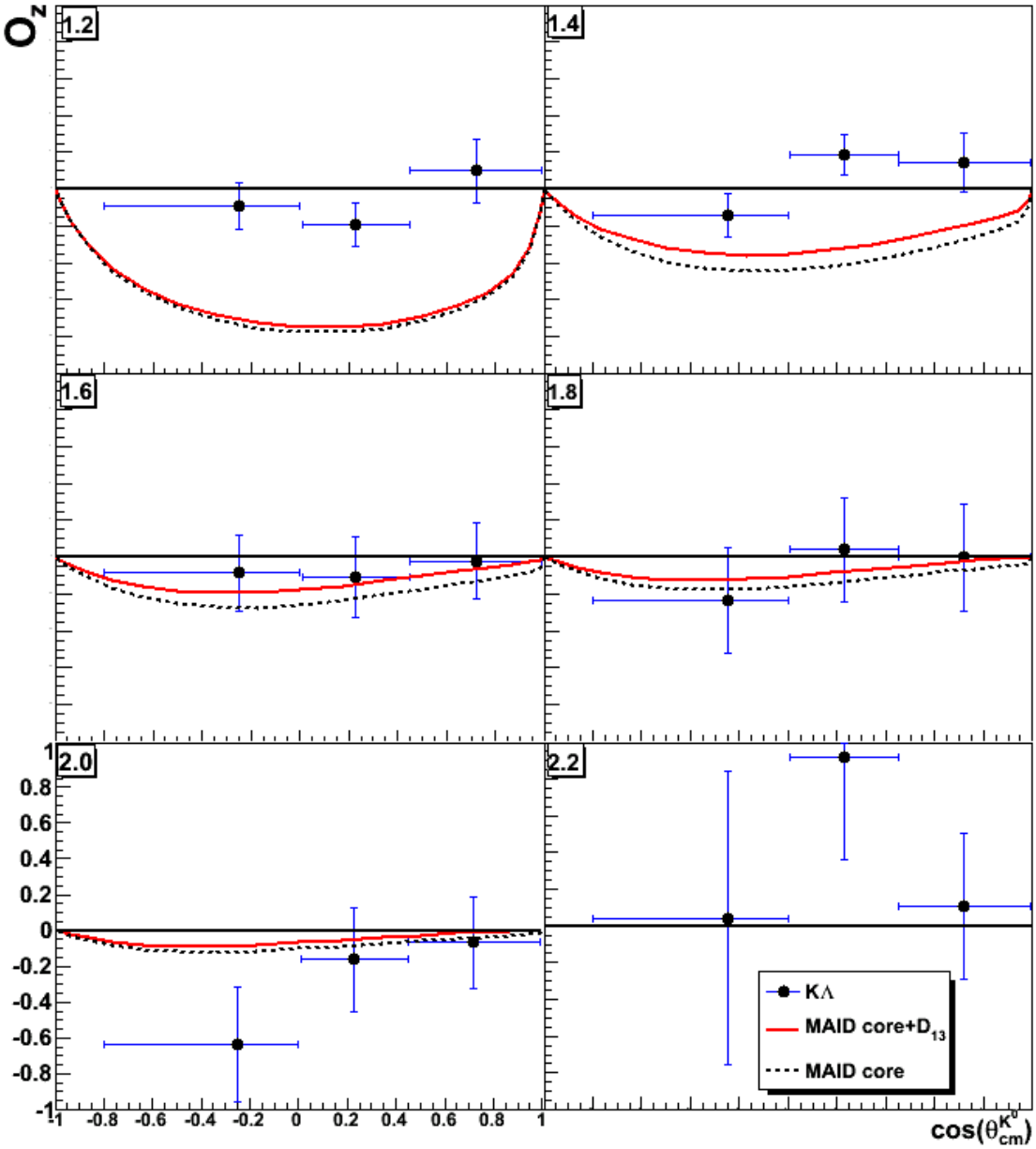

Figure 6.25: O_z double polarization observable for the reaction $\gamma n \rightarrow K^0\Lambda$ as a function of $\cos(\theta^{K^0}_{cm})$ ranging from E_γ= 1.2 GeV (top left) to 2.2 GeV (bottom right). Data are compared with model curves from the Kaon-MAID isobar model: core resonances (black dashed line) and including D_{13}(1900) (solid red line).

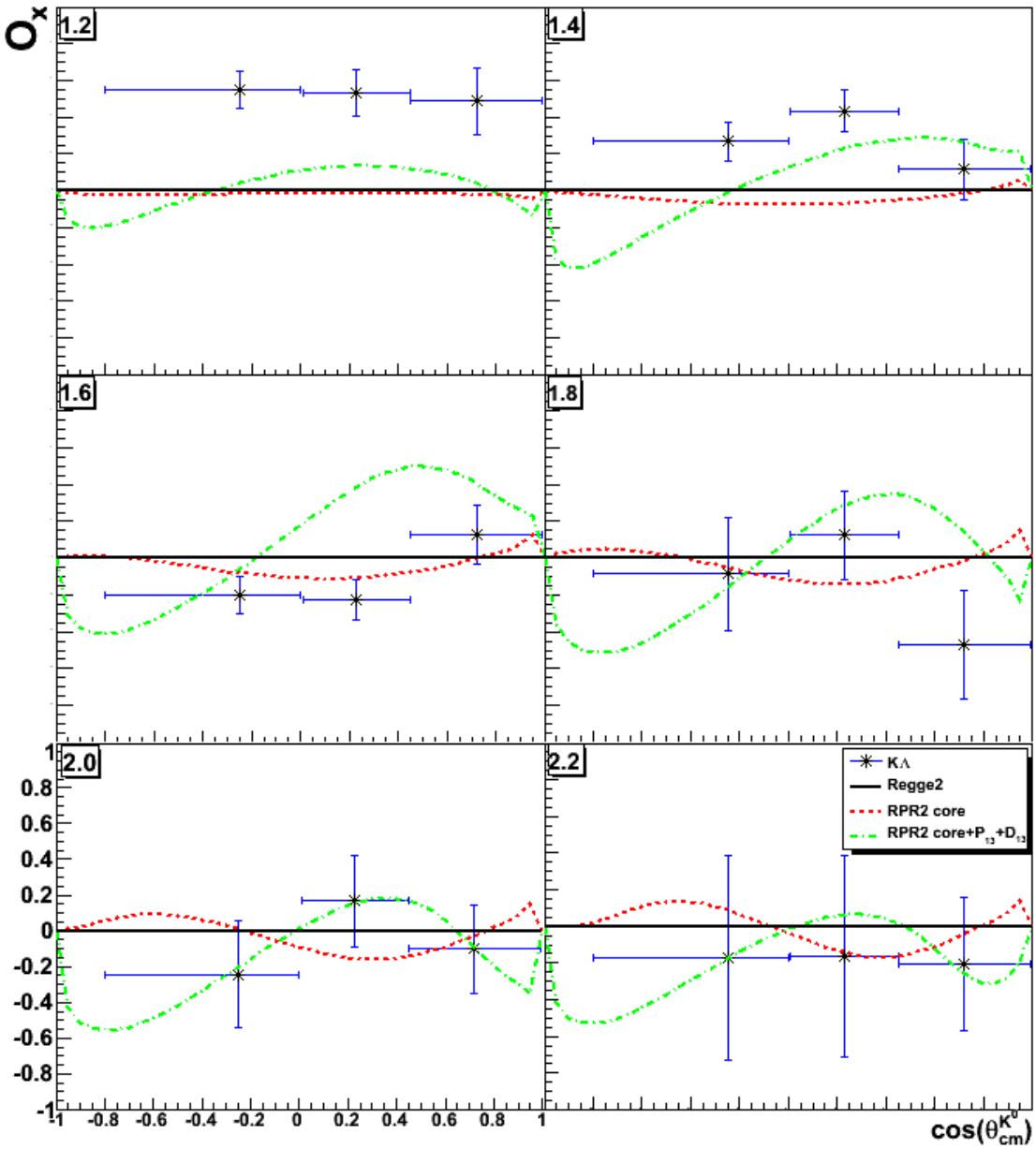

Figure 6.26: O_x double polarization observable for the reaction $\gamma n \rightarrow K^0\Lambda$ as a function of $\cos(\theta^{K^0}_{cm})$ ranging from E_γ= 1.2 GeV (top left) to 2.2 GeV (bottom right). Data are compared to model calculations from the Regge-plus-resonance approach: Regge background (solid black line), core resonances (red dashed line) core resonances plus the inclusion of $D_{13}(1900)$ and $P_{13}(1900)$ states (green dot-dash line).

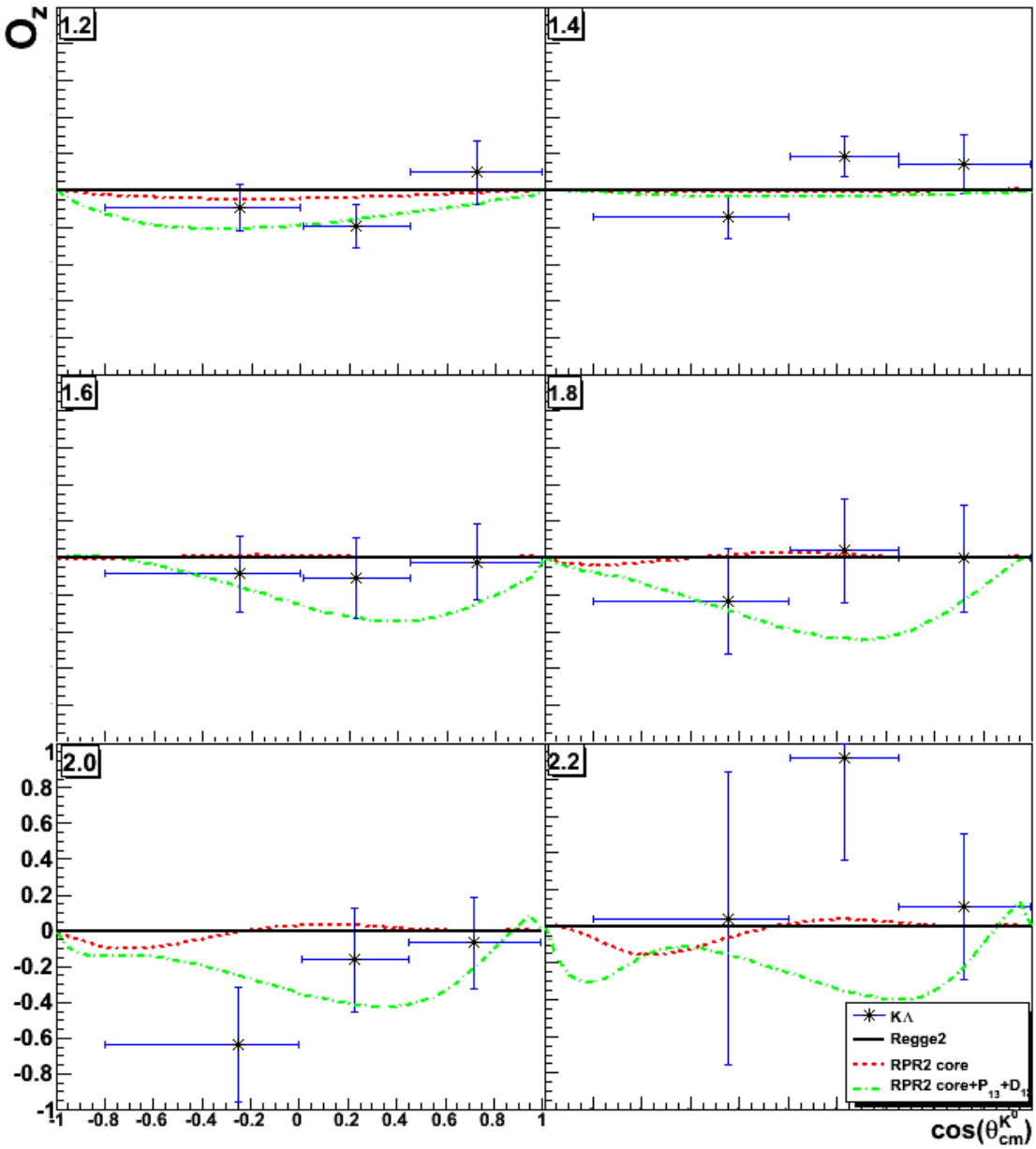

Figure 6.27: O_z double polarization observable for the reaction $\gamma n \rightarrow K^0\Lambda$ as a function of $\cos(\theta^{K^0}_{cm})$ ranging from E_γ= 1.2 GeV (top left) to 2.2 GeV (bottom right). Data are compared to model calculations from the Regge-plus-resonance approach: Regge background (solid black line), core resonances (red dashed line) core resonances plus the inclusion of $D_{13}(1900)$ and $P_{13}(1900)$ states (green dot-dash line).

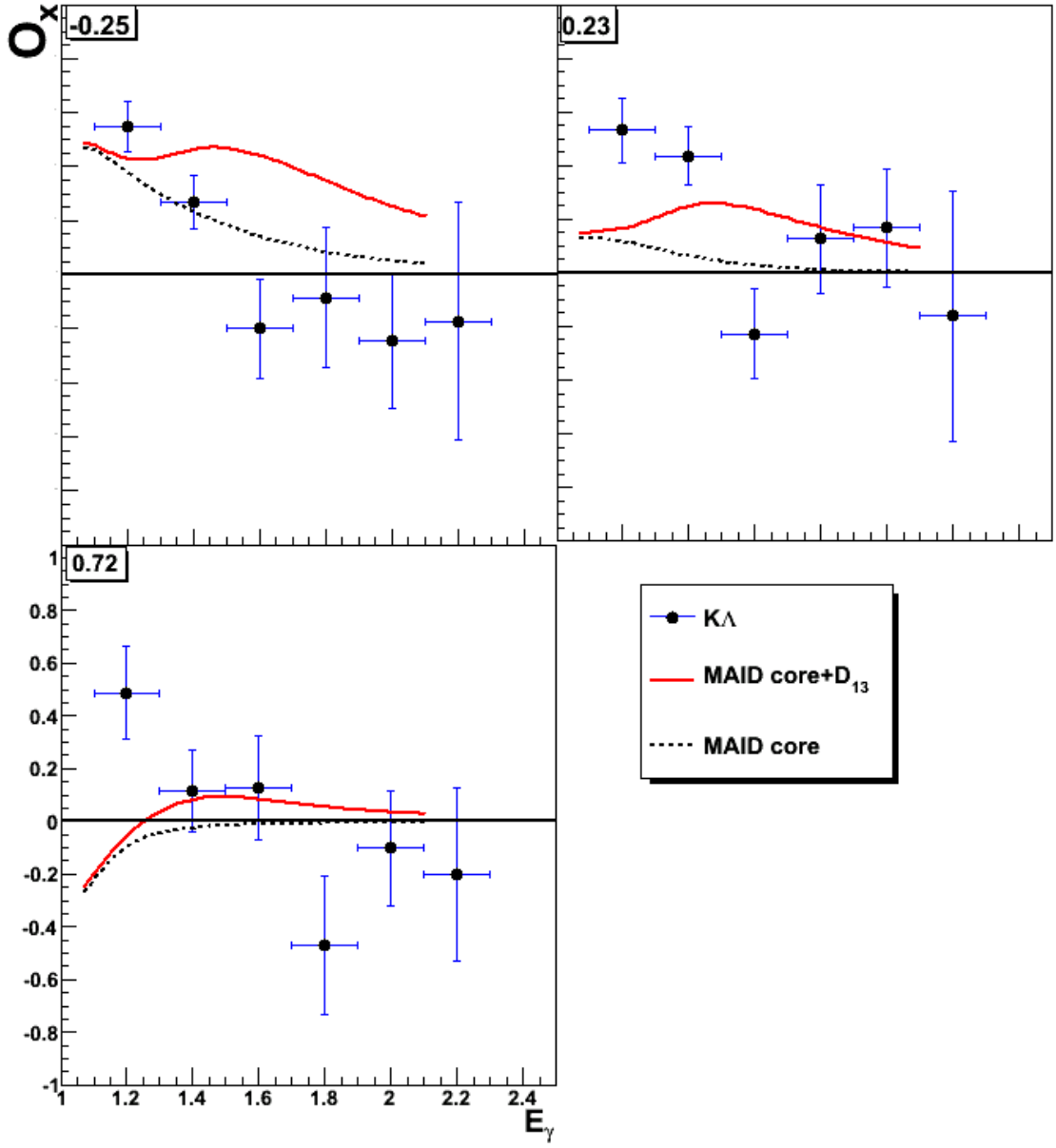

Figure 6.28: O_x double polarization observable for the reaction $\gamma n \rightarrow K^0\Lambda$ as a function of E_γ ranging from $\cos(\theta^{K^0}_{CM})$ = -0.4 (left) to 0.72 (right).

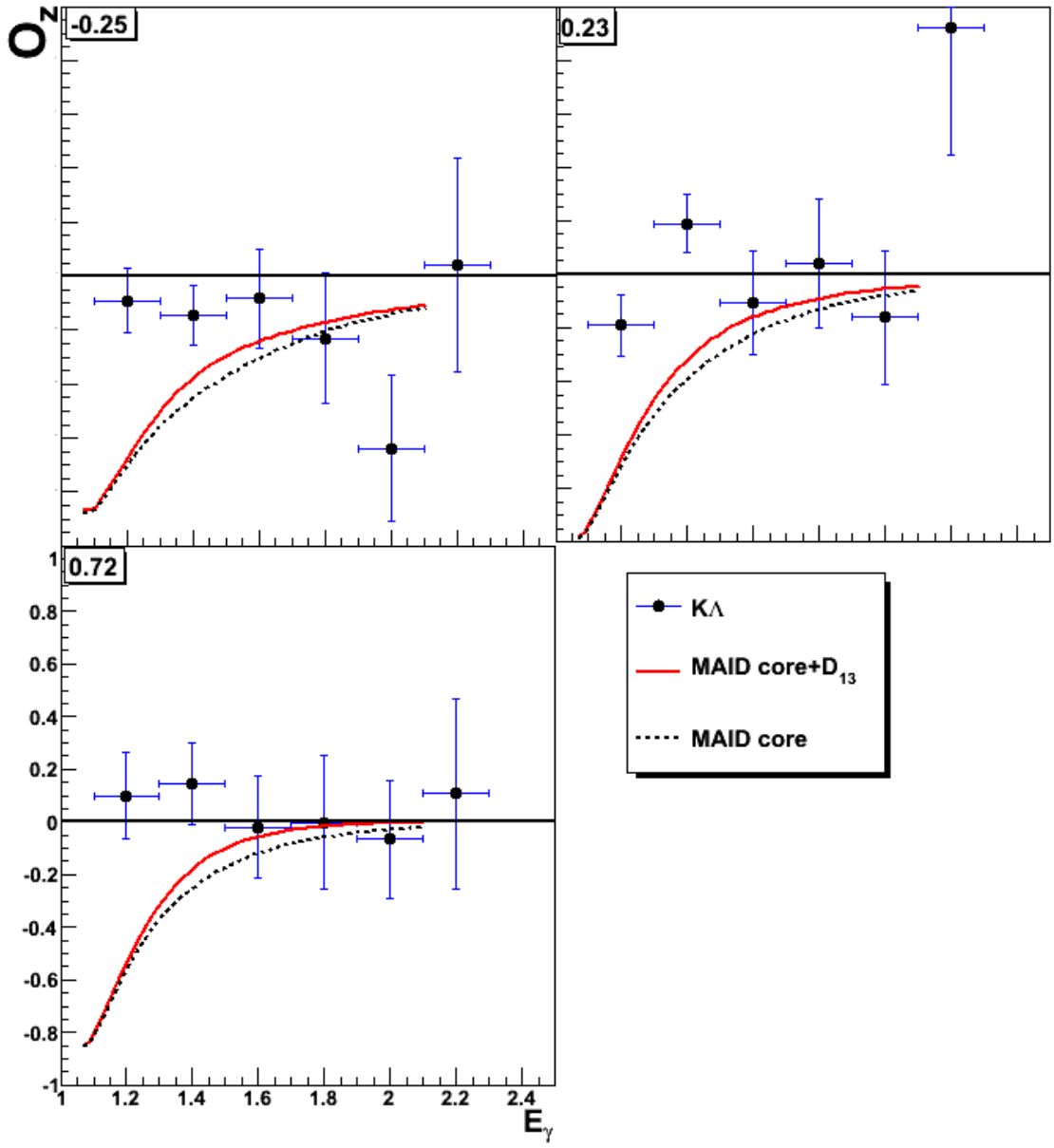

Figure 6.29: O_z double polarization observable for the reaction $\gamma n \rightarrow K^0\Lambda$ as a function of E_γ ranging from $\cos(\theta^{K^0}_{CM})$ = -0.4 (left) to 0.72 (right).

The O_z results are then compared to the Kaon-MAID model in Figure 6.31. This model describes the general trend of the data for O_z at 1.2 GeV well but fails to predict the magnitude of the asymmetry. At 1.4 GeV, the asymmetries are negative over backward to mid angles, becoming positive at forward angles. The model fails to account for the negative asymmetries at backward to mid angles as it rises to positive values much sooner than the data. The trend of the data at mid to forward angles at 1.6 GeV is reasonably well described by the model, however it does not agree with the data at backward angles. Again, at 1.8 GeV the model predicts the overall data trend at mid to forward angles well but over predicts the magnitude of the asymmetry in this region. The model differs in sign to the data at backward angles. The backward angle data at 2.0 GeV differs in sign to the model. At mid angles the model and data agree well, however at forward angles the model predicts a larger asymmetry than is measured. There are no calculations available for the 2.2 GeV energy data.

The O_x and O_z results are also compared to the RPR approach in Figures 6.32 and 6.33. The O_x results over all kinematics are not well described by the models including any resonant states. For a large range of the kinematics the results are consistent with zero. The Regge background models also predict a zero polarization over all kinematics.

The results for O_z are not well described by the RPR models. For energies between 1.2 and 2.0 GeV the measured polarization transfer is small. At 2.2 GeV, the backward angles show a large negative polarization transfer. The RPR models predict smaller positive polarizations at this energy.

The results are finally plotted as a function of E_γ and compared with Kaon-MAID core calculations in Figures 6.34 and 6.35. The data are again not well reproduced by the model curves.

6.6 Comparison of Photon Asymmetry and Hyperon Recoil Polarization with the free proton

The photon asymmetry and hyperon recoil polarization results are binned identically to those from the CLAS experiment [31] on the free proton. Figures 6.36 and 6.37 show the $K\Lambda$ and $K\Sigma^0$ photon asymmetry results plotted as a function of $\cos(\theta_{cm}^{K^0})$. Similar plots for the hyperon recoil polarization are plotted in Figures 6.38 and 6.39. The work from the free proton only reached photon energies of 2.1 GeV, where as the current work reached photon energies of 2.3 GeV. The results from the free proton are represented by the black triangles and the results of this

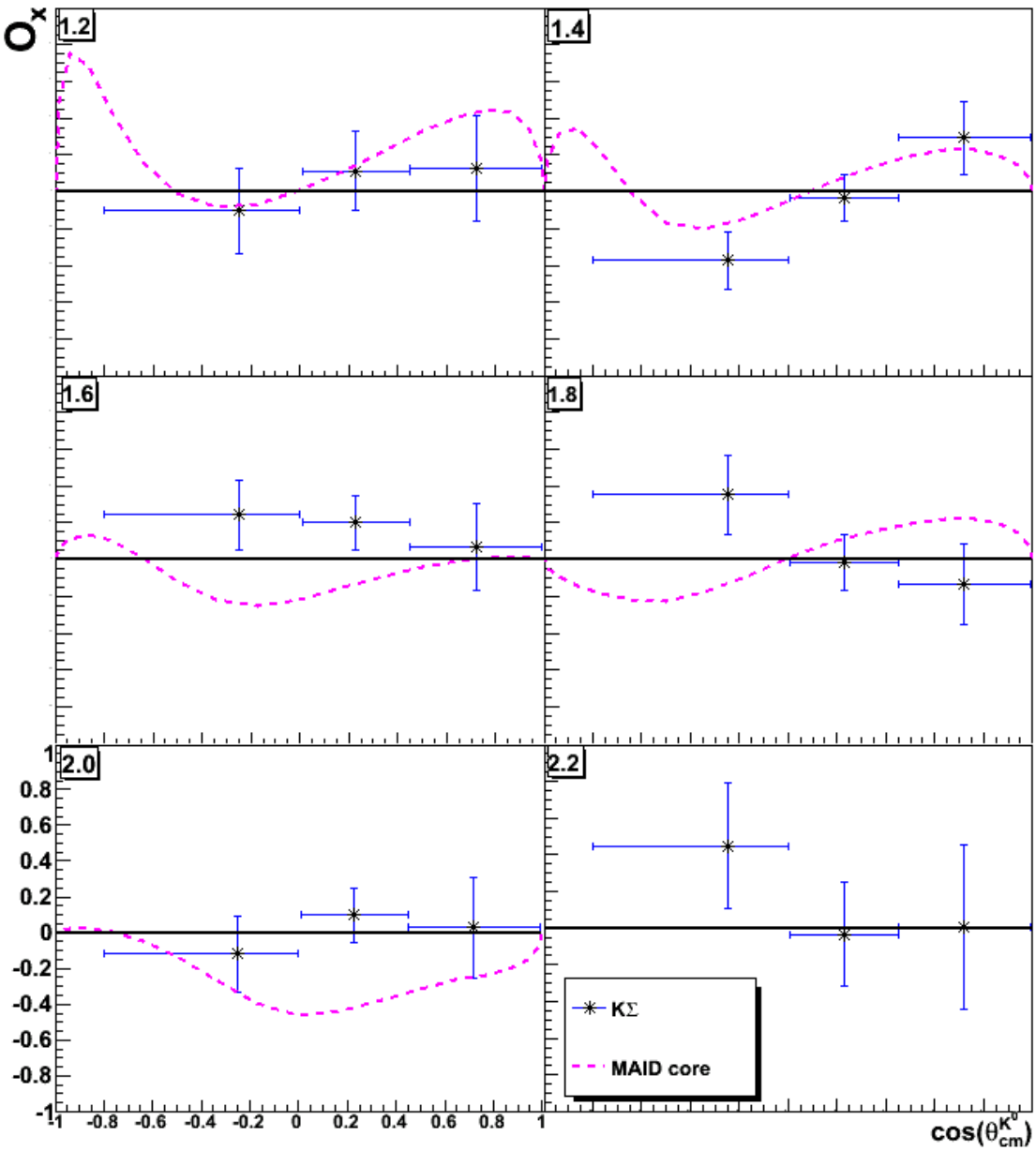

Figure 6.30: O_x double polarization observable for the reaction $\gamma n \rightarrow K^0\Sigma^0$ as a function of $\cos(\theta^{K^0}_{cm})$ ranging from E_γ= 1.3 GeV (top left) to 2.3 GeV (bottom right). Data are compared to model calculations from the Kaon-MAID model: core set of resonances (dashed pink line).

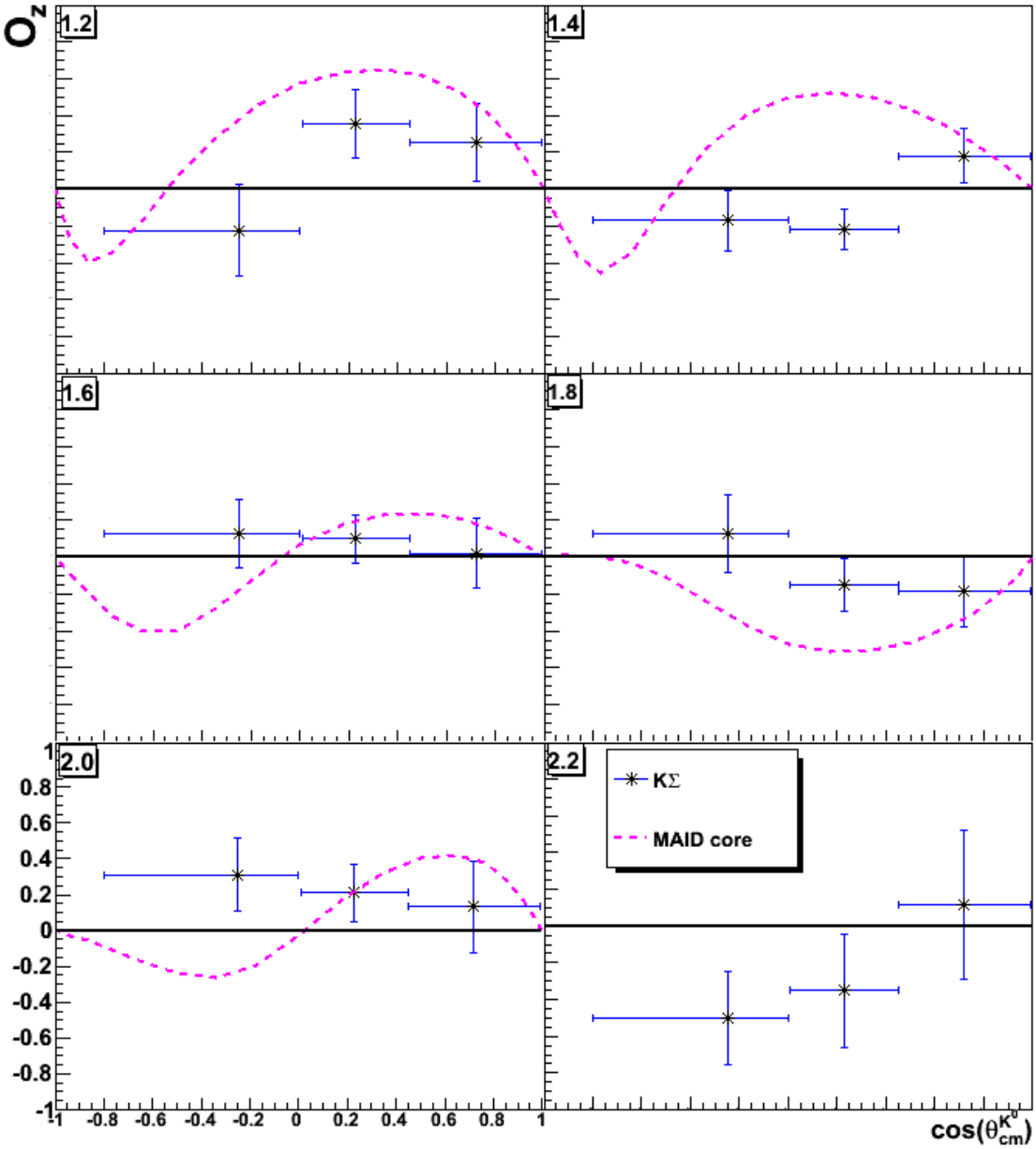

Figure 6.31: O_z double polarization observable for the reaction $\gamma n \rightarrow K^0\Sigma^0$ as a function of $\cos(\theta^{K^0}_{cm})$ ranging from E_γ= 1.3 GeV (top left) to 2.3 GeV (bottom right). Data are compared to model calculations from the Kaon-MAID model: core set of resonances (dashed pink line).

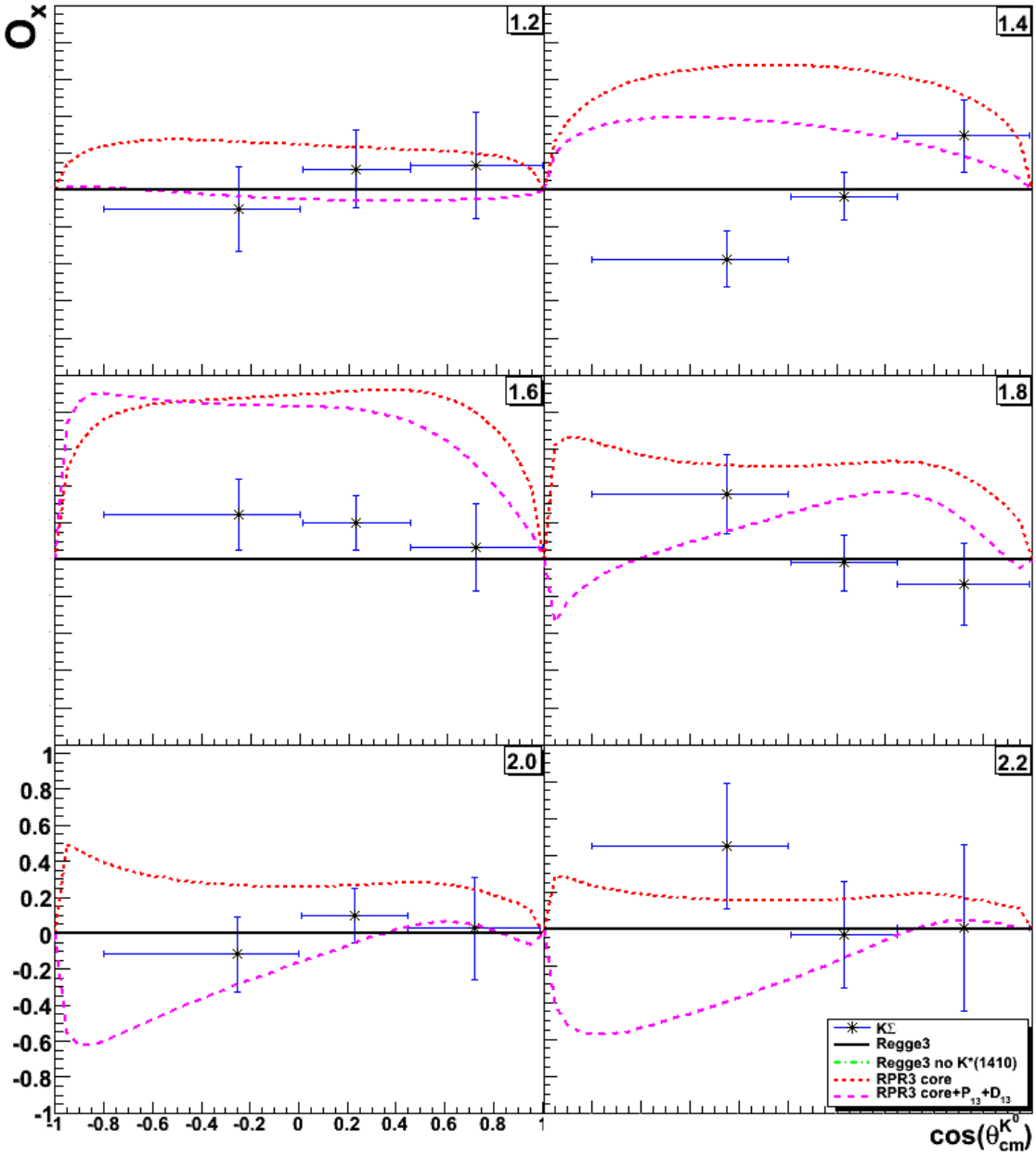

Figure 6.32: O_x double polarization observable for the reaction $\gamma n \rightarrow K^0\Sigma^0$ as a function of $\cos(\theta_{cm}^{K^0})$ ranging from E_γ= 1.2 GeV (top left) to 2.2 GeV (bottom right). Data are compared to model calculations from the Regge-plus-resonance approach: Regge background with K*(892) and K*(1410) trajectories (solid black line), Regge background with K*(892) trajectory only (green dot-dashed line), core resonances (red dashed line), core resonances plus inclusion of P_{13}(1900) (pink dashed line).

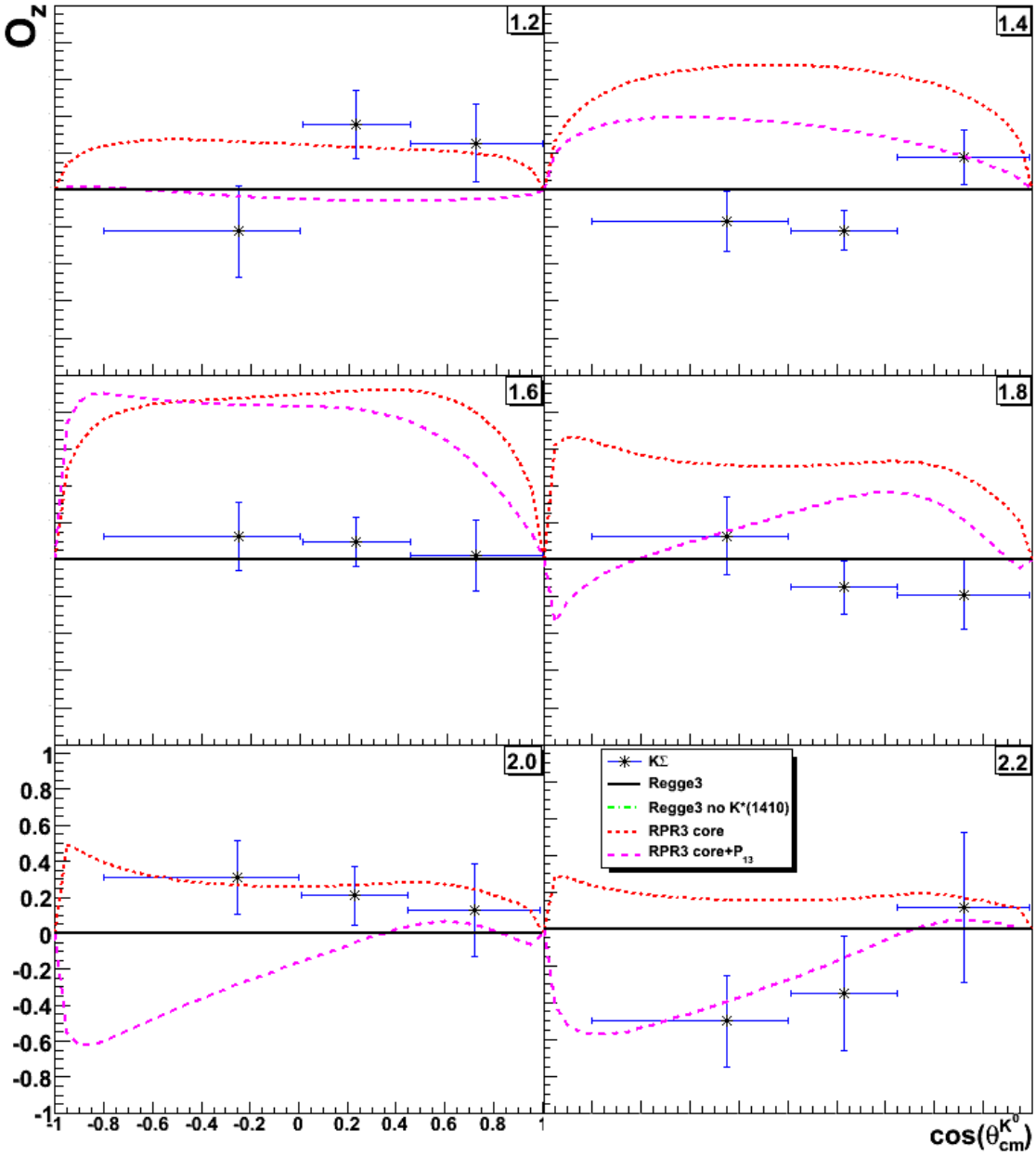

Figure 6.33: O_z double polarization observable for the reaction $\gamma n \rightarrow K^0\Sigma^0$ as a function of $\cos(\theta_{cm}^{K^0})$ ranging from E_γ= 1.2 GeV (top left) to 2.2 GeV (bottom right). Data are compared to model calculations from the Regge-plus-resonance approach: Regge background with K*(892) and K*(1410) trajectories (solid black line), Regge background with K*(892) trajectory only (green dot-dashed line), core resonances (red dashed line), core resonances plus inclusion of P_{13}(1900) (pink dashed line).

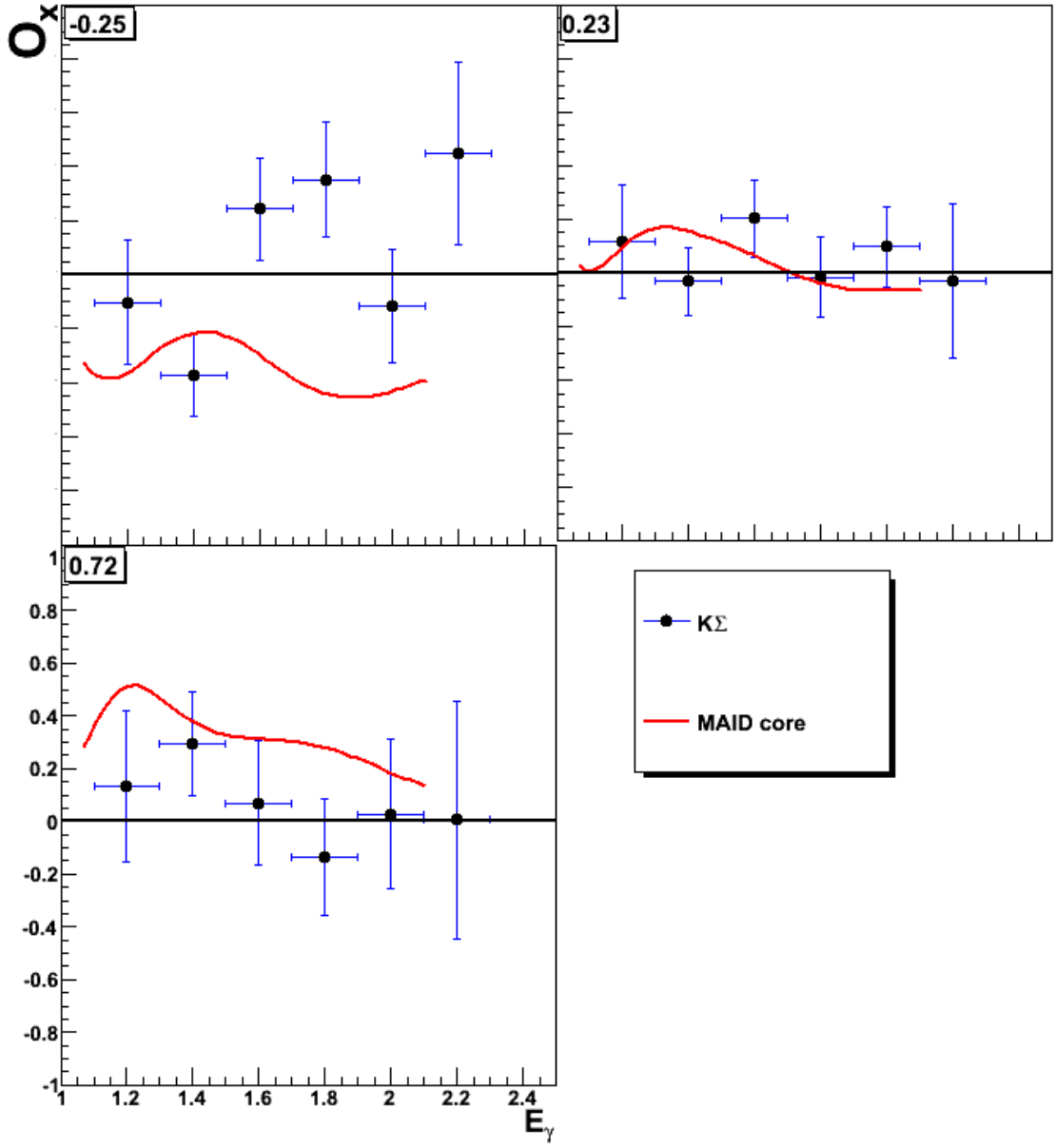

Figure 6.34: O_x double polarization observable for the reaction $\gamma n \rightarrow K^0\Sigma^0$ as a function of E_γ ranging from $\cos(\theta^{K^0}_{CM})$ = -0.4 (left) to 0.72 (right).

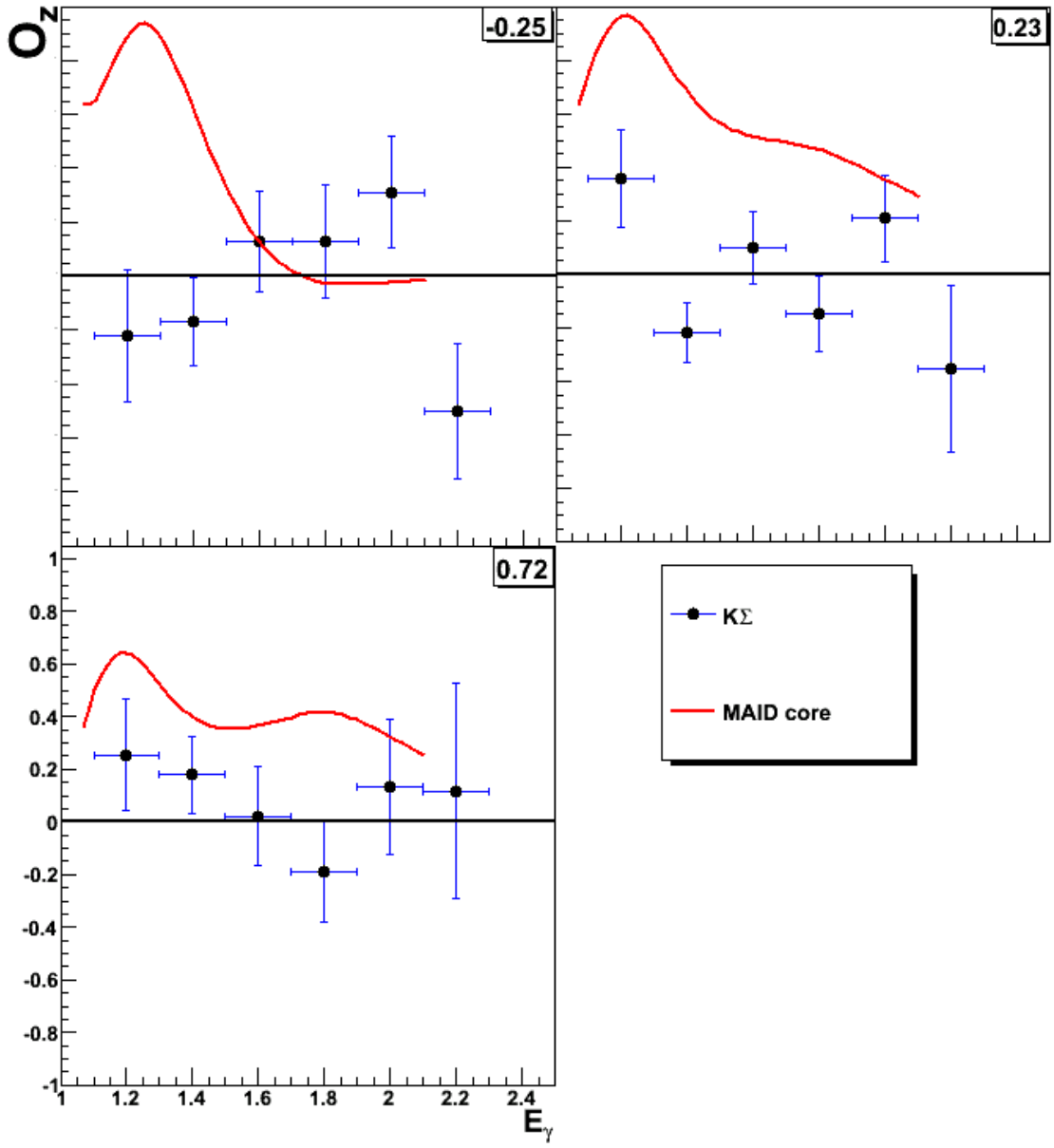

Figure 6.35: O_z double polarization observable for the reaction $\gamma n \rightarrow K^0\Sigma^0$ as a function of E_γ ranging from $\cos(\theta^{K^0}_{CM})$ = -0.4 (left) to 0.72 (right).

work are represented by green circles.

The photon asymmetry comparison for the KΛ channel shows the 1.3 GeV and 1.5 GeV data to exhibit some good overlap between the proton and neutron data. The 1.7 GeV and 1.9 GeV data show some difference at the backward angles. The proton data is positive over all angles where as the neutron data is negative at backward angles. The 2.1 GeV data for the proton starts to fall to zero showing a similar trend to the neutron data. The difference in sign between the proton and neutron data at backward angles could be a hint at a difference in the reaction production mechanism.

The comparison of the KΣ^0 results shows a sign difference in the photon asymmetry over all but the extreme forward angles over all energies. The free proton results are positive over all kinematics. The neutron results are negative except at the extreme forward angles where the asymmetry is positive.

The hyperon recoil polarization comparison between the free proton and bound neutron for the K$^0\Lambda$ channel shows some agreement at mid to forward angles as one moves to higher photon energies. Energies below 1.525 GeV show the recoil results from the neutron to be positive over all angles, whereas in the proton case the backward angle data are negative. At higher energies the backward angle data from the neutron become negative.

In the KΣ^0 case, the results from the neutron are predominantly positive over all energies. The results from the proton show a good proportion of the data to be negative.

6.7 Conclusions

This work presents the first ever results for several polarization observables for the reactions $\overrightarrow{\gamma}d\rightarrow K^0\Lambda$ (p$_s$) and $\overrightarrow{\gamma}d \rightarrow K^0\Sigma^0$ (p$_s$). Both single and double polarization observables have been measured; the photon beam asymmetry, recoil hyperon polarization, target asymmetry and the double polarization observables O$_x$ and O$_z$. The results for all observables are measured over a wide range of energies and angles.

The photon asymmetry results for the K$^0\Lambda$ channel are positive over all energies for mid to forward angles. The backward angles at all but the lowest energy setting show a negative photon asymmetry. Both the Kaon-MAID and RPR models require further development before any new physics claims can be made. For the K$^0\Sigma^0$ channel, the photon asymmetry is largely negative over all energies except at very forward angles. The Kaon-MAID model reproduces the

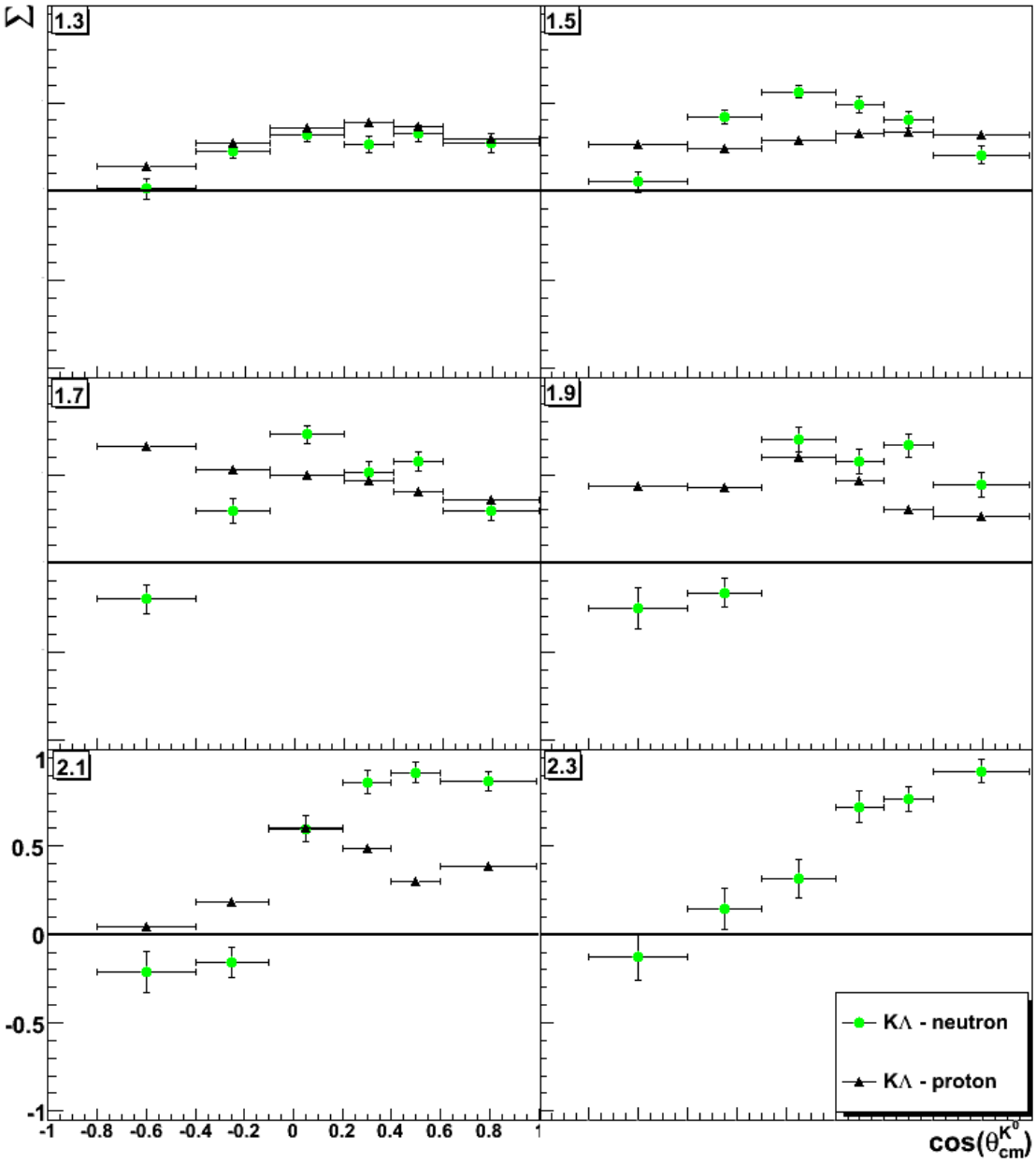

Figure 6.36: Photon asymmetry results for the KΛ channel from the free proton (black triangles) compared to the results from the bound neutron (green circles).

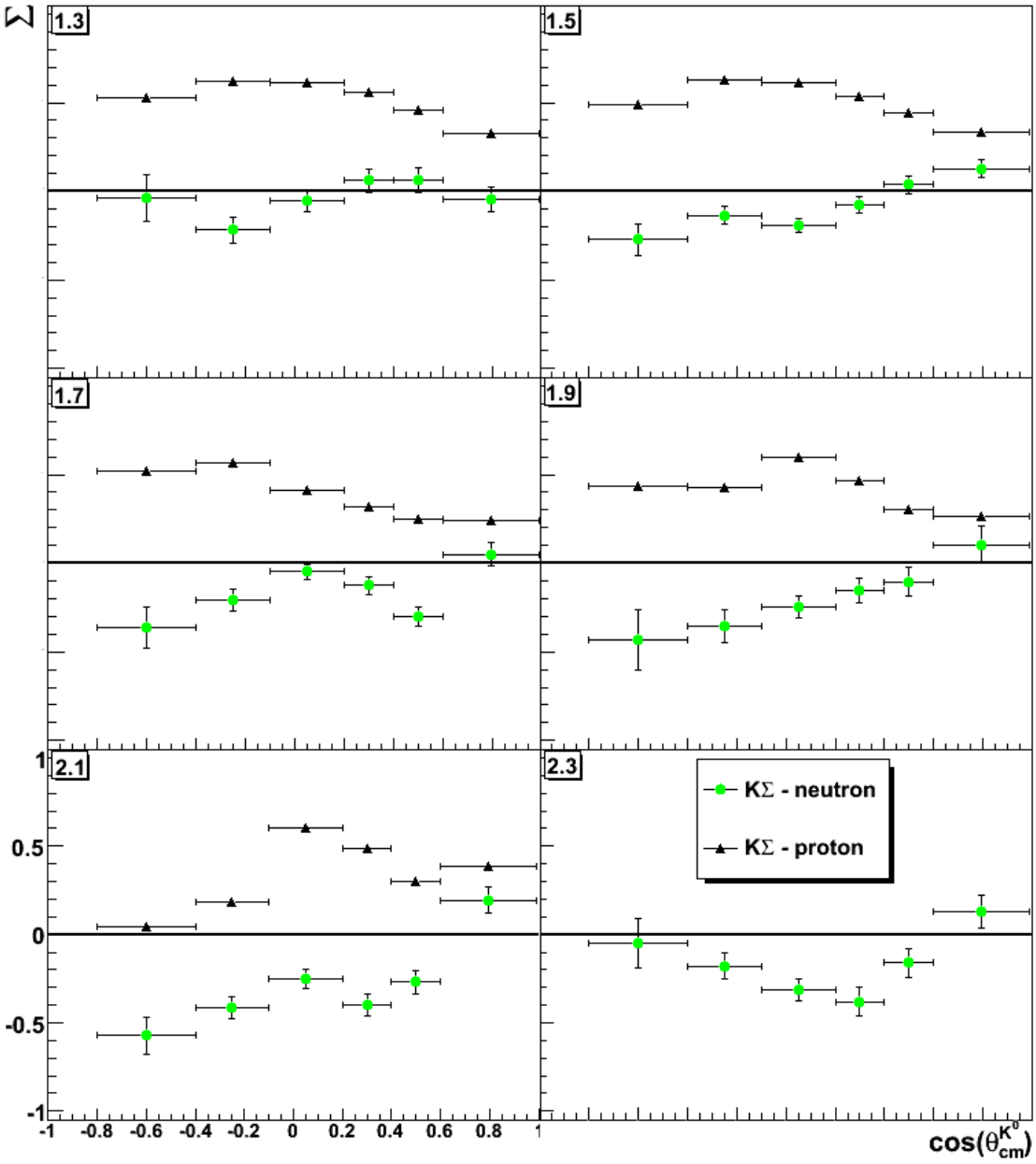

Figure 6.37: Photon asymmetry results for the $K\Sigma^0$ channel from the free proton (black triangles) compared to the results from the bound neutron (green circles).

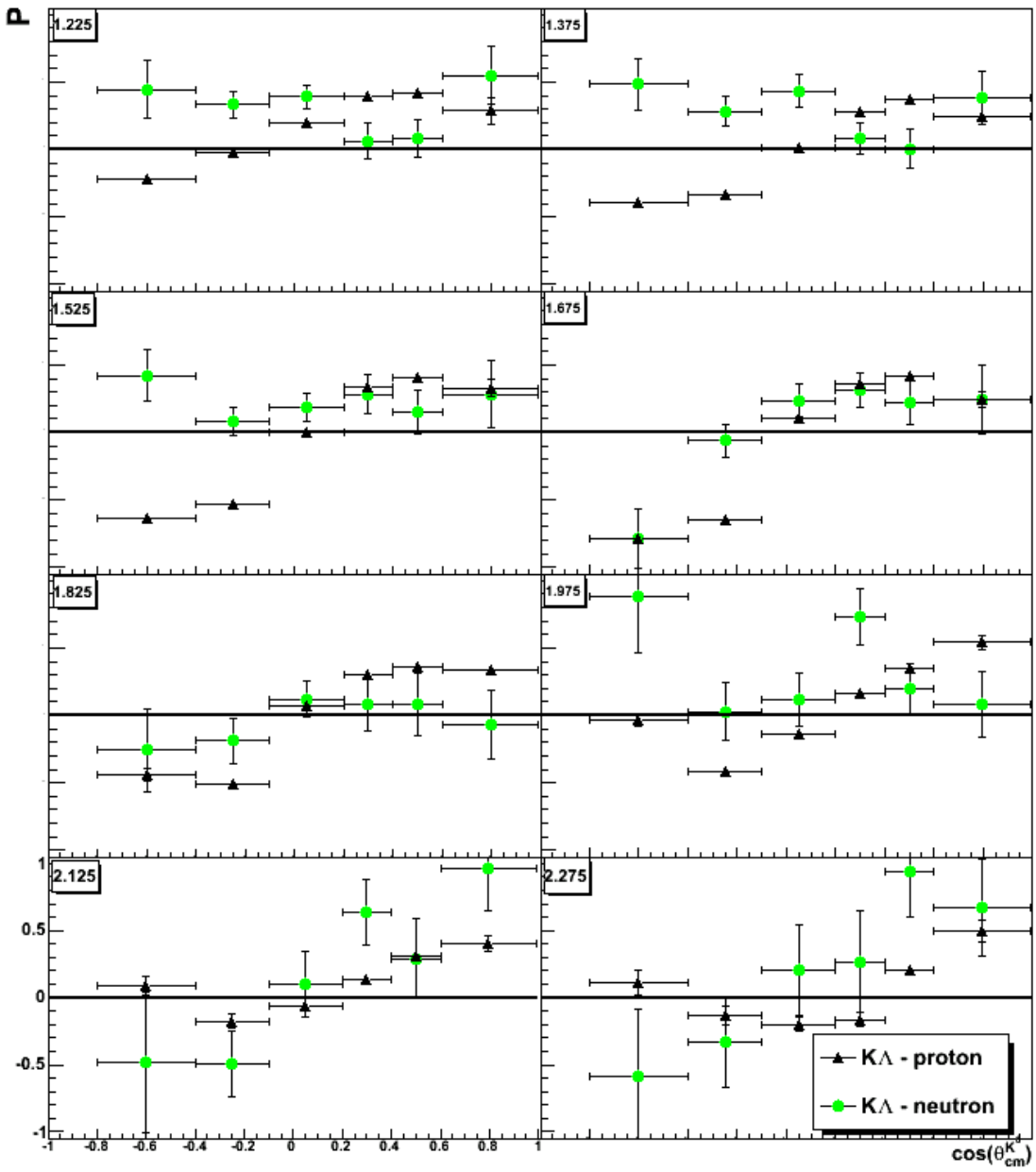

Figure 6.38: Hyperon recoil polarization results for the KΛ channel from the free proton (black triangles) compared to the results from the bound neutron (green circles).

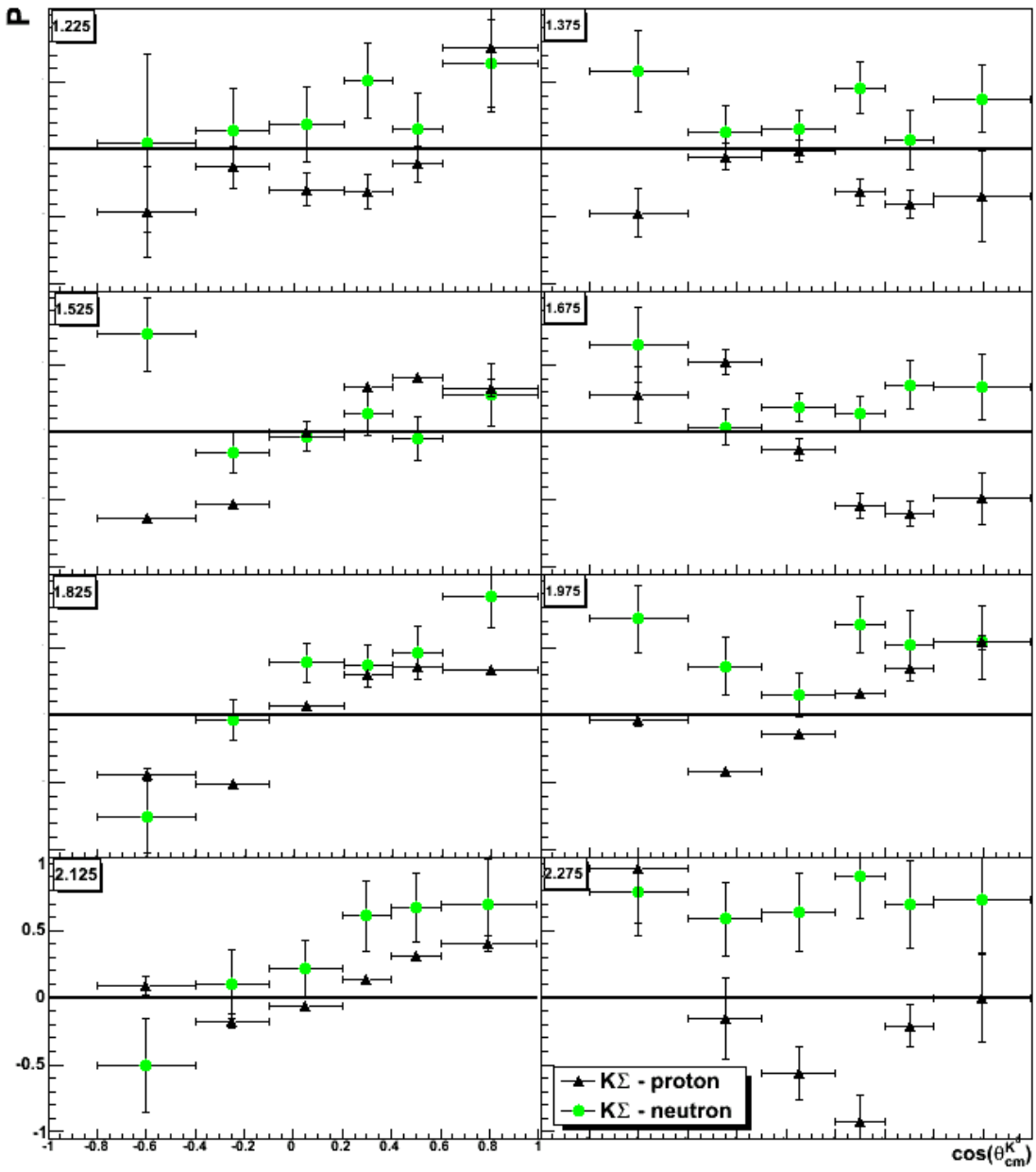

Figure 6.39: Hyperon recoil polarization results for the $K\Sigma^0$ channel from the free proton (black triangles) compared to the results from the bound neutron (green circles).

general trend of the data well at the lower energies. There is some disagreement in the sign and magnitude of the asymmetry between the data and model at the higher energies. The RPR model does not reproduce the data well. In both cases, the Kaon-MAID model and RPR approach clearly need more theoretical work in order to better reproduce the experimental results.

The O_x and O_z results are difficult to interpret as the lower statistics produce large error bars which makes comparisons with the different models difficult to make. In the $K^0\Lambda$ case for both O_x and O_z neither the Kaon-MAID or RPR models reproduce the data well. This suggests that more work is required on these models to provide calculations that accurately reproduce the experimental results. In the $K^0\Sigma^0$ case, the Kaon-MAID model for O_x including the core states describes the data well at lower energies but fails to accurately describe the data beyond 1.4 GeV. The Kaon-MAID core model for O_z reproduces the general trend of the data well at certain kinematics but does not provide an accurate description for all kinematics. The results for O_x and O_z are not well described by the RPR calculations. Clearly, further work is required to refine the model calculations.

The Kaon-MAID core and $D_{13}(1900)$ models for the $K^0\Lambda$ recoil polarization are indistinguishable which makes comparisons with the data very difficult. In general the RPR model does not provide an accurate description of the data. For the $K^0\Sigma^0$ reaction, the Kaon-MAID model describes the general trend of the data reasonably well except at the backward angles. It does not provide accurate predictions of the strength of the recoil polarization. The RPR model shows no agreement with the data over all kinematics.

Target asymmetry results for the $K^0\Lambda$ channel are in general not well described by the Kaon-MAID approach. There is some promising agreement between the data and models at 1.4 GeV and 2.0 GeV. However, the models are indistinguishable and therefore make drawing any conclusions difficult. Again in general the RPR model does not describe the data well. In the $K^0\Sigma^0$ case, there is a differing level of agreement between the Kaon-MAID model and the data. For energies between 1.2 - 2.0 GeV there is some agreement. The 1.8 GeV data shows excellent agreement with the Kaon-MAID core model. In contrast the RPR model does not describe the data well over all kinematics.

This work has highlighted the need for much more theoretical work to be done in developing accurate models for strangeness photoproduction on an effective deuteron target. In both cases the models are predictions based on information extracted from the $K^+\Lambda$ and $K^+\Sigma^0$ channels. It is assumed that the electromagnetic coupling constants of the resonances are isospin independent. This may not

be an accurate assumption as the comparison of the results for the photon beam asymmetry on the bound neutron with those on the free proton have highlighted a difference in the sign of the results in the $K^0\Sigma^0$ channel.

The work presented in reference [99] shows that for the photon beam asymmetry there is good overlap between the results for the free proton case and the bound proton in a deuteron. This gives confidence in the present analysis that by using the same spectator momentum cuts the contribution to the final results from re-scattering events will be negligible at the kinematics of this work. It can therefore be concluded that the deuteron is a suitable effective neutron target for measuring polarization observables.

Some of the results presented here have one obvious limitation in that they sometimes lie outwith the ± 1 limit. By construction polarization observables cannot have a value that is greater than unity. Statistically some level of disagreement is expected in the results. However, this constraint is enforced in the model calculations that the data are compared to. A Bayesian analysis on the data would ensure the data points and their error bars would lie within the ± 1 limits. The results from such a study could be compared to those obtained in this work for consistency checks. As the spin observables are not all independent, it would be interesting to assess their compatibility with one another. Further experimental work should also include measuring the remaining spin observables for the $\gamma n \rightarrow KY$ reactions which will allow for a model independent determination of the scattering amplitude. The next step would be for the Kaon-MAID and Regge-plus-resonance models to be refined by fitting them to the new data presented in this work. It is, however, important to note that the models used in this work represent only two of the many possible models available and all potential combinations of resonances and background terms available have not been exhausted.

To conclude, this work has produced the first ever measurements of five (Σ,P,T,O_x,O_z) polarization observables from the bound neutron. The results presented in this work have provided a further and significant step in determining the overall reaction amplitude for the $\gamma n \rightarrow KY$ channels and will provide stringent constraints for the new coupled-channels calculations aimed at resolving the ambiguities inherent in previous model approaches. The interpretation of these data is at an early stage and as the models develop, so too will our ability to interpret this data. These results are especially important for resonances that have significant neutron helicity amplitudes. In particular, the predicted large sensitivity of the $D_{13}(1900)$ missing resonance in the $\gamma n \rightarrow K^0\Lambda$ channel should

be resolved as theoretical support improves. No strong claims of finding a missing resonance can be made until there are improved theoretical models for strangeness production on the bound neutron. This work forms part of a much larger study aimed at finding missing resonances predicted by SU(6) $\otimes$ O(3) symmetric quark models. As the process of strangeness photoproduction is still not fully understood, there remains a great deal of information to be gained from polarization studies on the nucleon. This study has highlighted the limitations of the current theoretical models and has provided new data to help solve the missing resonance problem.

Bibliography

[1] S. Capstick and W. Roberts. Strange decays of nonstrange baryons. *Phys. Rev. D58:074011*, 1998.

[2] S. Janssen et al. *Phys. Rev. C65:015201*, 2001.

[3] T. Mart and C. Bennhold. Evidence for a missing nucleon resonance in kaon photoproduction. *Phys. Rev. C61:012201*, 1999.

[4] Donald H. Perkins. Introduction to high energy physics. *Cambridge University Press*, 1999.

[5] W. Heisenberg. *Eur. Phys. 77*, 1932.

[6] M. Gell-Mann and Y. Neeman. The Eightfold Way. *Benjamen*, 1964.

[7] O.W. Greenberg. Spin and unitary-spin independence in a paraquark model of baryons and mesons. *Phys. Rev. Lett. 13, 598-602*, 1964.

[8] M.Y. Han and Y. Nambu. Three triplet model with double SU(3) symmetry. *Phys. Rev. 139 B1006*, 1965.

[9] F.X. Lee et al. *hep-lat/0208070*, 2002.

[10] S. Eidelman et al. *Phys. Lett. B445, 20*, 2004.

[11] D. Faiman and A.W. Hendry. *Phys. Rev. 173, 1720*, 1968.

[12] C.P. Forsyth and R.E. Cutkosky. *Z. Phys. C18:219-227*, 1982.

[13] R. Koniuk and N. Isgur. Baryon decays in a quark model with chromodynamics. *Phys. Rev. D21:1868*, 1980.

[14] R.E. Cutkosky and R.E. Hendrick. Does the baryon spectrum reveal a diquark structure. *Phys. Rev. D16, 2902*, 1977.

[15] F.J. Keleman, D.B. Lichtenberg, and L.J. Tassie. *Phys. Rev. 167, 1535*, 1968.

[16] G. Penner and U. Mosel. Vector meson production and nucleon resonance analysis in a coupled-channel approach for centre of mass energies < 2 GeV. *Phys. Rev. C66:055212*, 2002.

[17] V. Shklyar, H. Lenske, and U. Mosel. Coupled-channel analysis of Kλ production in the nucleon resonance region. *Phys. Rev. C72:015210*, 2005.

[18] W. M. Yao et al (Particle Data Group). *J. Phys. Rev. G: Nucl. Part. Phys 33, 1*, 2006.

[19] M. Anselmino et al. *Rev. Mod. Phys. 65:1 199*, 1993.

[20] E. Santopinto. *Phys. Rev. C72:022201*, 2005.

[21] R. Bradford et al. First measurement of beam-recoil observables c_x and c_z in hyperon photoproduction. *Phys. Rev. C75:035205*, 2006.

[22] R. Bradford et al. *Phys. Rev. C75:035205*, 2007.

[23] U. Timm. Coherent bremsstrahlung of electrons in crystals. *Fortschritte der Physik*, 1969.

[24] R.A. Adelseck and B. Saghai. Kaon photoproduction: Data consistency, coupling constants and polarization observables. *Phys. Rev. C42, 108*, 1992.

[25] F.E. Low, G.F. Chew, M.L. Goldberger, and Y. Nambu. *Phys. Rev. 106, 1345*, 1957.

[26] I.S. Barker, A. Donnachie, and J.K. Storrow. Complete experiments in psuedoscaler photoproduction. *Nuclear Physics, B95, 347-456*, 1975.

[27] T. Mart and A. Sulaksono. *arXiv:nucl-th/0609077v1*, 2006.

[28] W-T Chiang and F. Tabakin. Completeness rules for spin observables in psuedoscalar meson photoproduction. *Phys. Rev. C55, 2054*, 1997.

[29] G. Keaton and R. Workman. *Phys. Rev C53:1434*, 1996.

[30] J.W.C. McNabb et al. Hyperon photoproduction in the nucleon resonance region. *Phys. Rev. C69:042201*, 2004.

[31] C. Paterson. *Polarization Observables in Strangeness Photoproduction with CLAS at Jefferson Lab.* PhD thesis, University of Glasgow, 2008.

[32] F. Klein et al. Search for missing nucleon resonances in the photoproduction of hyperons using a polarized photon beam and a polarized beam. *Jlab Internal Document.*

[33] P. Nadel-Turonski et al. Kaon production on the deuteron using polarized photons. *g13 proposal*, 2006.

[34] A.M. Sandorfi et al. Polarized neutrons in hd. *g14 proposal*, 2006.

[35] D. Glazier. *Private Communication.*

[36] K.H. Glander et al. *Eur. Phys. J. A19, 251*, 2004.

[37] M.Q. Tran et al. *Phys. Lett. B445:20-26*, 1998.

[38] R. Bradford. PhD thesis, Carnegie Mellon University, http://www.jlab.org/Hall-B/general/thesis/bradford/, 2005.

[39] B. Carnahan. *Strangeness Photoproduction in the $\gamma p \rightarrow K^0\Sigma^+$ Reaction.* PhD thesis, Catholic University of America, 2003.

[40] John W.C. McNabb. *Photoproduction of hyperons off protons in the Nucleon Resonance region using CLAS at Jlab.* PhD thesis, Carnegie Mellon University, 2002.

[41] T. Mart, C. Bennhold, H. Haberzettl, and L. Tiator. Kaon maid 2000. *http://www.kph.uni-mainz.de/MAID/kaon/kaonmaid.html*, 2000.

[42] A.V. Sarantsev et al. *Eur. Phys. J. A25, 441-453*, 2005.

[43] M. Vanderhaeghen, M. Guidal, and J.M. Laget. *Nucl. Phys. A627:645*, 1997.

[44] T. Cothal J. Ryckebusch and T. Van Cauteren. *Phys. Rev. C73:045207*, 2006.

[45] Bijan Saghail. From known to undiscovered resonances. *Nucl-th/0105001*, 2001.

[46] K. Hicks et al. Jlab Hall B completed experiment e-03-113. 2003.

[47] B. Mecking et al. Jlab Hall B completed experiment e-89-045. *http://www.jlab.org/expprog/proposals/89/PR89-045.pdf.*

[48] R.G.T Zegers et al. *Phys. Rev. Lett. 91, 092001*, 2003.

[49] H. Kohri et al. *hep-ex/0602015*, 2006.

[50] T. Watanabe et al. *arXiv:nucl-ex 0607022 v2*, 2006.

[51] T. Mizutani et al. *Phys. Rev. C58 75*, 1998.

[52] X. Artu, J.-M. Richard, and J. Soffer. *arXiv:nucl-th/0606050v2*, 2007.

[53] A. Waluyo. PhD thesis, The George Washington University, 2005.

[54] T. Feuster and U. Mosel. *Phys. Rev. C58:457*, 1998.

[55] V. Pascalutsa and J.A. Tjon. *Phys. Rev. C61:054003*, 2000.

[56] R.M. Davidson and R. Workman. *Phys. Rev. C63:025210*, 2001.

[57] M. Dugger et al. *Phys. Rev. Lett. 89, 222002*, 2002.

[58] T.P. Vrana, S.A. Dytman, and T.S.H. Lee. *Phys. Rep. 328, 181*, 2000.

[59] H. Thom. *Phys. Rev. 151, 1322*, 1966.

[60] C.E. Hyde-Wright, T. Mart, and C. Bennhold. *Phys. Rev. C51:R1074*, 1995.

[61] C. Bennhold L.E. Wright, R.A. Adelseck. *Phys. Rev. C32:1681*, 1985.

[62] C.R. Ji, R.A. Williams, and S.R. Contanch. *Phys. Rev. C46:1617*, 1992.

[63] G.H. Lamot J.C. David, C. Fayard and B Saghai. Electromagnetic production of associated strangeness. *Phys. Rev. C53:2613*, 1996.

[64] H. Haberzettl. *Phys. Rev. C56:2041*, 1997.

[65] S. Janssen et al. *Eur. Phys. J. A11, 105*, 2001.

[66] S. Janssen et al. *Phys. Rev. C66:035202*, 2002.

[67] D.G. Ireland, S. Janssen, and J. Ryckebush. *Nucl. Phys. A740, 147*, 2004.

[68] T. Corthals, J. Ryckebush, and T. Van Cauteren. *Phys. Rev. C73:045207*, 2006.

[69] A.V. Anisovich et al. *Eur. Phys. A25:427*, 2005.

[70] A.V. Anisovich et al. *Eur. Phys. A25:441*, 2005.

[71] K.H. Althoff et al. *Nucl. Phys. B137:269*, 1978.

[72] T. Regge. *Nuovo Cimento 14, 951*, 1959.

[73] M. Vanderhaeghen, M. Guidal, and J.M. Laget. *Phys. Rev. C61:025204*, 2000.

[74] S. Goers et al. *Phys. Lett. B464:331*, 1999.

[75] T. Corthals. *Regge Plus Resonance Approach to Kaon Production from the proton.* PhD thesis, Universiteit Gent, 2007.

[76] T. Van Cauteren, T. Corthal, D.G. Ireland, and J. Ryckebush. *arXiv:nucl-th/0612085v2*, 2008.

[77] B. Mecking. The CEBAF large acceptance spectrometer. *Nucl. Instr. and Meth. A503/03, 513*, 2003.

[78] C.W. Leeman et al. The Continuous Electron Beam Accelerator Facility: CEBAF at the Jefferson Laboratory. *Technical Report*, 2001.

[79] R.T Jones. Intense beams of polarized and nearly monochromatic photons from coherent bremmstrahlung. *Technical Report, Jlab internal publications*, 1999.

[80] T. Mart and C. Bennhold. *Phys. Rev. C61:012201*, 1999.

[81] Christopher I.O. Gordon. *Rho photoproduction using linearly polarized photons with the CLAS detector.* PhD thesis, University of Glasgow, 2004.

[82] Joseph James Melone. *Measurement of the photon asymmetry for the reaction $\gamma p \to K^+\Lambda^0$ at CLAS from 1.6 to 2.0 GeV.* PhD thesis, University of Glasgow, 2004.

[83] J. Kellie et al. The selection and performance of diamond radiators used in coherent bremsstrahlung experiments. *Nucl. Instr. and Meth. A545, 164-180*, 2005.

[84] W. J Briscoe et al. National Science Fund major research instrumentation, NSF award 9724489. *Technical Report.*

[85] D.I. Sober et al. *Nuclear Instruments and Methods in Physics Research A 440 263-284*, 1999.

[86] E.Smith et al. *Clas Note, 1999-011. Technical Report*, 1999.

[87] M. Amarian et al. The CLAS forward electromagnetic calorimeter. *Nucl. Instr. and Meth. A460, 239*, 2001.

[88] D.C Doughty et al. *Nucl. Sci. IEEE Transactions, 39:241-247*, 1992.

[89] Technical report Jefferson Lab online data acquisition. http://coda.jlab.org.

[90] V. Blobel. The BOS system, dynamic memory management. 1994.

[91] M. Ito. Mysql database for the monitoring of pass0/1 cooking of photon data. CLAS-NOTE 2004-003.

[92] E. Anciant et al. Clas-note 1999-04. Technical report, 1999.

[93] M.D. Mestayer. The CLAS drift chamber system. *Nucl. Instr. and Meth. A449, 81*, 2001.

[94] M. Guillo et al. EC time calibration procedure for photon runs in clas. *CLAS-NOTE 01-014*, 2001.

[95] A. Natter. http://www.pit.physik.uni.tuebingen.de/bremsanalytic.html.

[96] D. Cords et al. CLAS event format with BOS. *CLAS-NOTE 94-012*, 1994.

[97] K. Livingston. Rootbeer. Private Communication.

[98] E. Pasyuk. *Clas-note 2007-016, Technical Report*, 2007.

[99] J. R. Johnstone. *The Photon Beam Asymmetry for KY Production from the Bound Proton in Deuterium.* PhD thesis, University of Glasgow, 2009.

[100] D. Sohkan. PhD thesis, University of Edinburgh, 2009.

[101] Application Software Group/Geant. Detector description and simulation tool. Technical report, CERN, Geneva, Switzerland, 1993.

[102] D. Hamilton. *Private Communication*, 2009.

[103] K. Joo. GPP CLAS software routine. Technical report, Jefferson Lab.